Kyoto University

Doctor Thesis

Study of the neutrino mass hierarchy with the atmospheric neutrino data collected in Super-Kamiokande IV

Miao Jiang

A thesis submitted in fulfilment of the requirements
for the degree of Doctor of Science

in the

High Energy Physics Group
Department of Physics

March 2019

Abstract

Super-Kamiokande (SK) is a large underground water Cherenkov detector located in the Kamioka mine in Mt. Ikenoyama, Gifu Prefecture, Japan. The detector consists of a water tank holding 50 kt of ultra-pure water, and more than 11,000 photomultiplier tubes (PMT) for the Cherenkov light's detection. A new algorithm, named fiTQun, employs a maximum likelihood method using the charge and time information that is observed by the PMTs to reconstruct particle types and their kinematics in the detector. Comparing with the conventional reconstruction algorithm, fiTQun shows better performance.

An analysis of the neutrino mass hierarchy with the atmospheric neutrino data reconstructed by fiTQun in SK-IV with a livetime of 3118.5 days is presented in this thesis. Due to the improved performance of fiTQun, the fiducial volume (FV) is expanded from 22.5 kt to 29.7 kt by changing the FV cut from D_{wall}[1] > 200 cm to $D_{\mathrm{wall}} > 50$cm which provides higher statistics in this analysis. This analysis is performed for both the cases of free θ_{13} and θ_{13} constrained based on the result of reactor experiments. The best-fit results of the oscillation parameters for the analysis with constrained θ_{13} are $\sin^2\theta_{23} = 0.0425^{+0.046}_{-0.037}, |\Delta m^2_{32,31}| = 2.53^{+0.22}_{-0.12} \times 10^{-3}\mathrm{eV}^2, \delta_{CP} = 3.14^{+2.67}_{-1.35}$. The fit result also shows a weak preference for the normal hierarchy (NH) disfavoring the inverted hierarchy (IH) at 74% confidence level with a $\Delta\chi^2 \equiv \chi^2_{\mathrm{NH}} - \chi^2_{\mathrm{IH}} = -2.45$ assuming neutrino oscillations at the best fit of the analysis. The median expected sensitivity to the mass hierarchy is expected to over $\Delta\chi^2 = 3$ if the data collected in SK-I, II and III are also included. This sensitivity can be further improved to over $\Delta\chi^2 = 5$ if the data from the T2K experiment are analyzed simultaneously.

[1] The distance from the event vertex to the nearest wall of detector.

Acknowledgements

I sincerely appreciate the amazing people I met in this long journey. First and foremost, I would like to express my sincere gratitude to my advisor Prof. Tsuyoshi Nakaya. When I expressed the interests on neutrino physics, Prof. Tsuyoshi Nakaya kindly accepted me as a member of this excellent laboratory in Kyoto University and helped me a lot on the scholarship application. He also gave me enough freedom to select topics and many sage advice during research.

My work has benefited immensely from Roger Wendell, Michael Wilking, Shunichi Mine and Prof. Masato Shiozawa. Roger Wendell is both pragmatic and knowledgeable, and more importantly, always willing to go out of his way to help. He is delightful to have a conversation with on just about anything. Michael Wilking gave many insightful ideas from unique viewpoint about the fiducial volume expansion, which is essential part in this thesis. I learned many things about the energy scale and calibration from Shunichi Mine. He also showed me his academic rigor and research altitude, which inspired me a lot during my research. Prof. Shiozawa's comments always make me think about my analyses critically. My study always becomes more comprehensive during the discussion with him.

I appreciate all my friends from Kyoto University. My days at Kyoto University started with Tatsuya Hayashino, Keigo Nakamura, Ichinori Kamiji, Kota Nakagiri and Takuto Kunigo, who made me feel welcome in the new country and new environment. It was Tatsuya Hayashino who guided me through the first years on the life in Kyoto University and endured all my unsophisticated questions. Keigo Nakamura is always smiling and enthusiastic about helping others. I'm happy to have a mutual hobby with Ichinori Kamiji, who is kind and a lot of fun to talk with. The most friendly person in our laboratory is Kota Nakagiri, he often gives helpful advises to the juniors when they meet with trouble. Takuto Kunigo is a pretty cool guy with extensive observation and broad knowledge, I can always learn new things during conversation with him.

I would also thank senpai (senior students) who helped me a lot in Kamioka Observatory. Seiko Hirota is like a elder sister, she picked me up many times when I was lost in the Kamioka mountain or problems of physics. Kunxian Huang is a reliable brother, who led me on the road to python and pyROOT and taught me lot of things about data processing. Many thanks go to Shimpei Tobayama and Yusuke Suda, who gave me many insightful suggestions when I studied the new reconstruction algorithm, fiTQun, which is a crucial element of this thesis.

I appreciate the members of the ATMPD group who have endured my talks with increasing length over the years and gave me many helpful feedback. The work about the

retuning SK-I in this thesis is also benefited from the calibration and low-e group for the analysis of Nickel data and the simulation group for their help on SKDETIM.

It has been an honor to be member of Super-Kamiokande collaboration. Although I can't thank everyone whose path has crossed with the mine, your work ethic have been really inspiring. Your kindness has made the time in Kamioka Observatory one of my most treasured memories.

I appreciate the excellent laboratory of high energy physics at Kyoto University. Not only neutrino members, but also members from KOTO, ATLAS and CMB gave me stimulus of particle physics, and I benefit a lot from the discussions with them: Atsuko Ichikawa, Osamu Tajima, Masaya Ishino, Hajime Nanjo, Akihiro Minamino, Toshi Sumida, Kiseki Nakamura, Syunsuke Andachi, Shuhei Obara, Shunsuke Honda, Takahiko Masuda, Shota Takahashi, Naoki Kawasaki, Tatsuya Kikawa, Kento Suzuki, Daichi Naito, Yosuke Maeda, Shigeto Seki, Takuya Tashiro, Naoyuki Kamo, Shinichi Akiyama, Takaaki Hineno, Yuki Ishiyama, Kento Yoshida, Keisuke Kondo, Matoshi Shinohara, Saori Yanagita, Sei Ban, Mika Yamamoto, Ryutaro Monden, Kento Haneda, Ayami Hiramoto, Yohei Noguchi, Yoshie Nakanishi, Shunsuke Tanaka, Yosuke Ashida, Shunichi Akatsuka, Masamitsu Mori, Kazuhiro Nakamura, Yuuta Okazaki, Masashi Yoshida, Koichiro Kuniyoshi, Junta Komine, Kenji Yasutome, Tomofumi Abe, Takuji Ikemitsu, Takahiro Odagawa, Soichiro Kuribayashi, Masanori Tajima, Masayuki Hatano, Yuya Mino.

Also, I appreciate the financial support from Ministry of Education, Culture, Sports, Science and Technology of Japan (MEXT).

Finally, I give greatest thanks to my wife and my parents for their continuous support over the years and trust.

Contents

List of Figures

List of Tables

Chapter 1

Introduction

The neutrino is the second most abundant fundamental particle in the Standard Model, after only photons. Tens of billions of neutrinos pass through every square centimeter of the Earth every second. The neutrino was thought to be massless until the discovery of neutrino oscillation in late 1990s. Neutrino physics has achieved significant progress since then, however, many of the neutrino's characteristics are still unknown since neutrinos only interact with other matter via weak interactions. Nonetheless neutrinos are thought to have deep connections to the physics of the early universe and further study of these elusive particles may give insight into those processes.

1.1 Neutrino

The neutrino was first proposed by W. Pauli in 1930 to explain the continuum energy spectrum from the β decay ($n \to p + e^- + \bar{\nu}_e$). The first observation of neutrino was in 1956 by F. Reines and C. L. Cowan [29] by detecting anti-electron-neutrinos from a nuclear reactor via inverse β decay interaction: $\bar{\nu}_e + p \to n + e^+$. The second type of neutrinos ν_μ was discovered by L. M. Lederman, M. Schwartz and J. Steinberger in 1962 in the pion decay process at the Brookhaven's Alternating Gradient Synchrotron (AGS) [30]. In 2000, DONUT (Direct Observation of the NU Tau) experiment announced the discovery of the third species of neutrinos: ν_τ [31]. The result from the decay of Z^0 produced by e^+e^- collisions at Stanford Linear Collider (SLC) and Large Electron Positron collider (LEP) indicates that there are three (2.984±0.008) type of light neutrinos [1], which are affected by weak interaction [32].

One of the most frontier questions to today's astrophysicist and particle physicist is why our universe is matter-dominated. One of the conditions for such a matter-dominated

[1] Light means the mass of neutrino is less than half of Z^0 mass (∼91GeV).

universe, called Sakharov conditions, is the existence of CP violation: the violation of the combined charge and parity symmetries. The CP violation in quark sector has been discovered but its size is not large enough to explain the matter-antimatter imbalance observed today. Recent neutrino oscillation result from the T2K experiment indicates that the CP violation also exists for neutrinos with more than 95% probability [34], which means that the neutrino might play an important role in the creation of the matter-antimatter imbalance in the universe. The determination of δ_{CP} in the T2K experiment is based on the measurement of the oscillation probability difference between neutrino (e.g. $\nu_\mu \to \nu_e$) and antineutrino (e.g. $\bar{\nu}_\mu \to \bar{\nu}_e$). However, because of its fixed baseline, degeneracies between CP-violation and mass hierarchy in the oscillation probabilities limit the overall sensitivity. The sensitivity to the CP-violation can be improved by constraining the mass ordering (discussed below), for instance, from the measurement of atmospheric neutrinos sample, which is one of the goals of this thesis, to resolve such a degeneracy issue. Furthermore, atmospheric neutrinos themselves also offer additional sensitivity to the CP violation as well as other topics in neutrino oscillation physics.

1.2 Neutrino Oscillation

In the Standard Model of Particle Physics, neutrinos are assumed to be massless. However, neutrino oscillations observed in atmospheric [1], solar [35], accelerator [36] and reactor experiments [37, 38] indicate that neutrino flavor eigenstates actually consist of superposition of neutrino mass eigenstates, suggesting that the Standard Model needed revision.

In the neutrino oscillation diagram proposed by Maki, Nakagawa, Sakata [39] and Pontecorvo [40], the flavor eigenstates of neutrino can be written as mixing of mass eigenstates:

$$|\nu_\alpha\rangle = \sum_{i=1}^{3} U_{\alpha i}|\nu_i\rangle. \tag{1.1}$$

Here, $|\nu_\alpha\rangle$ represents the flavor eigenstate ν_e, ν_μ or ν_τ, $|\nu_i\rangle$ represents the mass eigenstate ν_1, ν_2 or ν_3. U is the Pontecorvo-Maki-Nakagawa-Sakata matrix (PMNS matrix), which is a 3×3 matrix describing the mixing of the flavor eigenstates and the mass eigenstates:

$$U = \begin{pmatrix} 1 & 0 & 0 \\ 0 & \cos\theta_{23} & \sin\theta_{23} \\ 0 & -\sin\theta_{23} & \cos\theta_{23} \end{pmatrix} \times \begin{pmatrix} \cos\theta_{13} & 0 & \sin\theta_{13}e^{-i\delta} \\ 0 & 1 & 0 \\ -\sin\theta_{13}e^{i\delta} & 0 & \cos\theta_{13} \end{pmatrix} \times \begin{pmatrix} \cos\theta_{12} & \sin\theta_{12} & 0 \\ -\sin\theta_{12} & \cos\theta_{12} & 0 \\ 0 & 0 & 1 \end{pmatrix}, \tag{1.2}$$

where $\theta_{ij}(i,j=1,2,3)$ represents the mixing angles between the mass eigenstates $|\nu_i\rangle$ and $|\nu_j\rangle$ and δ denotes the CP violation phase. The three matrices control the oscillations observed by atmospheric neutrinos experiments, reactor experiments [2] and solar neutrino experiments, respectively, which will be discussed later in this Chapter. The time evolution of the flavor eigenstates is

$$\begin{aligned} |\nu_\alpha(t)\rangle &= \sum_i U_{\alpha i} e^{-iE_i t} |\nu_i(t=0)\rangle \\ &= \sum_i \sum_{\alpha'} U_{\alpha i} U^*_{\alpha' i} e^{-iE_i t} |\nu'_\alpha(t=0)\rangle. \end{aligned} \tag{1.3}$$

Here, E_i represents the eigenvalue of the mass eigenstate $|\nu_i\rangle$. The probability for flavor eigenstate ν_α at $t=0$ to oscillate to state ν_β at time t is:

$$\begin{aligned} P(\nu_\alpha \to \nu_\beta) &= |\langle \nu_\beta(t) | \nu_\alpha(0) \rangle|^2 \\ &= |\sum_i U_{\beta i} U^*_{\alpha i} e^{-iE_i t}|^2 \\ &= \sum_i |U_{\alpha i} U_{\beta i}|^2 + \sum_{i \neq j} U_{\alpha i} U^*_{\beta i} U^*_{\alpha j} U_{\beta j} e^{-i(E_i - E_j)t}, \end{aligned} \tag{1.4}$$

The above equation shows that the transition phenomenon between different flavors, also known as neutrino oscillation, is due to the mass eigenstate mixing of neutrinos with finite mass.

The PMNS matrix U can be simplified for the case of the two-flavor mixing:

$$U = \begin{pmatrix} \cos\theta & \sin\theta \\ -\sin\theta & \cos\theta \end{pmatrix}. \tag{1.5}$$

Transition probability shown in Equation 1.4 can be simplified into:

$$P(\nu_\alpha \to \nu_\beta) = \sin^2 2\theta \sin^2 \left(\frac{(E_i - E_j)t}{2} \right). \tag{1.6}$$

[2] Strictly speaking, here refers to the reactor experiments with a short baseline such as Daya Bay ($\sim$ 50 km) and RENO ($\sim$ 1 km). The reactor experiments with a long baseline such as KamLAND ($\sim$ 180 km) is more sensitive to θ_{12}, like solar neutrino experiments.

For neutrinos with small finite mass, the following approximation can be made:

$$\begin{aligned} E_i - E_j &= \sqrt{(m_i^2 + p_i^2)} - \sqrt{(m_j^2 + p_j^2)} \\ &= p_i \left(1 + \frac{m_i^2}{p_i^2}\right)^{\frac{1}{2}} - p_j \left(1 + \frac{m_i^2}{p_j^2}\right)^{\frac{1}{2}} \\ &\approx \left(p + \frac{m_i^2}{2p}\right) - \left(p + \frac{m_j^2}{2p}\right) \\ &\approx \frac{\Delta m_{ij}^2}{2E}. \end{aligned} \tag{1.7}$$

Here, $\Delta m_{ij}^2 \equiv m_i^2 - m_j^2$ is defined as the mass-squared difference of the neutrino mass eigenstates. The momentum p_i and p_j are approximated to p and further approximated to E due to the small mass of neutrino. Substituting Equation 1.7 into Equation 1.6, with neutrino flight length L_ν and neutrino energy E_ν, in two-flavor mixing case, the survival probability of ν_α can be expressed as:

$$\begin{aligned} P(\nu_\alpha \to \nu_\alpha) &= 1 - P(\nu_\alpha \to \nu_\beta) \\ &= 1 - \sin^2 2\theta \sin^2 \left(\frac{\Delta m_{ij}^2 L_\nu}{4E_\nu}\right) \\ &= 1 - \sin^2 2\theta \sin^2 \left(\frac{1.27 \Delta m_{ij}^2(\mathrm{eV}^2) L_\nu(\mathrm{km})}{E_\nu(\mathrm{GeV})}\right). \end{aligned} \tag{1.8}$$

The oscillation probability therefore depends on the mixing angle θ, the mass square difference Δm_{ij}^2, flight length of neutrinos L_ν and energy of neutrinos E_ν. The oscillation amplitude is at maximum, i.e. the survival probability is at minimum when

$$\frac{L_\nu(\mathrm{km})}{E_\nu(\mathrm{GeV})} \sim \frac{\pi}{2.54 \times \Delta m_{ij}^2(\mathrm{eV}^2)}. \tag{1.9}$$

Therefore, neutrino oscillation experiments can measure the value of neutrino squared mass difference $|\Delta m_{ij}^2|$ and mixing angle $\sin^2 2\theta$ with 2-flavor oscillation paradigm by making suitable choices of L_ν and E_ν. To extract the sign of the mass difference and the precise mixing angle θ, oscillation between three flavor neutrinos needs to be considered, as will be discussed in Section 1.5.

1.3 Neutrino Oscillation Experiments

Neutrino oscillations have been confirmed by many experiments with various sources. Currently, the data are described well by the PMNS formalism involving all of the three active neutrino flavors, as introduced in previous section. Most of the oscillation

parameters have been experimentally measured [27]. In this section, some of those experiments which contributed to the discovery of neutrino oscillation or the oscillation parameter measurement will be introduced.

1.3.1 Atmospheric Neutrino and Accelerator Neutrino

As cosmic rays propagate in the atmosphere, they generate many pions and kaons in interactions with air nuclei as:

$$p + N \rightarrow N' + \pi^{\pm}/K^0/K^{\pm}, \tag{1.10}$$

where N and N' represent the nucleons in atmosphere. Atmospheric neutrinos are produced by decays of those mesons:

$$\begin{aligned} \pi^+ \rightarrow \quad & \mu^+ \quad +\nu_\mu \\ & \hookrightarrow \quad e^+ + \nu_e + \bar{\nu}_\mu, \end{aligned} \tag{1.11}$$

$$\begin{aligned} \pi^- \rightarrow \quad & \mu^- \quad +\bar{\nu}_\mu \\ & \hookrightarrow \quad e^- + \bar{\nu}_e + \nu_\mu. \end{aligned} \tag{1.12}$$

Therefore, both neutrinos and antineutrinos of both electron and muon type are contained in the atmospheric neutrino flux. The flavor ratio is expected to be $(\nu_\mu + \bar{\nu}_\mu) : (\nu_e + \bar{\nu}_e) \sim 2 : 1$. This ratio increases in high energy region due to the increase of the probability for $\mu^{\pm}$ to be observed before decaying. The flight length of atmospheric neutrinos ranges between $10 \sim 10^4$ km determined by the zenith angle of neutrino's path, which corresponds to the thickness of atmosphere and the diameter of the Earth, respectively. Together with energy range from 10^{-1} to 10^3 GeV, which can be detected by Super-Kamiokande detector (Super-K, SK), atmospheric neutrinos observed by Super-K cover a wide range of L/E, which means the sensitivity to Δm^2 is $10^{-1} \sim 10^{-4}$ eV^2 based on Equation 1.9.

In the early 1990's, a large deficit in the flavor ratio $(\nu_\mu + \bar{\nu}_\mu) : (\nu_e + \bar{\nu}_e)$ was observed by experiments using large underground water Cherenkov detectors such as Kamiokande [45] and IMB-3 [46]. The measured ratio was only a half of the expectation. This discrepancy is known as atmospheric neutrino anomaly, suggesting neutrino oscillations of a different kind from that affecting solar neutrinos, which will be introduced in next section, due to the very different L/E involved.

In 1998, a large deficit in the upward-going ν_μ events compared to the expectation assuming no oscillation (Figure 1.1) was reported by the Super-K collaboration [1]. This was the first evidence for the neutrino oscillation. Moreover, the zenith angle

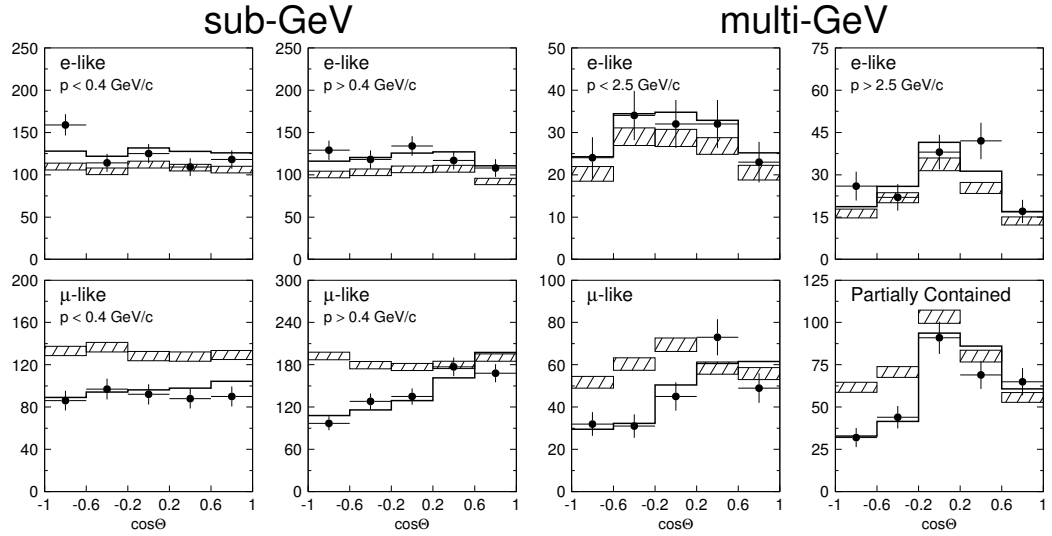

FIGURE 1.1: Zenith angle distributions for electron-like (top) and muon- like (bottom) events in sub-GeV (left) and multi-GeV (right) energy region, observed by Super-Kamiokande. Upward- and downward-going events are represented by negative and positive value of cos θ, respectively. The expectations without oscillations are represented by the hatched bands, while the black lines denote the best-fit to data with the oscillation between ν_μ and ν_τ. Taken from [1].

distributions of upward-going muons, which are created by ν_μ interactions in the rock around the detector such as MACRO [47] and Super-K [48], also show a disagreement to the non-oscillation expectation but consistency to the $\nu_\mu \leftrightarrow \nu_\tau$ oscillation hypothesis. A dip in the L/E distribution predicted from the neutrino oscillation was observed and reported by Super-K[49].

The atmospheric neutrino oscillation was then confirmed by experiments using neutrinos from accelerators. In such experiments, an intense ν_μ beam is generated by the hadronic showers from the collision between a high energy proton beam and a fixed target, and then the neutrinos are observed at a far detector, whose distance from the neutrino source is $O(100$ km). The accelerator neutrino beams generated in this way are almost pure ν_μ or $\bar{\nu}_\mu$ beams, which is controlled by changing the polarity of charge of the hadrons to be focused. In the accelerator neutrino beam, the contamination from ν_e or $\bar{\nu}_e$ is small. The neutrino energy is also tuned ~ 1 GeV to maximize the disappearance effect $\nu_\mu \to \nu_x$ at the far detector based on the Δm^2 obtained from the atmospheric neutrino. K2K [50] and MINOS [51] are the first of accelerator neutrino experiments with a long baseline. They reported consistent significant deficits in the number of observed events and distortions in the ν_μ energy spectrum. Their results are in a good agreement with the atmospheric neutrino measurement by Super-Kamiokande.

Many ongoing experiments are currently measuring the atmospheric neutrino mixing parameters (θ_{23} and $\Delta m^2_{32,31}$) with increasing precision. It should be noticed that the

sensitivity of current atmospheric and accelerator neutrinos experiment to the sign of Δm^2_{32} is limited, since the matter effect, which will be discussed in Section 1.5, is sub-dominant. [3]

The latest results for these two oscillation parameters from a combination of various experiments are as follows [27].
For normal mass hierarchy , $\Delta m^2_{32} > 0$:

$$\begin{aligned} \sin^2\theta_{23} &= 0.51 \pm 0.04 \\ |\Delta m^2_{32}| &= (2.45 \pm 0.05) \times 10^{-3}\text{eV}^2. \end{aligned} \tag{1.13}$$

For inverted mass hierarchy, $\Delta m^2_{32} < 0$:

$$\begin{aligned} \sin^2\theta_{23} &= 0.50 \pm 0.04 \\ |\Delta m^2_{32}| &= (2.52 \pm 0.05) \times 10^{-3}\text{eV}^2. \end{aligned} \tag{1.14}$$

1.3.2 Solar Neutrino and Reactor Neutrino

Electron neutrinos are generated by nuclear fusion reactions in Sun. The combined effect of the interaction in Sun can be written as:

$$4p \rightarrow {}^4\text{He} + 2e^+ + 2\nu_e + \gamma. \tag{1.15}$$

The energy of solar neutrinos varies from 0.1 MeV $\sim$ 10 MeV. The first experiment that observed solar neutrinos is the Homestake experiment [35]. A detector utilized 520 tons of chlorine to detect the electron neutrinos by counting the number of Ar produced by the reaction $\nu_e + {}^{37}\text{Cl} \rightarrow e^- + {}^{37}\text{Ar}$. Only about 1/3 of the prediction of the Standard Solar Model (SSM) were observed. Later experiments such as SAGE [52] and GALLEX [53], which utilize $\nu_e + {}^{71}\text{Ga} \rightarrow e^- + {}^{71}\text{Ge}$, and Kamiokande experiment [54], a water Cherenkov detector, also observed such deficits. This discrepancy between the measurement and prediction of solar neutrino flux, which was known as the solar neutrino problem, had been unresolved for more than 30 years until the discovery of the neutrino oscillation by Sudbury Neutrino Observatory (SNO) experiment [55].

The SNO [56], which is a heavy water (D_2O) Cherenkov detector, measures both ν_e flux and the total neutrino flux ($\nu_e + \nu_\mu + \nu_\tau$) from the Sun. Neutrinos in SNO are detected by the charged-current (CC) and neutral-current (NC) interactions on deuterium and

[3] It should be noted that this is not the case for Δm^2_{21}, since the electron densities in the Sun is very large which makes the matter effect is strong. Such effect observed in solar neutrinos (i.e. ν_e) are only possible if $\Delta m^2_{21} > 0$ which is similar to the atmospheric case discussed in Section 1.5.

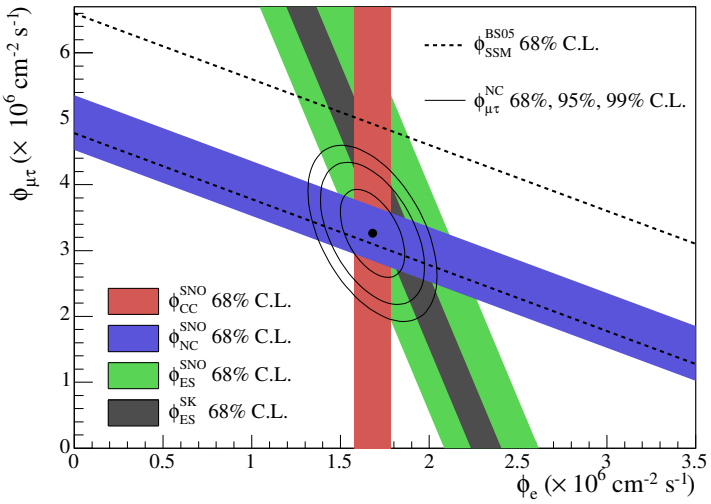

FIGURE 1.2: ^{8}B solar neutrino flux measured by SNO with different channels. The horizontal axis shows the ν_e flux and the vertical axis shows the sum of the ν_μ and ν_τ flux. The allowed regions at 68% from the measurements of CC, NC and ES channels are represented as the red, blue and green bands respectively. The gray band denotes the ES measurement result from Super-Kamiokande [2]. The dashed lines represents the prediction of the total neutrino flux based on Standard Solar Model. The point and the contours show the best estimate and the allowed regions at 68, 95 and 99% confidence levels by combining the results from CC and NC. Taken from [3].

also by elastic-scattering (ES) on electron as the following:

$$\text{CC} \quad : \quad \nu_e + d \rightarrow p + p + e^- \tag{1.16}$$

$$\text{NC} \quad : \quad \nu_x + d \rightarrow p + n + \nu_x \tag{1.17}$$

$$\text{ES} \quad : \quad \nu_x + e^- \rightarrow \nu_x + e^-, \tag{1.18}$$

where ν_x denotes any of the three neutrino flavors. The total number of neutrinos observed is consistent with the prediction from the SSM. As shown in Figure 1.2, about one third of the observed neutrinos are electron neutrinos, which is also consistent with the SSM prediction. The deficit of ν_e and presence of non-ν_e component in the solar neutrino flux was also observed by Super-Kamiokande experiment, an H_2O Cherenkov detector [2]. Combination results from SNO and Super-K showed that the non-electron neutrino flux is due to the flavor transition of the solar neutrinos via the mechanism called the large mixing angle (LMA) MSW solution[4] [57, 58].

Similar deficit of $\bar{\nu}_e$ flux was also confirmed by the KamLAND experiment [59], which detects $\bar{\nu}_e$ from nuclear reactors with energy from 0.9 MeV to 8.5 MeV using liquid

[4]The large mixing angle means a large value of θ in Equation 1.8. The value of $\tan^2(\theta)$ is around 0.4 for LMA, while it is only 4×10^{-4} for the small mixing angle solution, which was another possible solution at that time.

scintillator. In KamLAND, e^+ and neutron will be generated by inverse β-decay interaction $\bar{\nu}_e + p \rightarrow e^+ + n$ after $\bar{\nu}_e$ enter the detector. By combining the prompt signal from e^+ and the delayed signal from the gamma generated by the neutron capture, the background level can be suppressed significantly. Considering the energy of the $\bar{\nu}_e$ from the nuclear reactors is about 3 MeV and the average distance to the rectors is 180 km, the sensitivity to Δm^2_{12} is at the order of 10^{-5} eV, based on Equation 1.9.

The current known values for θ_{12} and Δm^2_{21} obtained from the combination of oscillation results of various solar and reactor neutrino experiments are [27]:

$$\Delta m^2_{21} = (7.53 \pm 0.18) \times 10^{-5} eV^2, \tag{1.19}$$

$$\sin^2 \theta_{12} = 0.307 \pm 0.013. \tag{1.20}$$

1.3.3 Mixing Angle θ_{13}

The third mixing angle θ_{13} was thought to be small since both solar and atmospheric neutrino results could be explained assuming it is zero, i.e. two flavor mixing, with two different Δm^2. The first attempt to measure θ_{13} was made by the CHOOZ experiment [60], which detected reactor $\bar{\nu}_e$ with a much shorter base line $\sim$ 1 km than that of KamLAND. The dominant contribution at this distance is θ_{13} and Δm^2_{31} rather than the "solar" oscillation parameters like KamLAND. The survival probability of reactor $\bar{\nu}_e$ can be expressed as:

$$P(\bar{\nu}_e \rightarrow \bar{\nu}_e) = 1 - \sin^2 2\theta_{13} \sin^2(\frac{1.27 \Delta m^2_{31} L}{E_\nu}). \tag{1.21}$$

CHOOZ finally found no evidence for $\bar{\nu}_e$ disappearance. The upper limit of $\sin^2 2\theta_{13}$ is given as less than 0.15 at 90% confidence level [60].

In 2012, the reactor experiments with a short baseline including Daya Bay[37], Double Chooz[61] and RENO[38] reported that $\sin^2 2\theta_{13} \sim 0.1$ separately. A clear deficit in the reactor $\bar{\nu}_e$ flux was observed. The hypothesis of a zero-value of θ_{13} was excluded by Daya Bay and RENO at 5.2σ and 4.9σ, respectively.

Besides the reactor experiments, the value of θ_{13} can also be obtained by observing the appearance of ν_e in a ν_μ beam generated by accelerator. The appearance probability of ν_e is proportional to $\sin^2 2\theta_{13}$, as Equation 1.25. The first decisive evidence for the ν_e appearance was shown by T2K in 2013 at 7.3 σ [62].

The current best constrains on θ_{13} are provided by the reactor experiments. The global averaged value is [27]:

$$\sin^2 \theta_{13} = 0.0210 \pm 0.0011. \tag{1.22}$$

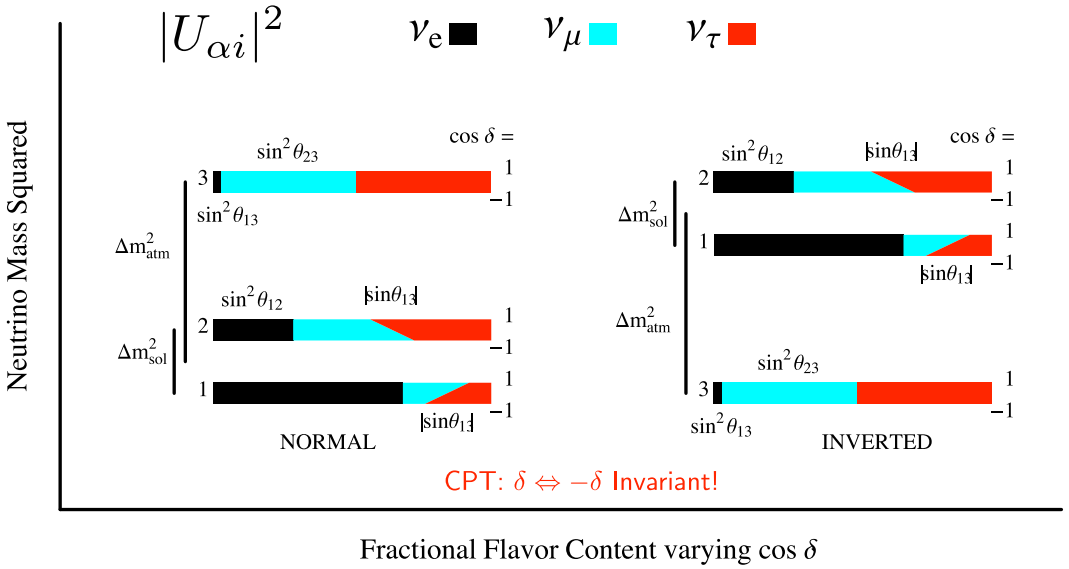

FIGURE 1.3: Two possible mass hierarchies for the three neutrino mass eigenstates. The varying width of the shadings shows the variation with respect to cosine of the CP violating phase δ. Taken from [4].

1.4 Unresolved Issues

The global best fit results to the parameters of neutrino oscillation are summarized in Table 1.1. Though most of these parameters have been experimentally measured [27], the ordering of the mass states with the largest splitting,[5] the octant of the atmospheric mixing angle θ_{23} ($\sin^2\theta_{23} < 0.5$ or > 0.5), and the value of the CP-violating phase are unknown.

Parameter	Best fit $\pm$ 1σ C.L.
Δm^2_{21}	$(7.53 \pm 0.18) \times 10^{-5}$ eV^2
$\sin^2\theta_{12}$	0.307 ± 0.013
$\sin^2\theta_{13}$	0.0210 ± 0.0011
$\sin^2\theta_{23}$	$0.51(0.50) \pm 0.04$
$\lvert\Delta m^2_{31}\rvert$	$(2.45(2.52) \pm 0.05) \times 10^{-3}$eV^2

TABLE 1.1: Summary of global best fit to the parameters of neutrino oscillation. The number in the parentheses represents the result for inverted hierarchy. Taken from [27]

While the value of the neutrino mass splitting have been measured with a certain precision, the sign of $\Delta m^2_{32,31}$ has not been determined yet. As shown in Figure 1.3, the case $\Delta m^2_{32,31} > 0$ is termed as normal hierarchy (NH) which means that the mass eigenstate ν_3 has the largest mass, whereas $\Delta m^2_{32,31} < 0$ is called inverted hierarchy (IH) in which case the mass eigenstate ν_3 has the smallest mass. For the problem related to the neutrino mass, besides the hierarchy, the absolute mass and its origin are still unknown.

[5] Also known as the mass hierarchy, and indicated by the sign of Δm^2_{32}.

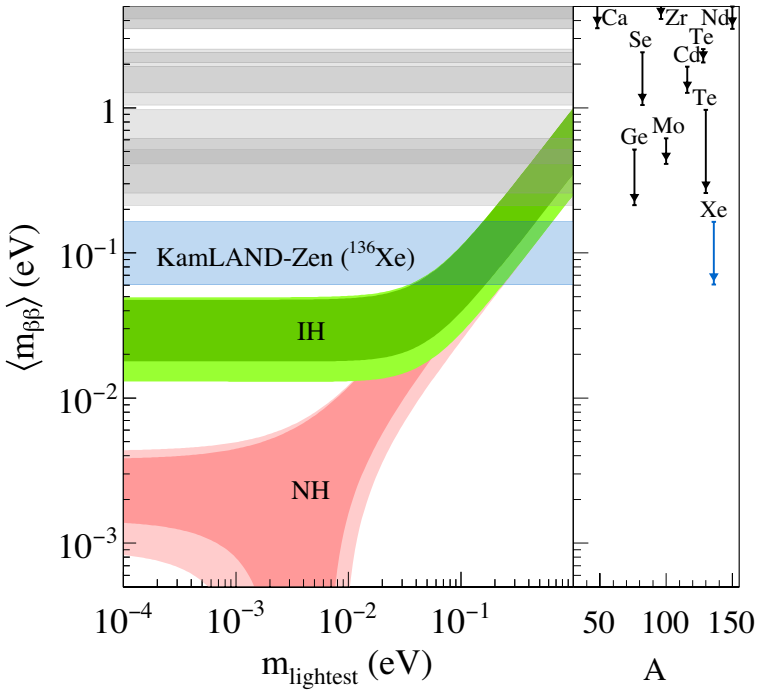

FIGURE 1.4: Effective Majorana neutrino mass $\langle m_{\beta\beta} \rangle$ as a function of the lightest neutrino mass m_{lightest}. The dark shaded region shows the expectations based on the best-fit values of neutrino oscillation parameters for both normal hierarchy (NH) and inverted hierarchy (IH), respectively. The light shaded regions considers the 3σ uncertainties of those parameters. The cyan horizontal bands indicate 90% C.L. upper limits on $\langle m_{\beta\beta} \rangle$ with ^{1}36Xe from KamLAND-Zen. Right panel shows the corresponding limits for each nucleus as a function of the mass number. Taken from [5].

Some theories assume that neutrinos are Majorana fermions, which means that a neutrino is its own antiparticle. The Majorana fermion is a new type of elementary particles and has never been observed until now. The next generation of neutrino-less double beta decay experiments might give us some insight on this issue if the mass hierarchy is determined to be inverted as shown in Figure 1.4 [5]. Therefore, the determination of the mass hierarchy could also provide valuable input to study the massive neutrinos' fundamental properties.

Furthermore, it is also not known whether θ_{23} mixing is exactly maximal ($\sin^2\theta_{23} = 0.5$), and if not, whether the angle is smaller ($\sin^2\theta_{23} < 0.5$, first octant) or larger ($\sin^2\theta_{23} > 0.5$, second octant). This issue is known as the octant of θ_{23}. A new underlying fundamental symmetry of the neutrino mixing matrix and of the lepton sector of particle physics might be revealed if θ_{23} mixing is found to be maximal. Furthermore, the size of matter effect, which will be discussed in Section 1.5, is crucial to the determination of the mass hierarchy and depends on the value of $\sin^2\theta_{23}$. The high precision measurement of $\sin^2\theta_{23}$ will also provide a test of many theories of neutrino masses and mixing. Current primary approach to measure θ_{23} is to observe the disappearance of ν_μ, which

depends on $\sin^2 2\theta_{23}$ dominantly. The measurement on subdominant oscillation effect, such as the oscillation between ν_μ and ν_e with a leading term depending on $\sin^2\theta_{23}$, is necessary to determine the octant of θ_{23}.

The final, and probably most important question is whether CP is violated for leptons. In some leading theories, the asymmetry between matter and antimatter in current matter-dominated universe can be contributed by the CP violation in the lepton sector [63]. As T2K and reactor experiments have shown a non-zero θ_{13}, the question of CP-violation in the lepton sector might be addressed by neutrino oscillation measurement, as the CP-violation phase δ_{CP} appears as a combination with θ_{13} in Equation 1.2. The determination of δ_{CP} is mainly based on the measurement of the oscillation probability difference between neutrino (e.g. $\nu_\mu \to \nu_e$) and antineutrino (e.g. $\bar{\nu}_\mu \to \bar{\nu}_e$). Since the matter effects could also cause such a difference on the oscillation probability, there is a degeneracy between CP-violation and mass hierarchy, especially for the accelerator experiment with a fixed beamline. The sensitivity to δ_{CP} of several ongoing and proposed neutrino oscillation experiments can be improved significantly if the mass hierarchy is known [64].

Some latest results, e.g. T2K [22], NOvA [41] and Super-Kamiokande [6] experiments have given us some insight to those unresolved issues. Next-generation experiments planned in both the U.S. [42], China [43], and Japan [44] also focus on these issues and exhibit the possibility to resolve them. Since the atmospheric neutrino cover a wide range of L/E, so it can contribute to the measurement of those parameters, as we will see in next Section.

1.5 Sub-Dominant Effects of Atmospheric Neutrino Oscillation

Beside the dominant oscillation channel between ν_μ and ν_τ, the oscillation $\nu_\mu \to \nu_e$ induced by θ_{13} and θ_{12} also affects the survival possibility for ν_μ and appearance possibility for ν_e.

As has been stated in previous section, the atmospheric neutrinos cover a wide range of L/E, which results in the sensitivity to Δm^2 from 10^{-1} to 10^{-4} eV^2. Therefore, both $\Delta m^2_{32,31}$ ($\sim 10^{-3}$ eV^2) and Δm^2_{21} ($\sim 10^{-5}$ eV^2) affect the transition possibility of $\nu_\mu \to \nu_e$. Their contributions vary as the neutrino energy.

For the multi-GeV region, which means the energy is larger than 1.33 GeV for the Super-K experiment, the contribution from Δm^2_{21} is enough small to be ignored, the leading

term of the probability for the oscillation between ν_e and ν_μ in vacuum therefore can be expressed as:

$$P(\nu_e \to \nu_e) = 1 - \sin^2 2\theta_{13} \sin^2 \left(\frac{1.27\Delta m^2_{32} L}{E} \right) \tag{1.23}$$

$$P(\nu_\mu \to \nu_\mu) \cong 1 - 4\cos^2 \theta_{13} \sin^2 \theta_{23} (1 - \cos^2 \theta_{13} \sin^2 \theta_{23}) \times \sin^2 \left(\frac{1.27\Delta m^2_{32} L}{E} \right) \tag{1.24}$$

$$P(\nu_\mu \to \nu_e) = P(\nu_e \to \nu_\mu) = \sin^2 \theta_{23} \sin^2 2\theta_{13} \sin^2 \left(\frac{1.27\Delta m^2_{32} L}{E} \right). \tag{1.25}$$

When the atmospheric neutrinos traverse the Earth, the potential from the Earth's matter effect due to the amplitude of forward scattering via charged current interactions between electrons and $\nu_e/\bar{\nu}_e$ has to be taken into account. Since ν_e, and only ν_e can interacts with the electrons in the Earth via $W^\pm$ bosons, the amplitude of forward scattering for ν_e differs from those of the other flavors (i.e. ν_μ and ν_τ). The effective potential for the interaction via $W^\pm$ bosons is therefore applied to ν_e, which is as the matter effect or the MSW effect of neutrino oscillations [57, 58]. For the scenario above the oscillation parameters $\sin^2 \theta_{13}$ and Δm^2_{32} in Equation 1.25 are replaced by their matter-equivalents [65],

$$\sin^2 2\theta_{13,M} = \frac{\sin^2 2\theta_{13}}{(\cos 2\theta_{13} - A_{CC}/\Delta m^2_{32})^2 + \sin^2 2\theta_{13}}, \tag{1.26}$$

$$\Delta m^2_{32,M} = \Delta m^2_{32} \sqrt{(\cos 2\theta_{13} - A_{CC}/\Delta m^2_{32})^2 + \sin^2 2\theta_{13}}. \tag{1.27}$$

Here $A_{CC} = \pm 2\sqrt{2} G_F N_e E_\nu$ is the effective potential and it is positive (> 0) for neutrino or negative (< 0) for antineutrino. The electron density N_e is assumed to be constant and G_F denotes the Fermi constant.

When $A_{CC}/\Delta m^2_{32} = \cos 2\theta_{13}$, these matter variables are resonantly enhanced. Since $\cos 2\theta_{13}$ is positive, the enhancement only happens for neutrinos if the hierarchy is normal (both of A_{CC} and Δm^2_{32} are positive) while it only occurs for antineutrinos for the case of the inverted hierarchy (both of A_{CC} and Δm^2_{32} are negative). Actually, electron density N_e changes as neutrinos travel through the Earth due to the varying matter profile. Neutrinos experience a variety of matter effects and similar enhancements to the oscillation probability. The most strong matter effect occurs for the neutrinos with a few to ten GeV of energy through the Earth's core, as shown in the top right figure in Figure 1.5.

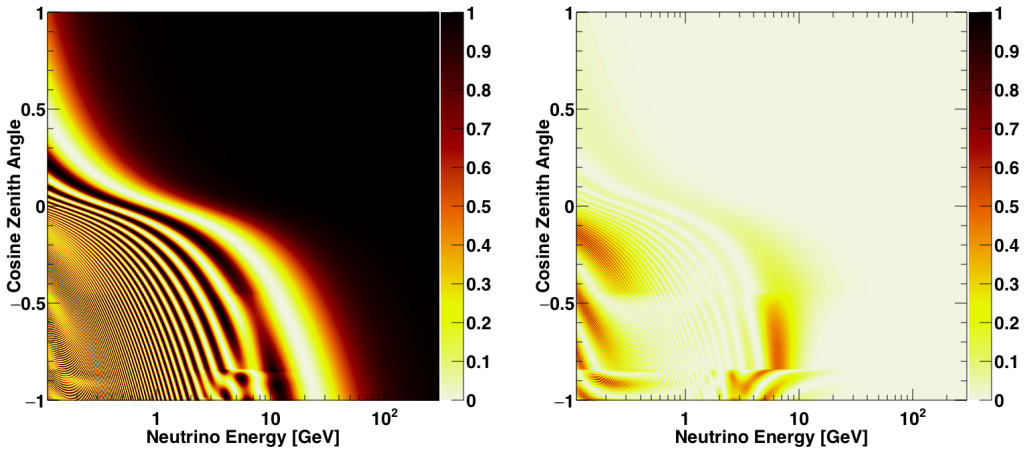

(a) $P(\nu_\mu \to \nu_\mu)$ (b) $P(\nu_\mu \to \nu_e)$

(c) $P(\bar{\nu}_\mu \to \bar{\nu}_\mu)$ (d) $P(\bar{\nu}_\mu \to \bar{\nu}_e)$

FIGURE 1.5: Oscillation probabilities for neutrinos (upper panels) and antineutrinos (lower panels) as a function of energy and zenith angle assuming a normal mass hierarchy. Matter effects in the Earth distorted the neutrino oscillation probability between 2 and 10 GeV, while there is no such distortion in the antineutrino figures. For an inverted hierarchy, the distortion caused by matter effects appear in the antineutrino figures. The discontinuities near $\cos\theta_{\text{zenith}} = -0.5$ and -0.8 are due to the matter density change between crust, mantle and core. Here the oscillation parameters are taken to be $\Delta m^2_{32} = 2.5 \times 10^{-3}\text{eV}^2$, $\sin^2\theta_{23} = 0.5$, $\sin^2\theta_{13} = 0.0219$, and $\delta_{CP} = 0$. Taken from [6]

On the other hand, the patterns on the oscillation probability below 1 GeV are driven by the solar neutrino mixing parameters, θ_{12} and Δm^2_{21}. The effect of θ_{13} can be ignored since it is subdominant, then the oscillation probabilities can be written as [67]:

$$\begin{aligned} P(\nu_e \to \nu_\mu) &= P(\nu_\mu \to \nu_e) \\ &= P_{ex} \cos^2 \theta_{23}, \qquad (1.28) \\ P(\nu_e \to \nu_e) &= 1 - P_{ex}, \qquad (1.29) \end{aligned}$$

where

$$P_{ex} = \sin^2 2\theta_{12,M} \sin^2 \left(\frac{1.27 \Delta m^2_{21,M} L}{E} \right). \qquad (1.30)$$

Here the matter effect has been considered and the corrected parameter $\Delta m^2_{21,M}$ and $\sin^2 2\theta_{12,M}$ can be written easily by replacing the mass splitting and mixing angle and in Equation 1.26 and 1.27 by θ_{12} and Δm^2_{21}. Considering contribution from both ν_e and ν_μ produced in the atmosphere, the observed ν_e flux after oscillation Φ_e is

$$\Phi_e = \Phi^0_e (1 - P_{ex}) + \Phi^0_\mu (P_{ex} \cos^2 \theta_{23}), \qquad (1.31)$$

where Φ^0_e and Φ^0_μ represent the flux of ν_e and ν_μ before oscillation. For simplicity, let $r := \Phi^0_e / \Phi^0_\mu$, which means the ratio of ν_μ and ν_e before oscillation, and then the Equation 1.31 can be rewritten as:

$$\frac{\Phi_e}{\Phi^0_e} - 1 = P_{ex}(r \cos^2 \theta_{23} - 1). \qquad (1.32)$$

The flux flavor ratio r is about 2 for low energy atmospheric neutrinos. Therefore, an excess of sub-GeV ν_e flux would be observed for $\theta_{23} < \pi/4$ case while a deficit would be seen instead when $\theta_{23} > \pi/4$.

For the full three flavor oscillation analysis, besides the θ_{13}, θ_{12} and their interference, the oscillation probability is also affected by the CP violation phase δ_{CP}, which results in a change about $\sim 2\%$ on the total ν_e flux observed in sub-GeV at maximum. The atmospheric neutrinos therefore have some sensitivity to CP violation. In Section 7.2, the oscillation effects discussed here will be revisited.

1.6 Thesis Overview

This thesis shows an analysis of 3118.5 days of SK-IV atmospheric data with a 30% larger fiducial volume (FV) than previous Super-K analyses for a 253.9 kiloton·year exposure. The detector is introduced in Chapter 2. In Chapter 3 the simulation of atmospheric

neutrino flux, neutrino interaction and data are discussed. The calibration method and its result, which are essential to the atmospheric neutrino oscillation analysis, are detailed in Chapter 4. The data reduction of atmospheric neutrino sample and event categorization are discussed in Chapter 5. The new reconstruction algorithm and its performance in comparison to the conventional reconstruction are detailed in Chapter 6. Based on this performance improvement, an analysis of the atmospheric neutrino data with the expanded fiducial volume and corresponding systematic errors is presented in Chapter 7, before concluding in Chapter 8.

Chapter 2

The Super-Kamiokande Detector

Super-Kamiokande is a cylindrical 50 kton water Cherenkov detector located at Kamioka Observatory of Institute for Cosmic Ray Research in Gifu Prefecture, Japan. The schematic view and the location of the detector are shown in Figure 2.1. The detector is located in a obsolete zinc mine in Mountain Ikenoyama. The mean rock overburden over the detector is $\sim$ 1000 m, which is $\sim$ 2700 m water equivalent. The flux of cosmic ray muon observed by Super-Kamiokande is therefore reduced by 5 orders comparing to that on the surface of the Earth.

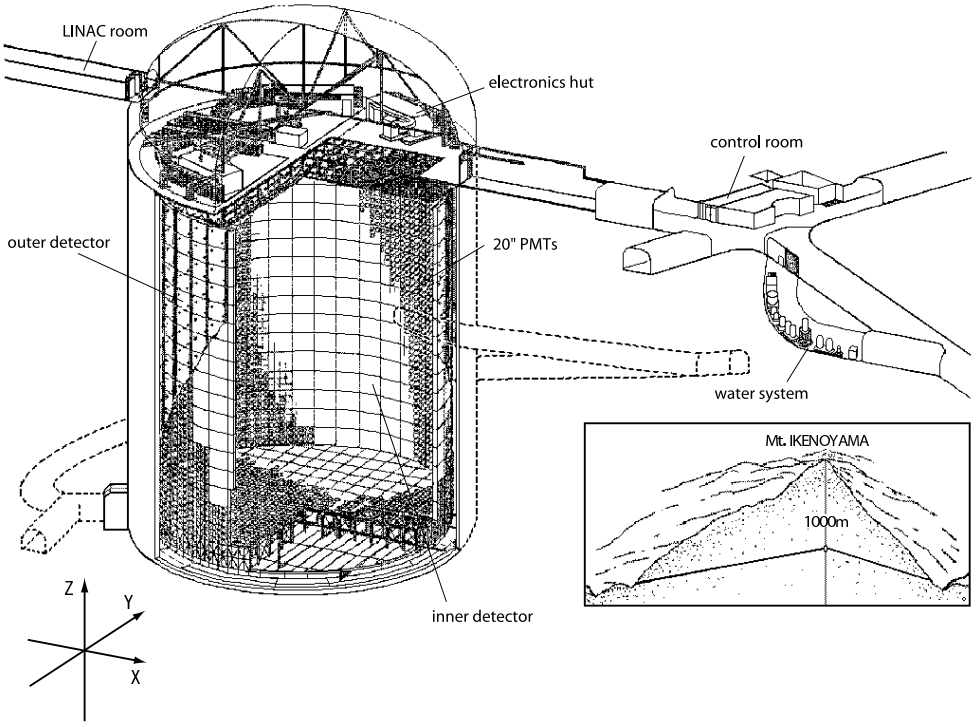

FIGURE 2.1: Super-Kamiokande detector and its location in Mountain Ikenoyama. Take from [7]

The main physics goal of the Super-Kamiokande experiment is the detection of nucleon decays and the studies of neutrinos from difference sources, including atmospheric neutrinos, solar neutrinos, supernova neutrinos and other astrophysical sources. Furthermore, the Super-Kamiokande detector is also utilized as a far detector for the T2K experiment, a long-baseline neutrino oscillation experiment using accelerator neutrinos [26].

The first phase of Super-Kamiokande experiment (SK-I) started observing in April, 1996 and continued to take the data for five years until the maintenance in July, 2001. An accident occurred during water refilling after the maintenance in November 2001. More than half of the PMTs were destroyed in that accident. The Suepr-Kamiokande detector resumed observation with half PMT density in the inner detector (ID) from October, 2002, which is referred to as SK-II period. SK-II kept measuring for three years and finished in October 2005 for PMT density resumption work. The observation of SK-III period is restarted in June, 2006 with the same density of PMT as SK-I. This phase of the experiment ended in August 2008 to upgrade electronics. The new phase, referred to as SK-IV, collected data from September 2008 till May 2018. In June 2018, refurbishment work starts as a preparation for Super-Kamiokande Gadolinium Project [69], which is aimed to increase the detection efficiency to low energy anti-neutrinos with neutron tagging, via the addition of water-soluble gadolinium salt.

In this thesis, only the data observed in SK-IV (2008-2018) is used. The configuration of the Super-K detector in SK-IV will be introduced in this Chapter.

2.1 Cherenkov Radiation

The charged particles are observed by the Super-Kamiokande detector by Cherenkov light detection. When a charged particle travel through the medium with a speed faster than the light speed in the medium, an electromagnetic radiation named as Cherenkov radiation will be emitted. The momentum thresholds of the Cherenkov radiation in pure water for charged particles frequently observed in Super-K detector are summarized in Table 2.1.

Particle type	electron	muon	charged pion	proton
Momentum threshold (MeV/c)	0.57	118	156	1051

TABLE 2.1: Momentum thresholds of Cherenkov radiation in pure water.

The Cherenkov radiation is emitted in a cone shape with a half opening angle θ_C with respected to the direction of the particle's momentum. The half opening angle (also referred to as Cherenkov angle) is determined by $\cos\theta_C = 1/n\beta$, where $\beta = v/c$ and n

represents the refractive index of the medium. The Cherenkov angle in water is about 42° for a relativistic particle with $\beta \sim 1$ and $n = 1.33$.

The number of photons produced by the Cherenkov radiation is a function of wavelength λ as [27]:

$$\frac{d^2N}{dxd\lambda} = \frac{2\pi\alpha}{\lambda^2}(1 - \frac{1}{n^2\beta^2}). \tag{2.1}$$

Here, x represents the path length of the particle and α represents the fine structure constant. In the sensitive region of the Super-K PMTs, whose wavelength ranges from 300 nm to 600 nm, about 340 photons are emitted per centimeter.

The projection of the Cherenkov light on the wall of the inner detector is a ring. The information of the particles, including its type, position and momentum are extracted from such a ring by the event reconstruction algorithm, which will be introduced in Chapter 6. A example of neutrino event observed by Super-K detector is shown in Figure 2.2.

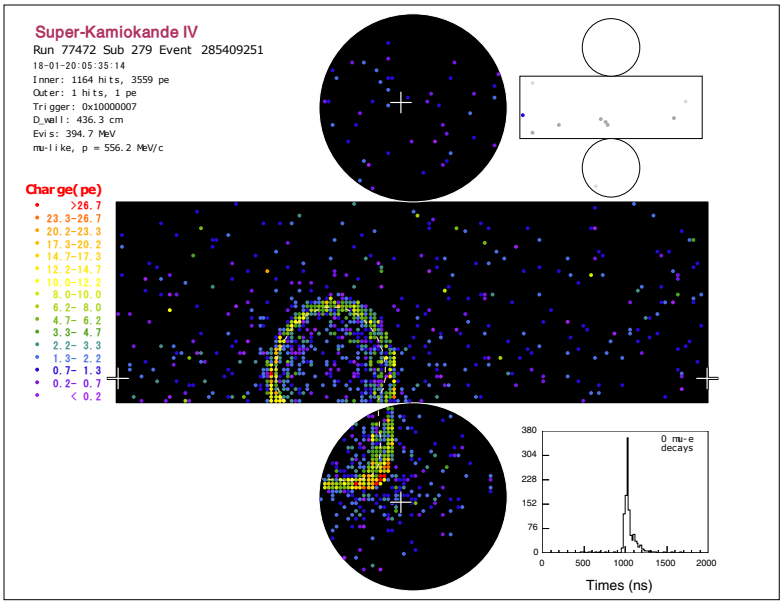

FIGURE 2.2: A example of neutrino event observed by Super-K detector. Each point denotes a PMT hit, whose charge is represented by the color. The Cherenkov ring pattern can be seen clearly.

2.2 Detector

2.2.1 Water Tank

The water tank of Super-Kamiokande, in which 50 kt ultra pure water is filled, is in a cylindrical shape with a height of 41.4 m and a diameter of 39.3 m. The water tank is separated into two concentric cylindrical regions by the PMT support structure, which is covered by opaque sheets on both surface as shown in Figure 2.3. The two regions are referred to as the inner detector (ID) and outer detector (OD), respectively. There is an 55 cm insensitive region between ID and OD to contain the supporting structure and cables for the PMTs.

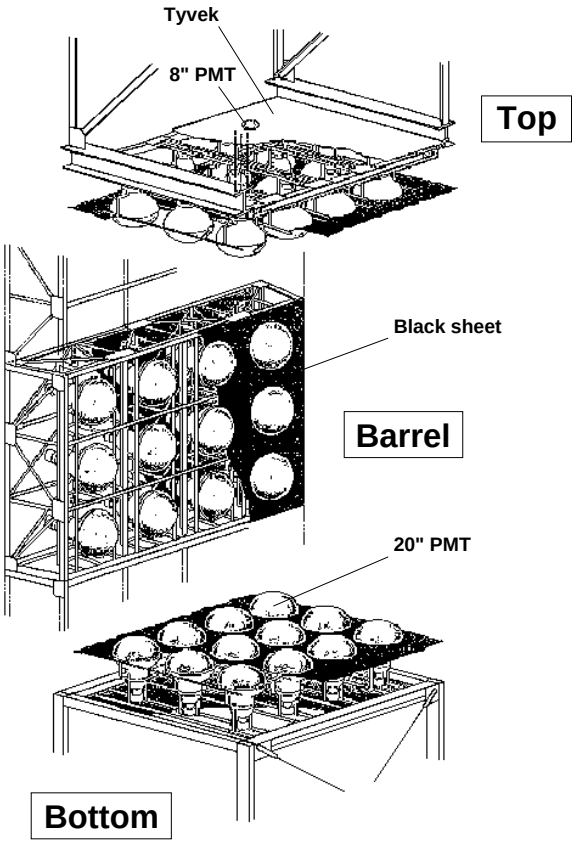

FIGURE 2.3: Supporting structure of PMTs. Taken from [7].

The inner detector (ID) is a cylinder with a height of 36.2 m height and a diameter of 33.8 m. There are 11,146 inward facing 20-inch PMTs attached to the supporting frame to detect the Cherenkov light generated from the 32 kton pure water contained. The photocathode coverage is around 40% in the ID, and the rest of the ID wall is covered with black polyethylene terephthalate sheet to reduce reflection and to separate the ID

and the OD optically. The photocathode coverage was reduced to about 20% in SK-II due to the accident and was resumed to 40% from SK-III.

The outer detector (OD), which surrounds the ID, is monitored by 1,885 outward facing PMTs with a size of 8 inches. The thickness of OD is 2.2 m along the barrel and 2.05 m on the top and bottom. To improve the light collection efficiency, a wavelength shifting plate with a size of 60 cm $\times$ 60 cm is attached to each OD PMT and the surface of supporting frame is covered by tyvek sheets as reflective material. The OD is used to reject cosmic ray muons and to distinguish the charged particles which penetrate the ID wall. The water layer in the OD also prevents the ID from the neutrons and gamma rays from surrounding rocks.

2.2.2 Photomultiplier Tube

The 20-inch PMTs in the ID (Hamamatsu R3600) were originally developed by Hamamatsu Photonics K.K. with the cooperation of Kamiokande collaborators [71]. The bleeder circuit and the dynode structure were upgraded later to improve timing response and photon-collection efficiency for Super-Kamiokande [72]. The schematic view and the specification of the PMT are shown in Figure 2.4 and Table 2.2.

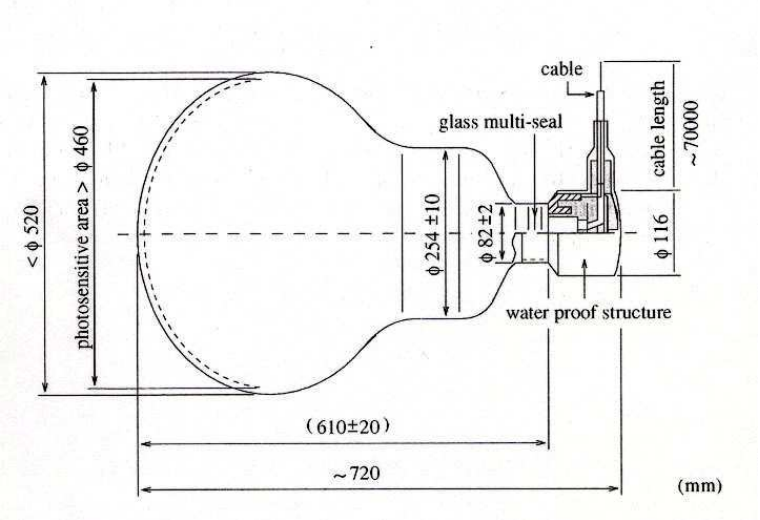

FIGURE 2.4: Schematic view of the 20-inch ID PMT for Super-Kamiokande experiment. Taken from [7].

The photocathode of the PMT is coated with bi-alkali (Sb-K-Cs) for its high quantum efficiency in the Cherenkov wavelength region ($\sim$ 22% for wavelength from 360 to 400 nm) and low thermionic emission. The collection efficiency at the first dynode is around 70% with a uniformity of 7% for different incident position on the photocathode. ID PMT's gain is 10^7 with a high voltage around 2000 V. The single photoelectron (p.e.)

Shape	Hemispherical
Photocathode area	50 cm diameter
Window material	Bialkali (Sb-K-Cs)
Quantum efficiency	22% at $\lambda = 390$ nm
Dynodes	11 stage Venetian blind type
Gain	10^7 at ~ 2000 V
Dark current	200 nA at 10^7 gain
Dark pulse rate	3 kHz at 10^7 gain
Cathode non-uniformity	<10%
Anode non-uniformity	<40%
Transit time	90 nsec at 10^7 gain
Transit time spread	2.2 nsec (1 σ) for 1 p.e. equivalent signals
Weight	13 kg
Pressure tolerance	6 kg/cm^2 water proof

TABLE 2.2: Specification of the 20-inch ID PMT for Super-Kamiokande experiment. Taken from [28].

peak can be seen clearly in the charge distribution for single p.e. signal as shown in Figure 2.5. The transit time spread for the single p.e. signal is about 2.2 ns, while the average rate of dark hits at 0.25 photoelectrons is about 3 kHz.

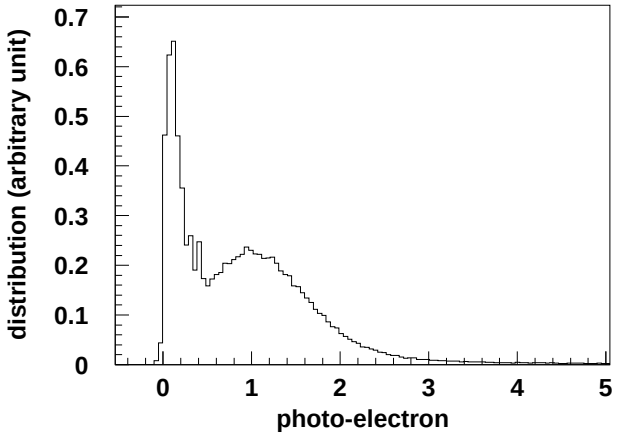

FIGURE 2.5: Single photoelectron distribution of the 20-inch PMT.

On November 12th, 2001, one PMT at the bottom wall of the ID tank imploded during the SK tank water refilling after the maintenance work. This implosion triggered a cascade implosions of PMTs and resulted in about 60% ID and OD PMTs destroyed. To prevent such an accident in the future, from SK-II all the inner PMTs are equipped with covers, which consists of a clear UV-transparent acrylic dome with a thickness of 12 mm and Fiber-Reinforced Plastic (FRP) shield for photocathode and side area protection, respectively. As shown in Figure 2.6, several holes are on the FRP to enable the water flow in and out of the acrylic cover freely. Transparency of the acrylic cover is more than 96% for photons with wavelength larger than 350 nm in water.

FIGURE 2.6: PMT case for 20-inch ID PMT since SK-II period.

For the OD PMT (Hamamatsu R1408), as mentioned before, their 8-inch photocathode are attached to 60 cm × 60 cm × 1.3 cm wavelength shift plate to increases light collection efficiency by 60% [73]. Although the timing resolution at single p.e. is degraded from 13 ns to 15 ns due to the wavelength shift plate, considering that OD is used as a calorimeter and veto counter rather than a particle tracker, a higher light collection efficiency is more important comparing with the sacrifice on the timing resolution.

2.2.3 Outer Detector (OD)

The OD aims to reject cosmic ray muons for the neutrino event samples. To reject the corner clipping muons more efficiently, tyvek sheet was installed between the end cap and barrel region in the OD before SK-III launch, as shown in Figure 2.7.

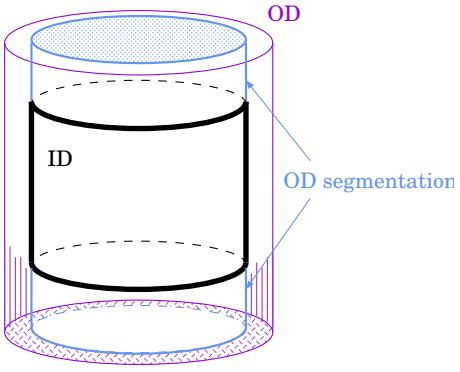

FIGURE 2.7: A schematic view of outer detector (OD). Taken from [8]

As an example, the distribution of OD hits for a simulated partially contained event is shown in Figure 2.8. The partially contained event means that a particle produced in the ID tank penetrated the ID wall and entered the OD. The exiting point on the wall is

around the edge of the tank's bottom wall. Both cases with and without tyvek sheet are shown in the figure. The OD signal for a detector with tyvek sheet can be seen clearly at the barrel region of the wall, while the OD signal is spread to the bottom wall if no tyvek sheet is installed, which makes it hard to distinguish from a corner clipping event.

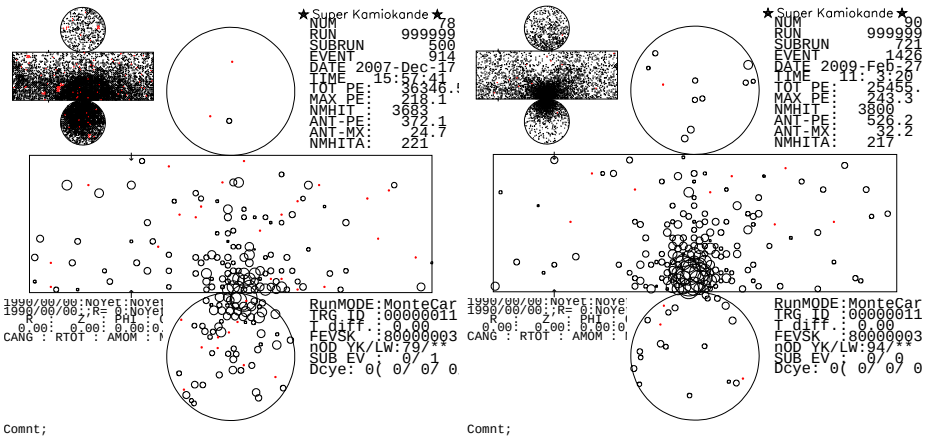

FIGURE 2.8: OD event display for a simulated partially contained event, without (with) tyvek sheet for left (right) figure. The distribution of OD hit is shown in the center of each figure, while the distribution of ID hits is shown on the top left corner.

2.3 Water Purification and Air Purification System

The Super-Kamiokande detector utilizes spring water in the mine as the medium in the tank. The water used in the tank is purified with a flow rate of 60 ton/hour by the water purification system continuously for a high purity. Furthermore, the radioactive impurities in the water, especially radon, which is one of the background sources for the observation of neutrino in the MeV energy region such as solar neutrino, are also removed by the water purification system.

To prevent the radon in air dissolving into the purified water, radon-free air produced by air purification system is pumped into the space above the water surface in the tank continuously. Radon contamination in the radon-free air is suppressed to less than 3 mBq/m^3. As a comparison, a typical radon concentration in the mine tunnel air without any purification in summer is about 1200 Bq/m^3, which is five orders of magnitude higher than the value after purification [74].

2.4 Electronics and Data Acquisition System for SK-IV

The front end electronics of Super-K were upgraded from Analog Timing Module [75] in September 2008 to a dead-time free data acquisition system based on new electronics

called QBEE (QTC-Based Electronics with Ethernet) [9].

The QTC (charge-to-time converter) for PMT signal readout used in QBEE and its surrounding are shown in Figure 2.9. For each QTC chip, there are three input channels with a charge dynamic range from 0.2 to 2500 pC. Each channel has three gain ranges, whose relative gain ratio are 1/49: 1/7 : 1 and corresponding to small, medium and large gain, respectively.

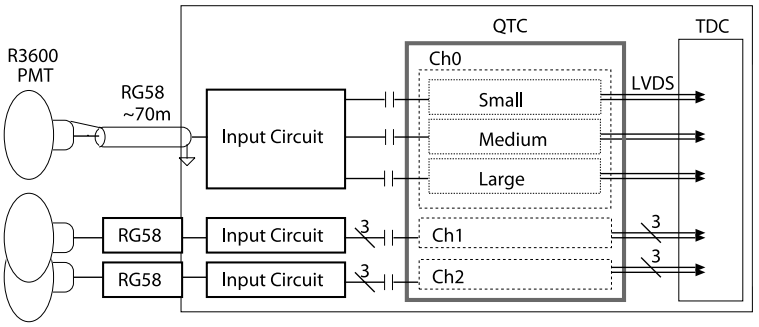

FIGURE 2.9: Block diagram and surroundings of QTC. Taken from [9].

Each QTC channel has a built-in discriminator to trigger itself and convert the integrated charge of the input signal to a timing signal. The leading edge of the time signal represents the signal timing and the width denotes the charge of input signal. The block diagram of one channel is shown in Figure 2.10. Input signals from PMTs are first amplified by a low-noise-amplifier (LNA), and then delayed by a low-pass filter (LPF). After processed by a voltage-to-current converter (V/I), the signals are finally integrated by a capacitor. All of the charge accumulated on the capacitors are monitored by an output signal called PMTSUM.

Besides the time information, which is obtained by measuring the leading edge of input signal from PMT, the QTC is also sensitive to charge. Integration of the input charge starts when the amplified input signal goes over the threshold given by discriminator. At the same time, a signal is generated to register a hit for the trigger. After the end of the charge integration, which is controlled by the timer block, the charge integrated on the capacitor starts to be discharged with a constant current. The discharging time, also the width of the output signal, is then proportional to the integrated charge of input signal. Hence, both timing and charge information are encoded into the timing output signal.

The timer block has three timers for charging, discharging and VETO, respectively. The time lengths of the gates are controlled by digital-to-analog converters (DACs) via adjusting the discharge current and threshold of comparator.

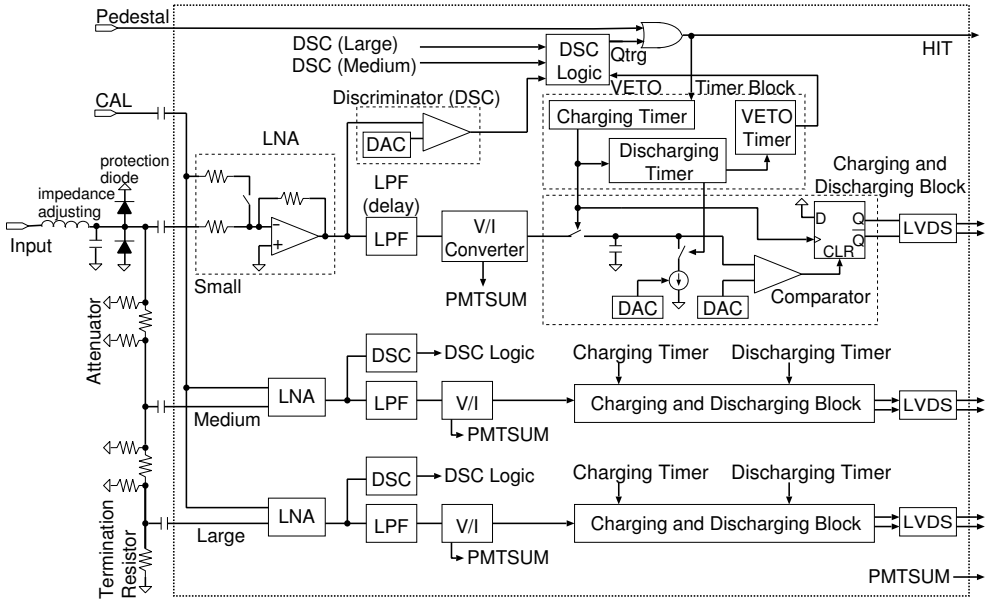

FIGURE 2.10: Block diagram of one QTC channel. There are three gain ranges for each channel. Taken from [9].

The timing chart for QTC operation is shown in Figure 2.11. The timer for charging after triggered by the output signal from discriminator, opens a charge gate for 400 ns. The switch between charging capacitor and the V/I converter closes in the charge gate, the input signal therefore accumulates in the capacitor. A discharge gate is opened by the discharging timer for $\sim$ 350 ns after the charge gate. The switch between capacitor and the discharging current source closes, then the input signals are ignored by opening the switch near the V/I converter. The time when the voltage of the integrated signal decreases to the threshold level of comparator is represented by the trailing edge of output signal from QTC. The output signal from QTC is then proportional to the charge of input signal. Reset and VETO signals are issued at the end of the discharge gate to reinitialize other QTC circuits. The time consumption for one input signal processing is $\sim$ 900 ns in total.

A hardware trigger is used in the triggering system for SK-I, SK-II and SK-III [75], while the software trigger is used in the new DAQ readout system used in SK-IV instead by recording and analyzing all hits. Seventeen microseconds worth of PMT data is read out at a frequency of 60 kHz and particle interactions are identified using the software trigger therein, which results in a dead-time free system in SK-IV and the decay electron tagging efficiency is therefore increased. In addition, the upgraded electronics also has a better linearity and a wider dynamic range, which make the precision of high energy event reconstruction higher.

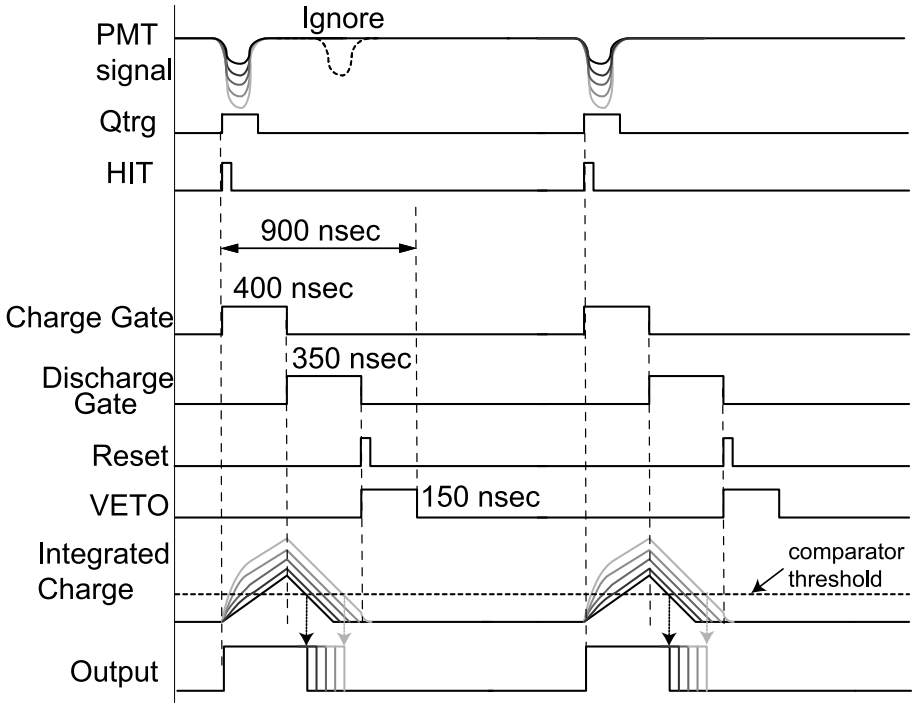

FIGURE 2.11: Timing chart for QTC operation. Taken from [9].

Chapter 3

Simulation of Atmospheric Neutrino

The simulation of atmospheric neutrino events in Super-Kamiokande is based on Monte-Carlo method and consists of three parts: flux of the atmospheric neutrino, interactions between neutrino and nucleons, and response of the detector. The events expected to be observed in the detector are simulated based on the atmospheric neutrino flux model and interaction model. The basic information of the particles in the final state, including particle type, vertex, direction, momentum and so on, are generated in this step. Then, the particle's track in the detector, emission of Cherenkov radiation, light propagation and response of detector hardware are simulated based on those information. Finally, the simulated events, also called Monte Carlo events, are saved in the same structure and reconstructed as the real observed data for the oscillation analysis.

This chapter describes the atmospheric neutrino flux model, neutrino interaction model and detector simulation, which are important to the systematic error evaluation and oscillation parameter fitting.

3.1 Atmospheric Neutrino Flux

In this analysis, atmospheric neutrino flux model calculated by M. Honda et al. [10, 76](Honda flux) is used as the default model, while other models, such as G. Battistoni et al. [77] (Fluka flux) and G. Barr at al. [78] (Bartol flux) are compared to the Honda flux for the systematic uncertainties estimation.

The primary cosmic ray flux model, as the input of the neutrino flux calculation, is determined by experimental measurements, including the BESS [79, 80] and AMS [81]

experiments. The cosmic ray flux is affected by solar activities, which changes periodically. The flux is higher for a intense solar activity (solar maximum) than that for a mild solar activity (solar minimum). The fluctuation of the cosmic ray flux in a solar cycle is more than a factor of two in 1 GeV region, while the difference is around 10 % when energy is around 10 GeV.

When primary cosmic ray particles, mostly protons, penetrate atmosphere, they interact with air molecules and produce secondary particles such as pions and kaons. The US Standard Atmosphere '76 model [82] is used in the Honda flux to describe the profile of the atmosphere's density and calculate the dependence of atmospheric neutrinos on zenith angle. Effects from geomagnetic field are estimated based on the IGRF2005 model [83].

Two theoretical models are used for the hadronic interactions between the air molecules and the cosmic rays: JAM [84] and DPMJET-III [85], which are interaction models for energies less and greater than 32 GeV, respectively. Mesons generated from those hadron interaction further decay into muons and neutrinos. Therefore, the DPMJET-III model, which is used in the Honda flux, is tuned based on the measurements of the cosmic ray muons flux by BESS [80, 86] and L3+C [87].

The track of the cosmic ray particles in the atmosphere are fully simulated in three-dimensions during the flux calculation. The zenith angle distribution of the atmospheric neutrino at Super-K calculated by the Honda model is shown in Figure 3.1. The flux peak at the horizon is mainly due to the longer track length in the atmosphere comparing with vertical direction, which means more time for decay. The large up-down asymmetry in the most left plot, in which neutrino's energy is around 0.32 GeV, is due to the geomagnetic field, while the cosmic rays with higher energy are less affected therefore no obvious up-down asymmetry in the most right plot.

The energy spectrum of atmospheric neutrinos at the Super-K site after averaging over all direction is shown in Figure 3.2. Besides the Honda flux (solid line), the Bartol flux (dashed line) and Fluka flux (dotted line), which have different hadronic interaction model and cosmic ray data set used for tuning, are also shown. The difference between different flux models is taken as systematic uncertainties.

The atmospheric neutrino MC events are generated with the predicted flux at Super-K without any oscillations. The effects of oscillation are applied by reweighting to each MC event based on its oscillation probability calculated using Equation 1.4.

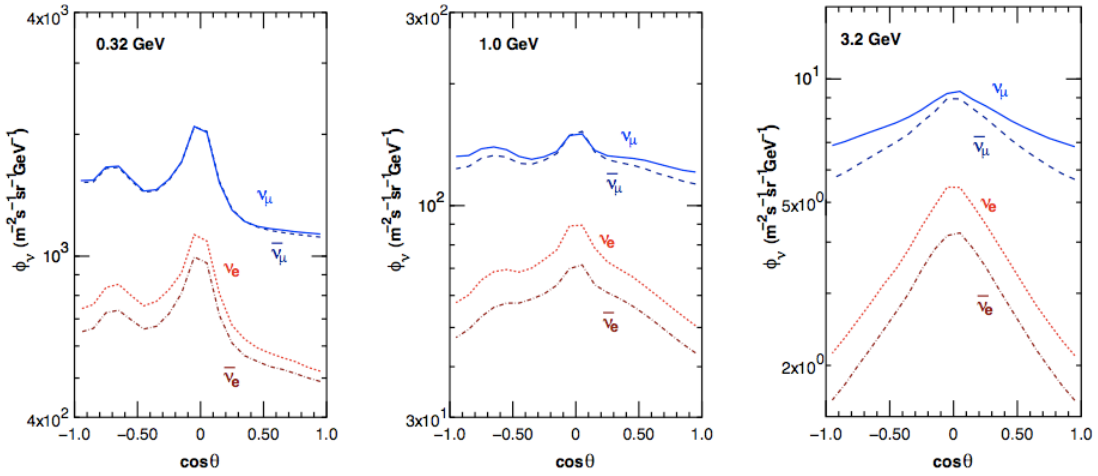

FIGURE 3.1: Dependence of atmospheric neutrino flux on zenith angle for different energy regions. The atmospheric neutrino is vertically downward going when cosθ = 1 and it is upward going when cosθ = -1. Taken from [10].

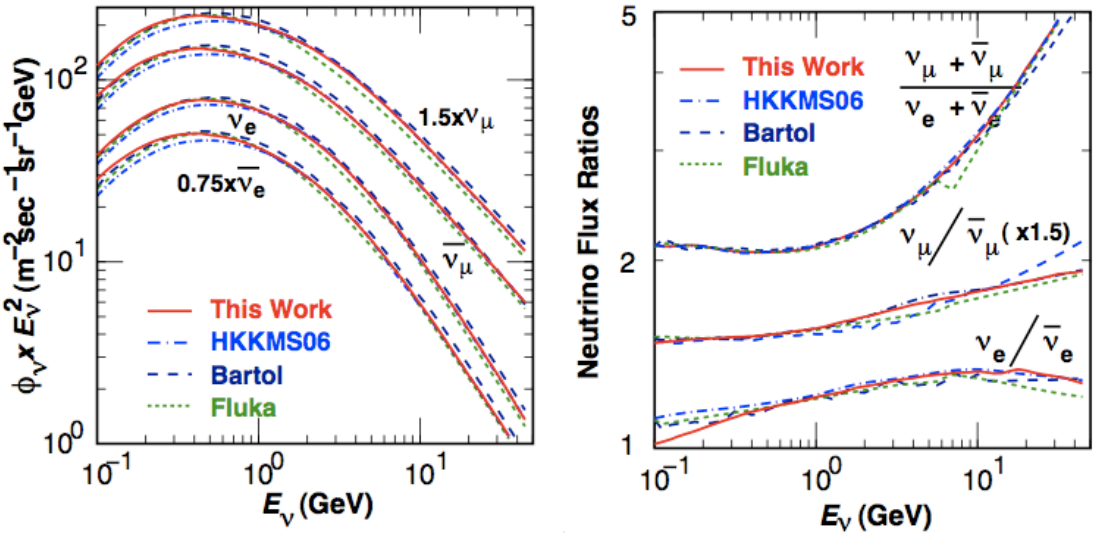

FIGURE 3.2: Atmospheric neutrino fluxes (left) and flavor ratio (right) after averaging over all directions. The prediction based on Honda 11 flux is shown by red solid line, while the result of the Bartol flux and the FLUKA flux are represented by dashed line and dotted line. Taken from [10].

3.2 Neutrino Interaction

Simulation of the interaction between atmospheric neutrinos and nuclei in water in the tank and the rock surrounding the Super-K detector is done by NEUT (version 5.4.0) [88]. The interactions between atmospheric neutrino and electrons are neglected in simulations due to the three orders of magnitude smaller cross sections comparing with the one between neutrino and nuclei.

Neutrino interactions can be classified into charged-current (CC) and neutral-current (NC) interactions determined by the type of bosons exchanged. The CC interaction, when a neutrino interacts with the target by exchanging a $W^{\pm}$ boson, produces a charged lepton (e.g. electron or muon) whose flavor corresponds to that of neutrino (e.g. ν_e or ν_μ). Therefore, the incoming neutrino in a CC event can be identified by distinguish the flavor of charged lepton, which is important in the observation of the effect of neutrino flavor change in an oscillation analysis. As for the NC interactions via Z boson exchange, no signal about the neutrino flavor left in the detector since the outgoing lepton is also a neutrino.

Besides electron and muon neutrinos, which exist in the original neutrino flux, tau neutrino (ν_τ) can also be detected by Super-K due to oscillation. The CC interaction for ν_τ can only occur in the multi-GeV energy region since tau lepton has a large mass value of 1.78 GeV/c^2. Interaction with ν_τ are simulated in the same manner as ν_e and ν_μ by NEUT, while the produced tau leptons, which decays with a short life time of 2.9×10^{-13}s, are simulated by TAUOLA [89].

In NEUT, the following interactions are considered:

1. CC/NC (quasi-)elastic scattering: $\nu + N \rightarrow l + N'$
2. CC meson exchange interaction: $\nu + NN' \rightarrow l + N''N'''$
3. CC/NC single meson production: $\nu + N \rightarrow l + N'$+meson
4. CC/NC coherent pion production: $\nu +^{16} O \rightarrow l +^{16} O + \pi$
5. CC/NC deep inelastic scattering: $\nu + N \rightarrow l + N' +$ hadrons.

Here, N, N', N'' and N''' represent nucleons (e.g. proton or neutron) and l represents a lepton.

3.2.1 (Quasi-)Elastic Scattering

NC elastic scattering is a process in which a neutrino simply scatters of a nucleon target by transferring momentum without producing any new particles. In CC Quasi-elastic scattering, the neutrino changes into the corresponding charged lepton and the target nucleon also changes to preserve the total electric charge, without generation of other particles. In NEUT, such interactions on free nucleon target are simulated by the Llewellyn-Smith model [90]. The differential cross section for the interaction with free

nucleon is:

$$\frac{d\sigma^{\bar{\nu}}}{dq^2} = \frac{M^2 G_F^2 cos^2\theta_C}{8\pi E_\nu^2}\left[A(q^2) + B(q^2)\frac{s-u}{M^2} + C(q^2)\frac{(s-u)^2}{M^4}\right]. \tag{3.1}$$

Here, M represents the nucleon mass, which equals 0.938 MeV, G_F represents the Fermi coupling constant, θ_C denotes the Cabibbo angle, E_ν denotes the neutrino energy, $q = p_\nu - p_l$ represents the transferred four-momentum, s and u are Mandelstam variables [90]. The factors A, B and C are expressed as:

$$\begin{aligned} A(q^2) &= \frac{m^2-q^2}{4M^2}\left[\left(4-\frac{q^2}{M^2}\right)|F_A|^2 - \left(4+\frac{q^2}{M^2}\right)|F_V^1|^2 \right. \\ &\quad -\frac{q^2}{M^2}|\xi F_V^2|^2\left(1+\frac{q^2}{4M^2}\right) - \frac{4q^2 F_V^1 \xi F_V^2}{M^2} \\ &\quad \left. -\frac{m}{M}((F_V^1+\xi F_V^2)^2 + |F_A|^2)\right] \qquad (3.2) \\ B(q^2) &= \frac{q^2}{M^2}(F_A(F_V^1+\xi F_V^2)) \qquad (3.3) \\ C(q^2) &= \frac{1}{4}\left(|F_A|^2 + |F_V^1|^2 - \frac{q^2}{4M^2}|\xi F_V^2|^2\right). \qquad (3.4) \end{aligned}$$

Here, the mass of the outgoing lepton is represented as m, ξ is defined as the anomalous magnetic moment $3.71\mu_N$[1]. Axial vector form factor $F_A(q^2)$, vector form factors $F_V^1(q^2)$ and $F_V^2(q^2)$ are expressed as:

$$\begin{aligned} F_A(q^2) &= -1.232\left(1-\frac{q^2}{M_A^2}\right)^{-2} \qquad (3.5) \\ F_V^1(q^2) &= \left(1-\frac{q^2}{4M^2}\right)^{-1}\left[G_E(q^2) - \frac{q^2}{4M^2}G_M(q^2)\right] \qquad (3.6) \\ \xi F_V^2(q^2) &= \left(1-\frac{q^2}{4M^2}\right)^{-1}[G_E(q^2) - G_M(q^2)] \qquad (3.7) \\ G_E &= (1+\xi)^{-1}G_M(q^2) = \left(1-\frac{q^2}{M_V^2}\right)^{-2}, \qquad (3.8) \end{aligned}$$

where G_E and G_M represent the electric form vector and the magnetic form vector, respectively. The vector mass M_V is determined as 0.84 GeV by the electron scattering experiments, and the MiniBooNE [91] experiment shows that the axial vector masses M_A is 1.05 GeV. The value of M_A is also consistent with former determinations of the nucleon axial mass as shown in Figure 3.3 [11].

For a nucleon bound in an oxygen nucleus, the local Fermi-Gas model made by Nieves [92, 93], is used for taking the nuclear effect such as Fermi motion and Pauli blocking

[1]The nuclear magneton μ_N is defined as $\frac{e\hbar}{2m_p c}$.

of the nucleons into account. The effect of random phase approximation correction and contribution from multi-nucleon effect are considered.

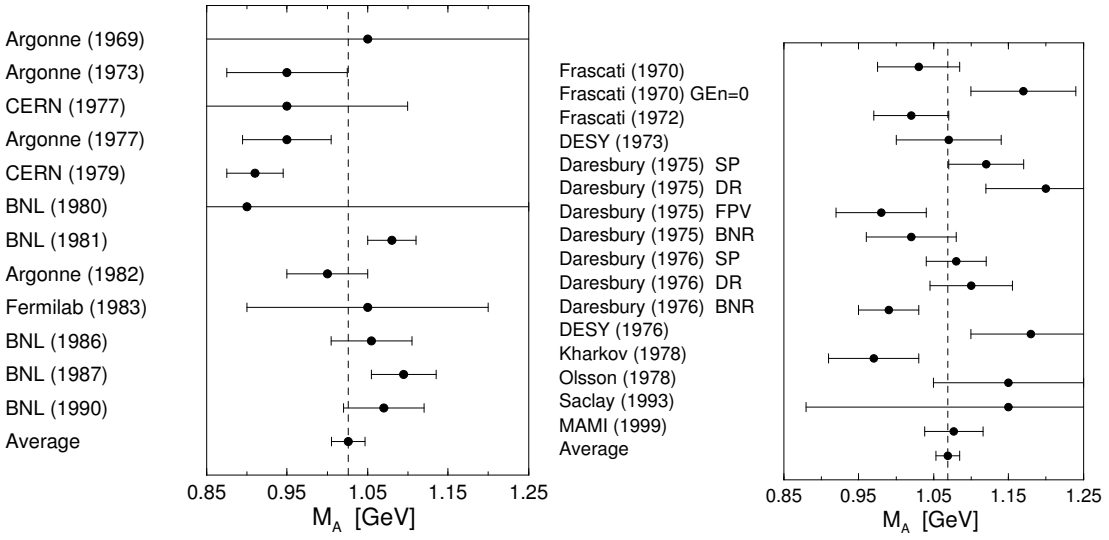

FIGURE 3.3: Axial mass M_A extractions. Left panel: From (quasi)elastic neutrino and antineutrino scattering experiments. The weighted average is $M_A = (1.026 \pm 0.021)\,\mathrm{GeV}$. Right panel: From charged pion electroproduction experiments. The weighted average is $M_A = (1.069 \pm 0.016)\,\mathrm{GeV}$. Taken from [11].

Figure 3.4 shows the interaction cross section of quasi-elastic scattering calculated by NEUT and experimental data. It should be noticed that the cross section of antineutrino is smaller than that of neutrino since the weak interaction only includes left-handed particle and right-handed antiparticle under relativistic limit and the angular momentum conservation constrains the scattering angle distribution of the output leptons for the antineutrino interaction.

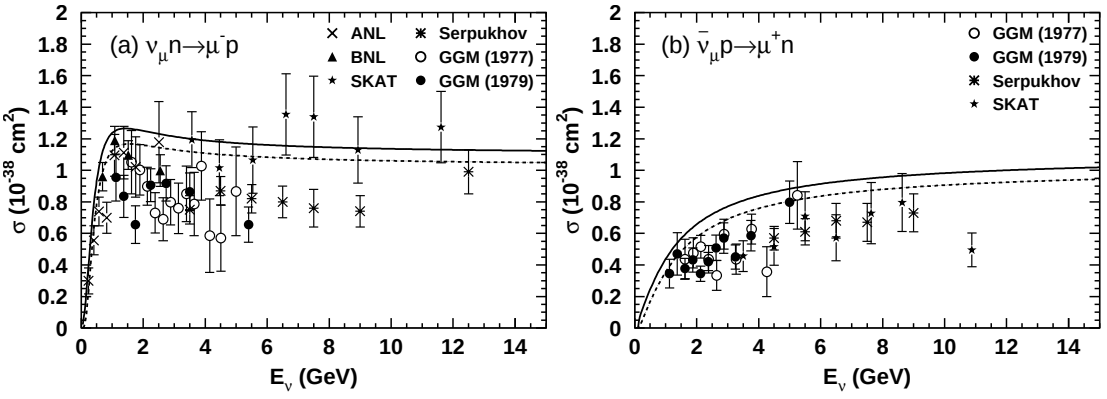

FIGURE 3.4: Cross section of Charged current quasi-elastic interaction of ν_μ (left) and $\bar{\nu}_\mu$ (right), with experimental data from ANL [12], Gargamelle [13] [14], BNL [15], Serpukhov [16] and SKAT [17]. Solid line represents the result for scattering off a free proton, the dashed line represents the result for scattering off bound nucleons in ^{16}O. Taken from [18]

3.2.2 Single Meson Production

The resonance production of single meson, e.g. π, η and K is modeled in NEUT mainly as an intermediate resonance decay:

$$\nu + N \rightarrow l + N^*, N^* \rightarrow N' + \text{meson}. \tag{3.9}$$

Here N and N' represent nucleons in the initial and final state, respectively. The intermediate resonance state is denoted by N^*. Only the events with an invariant mass W of the intermediate baryon resonances less than 2 GeV/c^2 is considered here. The interaction with W greater than 2 GeV/c^2, are simulated as a part of deep inelastic scattering, which is described in Section 3.2.4.

This interaction is simulated based on the model from Rein and Sehgal [94] with the revised form factor by Graczyk and Sobczyk [95], and the parameters characterizing the form factor were determined by bubble chamber data [96].

The angular distribution of the final state pion with respect to the $\Delta(1232)$ resonance is determined using Rein's method [97], while this distribution for other resonances are assumed to be isotropic in the rest frame of the resonance. For the decay from a baryon resonance, nucleon momentum is required to be greater than the Fermi surface momentum to simulate the Pauli blocking effect. Moreover, the absorption of mesons in a nucleus results in the absence of mesons in the resonance events [98]. The fraction of such phenomena is estimated to be 20% in NEUT.

Figure 3.5 shows the cross section of charged current single pion productions for ν_μ [18].

3.2.3 Coherent Pion Production

Coherent pion production, in which the incident neutrino interacts with the entire oxygen nucleus producing a pion, is simulated based on the Berger and Sehgal's model [99]. The pions and outgoing leptons are peaked at the forward direction since the momentum transferred to the oxygen nucleus is small.

3.2.4 Deep Inelastic Scattering

Multiple hadrons are often generated in deep inelastic scattering interactions by the interaction between incident neutrino interacts and the constituent quarks in the target nucleon. This process is dominant in multi-GeV region and considered in NEUT when the hadronic invariant mass W larger than 1.3 GeV/c^2. The DIS interaction is modeled

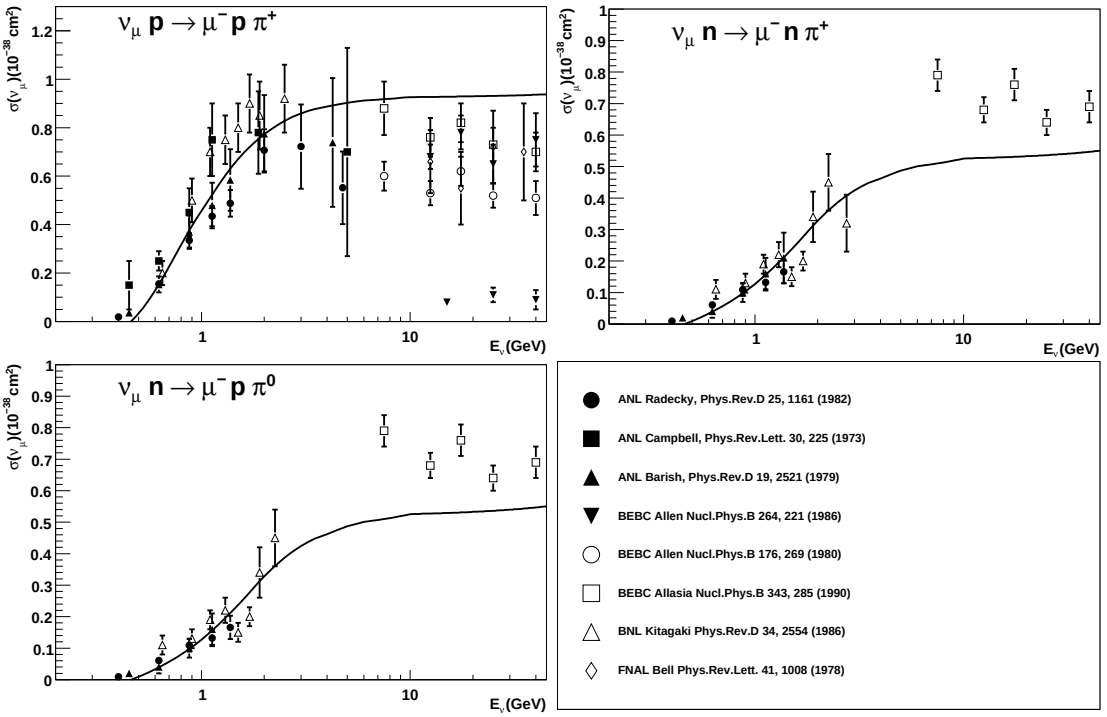

FIGURE 3.5: Cross section for ν_μ charged current single pion productions. Solid lines represents the calculation result of NEUT, points represent data from experiments shown in bottom right figure. Taken from [18].

using the GRV98 parton distribution function [100] and utilizing CKM matrix elements when calculating structure functions therefrom. Corrections for low q^2 scattering have been updated to those of Bodek and Yang [101].

For the interaction with W in the range from 1.3 GeV/c to 2.0 GeV/c, only pions are considered in the simulation as the outgoing mesons. The average multiplicity of pion is estimated from the results of bubble chamber experiment [102, 103]. Only the event with two or more pions are considered in DIS channel in this energy region since there is an overlap with the resonance pion production, as introduced before.

Cross sections of charged current DIS interactions for ν_μ and $\bar{\nu}_\mu$ are shown in Figure 3.6.

3.2.5 Nuclear Effects

The interactions of secondary particles produced in the neutrino-nucleon interactions inside the ^{16}O nuclei are also considered in NEUT. The meson, such as π, K and η, produced within ^{16}O nuclei are tracked from their creation to either their absorption inside the nuclei or exiting. This simulation is based on the cascade model and external data.

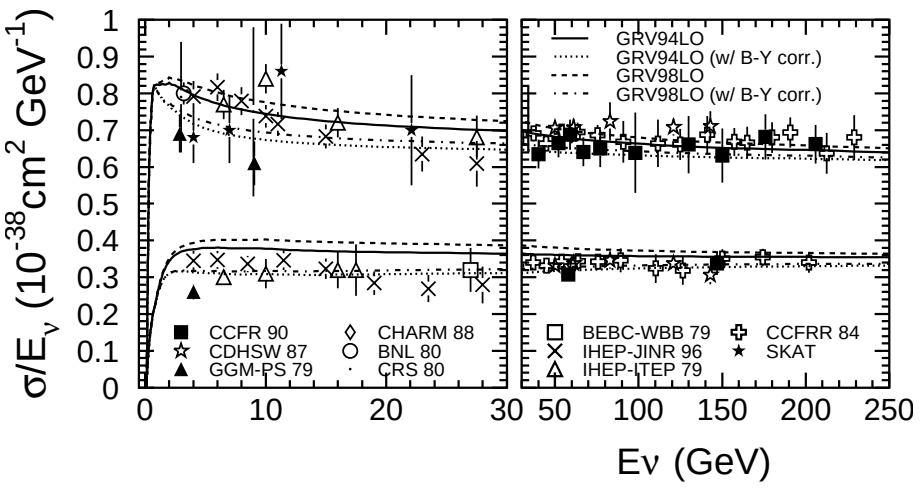

FIGURE 3.6: Cross section of charged current DIS for ν_μ (upper lines and points) and $\bar{\nu_\mu}$ (lower lines and points) interactions. Dashed lines show the prediction of NEUT, which uses GRV98 with Bodek-Yang correction. The experimental data is represented by the points. Taken from [18].

The most frequently seen hadrons at the Super-K detector is pions since the large production cross section from neutrino interaction and large pion-nucleon interaction cross section for $E_\nu > 1$ GeV. NEUT considers four pion interactions in ^{16}O nuclei: quasi-elastic scattering in which a single pion of the same charge remains after interaction, charge exchange in which a charged pion is converted into a π^0 or π^0 to charged pion, absorption in which no pion remain after interaction, and pion production.

The nuclear density distribution, which determines the interaction probabilities within a nucleus is described by the Wood-Saxon density profile [104]. The probabilities for four interactions are calculated at each simulation step.

The cross sections of $\pi^+ - ^{12}$C scattering as a function of the momentum of π^+ after tuning based on $\pi^+ - ^{12}$C data are shown in Figure 3.7 [19].

Besides pion, the quasi-elastic scattering and charge exchange interaction of kaon are also considered in NEUT, whose model is tuned based on the cross sections measured by $K^\pm - N$ scattering experiments [105–107]. The absorption of η ($\eta N \to N^* \to \pi(\pi)N$) is also considered [108].

3.3 Detector Simulation

Secondary particles produced by neutrino interactions are then propagated in the detector, which is simulated by a GEANT3[109]-based detector simulator called SKDETSIM. The interaction of the particles with water is simulated by GEANT while GCALOR[110]

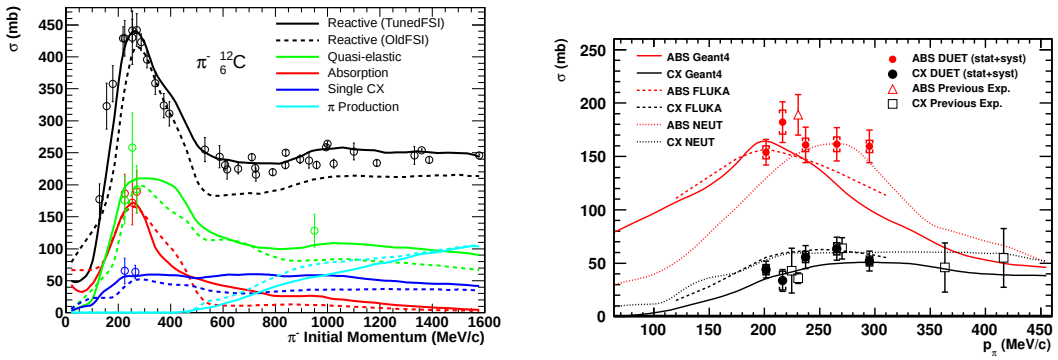

FIGURE 3.7: Cross section of $\pi^+ - {}^{12}$C scattering as a function of the momentum of π^+. Solid lines represent the result of NEUT calculation before tuning, while the result after tuning are represented by dashed lines. Experimental data are shown as the points with error bars. Taken from [19]. Right figure is the update for the absorption (ABS) and charge exchange (CX) based on new scattering data [20]

is used to simulate hadronic interactions except the interaction with pions below 500 MeV/c, for which a cascade model is used.

The Cherenkov photons produced by the particles are then propagated in the detector as described in Section 2.1. Reflectivity of the PMT and the black sheet are also modeled using the result obtained in Section 2.2.

The charge and time responses of the PMT and the electronics are simulated based on the calibration measurements. Then the detector simulation provides the same data structure as the observed data so that these two can be analyzed in the same manner.

Chapter 4

Calibration

Calibrations are performed in the SK detector in order to understand the detector and keep its performance high. The calibration results are utilized for the detector simulation described in Section 3.3 as well as for the data analysis. Further details of the Super-K calibration can be found in [21].

The signal observed and recorded by Super-K is the charge and time information from PMT through the electronics. Besides the response of PMT itself, which is affected by the individual difference on quantum efficiency and the gain of PMTs, the water quality and other detector's characteristics also need to be measured precisely in order to model the propagation of Cherenkov photon for the detector simulation and event reconstruction. A good detector calibration and a precise evaluation for the calibration result relate to the event reconstruction performance and therefore play important roles in the neutrino oscillation analysis.

4.1 Detector Calibration

4.1.1 Relative Gain Calibration

The high voltage of each PMT is set individually to get a uniform charge response for all the PMTs in the detector. The relative gain calibration is performed by flashing a laser with a similar apparatus as the timing calibration described in Section 4.1.4 to measure and correct the remaining individual variations of the PMT gain.

A pulsed laser near the ID center is flashed isotropically and repeatedly with two different intensities: a high intensity and a low intensity. For the high intensity case, every PMT detects a proper number of photons, creating an average charge $Q(i)$ for each ID PMT i.

For the other case, the laser is flashed at a low intensity, only a few PMTs get a hit at a time and each hit is a single p.e.. The number of hits observed by i-th PMT is counted and recorded as $N(i)$. The complicating factors in estimating those two intensities $Q(i)$ and $N(i)$ are similar since the light source is at the same position:

$$Q(i) \propto I_H \times a(i) \times \epsilon_{qe}(i) \times G(i) \tag{4.1}$$

$$N(i) \propto I_L \times a(i) \times \epsilon_{qe}(i), \tag{4.2}$$

where I_H (I_L) represents the average intensities of the high (low) intensity flashes. The value of $a(i)$, ϵ_{qe} and $G(i)$ represent the acceptance, quantum efficiency and gain of i-th ID PMT, respectively. The relative gain of each PMT $G(i)$ can then be obtained by taking the ratio of $Q(i)$ to $N(i)$ as:

$$G(i) \propto Q(i)/N(i). \tag{4.3}$$

The standard deviation of the gain for all PMTs is found to be 5.9%. The individual relative gain factor obtained above is used to correct the coefficient to converse the output charge to the number of photoelectrons observed for each PMT.

4.1.2 Absolute Gain Calibration

The absolute gain is used to convert the charge recorded by a PMT in pico Coulomb (pC) into the number of incident photoelectroncs. The absolute gain was measured by observing the charge distribution of single photoelectron signals with a spherical gamma-emitting nickel source, which emits 9 MeV gamma rays isotropically by capturing neutrons emitted from a ^{252}Cf source in it. The nickel source was placed near the center of the ID tank and delivered 0.004 p.e/event for each PMT, which ensures more than 99% hits are single p.e. hits.

The observed charge distribution for the single p.e. signals is shown in Figure 4.1. The hits from all PMTs are corrected for the relative gain variation and accumulated. The conversion factor from the observed charge to the number of p.e.s is determined to be 2.658 pC/p.e, which is the peak of the single p.e.. This distribution is also used for the detector simulation described in Section 3.3.

Furthermore, as shown in Figure 4.2, the peak of charge distribution for the dark hits, which is proportional to the absolute gain of PMT, increased as time passes and the increasing rate depends on the production year of PMT. The reason of such an increase of the gain is not clear yet, but a correction is applied on the gain to reduce the effect.

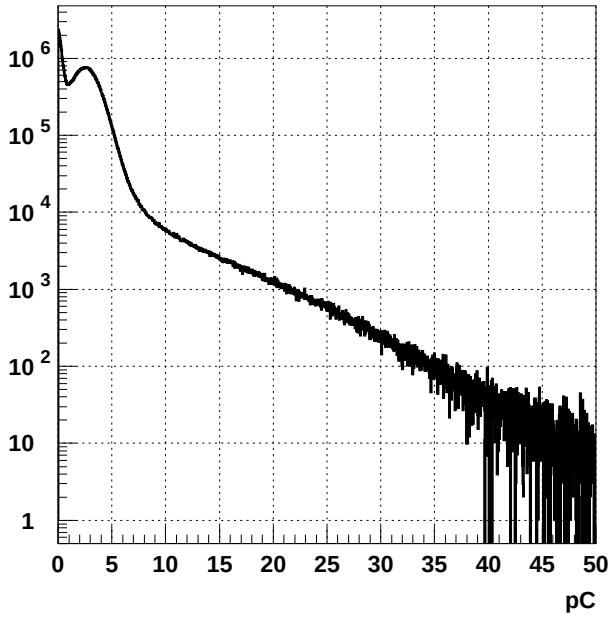

FIGURE 4.1: Distribution of the observed charge for single p.e. signals obtained from the calibration data with nickel source. Taken from [21].

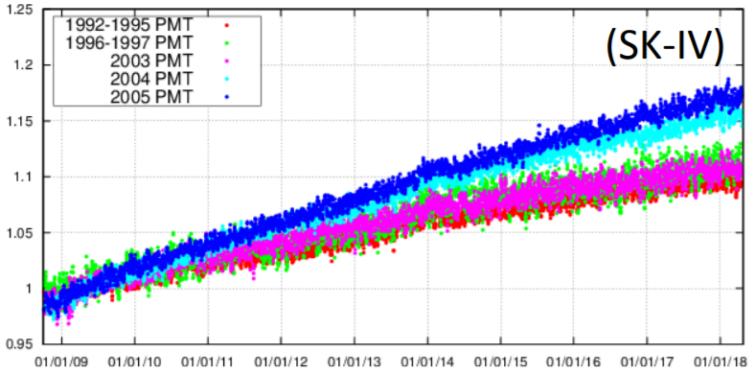

FIGURE 4.2: Time variation of the peak of the charge distribution for the PMT dark hits. Different color denote the different production year of PMT. A correction on PMT gain is applied based on this measurement.

4.1.3 Quantum Efficiency Calibration

Besides the gain, the relative difference of quantum efficiency (Q.E.) is also measured for each PMT since it affects the charge response for small number of incident photons. The measurement utilizes the same nickel source as the absolute gain calibration described in Section 4.1.2.

As Equation 4.2, the average number of hits on a PMT with a low intensity of incident light is proportional to the quantum efficiency $\epsilon_{qe}(i)$. The relative Q.E. for each PMT $\epsilon_{qe}(i)$ is obtained by comparing the simulated events, which account for the acceptance factor $a(i)$ but does not include the variations in $\epsilon_{qe}(i)$ and the real nickel source data. The resulting Q.E. for each individual PMT is also used in the detector simulation.

4.1.4 Relative Timing Calibration

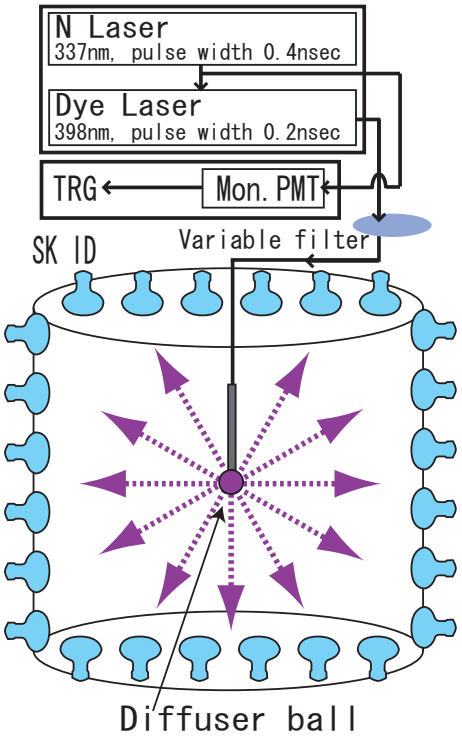

FIGURE 4.3: Schematic view of the timing measurement system using a laser. Take from [21].

The time response is important for the precise reconstruction of event vertices and track directions. It varies between PMTs due to many factors such as the difference on length of cable, the process time of electronics etc. Moreover, the time response also depends on the observed charge, since hits with larger charge exceed threshold of TDC discriminator earlier than those with less charge. This phenomenon is known as time-walk effect. The goal for the timing calibration is to make a correction table for the time-walk effect for each PMT in the detector with also consideration of the overall process time.

The schematic view of the system for the timing calibration is shown in Figure 4.3. A fast pulse of 0.4 ns FWHM at a wavelength of 337 nm is generated by a nitrogen laser and monitored by a 2-inch PMT with a fast response for trigger. The laser light pulse is then shifted to 398 nm by a dye, where the overall response including Cherenkov

emission spectrum, light absorption in water and quantum efficiency of the PMTs is almost maximum. The light intensity can be changed by adjusting the optical filter, which enable us to measure the time responses at various pulse height, i.e. the charge. The TQ distribution is obtained for each PMT individually, as shown in Figure 4.4, and then fitted by a polynomial as a function of charge to extract the calibration constants, named the TQ map. The uniformity of the time response of the PMTs in the entire detector is ensured.

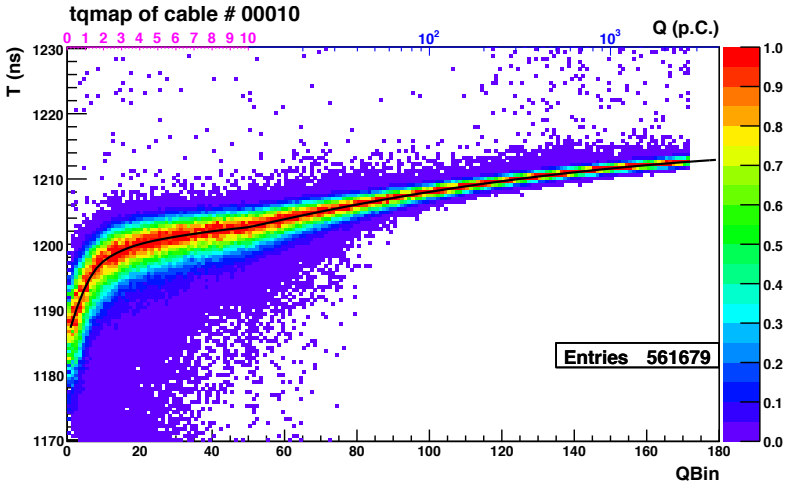

FIGURE 4.4: A typical TQ distribution for ID PMT. The horizontal axis and the vertical axis show the charge and TOF-corrected hit time, respectively. The scale of horizontal axis is linear up to 10 pC and then goes to log scale. A larger T value corresponds to earlier hit in this plot. Taken from [21].

4.1.5 Water Property Calibration

The photon propagation in water is modeled empirically with considering the light scattering and absorption. The attenuation of light in water can be expressed as $\exp(-l/L(\lambda))$, where l is the distance the light traveled and $L(\lambda)$ represents the attenuation length as a function of wavelength λ.

In Super-K simulation, $L(\lambda)$ is defined as

$$L(\lambda) = \frac{1}{\alpha_{abs}(\lambda) + \alpha_{asym}(\lambda) + \alpha_{sym}(\lambda)} \tag{4.4}$$

where α_{abs}, α_{asym} and α_{sym} are coefficients for absorption, asymmetric scattering and symmetric scattering, respectively. The asymmetric term α_{asym} is used to account for forward Mie scattering, while the effect of symmetric scattering α_{sym} takes the Rayleigh scattering and symmetric Mie scattering into account and can be described by $1 + \cos^2\theta$, where θ represent the direction of the scattered photon.

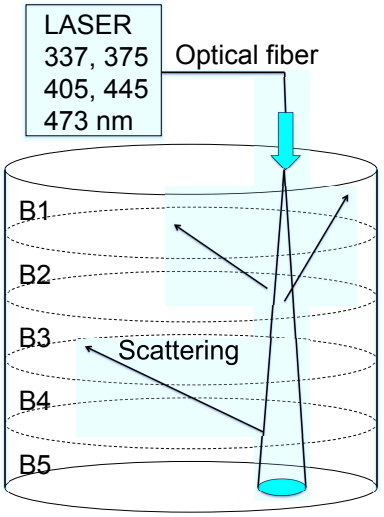

FIGURE 4.5: The laser injector system for the water property measurement. Taken from [21].

Figure 4.5 shows the laser injector system to measure the water constants. An collimated laser beam with adjustable wavelength is injected at the top of Super-K tank and vertically down. The scattered and reflected light is detected by the PMT belonging to five divisions of the barrel region labeled from B1 to B5, and the top wall of the detector. The hit time distribution after subtracting the time of flight for the PMTs in each detector region is shown in Figure 4.6. The sharp peaks on the right between 1830 to 1900 ns represent photons reflected by the PMTs and black sheets on the bottom wall, while those earlier hits are due to the photon scattered in water.

The water calibration constants, α_{abs}, α_{asym} and α_{sym} are tuned to achieve the best agreement between simulation and data. Figure 4.7 shows the result based on the data taken in Apr 2009. The water parameters are always monitored by this system during the Super-K operation. The time variation of the measured coefficients at various wavelengths is shown in Figure 4.8.

4.2 Energy Scale

The momentum reconstruction of neutrino event is mainly based on the charge observed by the PMTs in the tank. The factors discussed above, including water property or PMT gain will affect the performance of momentum reconstruction. On the other hand, the precise momentum determination of the neutrino event is necessary for the neutrino

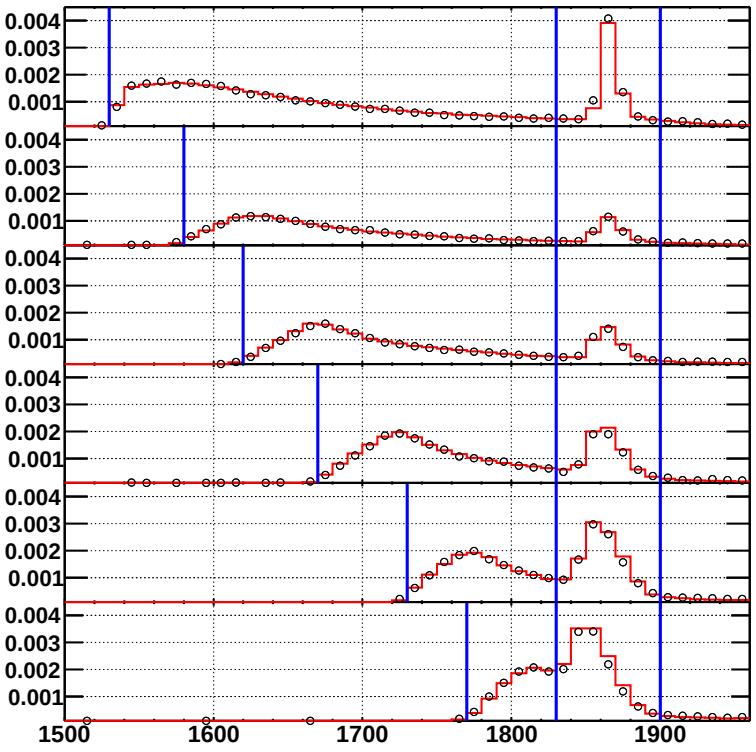

FIGURE 4.6: PMT hit time distribution in different detector regions for data (open circle) and Monte Carlo (red line) after tuning by scattering and absorption parameters. Taken from [21].

oscillation analysis since the oscillation probability is highly related to the energy of neutrinos. Four well-known independent control samples are used for the energy scale calibration [6] and systematic evaluation in different momentum range:

- Track length of high energy stopping muons (1$\sim$ 10 GeV/c)
- Cherenkov angle of low energy stopping muons (200 $\sim$ 500 MeV/c)
- Invariant mass of π^0 produced by neutrino interactions ($\sim$ 130 MeV/c)
- Momentum distribution of decay electron ($\sim$ 40MeV/c)

The absolute energy scale error, the time variation and the detector uniformity are discussed in this section. The data except the π^0 samples for the absolute error estimation was taken in April 2009, which is also used to calibrate the simulation software, while π^0 sample taken in full SK-IV are used. Time dependent attenuation length correction and PMT-by-PMT gain correction, which is introduced in Section 4.1.2, are applied.

A new reconstruction algorithm fiTQun, which will be introduced in Section 6.2, is used to reconstruct calibration samples here for the consistency with the neutrino oscillation analysis. As will be discussed in Section 7.3, recent Super-Kamiokande results have

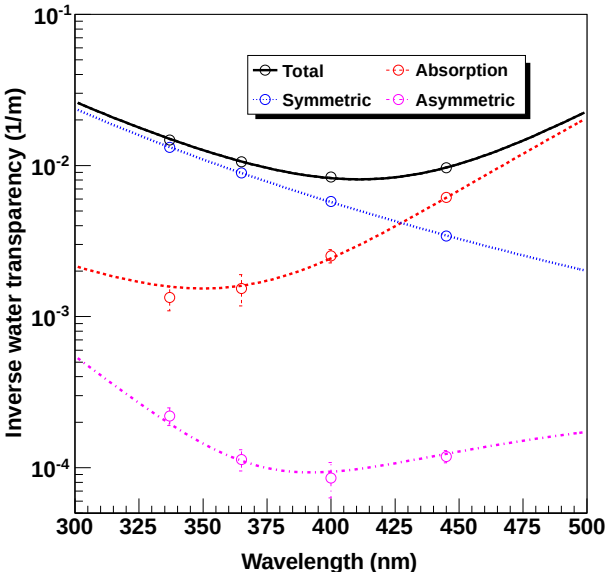

FIGURE 4.7: An example of water parameter fitting. The data used here is taken in Apr 2009. Points represent the average value of coefficients. The errors on the average value are represented as error bars. The vertical axis represent the coefficient α in Equation 4.4. Taken from [21]

been limited by a lack of statistics, so a larger fiducial volume (where the distance from the vertex to the nearest wall, $D_{\text{wall}} > 50$ cm) of the Super-K detector than its predecessor ($D_{\text{wall}} > 200$ cm) is used for the oscillation analysis. The energy scale for both the conventional fiducial volume ($D_{\text{wall}} > 200$ cm) and the expanded fiducial volume ($D_{\text{wall}} > 50$ cm) are evaluated to validate such a fiducial volume expansion.

4.2.1 High Energy Stopping Muons

The high energy stopping muon events are used to check the energy scale around 1-10 GeV/c by taking ratios of the reconstructed momentum of muons to their track lengths (p/range), since the energy loss dE/dx is approximately constant. The range is estimated from the muon entering position and the Michel electron vertex, both of which are assumed to be independent on the momentum reconstruction. Selection criteria for stopping muons are as follows:

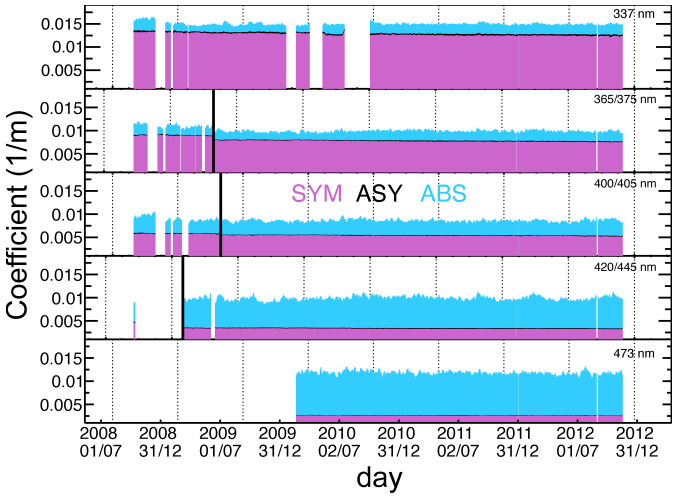

FIGURE 4.8: Time variation of the light absorption and scattering coefficients measured at various wavelengths. The coefficients for absorption α_{abs}, asymmetric scattering α_{asym} and symmetric scattering α_{sym} for various wavelength are shown in the blue (top), black (middle) and purple (bottom), respectively. In 2008, the wavelength was changed from 365 nm to 375 nm, from 400 nm to 405 nm, and from 420 nm to 445 nm. The time of this change is indicated by the black vertical bars. Taken from [21]

1. Total number of p.e. in ID is larger than 1000 p.e.
   This cut is to ensure the energy of muon is high enough to have a long track length.

2. Event is reconstructed as single-ring μ-like event.

3. Entering position of the cosmic ray muon is on the top wall of the detector: $z >$ 1760 cm and $r <$ 1640 cm.

4. Direction of the stopping muon is downward ($\cos\theta_{\text{zenith}} > 0.94$).
   Cuts 2 $\sim$ 4 are used to select the muon events which have a clear Cherenkov ring therefore can be reconstructed well.

5. Only one decay electron is detected.

6. Muon track length is longer than 500 cm.

7. Number of PMT hits within a 50 ns sliding time window is larger than 60.
   This cut is used to remove accidental coincidence gamma signal from radioactive isotopes.

8. Decay time is longer than 2000 ns.
   This cut is to ensure that the reconstruction of the decay electron is not affected by the light from the parent muon.

9. Vertex position of the decay electron is reconstructed within the fiducial volume.

Figure 4.9 shows p/range distributions of data and MC in the range from 5 m to 35 m with a binning width of 5 m and a fiducial volume cut of 50 cm on the decay electron. The errors are evaluated at each bin by comparing the peak value of both of data and MC after fitting to Gaussian function. The largest error, which comes from the longest range bin, i.e. the highest energy bin, is -1.68%. For the conventional fiducial volume case ($D_{\mathrm{wall}} > 200$ cm), similar distribution can be observed and the largest error is -1.54%, which also comes from the highest energy bin.

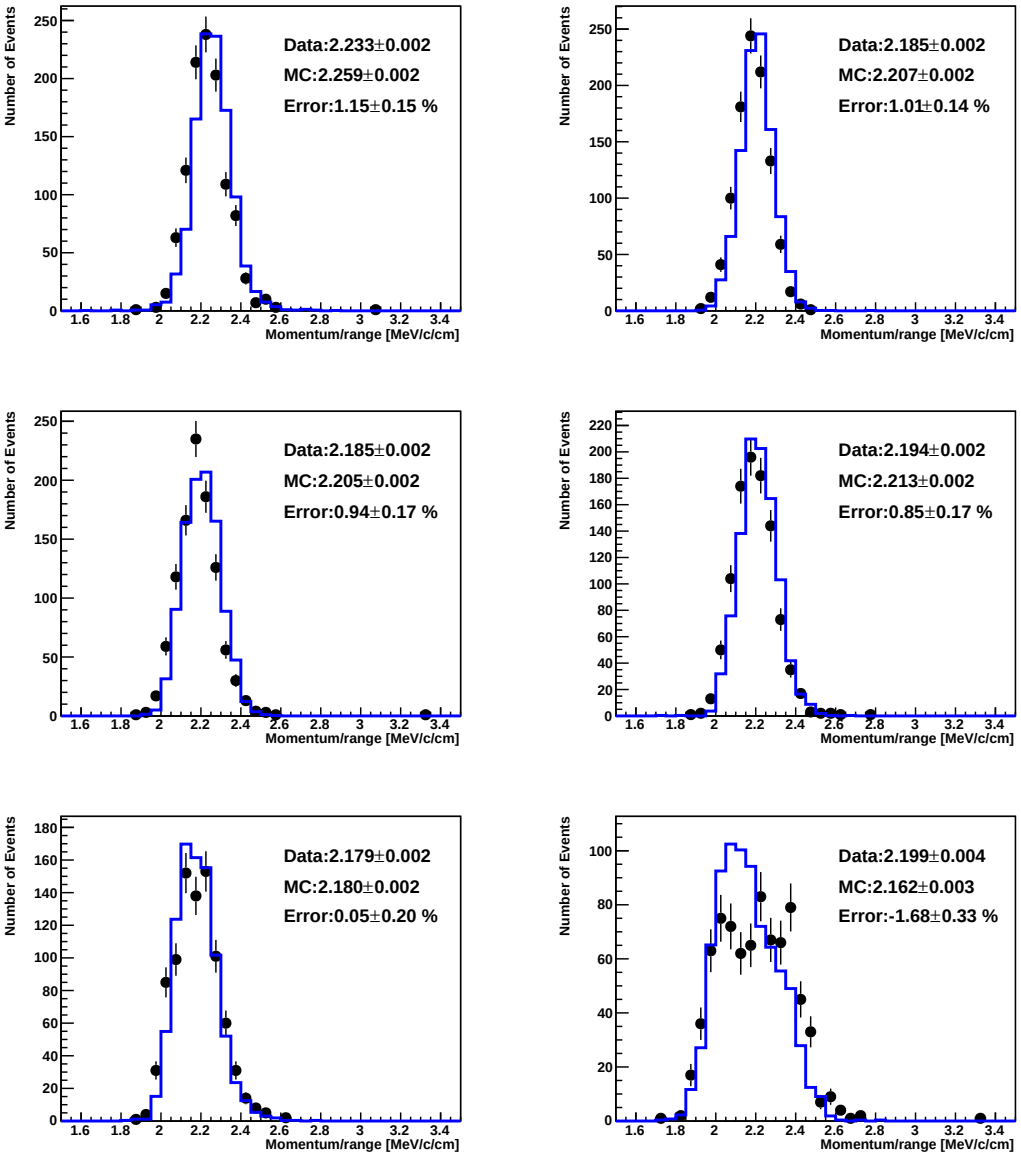

FIGURE 4.9: Momentum over the range of the stopping muon events with various track length for the data (black dots) and MC (blue line). From the top left plot to the bottom right plot, the track length is 5-10 m, 10-15 m, 15-20 m, 20-25 m, 25-30 m and 30-35 m, respectively. The fiducial volume for the decay electron used to determine the track length is defined as $D_{\mathrm{wall}} > 50$ cm. MC are normalized to data by area.

4.2.2 Low Energy Stopping Muons

The momentum of stopping muons with low energy (< 500 MeV/c) can be estimated by Cherenkov angle as following:

$$p(\theta) = \frac{m_\mu}{\sqrt{n^2 \cos^2(\theta) - 1}} \tag{4.5}$$

where θ, n, β, m_μ and $p(\theta)$ represent the Cherenkov angle, refraction index, ratio between velocity and the light of speed, muon mass and momentum respectively.

Selection criteria for the low energy stopping muons are:

1. Entering point is at the top wall of the detector: $z > 1720$ cm.
2. Direction of the stopping muon is downward: $\cos\theta_{\text{zenith}} > 0.87$.
3. Momentum estimated based on the Cherenkov angle is between 200 MeV and 440 MeV.
4. Goodness of reconstruction based on the Cherenkov angle is larger than 0.6.
5. Total number of p.e. in ID is between 500 p.e. and 5000 p.e.
6. Only one decay electron is detected.
7. Decay time is longer than 1200 ns.

Cuts $1 \sim 5$ are used to select the muon events which have a clear Cherenkov ring and can be reconstructed well. The event selection is optimized for the Cherenkov angle reconstruction tool. For cuts $6 \sim 7$, although the information of the decay electron is not used like the high energy cosmic ray muon, the requirement of one decay electron is to increase purity of muon in the sample. The requirement on the decay time is to ensure the reconstruction of the parent muon is not affected by the decay electron.

The ratios of the reconstructed momentum p(p.e.) to $p(\theta)$ are evaluated at three $p(\theta)$ bins. Figure 4.10 shows the distribution of p(p.e.)/$p(\theta)$ for different $p(\theta)$ range. The largest error, which comes from the lowest energy bin, is -0.85%. This value is common for both of the conventional fiducial volume ($D_{\text{wall}} > 200$cm) and the expanded fiducial volume ($D_{\text{wall}} > 50$ cm) since the event selection doesn't rely on the fiducial volume.

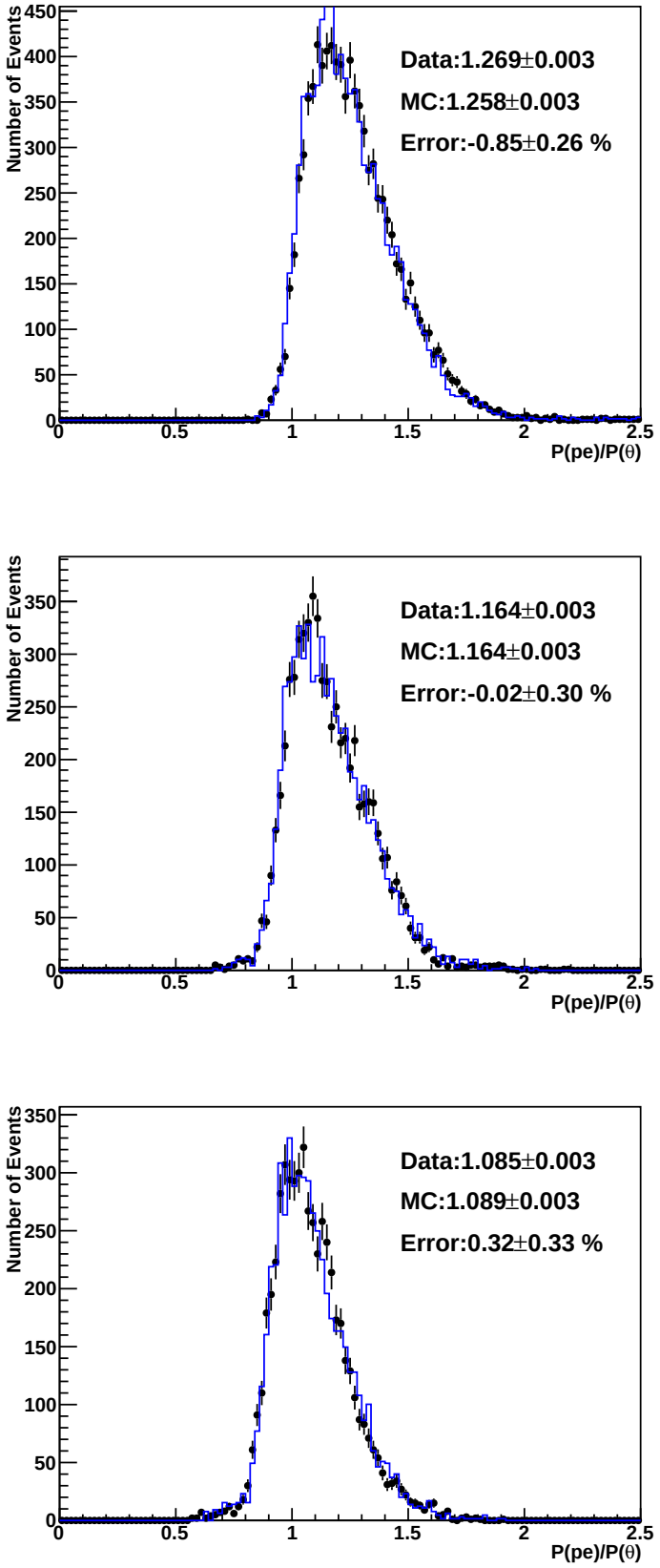

FIGURE 4.10: Distribution of p(p.e.)/$p(\theta)$ at each $p(\theta)$ bin for data (black dots) and MC (blue line). From the top, the $p(\theta)$ range is 200-280 MeV/c, 280-360 MeV/c and 360-440 MeV/c, respectively. MC are normalized to data by area.

4.2.3 Neutrino Induced π^0 Events

Single π^0 events are produced by neutral current interactions of atmospheric neutrinos in the detector. Since the produced π^0 decays into two photons almost immediately, the invariant mass of π^0 can be calculated with the reconstructed momentum of the two photons ($P_{\gamma 1}$ and $P_{\gamma 2}$):

$$M_{\pi^0} = \sqrt{2P_{\gamma 1}P_{\gamma 2}(1 - cos\theta)} \tag{4.6}$$

where θ represents the opening angle between the two photons. The selection criteria for the neutral current π^0 events are:

1. Pass the FC reduction, which is introduced in Section 5.1.
2. Two e-like rings are detected.
3. No decay electron is detected
4. Vertex position is reconstructed within the fiducial volume.

The distribution of the invariant π^0 mass for data and MC within different fiducial volume cuts are shown in Figure 4.11. The error is calculated by comparing the Gaussian fitted peak positions for both data and MC. The error in the new region (200cm $>$ D_{wall} $>$ 50cm), 1.44 $\pm$0.80%, is at the same level of the conventional FV (D_{wall} $>$ 200cm), -0.63 $\pm$0.34%. The final error for $D_{\text{wall}} > 50$ cm is -0.23$\pm$ 0.31%.

4.2.4 Decay Electrons

Stopping cosmic ray muons produce large number of decay electron events. The selection criteria for the decay electrons are listed as follows:

1. Total number of p.e. in ID is larger than 1000 p.e. for parent event.
2. Parent event is single-ring μ-like event.
3. Only one decay electron is detected.
4. Number of PMT hits within a 50 ns sliding time window is larger than 60.
5. Decay time is longer than 1200 ns.
6. Vertex position of the decay electron is reconstructed within the fiducial volume.

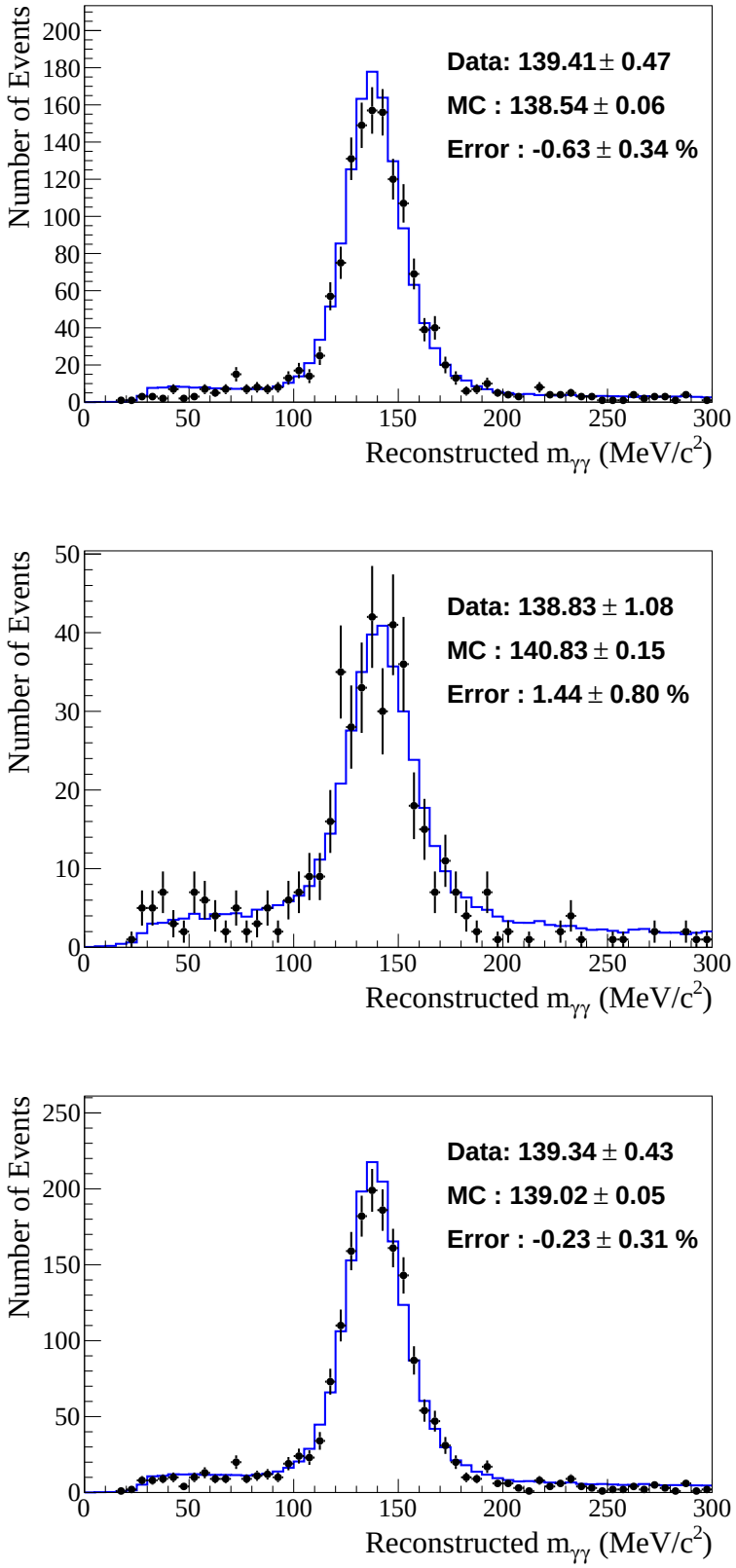

FIGURE 4.11: Invariant mass of neutral pions for the data (black dots) and MC (blue lines). From the top, the D_{wall} range is > 200 cm, $50 \sim 200$ cm and > 50 cm. MC are normalized to data by livetime.

Cuts 1∼3 are used to ensure the decay electron comes from a muon. Cut 4 rejects γ rays with energy of 6 MeV from μ^- capture on nucleons. Cuts 5 and 6 are used to select good electrons, which are not affected by the light from the parent muon and within the target region in the detector. Figure 4.12 shows the reconstructed momentum distribution with different fiducial volume cuts. The error is calculated by comparing the mean value of the spectrum for both data and MC. The error in the new region (50cm $< D_{\text{wall}} <$ 200cm), -1.07 $\pm$0.29%, is at the same level of the conventional FV ($D_{\text{wall}} >$ 200cm), -2.09 $\pm$0.14%. The final error in $D_{\text{wall}} > 50$ cm is -1.92$\pm$0.13 %.

4.2.5 Time Variation of Energy Scale

Stability of the detector's energy scale is confirmed with the high energy stopping muons and decay electrons as Figure 4.13. The p/range value of the stopping muons is stable (-0.01%$\pm$0.02%/year) while the average momentum of the decay electrons is increasing as 0.19%$\pm$0.02%/year. As introduced in Section 4.1.2, the PMT gain increases as time passes. The dark hit rate also increases due to the unchanged trigger threshold. The increase of the PMT dark hit rate, which cannot be cancelled by the gain correction, is considered to be the reason of the increase in the decay electron momentum. The time variation uncertainties are defined as the larger value of the ratios between the RMS to the mean in the two samples. The time variation error of the decay electrons in the new region (50 cm $< D_{\text{wall}} <$ 200 cm) is 0.88%, which is at the same level as the one in conventional FV, 0.59%. The final time variation uncertainty is 0.62% from the decay electron in the region of $D_{\text{wall}} > 50$ cm.

4.2.6 Detector Uniformity of Energy Scale

Uniformity of the detector is evaluated with the decay electrons from the stopping cosmic ray muons. Vertexes and the direction of the decay electrons distribute almost uniformly in the fiducial volume, which makes them a good calibration sample for the detector uniformity check. Besides the selection criteria shown in Section 4.2.4, decay electrons are also required to be perpendicular to their parent muon direction in order to avoid muon polarization effect. This condition is $-0.25 < \cos\theta_{e\mu} < 0.25$, where $\cos\theta_{e\mu}$ is the opening angle between the decay electron and the parent muon directions. The error is defined as the central value most deviated from one, which comes from the horizontal direction as shown in Figure 4.14, for all the three regions. The value for 50 cm $< D_{\text{wall}} <$ 200 cm, 1.08%, is at the same level as the value for $D_{\text{wall}} >$ 200 cm, 0.58%. The final energy uniformity error for $D_{\text{wall}} > 50$ cm is 0.67%.

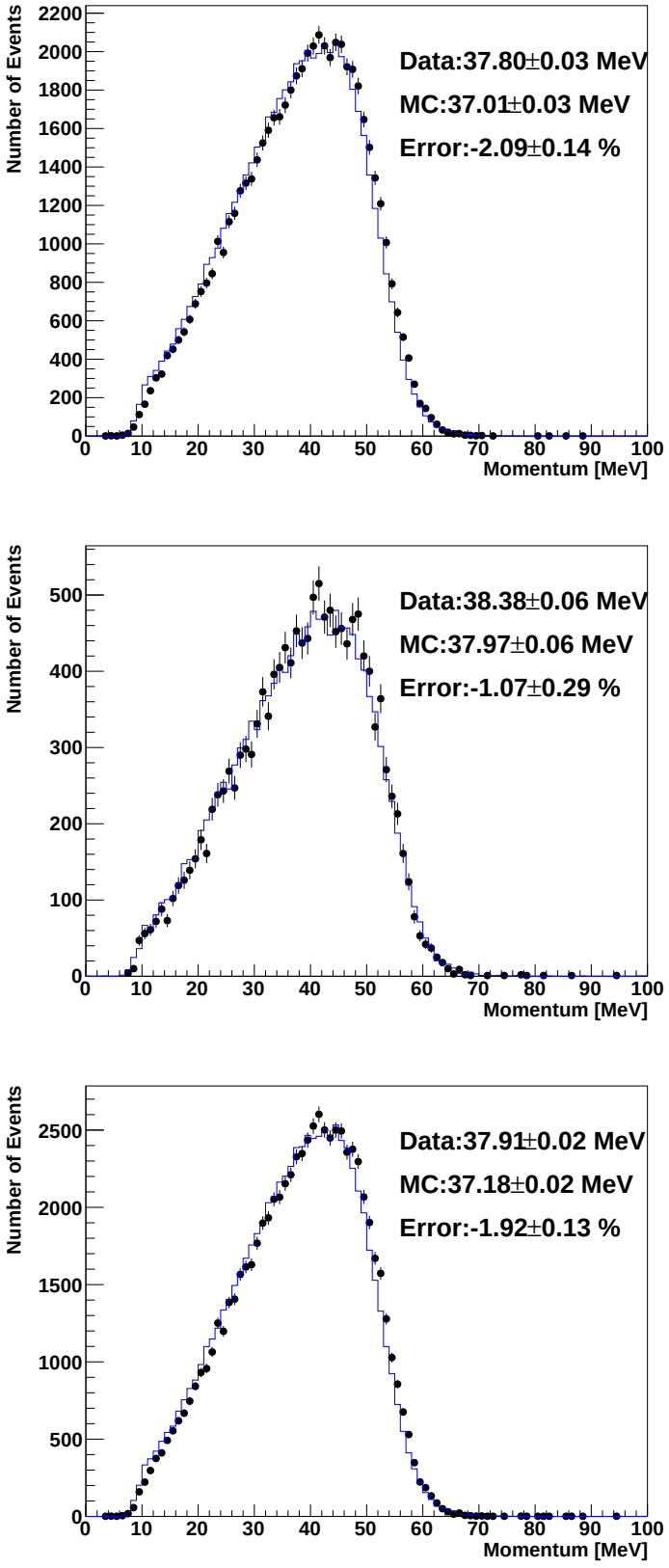

FIGURE 4.12: Momentum of decay electrons for the data (black dots) and MC (blue line). From the top, the D_{wall} range is > 200 cm, $50 \sim 200$ cm and > 50 cm. MC are normalized to data by area.

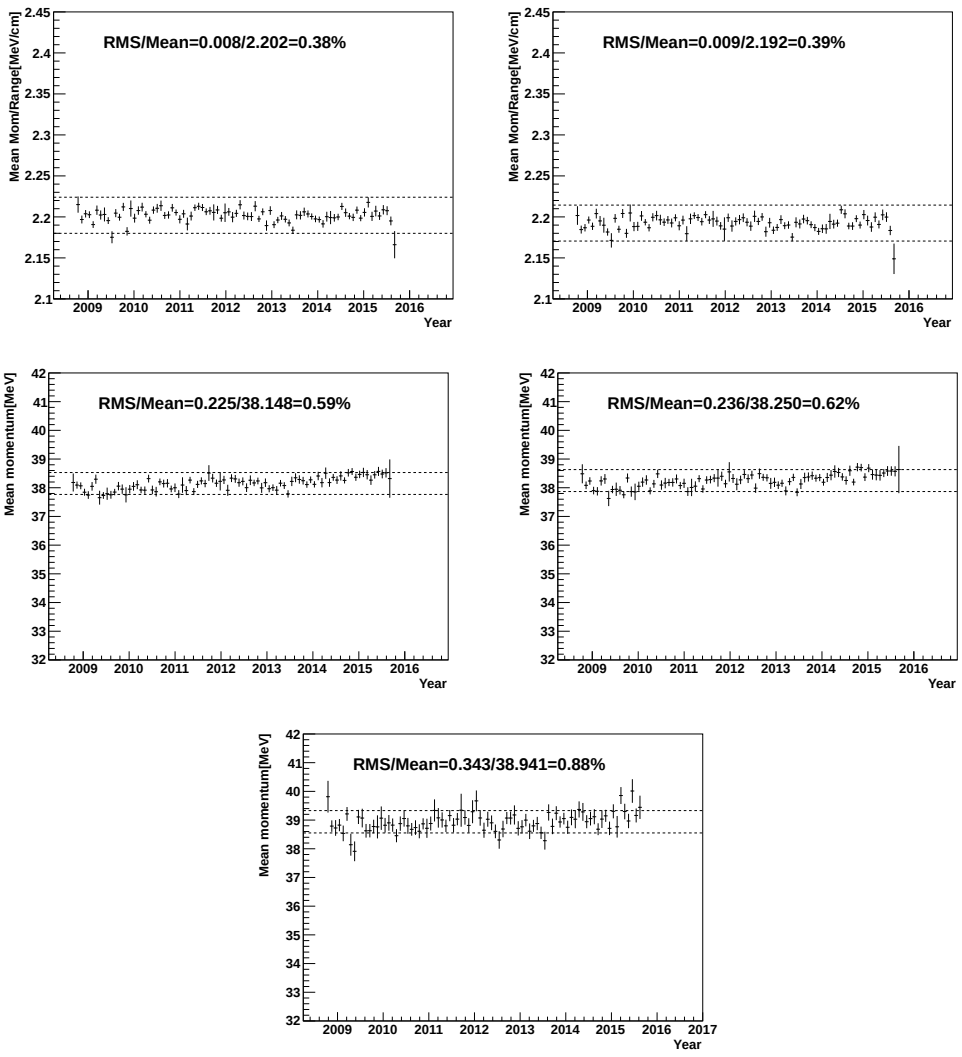

FIGURE 4.13: Time variation plots of the p/range of muon (top figures) and the momentum of decay electron (bottom three figures) for fiTQun. The left two figures show the result for $D_{\mathrm{wall}} > 200$ cm, while the right two figures are for $D_{\mathrm{wall}} > 50$ cm. The bottom figure shows the time variation of the momentum of decay electron with 200cm $> D_{\mathrm{wall}} > 50$ cm. The dashed line shows the range of average value with $\pm 1\%$ error.

4.2.7 Summary of the Energy Scale Error

The absolute energy scale error is evaluated by various samples for different momentum ranges and summarized in Figure 4.15 and Table 4.1. The final absolute energy scale error is obtained from the most discrepant sample, which is 1.92% (2.09%) from the decay electron for $D_{\mathrm{wall}} > 50(200)$ cm. The statistical uncertainty shown here is just for reference and not considered in the final uncertainties determination. By adding the absolute energy scale uncertainties to the time variation uncertainties in quadrature, the final energy scale uncertainties is 2.02% (2.17%) for $D_{\mathrm{wall}} > 50(200)$ cm. The energy scale related uncertainties in the new region (50 cm $< D_{\mathrm{wall}} <$ 200 cm) are also

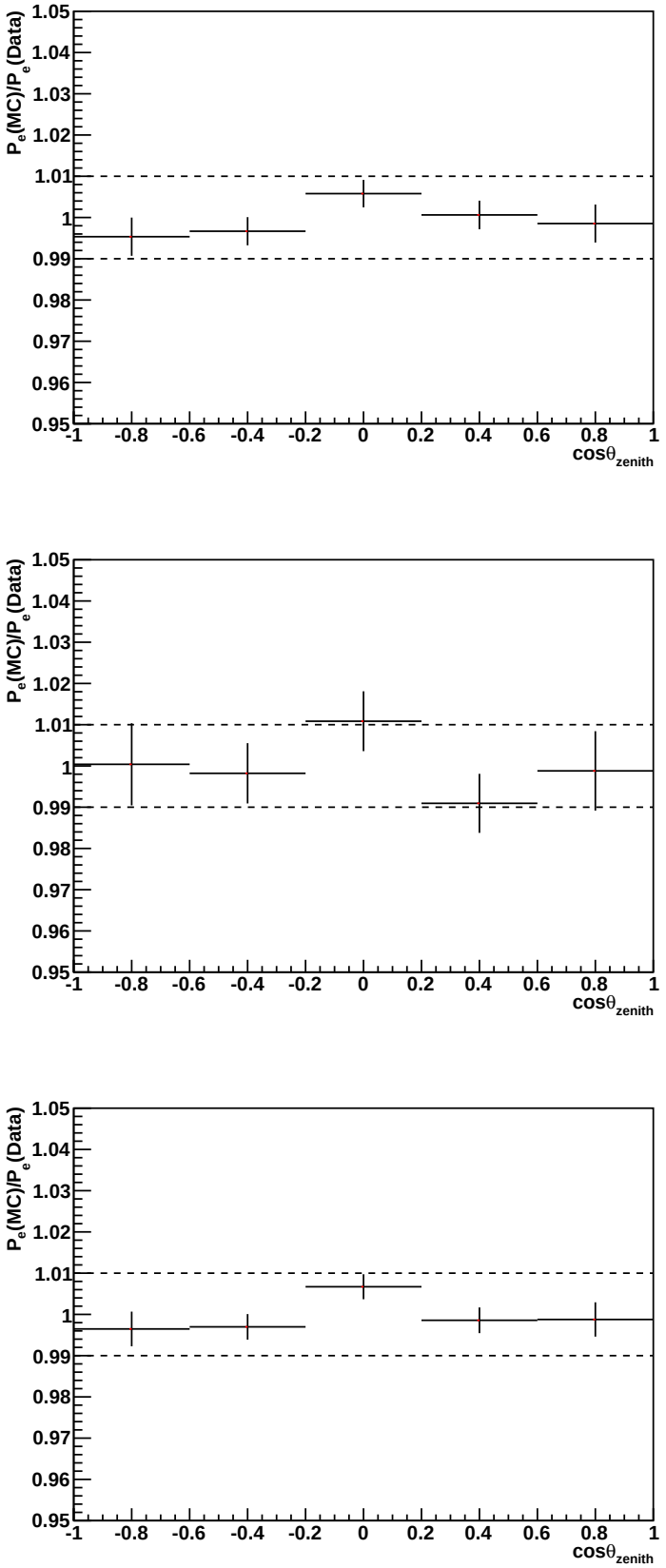

FIGURE 4.14: Uniformity of the detector as a function of zenith angle of decay electrons. Y axis is the ratio of MC to data of the average momentum of decay electrons. X axis is direction of the electron on z axis, a positive value represents a downward direction. From the top, the D_{wall} range is > 200 cm, $50 \sim 200$ cm and > 50 cm. The dashed line shows the $\pm 1\%$ error range.

summarized in Table 4.1. The uncertainty evaluated based on the low energy cosmic ray muon sample is common for all three detector regions since the event selection doesn't rely on the FV cut. The energy uniformity error is assumed to be independent from the energy scale error since it is shown that the energy scale related systematic errors keep stable even if we expand the fiducial volume to $D_{\mathrm{wall}} > 50$ cm, as shown in Table 4.2.

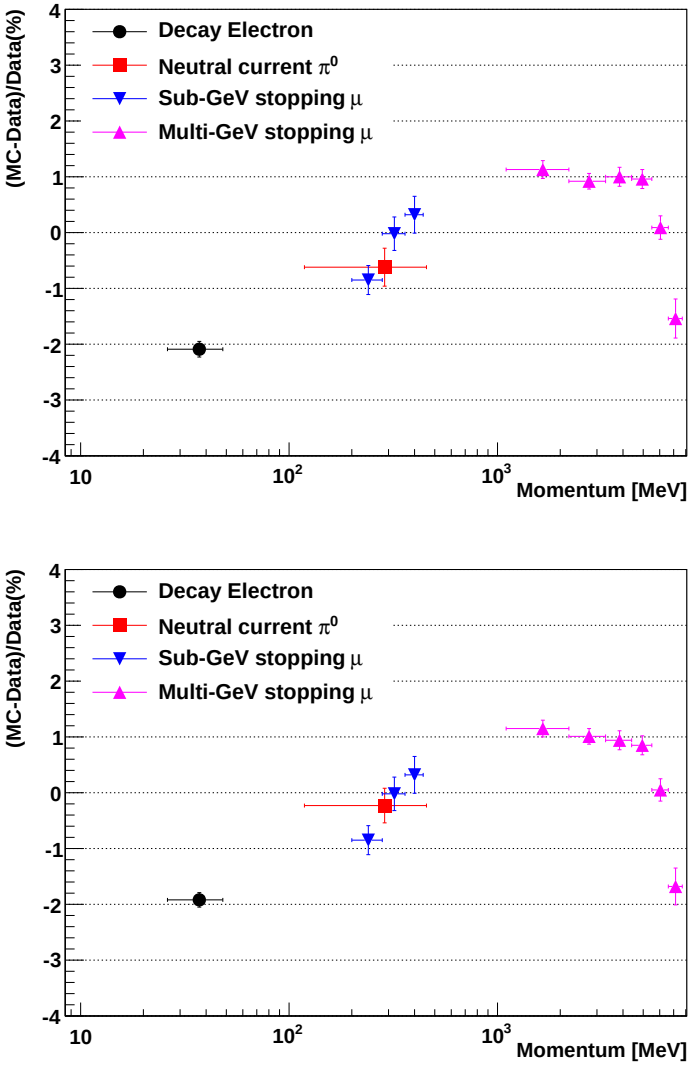

FIGURE 4.15: Absolute energy scale error with $D_{\mathrm{wall}} > 200$ cm (top) and $D_{\mathrm{wall}} > 50$ cm (bottom). The statistical uncertainty is denoted by the vertical error bars. The momentum range of each sample used to evaluate energy scale error is shown by the horizontal error bar. The final absolute energy scale error 2.09% (1.92%) for $D_{\mathrm{wall}} > 200(50)$ cm.

D_{wall} range	> 50 cm	50 cm$\sim$200 cm	> 200 cm
High energy stopping muon			
Track length			
5 m $\sim$ 10 m	$1.15\% \pm 0.15\%$	$1.60\% \pm 0.50\%$	$1.13\% \pm 0.16\%$
10 m $\sim$ 15 m	$1.01\% \pm 0.14\%$	$-0.11\% \pm 0.64\%$	$0.92\% \pm 0.14\%$
15 m $\sim$ 20 m	$0.94\% \pm 0.17\%$	$-0.80\% \pm 1.03\%$	$1.00\% \pm 0.17\%$
20 m $\sim$ 25 m	$0.85\% \pm 0.17\%$	$-0.54\% \pm 0.94\%$	$0.96\% \pm 0.17\%$
25 m $\sim$ 30 m	$0.05\% \pm 0.20\%$	$0.33\% \pm 1.26\%$	$0.09\% \pm 0.21\%$
30 m $\sim$ 35 m	$-1.68\% \pm 0.33\%$	$1.08\% \pm 2.03\%$	$-1.54\% \pm 0.35\%$
Low energy stopping muon			
Momentum range			
200 MeV $\sim$ 280 MeV		-0.85%±0.26%	
280 MeV $\sim$ 360 MeV		-0.02%±0.30%	
360 MeV $\sim$ 440 MeV		0.32%±0.33%	
Neutrino induced π^0			
	-0.23%±0.31%	1.44%±0.78%	-0.62%±0.34%
Decay electron			
	-1.92%±0.13%	-1.07%±0.29%	-2.09%±0.14%

TABLE 4.1: Summary of absolute energy scale error. The final absolute energy scale value is obtained from the most discrepant sample, i.e. decay electron in this study.

D_{wall} range	> 50 cm	> 200 cm
Energy scale error		
	2.02%	2.17%
Absolute energy scale		
	1.92%	2.09%
Time variation		
	0.62%	0.59%
Energy uniformity error		
	0.67%	0.58%

TABLE 4.2: Summary of energy scale check. The energy scale error is the quadratic-sum of absolute energy scale error and the time variation error. The absolute energy scale error value is obtained from the most discrepant sample, i.e. decay electron in this study.

Chapter 5

Neutrino Event Selection

At trigger level, the Super-Kamiokande event sample consists mainly of downward-going cosmic ray muons and low energy radioactivities from contaminants in the water such as radon. The neutrino data selection method directly determines the quality of the sample used for analysis. An efficient selection method is essential to achieve a higher sensitivity for the atmospheric neutrino oscillation analysis.

Atmospheric neutrino events observed in SK are categorized into three types:

- Fully contained (FC)
- Partially contained (PC)
- Upward-going muon (Up-μ)

For events classified as FC and PC, the neutrino interacts within the fiducial volume, defined as the region located more than 200 cm from the ID wall ($D_{\rm wall} > 200$ cm) in previous analyses. The fiducial volume has been expanded to ($D_{\rm wall} > 50$ cm) for a higher statistics in this analysis, which will be described in Section 7.3. Events with no activity in the outer detector are classified as FC. If energy deposition in the OD is observed, generally from a high energy muon exiting the ID, the event is classified as PC.

Muons created by neutrino interactions in the rock around SK or in the OD water and traveling upward through the detector form the Up-μ sample. The reason why only upward muons are used is that those events are hard to be distinguished from the cosmic rays muons, which travels in downward direction. The FC data are subdivided into several categories according to the visible energy [1], the number of observed

[1] Visible energy is defined as the energy of an electromagnetic shower producing the same amount of Cherenkov light as observed in the event.

Cherenkov rings, the particle ID (PID) of the most energetic ring, and the number of observed electrons from muon decays. The detailed category for FC events will be discussed in Section 7.1.1. All FC events have been reconstructed and categorized by the new reconstruction algorithm, which will be introduced in Section 6.2.

The events categorized as PC and Up-μ samples after reduction are further divided into "through-going" and "stopping" subsamples according to the muon stopping point. The Up-μ events categorized as "through-going" are further divided into "showering" if an associated electromagnetic shower is found in the ID or "non-showering" if not. These two samples are reconstructed using the conventional reconstruction algorithm, which will be introduced briefly in Section 6.1. Only the FC reduction will be focused in this section since the new reconstruction algorithm is currently only used for FC events as has been stated above. More detail about the data reduction and event reconstruction for PC and Up-μ events can be found in [111].

The schematic view of each event type are summarized in Figure 5.1. The neutrino mean energies are ∼1 GeV for FC events, ∼10 GeV for PC events and stopping Up-μ events, ∼100 GeV through-going Up-μ events, as shown in Figure 5.2.

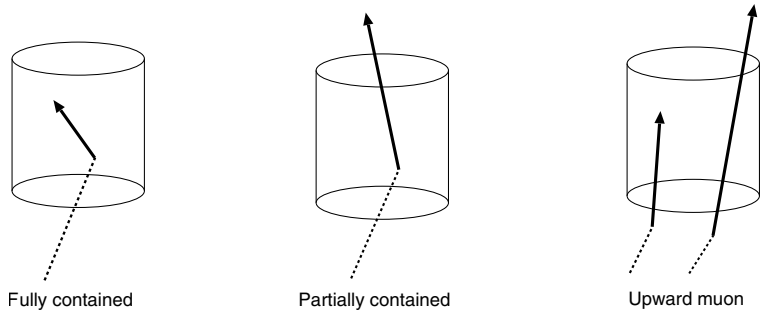

FIGURE 5.1: Schematic view of observed atmospheric neutrino in SK. Dashed lines represent the track of atmospheric neutrinos, while the solid lines show the lepton's track.

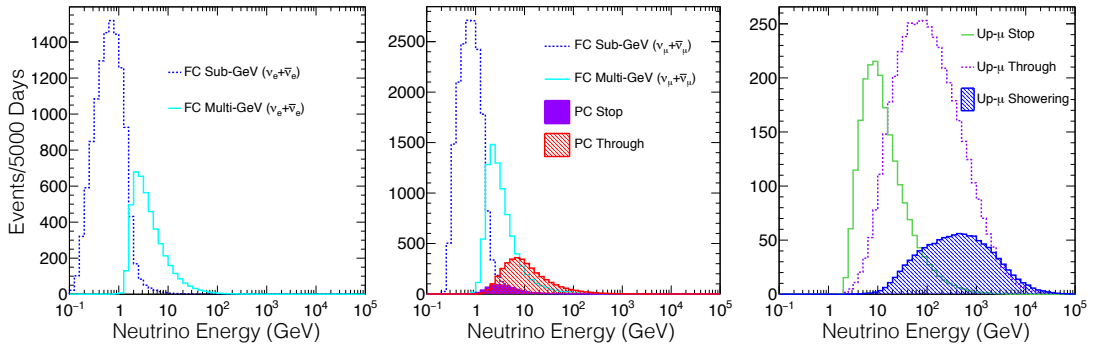

FIGURE 5.2: Expected neutrino energy spectra of different event categories. Taken from [6].

The event reduction is aimed to remove background events including cosmic ray muon and flasher events, which are caused by internal coronal discharge of a PMT, to purify the final sample in neutrino events. Each sample, including FC, PC and Up-μ, have their own reduction processes, which are optimized for the topology and the OD activity of neutrino events.

It should be noticed that the criteria in event reduction are different for different Super-K phases since the condition of the detector changed. Only the criteria for Super-K IV is discussed here, the detail of the event reduction for other Super-K phases can be found in [8].

5.1 Reduction for Fully Contained Events

FC events are distinguished from PC events based on the number of OD hits in the highest charge cluster. The process of the FC data reduction consists of five steps.

5.1.1 First Reduction

The event trigger is fired at a rate of 10^6 times a day, which consists mainly of downward-going cosmic ray muons and radioactivities with low energy due to contaminants in the water. Two criteria are applied to remove those backgrounds in the first step of the FC reduction.

1. $\mathrm{PE}_{300} > 200$ p.e.s
   where PE_{300} is the maximum number of total photoelectrons (p.e.s) observed by the ID PMTs within a sliding 300 ns time window.

2. $\mathrm{NHITA}_{800} \leq 55$
   where NHITA_{800} denotes the number of OD hits in a fixed time window from 500 ns to 1300 ns, which is around the event trigger at 900 ns.

Most of the low energy background events can be rejected by the first cut. The second cut is aimed to reject the cosmic ray muon events, which have many OD hits. After the first reduction, the event rate is decreased to the order of 10^3 events/day.

5.1.2 Second Reduction

Selection criteria for the second reduction include:

1. $\text{NHITA}_{800} \leq 30$ or $\text{PE}_{\text{total}} > 100{,}000$ p.e.s
   where PE_{total} is the sum of the observed p.e.s of the ID PMT.

2. $\text{PE}_{\text{max}}/\text{PE}_{300} < 0.5$
   where PE_{max} is the maximum number of p.e.s observed by a single ID PMT.

Stronger rejection to events with OD activity is done by the first cut while very high energy FC events with light leakage into the OD side are accepted. The second cut mainly rejects the electrical noise events caused by a single PMT with a high charge. Event rate becomes $\sim 10^2$ events/day after the FC second reduction.

5.1.3 Third Reduction

Remaining background events are mainly noise events and cosmic ray muons with a small number of OD hits or high momentum. They are rejected by the following cuts in the third reduction.

Hard Muon Cut

Cosmic ray muons with a very high energy (e.g. > 1 TeV), also called "hard muon", would be identified and rejected by the following cut:

1. $\text{NHITA}_{500} \geq 40$
   where NHITA_{500} is the number of OD hits in a sliding 500 ns time window before 1300 ns, which is just after the main trigger (~ 900 ns).

Through-going Muon Cut

Through-going muons have very high energy and deposit large energy in the ID. A through-going muon fitter is applied when:

1. $\text{PE}_{\text{max}} > 231$

2. Number of hits for ID PMTs ≥ 1000

This fitter finds the entering and exiting points of the through-going muon in the ID and calculated the goodness of fit based on the observed and expected hit time information of PMTs. The maximum value of the goodness is 1 when the expected and observed

distribution of PMT hit time are identical. A minus value would be returned if the fitter failed finding the entrance or exiting points.

The criteria to reject the through-going muon is:

1. Goodness of the through-going muon fit > 0.75
2. $\mathrm{NHITA_{in}} \geq 10$ or $\mathrm{NHITA_{out}} \geq 10$
   where $\mathrm{NHITA_{in}}$ ($\mathrm{NHITA_{out}}$) denotes the number of OD hits within 8 m from the entrance (exit) in a fixed 800 ns time window.

Events that passed those criteria are rejected as through-going muon.

Stopping Muon Cut

A stopping muon fitter, which is similar to the through-going muon fitter, is applied to find the entrance point of muon for the stopping muon rejection. Events fulfilling the following criteria are rejected as stopping muons:

1. Goodness of the stopping muon fit ≥ 0
   which means that the fitter finds the entrance point successfully
2. $\mathrm{NHITA_{in}} \geq 10$

Cable Hole Muons

There are twelve cable holes on top of the SK detector tank. No OD PMT was installed on the cable holes to enable the high voltage supply cables and signal cables to pass through. Therefore, cosmic ray muons are able to enter the detector without OD activity if they cross those holes.

Four 2 m $\times$ 2.5 m plastic scintillation counters were installed in April, 1997 on four cable holes near the ID wall among all twelve holes to reject those cable hole muons. The rejection criteria with the veto counters are:

1. One hit on plastic scintillation counter.
2. Both $\mathrm{L_{veto},}_x$ and $\mathrm{L_{veto},}_y < 4$ m
   where $\mathrm{L_{veto},}_x$ and $\mathrm{L_{veto},}_y$ are the distances between the cable hole and the reconstructed vertex in the direction of x and y, respectively.

Flasher Event Cut

Flasher events caused by the internal coronal discharges of PMT usually have a border hit timing distribution than that of neutrino events. A TOF fitter aimed to find the light source assuming all photons are emitted from a point-like source simultaneously, will also be used to fit the event when the total number of hits in ID is less than 250. The goodness of fit is expected to be small for the flasher events since the process of internal discharge is slow which makes the emitting of photons is not able to be regarded as at the same time.

The criteria for the flasher events rejection are:

1. $\mathrm{NMIN}_{100} \geq 20$
   where NMIN_{100} represents the minimum number of ID hits in a sliding 100 ns time window from +300 ns to +800 ns after the trigger.
2. Goodness of the TOF fitter ≤ 0.4

Accidental Coincidence Events Cut

When a cosmic ray muon event follows a low energy event within the trigger gate, the cosmic ray muon might survive from the cuts on OD hits since the OD activities caused by the muon are much later than the trigger timing. Those events, which is termed as accidental coincidence events, are removed by applying cut on the hit happened later than the trigger time:

1. $\mathrm{NHITA}_{\mathrm{off}} \geq 20$
   where $\mathrm{NHITA}_{\mathrm{off}}$ is the number of OD hits in a fixed 500 ns time window which is from +400 ns to +900 ns after the trigger timing, also called off-time window.
2. $\mathrm{PE}_{\mathrm{off}} > 5000$ p.e.s
   where $\mathrm{PE}_{\mathrm{off}}$ is the number of p.e.s in the ID within the off-time window.

Low Energy Events Cut

The radioactive background and electrical noise events which survive from the previous reduction step are suppressed by:

1. $\mathrm{NHIT}_{50} < 50$
   where NHIT_{50} is the number of ID hits in a sliding 50 ns time window.

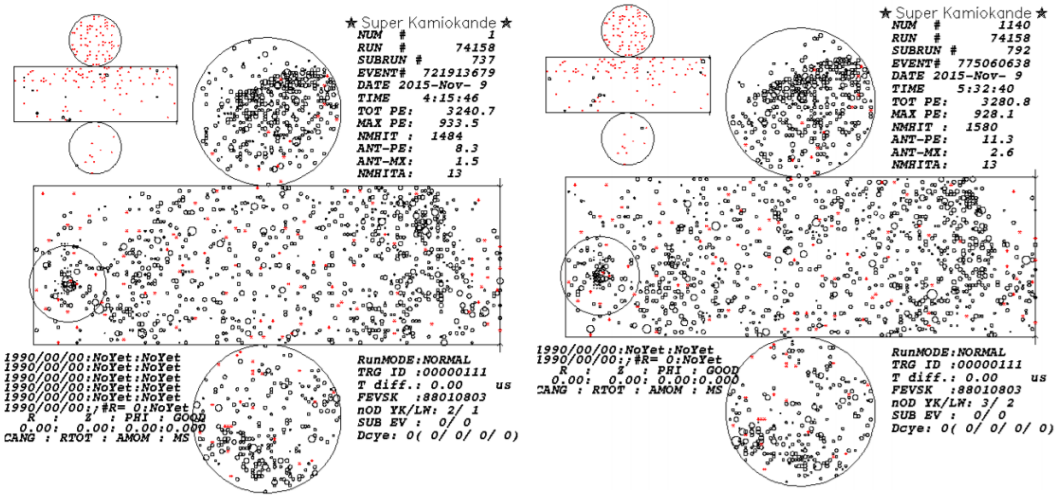

FIGURE 5.3: Two flasher event displays in SK-IV. Each circle represents a hit on PMT. A larger circle denotes a higher charge signal for the PMT. The flash light for both events come from the same PMT on the left part of plots, therefore similar hit pattern observed.

The time windows defined here considers the time of flight for each photon, which is assumed to be from a common light source. $\mathrm{NHIT}_{50} = 50$ is a typical value for an electron with an energy of 9 MeV. This cut is optimized for a high efficiency of the neutrino events selection in the oscillation analysis, which requires the visible energy larger than 30 MeV.

5.1.4 Fourth Reduction

The FC fourth reduction is mainly aimed to reject the flasher events. Failing tubes often produce multiple events with similar topologies as these discharges repeat. Typical flasher events have spatially similar hit distributions, as shown in Figure 5.3.

Two methods, including a pattern matching algorithm and the Kolmogorov-Smirno (KS) test, are used to evaluate the similarity of the past events which passed the third step of the FC reduction and the event for test. Only events within latest two years will be used as the past events since the possibility that two neutrino events have similar hit pattern increases.

The PMTs in the ID is divided into 1450 part for 2 m × 2 m square, called patches. The pattern matching algorithm calculate a correlation parameter r defined as

$$r = \frac{1}{N} \sum_i \frac{(Q_i^A - \langle Q^A \rangle) \times (Q_i^B - \langle Q^B \rangle)}{\sigma_A \times \sigma_B} \tag{5.1}$$

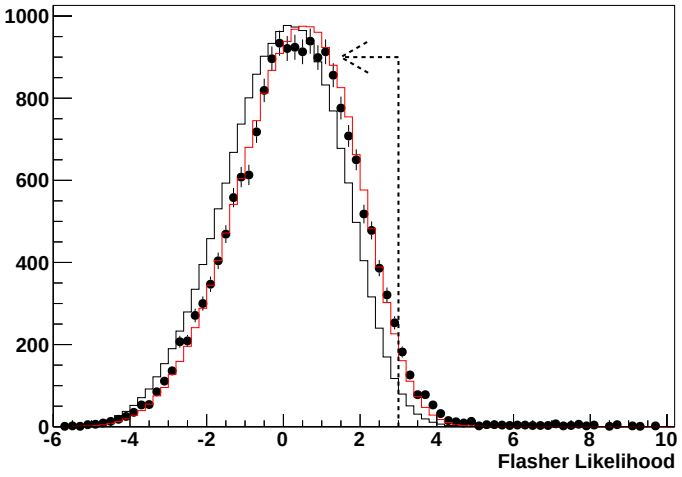

FIGURE 5.4: Final likelihood for flasher event rejection. Points show the distribution of data, while the black (red) solid line shows the distribution of nominal MC (fitted MC).

where N represents the number of patches, $\langle Q^A \rangle$ and σ_A represent the average charge and its standard deviation for event A, respectively. The meaning of $\langle Q^B \rangle$ and σ_B are defined similarly.

On the other hand, the KS test will also be done based on the patches. The final selection will consider the result from both two methods and reject the event with high similarity to past events. Figure 5.4 shows the final likelihood distribution to reject the flasher events. A larger value represents a higher possibility for a flasher event. The threshold is shown as the dashed line. Points show the distribution of data, while the black (red) solid line shows the distribution of nominal MC (fitted MC). The difference between the nominal MC and the fitted MC is 1.3%, which is regarded as the uncertainty from the flasher rejection.

5.1.5 Fifth Reduction

The final reduction consists of several criteria optimized for different background sources. Event that passed the third reduction will be reconstructed by APFit, which is a conventional reconstruction for neutrino events. The reconstruction information can be utilized for the background rejection with higher precision. The detail about APFit will be introduced in Section 6.1.

Invisible Muon Cut

Cosmic ray muons with energy lower than the Cherenkov threshold after entering ID generate no ID PMT hits. The Michel electron from such invisible muons can emit light inside the ID, like a neutrino event. A typical invisible muon has an OD signal earlier than the trigger timing and a low energy ID signal from the Michel electron. Events passing the following criteria are rejected as invisible muons:

1. $\mathrm{PE_{tot}}$ <1000 p.e.s
2. $\mathrm{NHITAC_{early}} \geq 5$
   where $\mathrm{NHITAC_{early}}$ is the maximum number of OD hits in the cluster in a sliding 200 ns time window from -8800 ns to -100 ns.
3. $\mathrm{NHITAC_{early}} + \mathrm{NHITAC_{500}} \geq 10$ if $\mathrm{DIST_{clust}} < 500$ cm
   $\mathrm{NHITAC_{early}} \geq 10$ otherwise
   where $\mathrm{NHITAC_{500}}$ is the number of OD hits in the cluster in a fixed 500 ns time window from -100 ns to $+400$ ns. $\mathrm{DIST_{clust}}$ represents the distance between the OD hit clusters used for the calculation of $\mathrm{NHITAC_{early}}$ and $\mathrm{NHITAC_{500}}$.

Coincidence Muon Cut

The accident coincidence muon events which survive from the third reduction are rejected by the following criteria:

1. $\mathrm{PE_{500}} < 300$ p.e.s
   where $\mathrm{PE_{500}}$ is the total number of p.e.s observed in the ID in a fixed 500 ns time window from -100 ns to $+400$ ns.
2. $\mathrm{PE}_{late} \geq 20$ p.e.s
   where PE_{late} is the maximum number of OD hits in a 200 ns sliding time window from $+400$ ns to $+1600$ ns.

Long-tail Flasher Cut

A tighter flasher cut than the one in the third reduction step is used to remove remaining flasher events:

1. $\mathrm{NMIN_{100}} \geq 6$ if goodness of TOF fitter < 0.4
   where $\mathrm{NMIN_{100}}$ is the minimum number of ID hits in a sliding 100 ns time window

from +300 ns to +800 ns. The definition is the same as the one in the third reduction step.

Stopping Muon Cut

A tighter cut is applied when the stopping muon event is reconstructed well, as

1. $\text{NHITA}_{\text{in}} \geq 5$ when goodness of stopping muon fit ≥ 0.5

Furthermore, the reconstructed variable from APFit is also utilized to reject the stopping muon.

1. $\text{NHITA}_{\text{APFit}} \geq 4$
   where $\text{NHITA}_{\text{APFit}}$ is the number of OD hits within 8 m from the muon's entrance point, reconstructed by APFit, in a sliding 200 ns time window from -400 ns to +400 ns.

Events that pass either cut will be rejected as stopping muon events.

Cable Hole Muon Cut

Similarly, the cut for cable hole muon is tighter when the stopping muon event is reconstructed well, as

1. Goodness of the stopping muon fit ≥ 0.4
2. $\text{PE}_{\text{tot}} > 4000$
3. cos value of the muon's direction on z axis < -0.6
4. the distance from the muon entering point to the nearest cable hole < 250 cm

Backgrounds due to hardware issue

Some non-physical background events might be contaminated due to some hardware issues. Events are rejected if any of the following conditions are satisfied.

- $N_0 \geq 250$ and N_0 - $N_1 \geq 100$
  - N_0 (N_1) is the number of hits for ID PMTs with less (larger) than single p.e.

  - This cut is used to reject electronic noise from high voltage system or electronic boards, which create lots of hits with small charge.

- NHITA < 1 for any electronic hut
  - NHITA is the number of OD hits.
  - This cut is used to reject events with electronic hut doesn't work.
- Reference PMT for laser or xenon lamp are hit.
  - This cut is used to reject the event for calibration, which utilized laser or xenon lamp.

5.1.6 FC Reduction Summary

The final FC neutrino samples are selected by:

1. Event vertex is within the fiducial volume (FV)
   The definition of FV is 200 cm away from the ID wall in the previous analysis. In this analysis, FV will be extended to 50 cm, which will be discussed in Section 7.3.
2. Number of OD hits in the highest charge OD cluster (NHITAC) < 16.
3. Visible energy (E_{vis}) > 30 MeV.

Selection efficiencies in each step of the FC reduction are evaluated based on atmospheric neutrino MC and summarized in Table 5.1. The final event rate is 8.09 events / day, within the conventional FV ($D_{wall} > 200$ cm). Although the reconstruction tool used in Table 5.1 is APFit rather than fiTQun, the result for fiTQun is expected to be similar due to the similarity of the vertex reconstruction performance of these two reconstruction tools, as we will see in next Chapter.

The systematic error from the FC reduction is estimated by comparing the cut variables' distribution between data and MC. The largest discrepancy between data and MC is found to be from the flasher on the fourth reduction and the discrepancy is evaluated to be 1.3% as presented in Section 5.1.4. This value is regarded as the final FC reduction uncertainty.

Most of the background contamination in the final FC samples are flasher events and cosmic ray muons. All events passing the reduction are scanned by eye to determine the level of background contamination in the final analysis sample and to estimate the uncertainty inherent to the reduction process. Table 5.2 summarizes the contamination for each sample.

Reduction step	Number of events for data	Event rate for data	Efficiency
1st	6295064	2018.65 / day	100.0%
2nd	1115962	357.86 / day	99.99%
3rd	138353	44.36 / day	99.83%
4th	130446	41.83 / day	99.00%
5th	120659	38.69 / day	98.95%
Final	25231	8.09 / day	98.02%

TABLE 5.1: Selection efficiencies and number of events for FC sample with livetime of 3118.45 days for SK-IV. Selection efficiencies are for events whose real vertex is within the FV and number of OD hits < 16 and visible energy > 30 MeV. The FV cut is 200 cm and the variable reconstructed by APFit is used in this Table.

Background contamination	e-like (flasher)	μ-like (cosmic ray muons)
Sub-GeV	0.03%	0.02%
Multi-GeV	0.07%	0.14%

TABLE 5.2: Estimated contamination for each background source. The term "sub-GeV" represent events with $E_{\mathrm{vis}} < 1.3$ GeV, while "multi-GeV" represent events with $E_{\mathrm{vis}} > 1.3$ GeV.

5.2 Reduction for Partially Contained Events and Up-μ Event

The PC and Up-μ samples also have their own reduction processes, which are optimized for the topology of OD activity of neutrino events. These two samples are reconstructed using the pre-existing reconstruction algorithm (APFit) and are divided into "stopping" and "through-going" subsamples based on the estimated muon stopping point for PC and Up-μ events. The "through-going" events in the Up-μ sample are further divided into "showering" and "non-showering" based on whether the event induces an electromagnetic shower while traversing the ID. More detail about the data reduction and event reconstruction for PC and Up-μ events can be found in [111]. The final event rate for PC event is 0.66 events/day, while it is 1.41 events/day for Up-μ events.

Chapter 6

Event Reconstruction

The Super-K event reconstruction algorithms determine the physical properties of the event based on the PMT hit information. The properties include the interaction vertex, number of particles, particle types, momenta and directions. There are two different reconstruction tools, APFit and fiTQun. Since the beginning of SK, APFit has been the original fitter and serves for more than 20 years, and fiTQun is a newly developed fitter based on the maximum likelihood method. Before moving to describe the algorithm used in the thesis, fiTQun, the reconstruction scheme of APFit will be introduced briefly. The performance of fiTQun and its comparison with that of APFit will also be discussed. As we will see, fiTQun exhibits better performance than APFit, which allows us to expand the fiducial volume (FV) without reducing the sample purity during categorization of atmospheric neutrino event, resulting in a higher sensitivity.

6.1 Conventional Event Reconstruction

The conventional event reconstruction algorithm, APFit, was introduced at the beginning of Super-K. APFit contributed to the discovery of atmospheric neutrino oscillation in 1998 [1] and has been also used in both the K2K [50] experiment and the T2K experiment [62].

APFit is a fitter with single iteration based on the time and charge information observed by PMTs [112]. The interaction vertex is reconstructed based on the hit timing information after the time of flight correction of photon. Then the direction of the first found ring, usually with the highest energy, is determined based on the observed charge distribution with respect to the interaction vertex. Additional ring candidates are found using a Hough-transform based method and selected by a optimized likelihood function

for spurious ring candidates rejection. After determining the number of Cherenkov rings in the event, the particle type of each ring is determined based on the Cherenkov ring pattern and opening angle. Rings from electrons often have rough edges from the light generated by their electromagnetic showers, while rings from muons or charged pions mainly produce crisp edges, as shown in Figure 6.1.

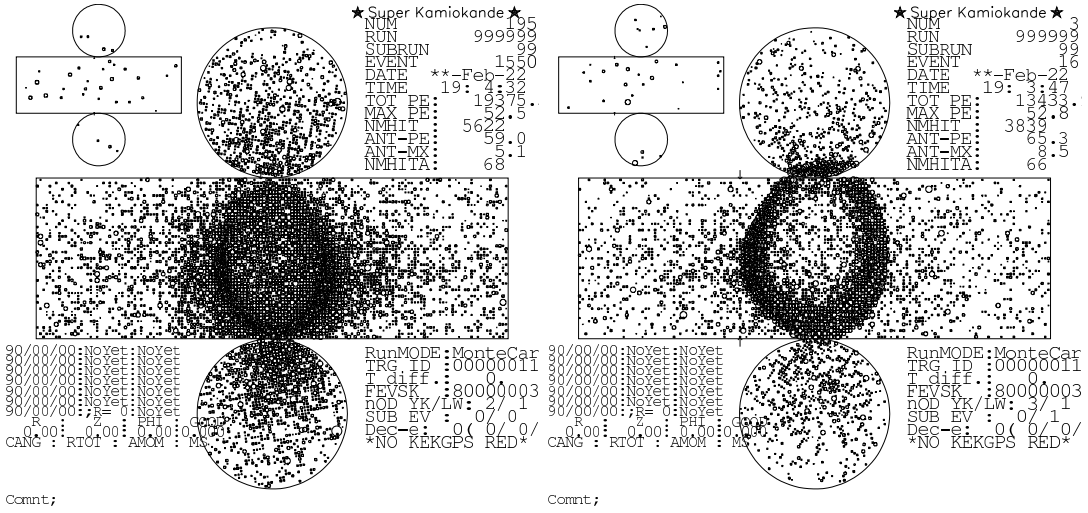

FIGURE 6.1: Event display of single-ring electron (right) and single-ring muon (left) neutrino MC event. Each circle denotes a PMT hit, whose observed charge is represented by the size of the circle.

In the final step of the fit, the momentum of each ring is evaluated based on the charge information observed by the PMTs whose angular position with respect to the line from the interaction vertex to each ring's center is less than 70°. Corrections and adjustments would be applied if two rings were overlapped.

It is worth noting that in APFit the hit time information is only used in the first step to find the initial vertex candidate and not used in the following steps such as particle identification or ring counting.

6.2 New FC Event Reconstruction

The new algorithm called fiTQun uses the maximum likelihood method to reconstruct particle types and, at the same time, determine their kinematics in the detector. The algorithm is based on methods developed for the MiniBooNE experiment [113]. FiTQun was developed from scratch for Super-K with additional functions such as reconstruction for multi-ring events. In comparison to the fitting procedure of APFit, more information, including the PMT hits outside the Cherenkov cone and the hit time, is taken into account by fiTQun. As we will see later, the fit process in fiTQun will run multiple times to

find the best kinematics parameters (e.g. vertex, momentum, direction) for each possible particle configuration hypothesis (e.g. particle types) and choose the best one finally. On the other hand, APFit only fits once and determines the kinematic parameters or particle configuration one by one. Since the launch of Super-Kamiokande in 1996, the remarkable evolution of computing power has allowed fiTQun to achieve a greater accuracy of reconstruction at a similar time consumption as APFit used to be. Currently, fiTQun has already been used in the T2K analyses for fiducial volume expansion due to its improved resolution of reconstructed quantities and particle identification [34].

6.2.1 Likelihood Function

An event topology hypothesis Γ (e.g. single-ring μ-like) is taken into account in the fitting along with its associated kinematic parameters θ, including vertex positions, particle generation times, particle directions and their momenta. The likelihood function for a given hypothesis to estimate the kinematic variables in fiTQun is based on the observed charge and hit time of each PMT and defined as:

$$L(\Gamma,\theta) = \prod_{j}^{\text{unhit}} P_j(\text{unhit}|\Gamma,\theta) \prod_{i}^{\text{hit}} \{1 - P_i(\text{unhit}|\Gamma,\theta)\} f_q(q_i|\Gamma,\theta) f_t(t_i|\Gamma,\theta). \quad (6.1)$$

In this equation, index j runs over all PMTs with no hits, also called unhit PMTs. The probability of not registering a hit with a fitting hypothesis (Γ,θ) is calculated as $P_j(\text{unhit}|\Gamma,\theta)$ for each unhit PMT. The index i labels PMTs that registered a hit. The charge likelihood, $f_q(q_i|\Gamma,\theta)$, represents the likelihood density for observing charge q_i for these PMTs under hypothesis (Γ,θ). In the same way, the likelihood density of producing a hit at the observed time t_i is defined as $f_t(t_i|\Gamma,\theta)$.

Indeed, the propagation processes of particle and optical photon in the detector are independent from the response of the PMT and the electronics. The charge likelihood therefore can be rewritten in terms of the expected number of photoelectrons generated (the predicted charge) at the i-th PMT given the hypothesis, $\mu_i(\Gamma,\theta)$. The likelihood function then becomese

$$L(\Gamma,\theta) = \prod_{j}^{\text{unhit}} P_j(\text{unhit}|\mu_j) \prod_{i}^{\text{hit}} \{1 - P_i(\text{unhit}|\mu_i)\} f_q(q_i|\mu_i) f_t(t_i|\Gamma,\theta). \quad (6.2)$$

Here, the unhit probability $P_j(\text{unhit}|\mu_j)$ and the charge likelihood density $f_q(q_i|\mu_i)$ are only characteristics of the PMT. The processes of Cherenkov photon emission and propagation in water are considered in the calculation of the predicted charge $\mu_i(\Gamma, \theta)$ and separated from the electronics of detector.

During the calculation process of the predicted charge μ_i, the observed photons are divided into two categories: one is generated by the Cherenkov process and hit the PMT directly through water in the detector, also called unscattered light or direct light; the other is the photons which have been scattered or reflected before observed by PMT, called indirect light. These two kinds of photons are considered separately and summed to form the final predicted charge.

The predicted charge from direct light arriving at a PMT is calculated by integrating the Cherenkov radiation profile along the track with considering the correction from the light transmission in water, the distance between the light source and the PMT, and the PMT angular acceptance. The charge generated by indirect light arriving at the PMT is predicted by integrating the product of the direct light emission profile and a scattering function. This function is generated in advance with considering the effects from the position of the PMT, light source and the wall. In the multiple ring case, the predicted charge of each ring is first calculated separately and then summed up to calculate a total expected charge. The final charge likelihood $f_q(q_i|\mu_i)$ is calculated by comparing the prediction assuming that the photoelectrons generation obeys the Poisson distribution to the observed charge in the PMT.

The time likelihood term is written as $f_t(t_i|t_i^{\text{exp}}, \Gamma, p, \mu_i)$, where p is the particle momentum under the topology hypothesis Γ, and t_i^{exp} represents the expected hit time, which is defined as the arrival time of unscattered photons emitted from the midpoint of track and arriving at the PMT directly as

$$t_i^{\text{exp}} = t + s_{\text{mid}}/c + |\boldsymbol{R}_i^{\text{PMT}} - \boldsymbol{x} - s_{\text{mid}}\boldsymbol{d}|/c_n. \tag{6.3}$$

Here t and $\boldsymbol{x}$ are the creation time and vertex of the particle, respectively, $\boldsymbol{d}$ is the particle direction, $\boldsymbol{R}_i^{\text{PMT}}$ is the position of i-th PMT and s_{mid} represents half of the track length. The parameters c and c_n are the group velocity of Cherenkov light in vacuum and water, respectively. The reason why the time likelihood depends on the predicted charge is that the first photon reaching a PMT is recorded as the hit time, which results in a narrower time likelihood density distribution for more incident photons, i.e. more predicted charge. The track length of a particle s determined by the topology Γ and momentum p also affects the shape of likelihood density since not all photons are generated in the middle of the track. The shape of time likelihoods from direct and indirect photon hits are determined based on particle gun simulations. During the fitting

process, contributions from those two likelihoods are calculated separately in the same way as the charge likelihood. The final time likelihood for a single particle is obtained by merging those two likelihoods according to their relative intensities. For multi-particle topology hypothesis, the time likelihood is calculated ring-by-ring and then merged to a final likelihood function assuming the photons from a particle with earlier $t_i^{\rm exp}$ always arrive earlier than the photons from any other particles whose $t_i^{\rm exp}$ values are later.

The best set of the kinematic parameters $\hat{\theta}$ for a given event topology hypothesis Γ is obtained by maximizing likelihood value $L(\theta|\Gamma)$. The best estimation of a given event is determined by comparison of $L(\Gamma, \hat{\theta})$ among all hypotheses, Γ. It worth noting that the best estimation is not always the hypothesis with the largest likelihood value. A hypothesis with more rings, i.e. more parameters, always fits the observation better and therefore has a higher likelihood value due to the increased number of degrees of freedom. Therefore care is needed when determining the best hypothesis. The detail of the topology selection, including ring counting and particle identification, will be introduced in next section.

6.2.2 Fitting Procedure

The fiTQun reconstruction process can be divided into four steps.

1. Vertex pre-fitting
   The interaction vertex is estimated based on the PMT timing information roughly.

2. Hit clustering
   PMT hits are clustered in time to find candidates for particle activities.

3. Single-ring reconstruction
   Events are fitted assuming event topologies with only a single light-producting particle,

4. Multi-ring reconstruction
   Events are fitted using hypotheses with multiple particles. The results from single-ring reconstruction are used as seeds for fitting.

MINUIT[114] package is used to minimize the negative log likelihood -ln $L(\Gamma, \theta)$ with respect to θ during the fits.

Vertex pre-fitting

The vertex pre-fitter is a fast algorithm which estimates an initial vertex position with only the hit time information from PMTs around the primary event trigger. It is assumed that all observed light is emitted from a single position in this step. The estimation is done by searching for time t and the vertex position $\boldsymbol{x}$ which maximize the goodness function:

$$G(\boldsymbol{x}, t) = \sum_{i}^{\text{hit}} e^{(-(T_i^{\text{res}}/\sigma)^2/2)}, \tag{6.4}$$

where

$$T_i^{\text{res}} = t_i - t - |\boldsymbol{R}_i^{\text{PMT}} - \boldsymbol{x}|/c_n \tag{6.5}$$

is the residual hit time calculated assuming a point-like light source at the interaction vertex and accounting for the photon's time-of-flight. The position of the i-th PMT is denoted by $\boldsymbol{R}_i^{\text{PMT}}$. As the time and vertex approach their true values during a grid search process, the T_i^{res} distribute near zero, resulting in a large goodness value. The vertex returned during this step is just a rough estimation, called the pre-fit vertex. This vertex will be fitted again with higher precision during the minimization of $L(\Gamma, \theta)$ in Step 3 and Step 4.

Hit clustering

Events in Super-K are defined by detector activity in an $O(10\ \mu\text{s})$ time window around an event trigger. Multiple subevents representing clusters of PMT hits separated in time from the primary trigger might be contained in one event. Muon decay is one example: the primary event trigger is generated by muon while a delayed subevent is produced by the additional hits from its decay electron. In order to separate the hits from the particles created in different time for further fitting, the activity around the primary trigger and additional subevents, if any, are searched for and selected by the hit clustering algorithm.

The algorithm starts by searching for the subevent activities around the time of the event trigger with a peak-finding algorithm. The vertex goodness $G(\boldsymbol{x}, t)$ from Equation 6.4 is scanned in t while fixing the vertex $\boldsymbol{x}$ to the pre-fit vertex for the additional delayed peaks' search. Figure 6.2 shows the goodness distribution from a muon decay

event as an example. The parent muon and its Michel electron are the two dominant peaks. Scattered or reflected light can cause fake peaks in or near a true cluster of hit activity. Therefore, peaks are required to be above a minimum threshold $F(t)$, which is shown as the blue curve in Figure 6.2. The definition of $F(t)$ is

$$F(t) := 0.25 \arg\max_{i \in M} \{ \frac{G(\boldsymbol{x}, t_i)}{(1 + ((t - t_i)/\gamma)^2} \} + \eta, \tag{6.6}$$

where M represents all local maxima of the goodness function $G(\boldsymbol{x}, t)$. The time constant γ is assigned as 25 ns (70 ns) when $t < t_i$ ($t > t_i$). In order to suppress hits from dark noise of the PMTs, the threshold function is offset by $\eta = 9$. The minimum goodness between any two peaks is required to be below $0.6 \times F(t)$, which is shown as green dashed curve. The figure shows only two peaks that pass these criteria (marked by red triangles) which will be subject to further fitting.

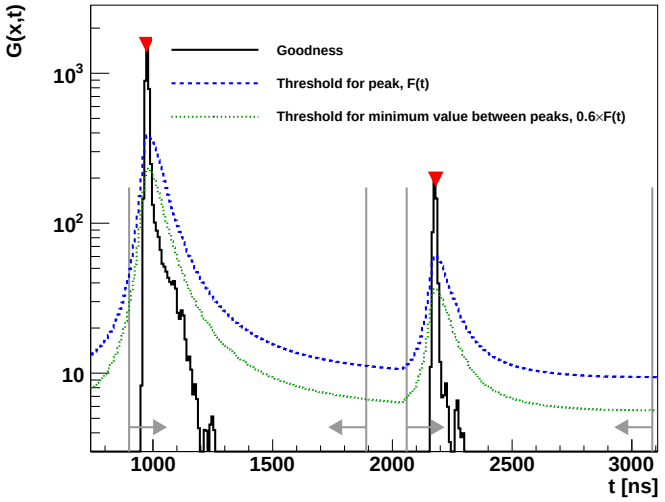

FIGURE 6.2: An example of the goodness function with respect to hit time. A muon event with its decay electron is shown here. The goodness function with respect to hit time is shown as the black line, while the vertex is fixed to the pre-fit vertex. Thresholds for identifying candidate peaks: $F(x)$ and $0.6 \times F(x)$ are denoted by blue (dashed) and green (dotted) curves. Candidates found by the hit clustering algorithm are marked by red triangles and their associated time windows are indicated by gray vertical lines. Overlapped time windows are merged into one.

All vertex positions are assumed to be close to the pre-fit vertex in the first step of hit clustering. However, this assumption is broken when the primary particle (e.g. muon with high momentum) travels a long distance from the interaction vertex. In this case, the goodness distribution will be smeared and might be lower than the threshold resulting in a subevent missing and a lower decay electron tagging efficiency. To improve the tagging efficiency, the vertex pre-fitting is rerun after masking the hits caused by the primary particle for a vertex close to the vertex of the secondary particle. After that the

peak-finding algorithm uses the new vertex as the position in the goodness function $\boldsymbol{x}$ to search for possible missing goodness peaks. More details can be found in Appendix E.

For each found peak, its associated hits are contained by a time window defined as -180 ns $< T_i^{\mathrm{res}} <$ 800 ns. Those hits will be input to the vertex pre-fitter and peak finder once again to get the final subevent candidates with a higher precision for the full event reconstruction. The interaction time and vertex fitted in each window will be used as the seeds for fitting in next steps.

Single-ring reconstruction

The single-ring fitter, whose topology hypothesis Γ in Equation 6.1 is single-particle, is applied to each time window determined by the previous step firstly. The likelihood function is maximized against the charge and time distribution observed by PMTs by changing the kinematic parameters of the event, including the created vertex and time, the particle momentum, and direction. This process will run iteratively for each of the hypothesis considered by the single ring fitter: electron, muon, and charged-pion. Particle identification (PID) is then determined by comparing the best-fit likelihood values of them. For example, the distinguishment between electrons and muons of a event is based on the value of the logarithm of the ratio between the likelihood value with best-fit electron and muon hypotheses: $\ln(L_e/L_\mu)$. Figure 6.3 demonstrates the distribution of this variable for the FC atmospheric neutrino samples. The distributions of data and MC are in good agreement. A clear separation of the likelihood ratio between electron-like (e-like) and muon-like (μ-like) events can be seen for both sub-GeV and multi-GeV energy regions.

The distribution of the distance from the reconstructed to true vertex of the FC single-ring charged-current quasi-elastic (CCQE) event sample in the atmospheric neutrino MC whose true interaction vertex lies within the conventional fiducial volume ($D_{\mathrm{wall}} > 200$ cm) is shown in Figure 6.4, which is used to evaluate the vertex resolution by calculation the 68 percentile. Figure 6.5 shows vertex resolution as the function of visible energy. The vertex resolution of fiTQun for CCQE ν_e events is stable at 20.6 cm with the visible energy in the range from 100 MeV to 1330 MeV, while the resolution of APFit varies from 34.6 cm to 25.3 cm in the same range. The vertex resolution of fiTQun for CCQE ν_μ events, which varies from 29.2 cm to 15.9 cm, is better than that of APFit, which changes from 34.2 cm to 18.2 cm. Similar plots for direction resolution are shown in Figure 6.6 and Figure 6.7. The performance of fiTQun for direction reconstruction is the same as that of APFit. The distribution of the ratio between the reconstructed momentum and true momentum are shown in Figure 6.8. In the same energy range, the

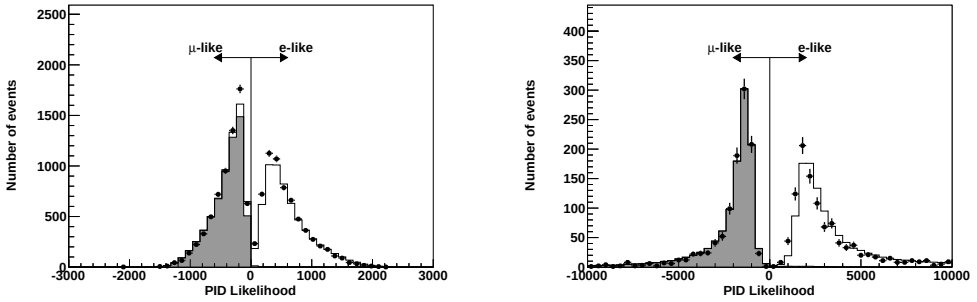

(a) Sub-GeV events (b) Multi-GeV events

FIGURE 6.3: PID likelihood distribution of FC single-ring events. Left figure is for sub-GeV events and right figure is for multi-GeV events. Distribution for neutrino data is denoted by points and that for atmospheric neutrino MC after oscillation is shown as histograms. The true hierarchy is assumed to be normal hierarchy. The oscillation parameters is taken to be $\sin^2\theta_{13} = 0.0210$, $\sin^2\theta_{23} = 0.5$, $\Delta m^2_{23} = 2.4 \times 10^{-3}\text{eV}^2$, and $\delta_{CP} = 0$. Same parameters are applied below. Charged-current ν_μ interaction component is shown as the shaded histograms. The statistical error are denoted by error bars. The reconstructed event vertex to the nearest ID wall (D_{wall}) is required to be larger than 200 cm.

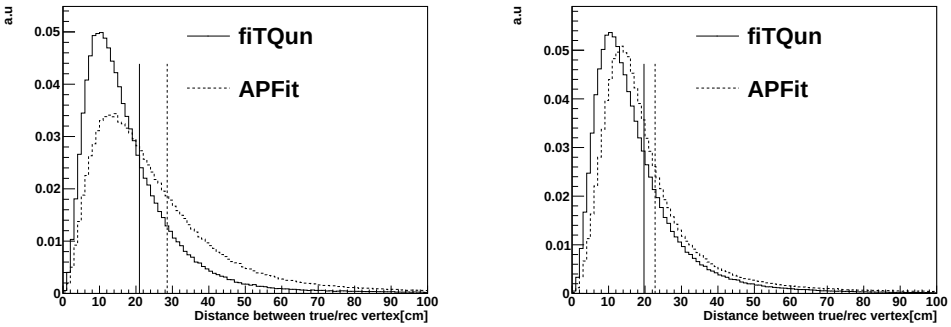

FIGURE 6.4: Single-ring electron(left) and muon(right) vertex resolution for FC true-fiducial CCQE events in atmospheric neutrino MC, compared between APFit(dashed line) and fiTQun(solid line). The resolution is defined as the 68 percentile of the respective distributions, which is shown by corresponding vertical line.

momentum resolution of fiTQun for CCQE ν_e events improves from 5.39% to 2.58% as the visible energy increases, while the resolution of APFit varies from 7.04% to 3.32%, as shown in the top left plot of Figure 6.9. The momentum resolution for CCQE ν_μ events is stable across the energy range, being lower than 2.5% for fiTQun and slightly worse for APFit. FiTQun also shows a higher ability to discriminate between electrons and muons with less than a 1% mis-identification rate in the same energy range (Figure 6.10). The typical values of the metrics used to measure fit quality are summarized in Table 6.1, which show that fiTQun performs as well or better than APFit in general.

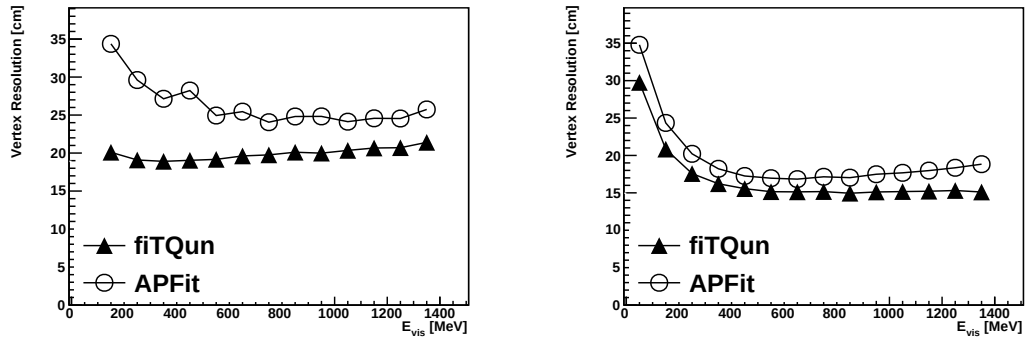

FIGURE 6.5: Vertex resolution of FC single-ring charged current quasi-elastic (CCQE) event as a function of visible energy. Left figure is for CC ν_e events and right figure is for CC ν_μ events. The performance of fiTQun is indicated by the full triangles, while that for APFit is indicated by the open circles.

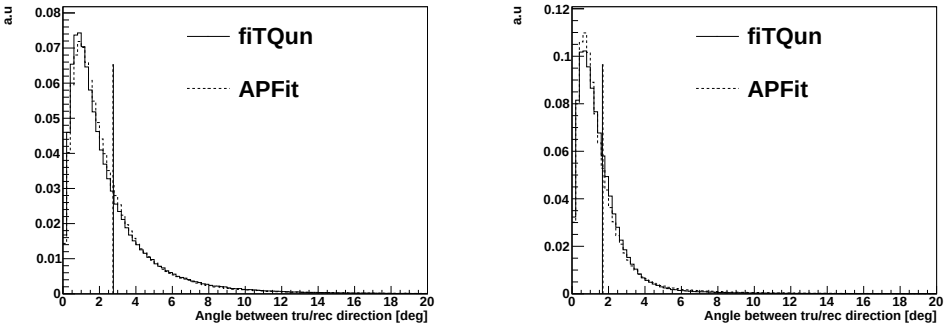

FIGURE 6.6: Single-ring electron (left) and muon (right) direction resolution for FC CCQE events in atmospheric neutrino MC, compared between APFit (dashed line) and fiTQun (solid line). The resolution is defined as the 68 percentile of the respective distributions which is shown by corresponding vertical line.

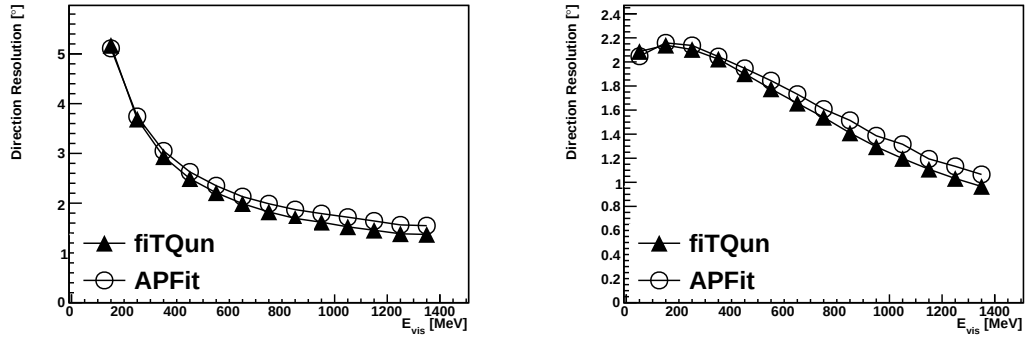

FIGURE 6.7: Direction resolution of single-ring electron (left) and muon (right) events in the FC CCQE event sample in the atmospheric neutrino MC, plotted as a function of visible energy. The full triangles indicate the performance of fiTQun and the open circles are for APFit.

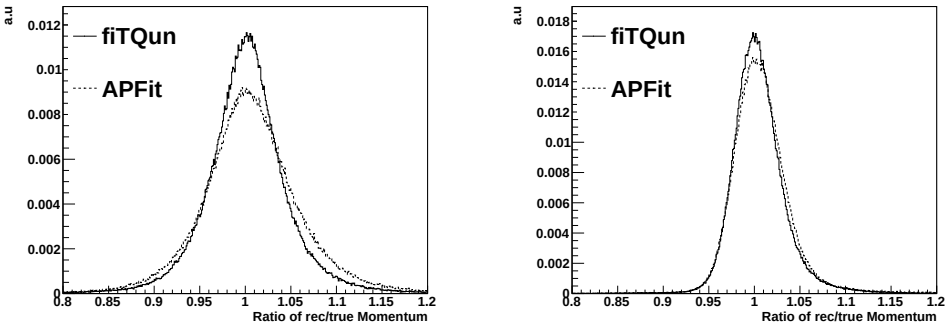

FIGURE 6.8: Single-ring electron (left) and muon (right) momentum resolution for FC CCQE events in atmospheric neutrino MC, compared between APFit (dashed line) and fiTQun (solid line). The bias (resolution) is defined as the mean (RMS) value of the ratio distribution between the reconstructed momentum and true momentum.

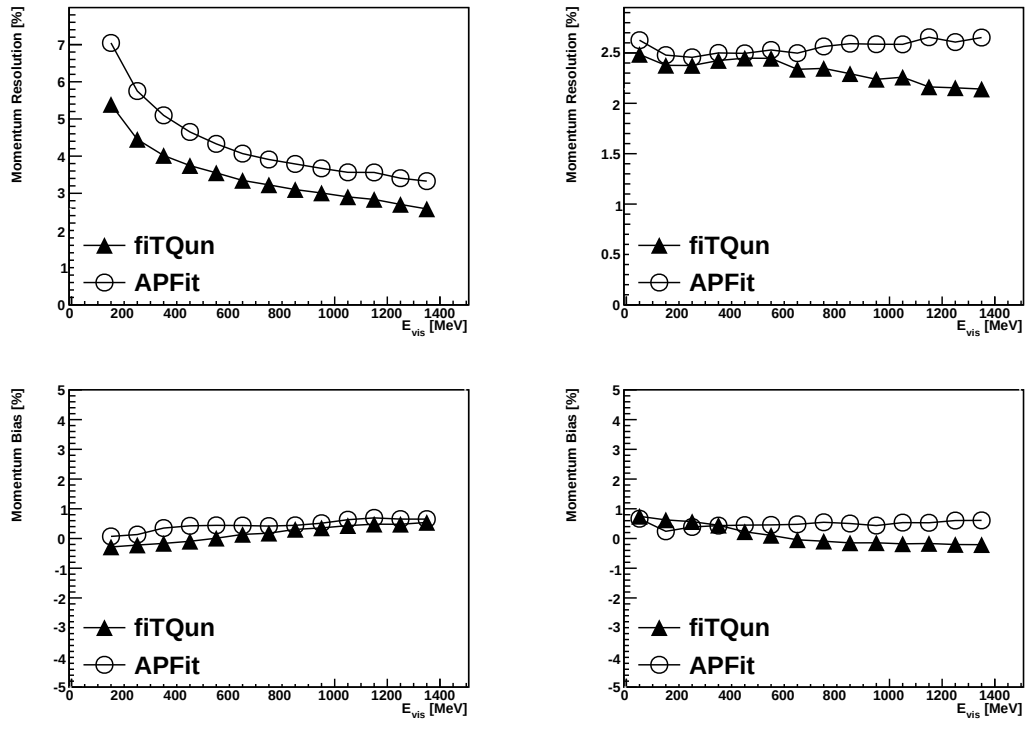

FIGURE 6.9: Momentum resolution and bias as a function of visible energy. Top two figures show the momentum resolution and bottom ones show the momentum bias. Left two figures are for FC CCQE ν_e events in the atmospheric neutrino MC while right ones are for ν_μ events. The performance of fiTQun is indicated by the full triangles, while that for APFit is indicated by the open circles.

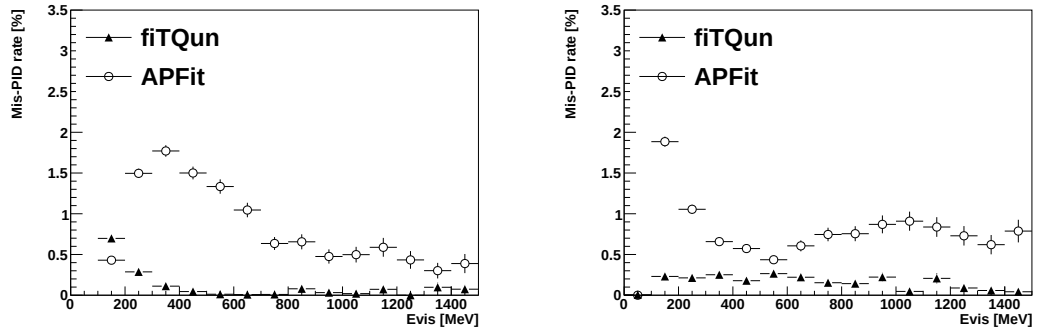

FIGURE 6.10: Mis-identification rate as a function of visible energy. Left figure shows the result of FC CCQE ν_e events in the atmospheric neutrino MC, while right figure shows the result of CCQE ν_μ events. The performance of fiTQun is indicated by the full triangles, while that for APFit is indicated by the open circles. The statistical error are denoted by error bars.

Reconstruction	fiTQun	APFit
True CCQE ν_e sample		
Vertex Resolution	20.6 cm	24.9 cm
Direction Resolution	1.48°	1.68°
Momentum Bias	0.43%	0.63%
Momentum Resolution	2.90%	3.56%
Mis-PID rate	0.02%	0.50%
True CCQE ν_μ sample		
Vertex Resolution	15.8 cm	17.3 cm
Direction Resolution	1.00°	1.28°
Momentum Bias	-0.18%	0.54%
Momentum Resolution	2.26%	2.60%
Mis-PID rate	0.05%	0.91%

TABLE 6.1: Basic performance of reconstruction algorithms on the FC CCQE single-ring event sample. Both result of APFit and fiTQun are shown here. The visible energy of the sample used here is 1 GeV.

Multi-ring reconstruction

A large fraction of atmospheric neutrino events with multi-GeV energies, which have high sensitivity to the mass hierarchy, have multi-particle final states, therefore the reconstruction performance for multiple light-producing particles is essential to the atmospheric neutrino oscillation analysis. In fiTQun, the multi-ring fitter is only applied to the first time window, which is around the primary event trigger and not to any delayed ones, to reduce the computing time consumption. The multi-ring hypothesis for fitting is constructed by adding a new ring to the previous fit result iteratively. After adding a new ring, the kinematic parameters in the likelihood function (c.f. Equation 6.2) are varied to find their best fit values. All of the three hypotheses used in the single-ring

True Number of Rings	fiTQun Reconstruction			APFit Reconstruction		
	1 ring	2 rings	$\geq$ 3 rings	1 ring	2 rings	$\geq$ 3 rings
True 1 ring	95.0%	4.64%	0.41%	95.9%	3.85%	0.29%
True 2 rings	27.8%	66.7%	5.56%	42.5%	52.8%	4.63%
True $\geq$3 rings	7.04%	25.5%	67.5%	20.2%	33.0%	46.8%

TABLE 6.2: Ring counting performance on FC atmospheric neutrino events. Both result of APFit and fiTQun are shown here. The number of reconstructed rings are denoted by columns and the number of true rings are denoted by rows. The true rings are defined as only final state particles with energy 30 MeV higher than the Cherenkov threshold.

reconstruction, e-like, μ-like and π^+-like rings are tested. The new ring is validated based on the likelihood ratio between the result of the updated fit and the original one for each of the hypotheses and accepted only if the likelihood ratio pass the criterion for ring counting. The processes to search for new rings are repeated until either the hypothesis with new ring is rejected by the criterion or six rings exist in the hypothesis. The likelihood ratio between the 2-ring and 1-ring hypotheses for both sub-GeV and multi-GeV events are shown in Figure 6.11. A cut on this likelihood ratio, which is determined at 9.35 (11.83) based on MC study, is used for single- and multi-ring separation for the hypothesis with e-like (μ-like) first ring. Furthermore, MC studies indicate that ring candidates that have an angular separation of less than 20° with other rings are typically due to the particle scattering rather than a new particle, so those candidates are discarded as spurious. When this occurs, a new topology hypothesis with one ring at the position of the original two close rings is generated to merge them. The merged ring is refitted for all particle hypotheses while keeping all other rings fixed. This procedure, ring merging and refitting, is run over for all ring candidates of the event in descending order of their energies.

The performance of the ring counting in both APFit and fiTQun using atmospheric neutrino MC events is summarized in Table 6.2. In this table, only charged particles with energy more than 30 MeV above the Cherenkov threshold in the final states, which makes them observable, are considered as true ring candidates and their angular separation with other particles are not required. FiTQun shows a greater ability to reconstruct multi-ring events than APFit and the ability to correctly identify single-ring topologies is at the same level for both algorithms. Although the fake ring ratio of fiTQun is slightly larger than that of APFit for true single-ring or two-ring event reconstruction, the increase of fake ring ratio is not large enough to neutralize the benefit from the higher fraction of the events reconstructed correctly.

The PID likelihood distribution of the ring with the highest energy in fully contained multi-ring events is shown in Figure 6.12. The separation between e-like and μ-like is not

as good as that for single-ring events due to the overlap of Cherenkov rings. However, the peak for both of e-like events and μ-like events still can be seen clearly.

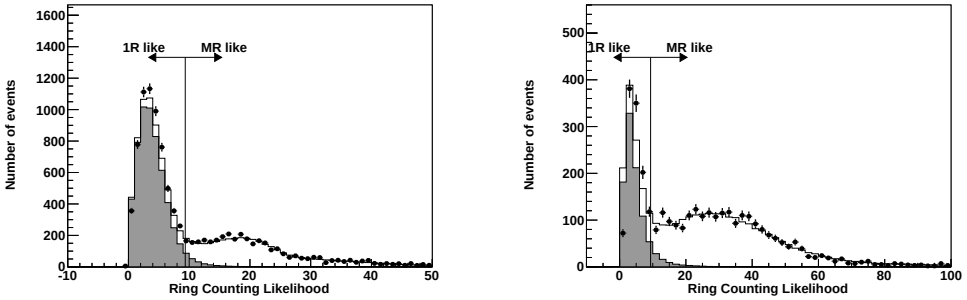

(a) Sub-GeV events (b) Multi-GeV events

FIGURE 6.11: The distribution of the likelihood ratio between the best-fit result of single-ring hypothesis and multi-ring hypothesis of FC atmospheric neutrino events. The most energetic ring is required as e-like ring. Left figure shows the result of sub-GeV events, while right figure shows multi-GeV events' result. Distribution for atmospheric neutrino data is denoted by the points and the MC prediction including neutrino oscillations is denoted by the histogram. The events with single-ring final state is shown by the shaded histogram. The statistical error are denoted by error bars. The terms "1R" and "MR" in the figures represent single-ring and multi-ring, respectively. The reconstructed event vertex to the nearest ID wall (D_{wall}) is required to be larger than 200 cm.

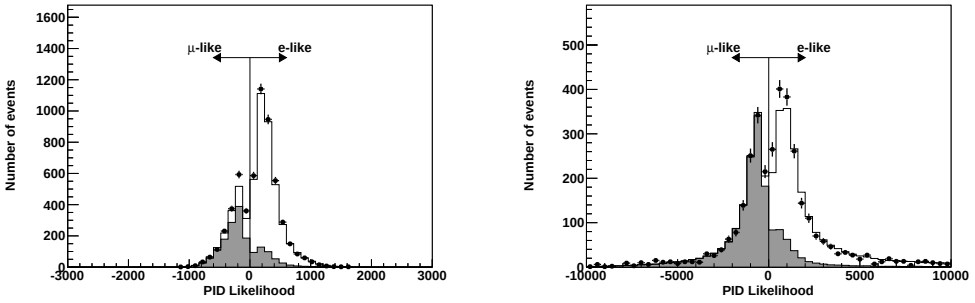

(a) Sub-GeV events (b) Multi-GeV events

FIGURE 6.12: PID likelihood distributions of the most energetic ring for fully contained multi-ring events. Left figure shows the results of sub-GeV events while right figure are for multi-GeV events. Distribution for atmospheric neutrino data is denoted by the points and the MC prediction including neutrino oscillations is denoted by the histogram. The component of ν_μ charged-current interactions is shown by the shaded histogram. The statistical error are denoted by error bars. The reconstructed event vertex to the nearest ID wall (D_{wall}) is required to be larger than 200 cm.

The distribution of reconstructed invariant mass of π^0s in charged-current single pion (CC1π^0) events is studied to check the multi-ring fitter's kinematic reconstruction performance. The invariant mass based the second and the third rings in order of energy for events with three e-like rings (eee events) is shown in Figure 6.13. The true CC$\nu_e 1\pi^0$

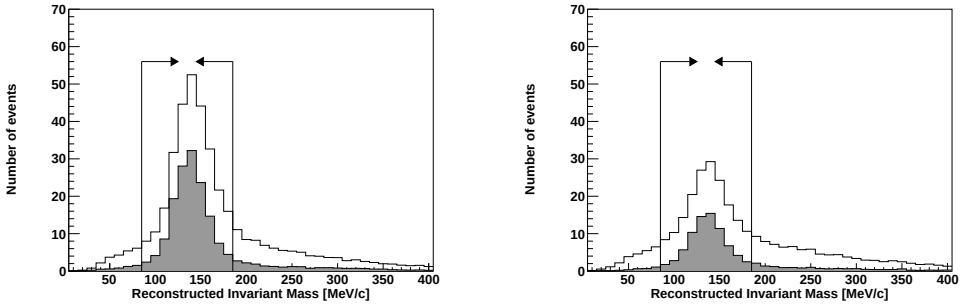

(a) Event selected by fiTQun (b) Event selected by APFit

FIGURE 6.13: Reconstructed invariant mass calculated based the second and the third rings in order of energy for events with three e-like rings in the sub-GeV atmospheric neutrino MC sample. Left figure shows the events reconstructed by fiTQun, and right figure is for the events reconstructed by APFit. True CC$\nu_e 1\pi^0$ events are denoted by shaded histograms. The invariant mass range used for the event rate and purity calculation is shown by arrows. The reconstructed event vertex to the nearest ID wall (D_{wall}) is required to be larger than 200 cm.

Topology	fiTQun selection		APFit selection	
	Event rate	Purity	Event rate	Purity
***eee* events** (target: ν_eCC1π^0)				
Sub-GeV	278.5	52.1%	175.9	42.9%
Multi-GeV	112.1	47.0%	32.8	36.2%
***μee* events** (target: ν_μCC1π^0)				
Sub-GeV	384.5	54.6%	201.2	38.0%
Multi-GeV	143.5	64.6%	51.6	32.0%

TABLE 6.3: Performance of CC1π^0 events reconstruction and selection in atmospheric neutrino MC events with three-ring final state. The reconstructed PID of the three rings in order of momentum are denoted by *eee* or μee, which represent candidates of ν_eCC1π^0 and ν_μCC1π^0 events, respectively. The number of events passing the π^0 invariant mass cut is shown in the event rate column. The purity of target events in the π^0 invariant mass region is shown in the purity column.

components are shown by shaded histograms. Comparing with the peak near the π^0 mass in the invariant mass distribution of APFit, the one of fiTQun is larger, sharper and has fewer backgrounds, which indicates a higher selection efficiency, better energy resolution and lower background contamination. Table 6.3 shows the event rate and the purity of the CC$\nu_e 1\pi^0$ events with $85 < m < 185$ MeV (indicated by the arrows in the figure). The study on CC$\nu_\mu 1\pi^0$ events (μee) is also done in the same way and the result is summarized in Table 6.3. As a conclusion, the fiTQun algorithm shows an improved performance for the multi-ring event reconstruction over APFit.

The performance of multi-ring event reconstruction determines the separation ability of neutrino and antineutrino components for multi-GeV multi-ring events directly, which

affects the sensitivity to the mass hierarchy significantly. The separation between the neutrino and antineutrino components for multi-ring events is done by a two-stage likelihood method. The detail of the method and its performance will be discussed in Section 7.1.2. As a conclusion, fiTQun shows higher purity and efficiency than that of APFit in multi-GeV multi-ring e-like events selection.

From these distributions and numbers, we can see that fiTQun has better performance than that of APFit for both of single-ring and multi-ring events. Better sensitivities to $\sin^2\theta_{13}$ and mass hierarchy are expected due to higher reconstruction precision and lower background.

6.2.3 FiTQun in SK-I to SK-III

As mentioned in Chapter 2, there are four distinct detector phases in Super-K, and only the data from the latest phase SK-IV is used in this thesis. The data collected from SK-I to III phases is not used at the this moment due to the large data-MC discrepancies observed in the reconstructed variable distributions from fiTQun. Further improvements in the detector simulation is necessary to use those data. In fact, comparing with APFit, fiTQun utilizes more information such as hit information outside the Cherenkov cone and time information during fitting and does the fit with higher precision, so discrepancies between data and MC that were unseen in previous, less-precise reconstruction before might cause a significant effect for fiTQun.

As an example of such a data-MC discrepancy, Figure 6.14 shows the data-MC comparison of the distribution of PID likelihood the for the FC sub-GeV single-ring atmospheric neutrino events for SK-I. Large discrepancies between data and MC can be found in the e-like sample, namely, the single electron events in data are shifted to the left. Some work has been done to resolve this issue (see Appendix A), but the systematic error evaluation is not finished yet, therefore the data taken in SK-I is not available for the analysis in this thesis.

In general, SK-IV is the most stable phase among all four detector phases, due to various hardware improvements including the electronics and the water system. A more sophisticated calibration method described in Chapter 4 also helps the detector simulation tuned more precisely. The data-MC agreement is therefore overall better in SK-IV compared to the other phases.

One of the potential improvements one can make in the detector simulation for SK-I to III is the simulation on detector response with small p.e. for atmospheric neutrino events. Due to the computation power limitation, the simulation for high energy events

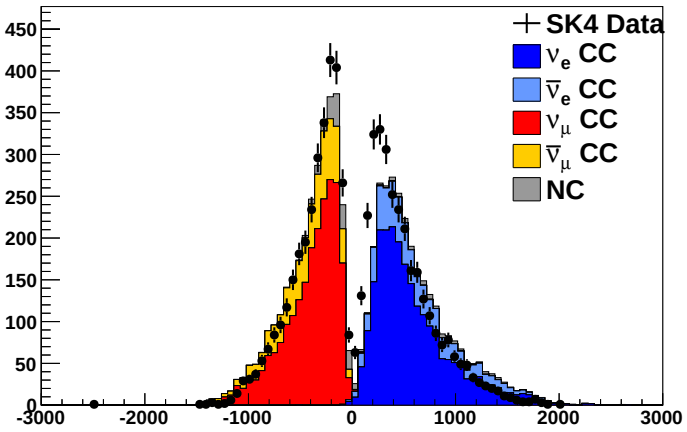

FIGURE 6.14: PID Likelihood distribution of SK-I for sub-GeV single-ring events. Error bars represent the statistical uncertainty of the data. Events with negative (positive) likelihood values are designated μ-like (e-like). Color denotes the true flavor interaction component.

(e.g. atmospheric neutrino events) are different from those for low energy events (e.g. solar neutrino events) before SK-IV. Therefore, the detector response with small p.e. for atmospheric neutrino events for SK-I to SK-III is not calibrated as well as SK-IV. Although Super-K does have several important results with low energy events (e.g. solar neutrinos, [115–117]) in early SK phase, the simulation and calibration method are different for analysis using low energy sample and atmospheric neutrino. Unlike APFit, fiTQun considers the unhit probability therefore the those hits with small charge can cause a large discrepancy on fiTQun while their effects on APFit are limited.

Another possible improvement is to introduce the effect of time variation to MC simulation. The time variation of water quality for SK-I to III is larger than that for SK-IV, as shown in Figure 6.15. The reconstruction would be affected since the charge pattern of the Cherenkov ring changes due to the variations on the water quality. Such a variation is not implemented yet in the current atmospheric neutrino MC. The simulation is done based on the calibration constants measured at a single point in time in each detector phase. For instance, the water in SK-IV is simulated based on the water calibration data taken in April 2009. When the property of the water deviates in data significantly from the calibration point for simulation, the difference manifests as data-MC discrepancies in the fiTQun likelihoods.

It is thus expected that the detector simulation in SK-I to III can be improved in the future based on the available calibration data so that one can benefit from the advanced reconstruction performance of fiTQun while analyzing the data from the other SK phases.

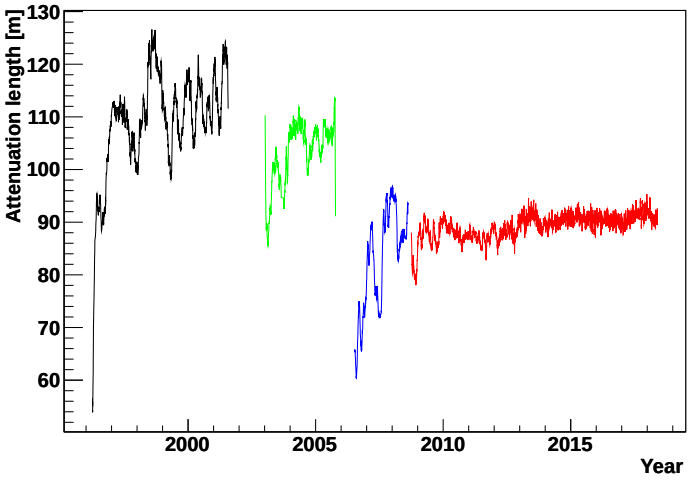

FIGURE 6.15: Time variation of the light attenuation length in water. Different color denote different Super-K phases, SK-I, II, III and IV are shown in black, green, blue and red, respectively.

Chapter 7

Neutrino Oscillation Analysis

7.1 Overview

In this chapter, a neutrino oscillation analysis using the SK atmospheric neutrino data is described in detail. As mentioned in Chapter 1, in atmospheric neutrino data, oscillation effects manifest in the energy and the zenith angle distributions of the observed neutrino events. In this analysis, the atmospheric neutrino data is first selected into several subsamples in order to separate the events in terms of neutrino type, and for each sample the events are binned in the 2D distribution of the observed momentum and the zenith angle of the direction. The oscillation parameters are then extracted by comparing the binned data to the expectation calculated from MC simulation at different oscillation parameters.

All the data samples including FC, PC and Up-μ in SK-IV are used for this analysis. The livetime is 3118.45 days. Five hundreds years equivalent MC atmospheric neutrino events are used. The FC events are reconstructed by fiTQun while PC and Up-μ samples are reconstructed by APFit since the fiTQun tuning processing for those two samples was not ready at the time of this thesis. However, since the selection of these samples is distinct from the FC sample and those samples have sensitivity to the mass hierarchy and the atmospheric mixing parameters, they are included here. For the oscillation parameter estimation, a χ^2 method is employed to make predictions on the oscillation parameters based on the observed data. The following sections describe each of the analysis elements in detail.

7.1.1 FC Event Selection and Binning

This section describes the event selection and the binning which are used as an input for the oscillation analysis. FC data is categorized into subsamples based on the reconstructed particle information from fiTQun, and then binned in reconstructed momentum and zenith angle. Since the oscillation effects manifest differently between the flavours of atmospheric neutrinos as shown in Figure 1.5, it is important to implement an event selection scheme which is capable of categorizing the observed neutrino events by the neutrino flavour (electron or muon). In addition, statistical separations of neutrinos and antineutrinos are done in order to improve the sensitivity to the oscillation effects such as the ones from the mass hierarchy, which happen differently for neutrinos and antineutrinos, as discussed in Section 1.5.

As introduced in Chapter 5, the FC events used in the analysis are required to have a visible energy greater than 30 MeV. The visible energy, $E_{\rm vis}$, is defined as the sum of the reconstructed kinetic energy above the Cherenkov threshold for all rings, taking into account the assumed particle type (electron, muon or π^+) of each ring. The fiducial volume cut is also applied, which requires that the distance from the reconstructed vertex of the most energetic ring to the nearest point on the wall, also called $D_{\rm wall}$ to be greater than the threshold. Both of the conventional FV cut used in the previous Super-K atmospheric analysis ($D_{\rm wall} > 200$ cm) and the expanded FV cut ($D_{\rm wall} > 50$ cm) are studied. The FC events which pass these basic selections are further divided into 13 event categories based on the reconstructed information from fiTQun as follows:

1. Sub-GeV: $E_{\rm vis} < 1.33$ GeV

   (a) single-ring e-like 0-decay electron sample
   Single e-like ring with $p > 100$ MeV/c, $n_{\rm dcy} = 0$.

   (b) single-ring e-like 1-decay electron sample
   Single e-like ring with $p > 100$ MeV/c, $n_{\rm dcy} \geq 1$.

   (c) single-ring μ-like 0-decay electron sample
   Single μ-like ring with $p > 200$ MeV/c, $n_{\rm dcy} = 0$.

   (d) single-ring μ-like 1-decay electron sample
   Single μ-like ring with $p > 200$ MeV/c, $n_{\rm dcy} = 1$.

   (e) single-ring μ-like 2-decay electron sample
   Single μ-like ring with $p > 200$ MeV/c, $n_{\rm dcy} \geq 2$.

   (f) FC sub-GeV 2-ring π^0-like sample
   Two e-like rings with invariant mass between 85 and 215 MeV/c^2, $n_{\rm dcy} = 0$.

2. Multi-GeV: $E_{\rm vis} > 1.33$ GeV

   (a) single-ring ν_e-like sample
   Single e-like ring , $n_{\rm dcy} \geq 1$.

   (b) single-ring $\overline{\nu}_e$-like sample
   Single e-like ring , $n_{\rm dcy} = 0$.

   (c) single-ring μ-like sample
   Single μ-like ring.

   (d) multi-ring ν_e-like sample
   2 or more rings and the most energetic ring is e-like
   Passed through the MME likelihood cut defined below and multi-ring ν_e-like cut

   (e) multi-ring $\overline{\nu}_e$-like sample
   2 or more rings and the most energetic ring is e-like
   Passed through the MME likelihood cut and but failed the multi-ring ν_e-like cut

   (f) multi-ring μ-like sample
   2 or more rings and the most energetic ring is μ-like
   $E_{\rm vis} > 600$ MeV and $p_\mu > 600$ MeV/c

   (g) multi-ring e-like other
   2 or more rings and the most energetic ring is e-like
   Failed the MME likelihood cut

Here, e-like and μ-like are the reconstructed PID information of the output charged lepton generated by neutrino interaction as presented in Section 6.2.2, $n_{\rm dcy}$ represents the number of detected decay electrons.

Figure 7.1 shows the schematic diagram which summarizes the steps for selection of FC samples.

The reason to do categorization based on the number of detected decay electrons is to distinguish the interaction mode. Comparing with the quasi-elastic interactions, more decay electrons would be generated from the neutrino interaction with charged pion production.

PC and Up-μ samples after the reduction process are reconstructed by APFit and divided into "stopping" and "through-going" subsamples based on the energy deposition within the OD. The "through-going" events in Up-μ sample are further divided into "showering" and "non-showering". The detail about the data reduction and event reconstruction for

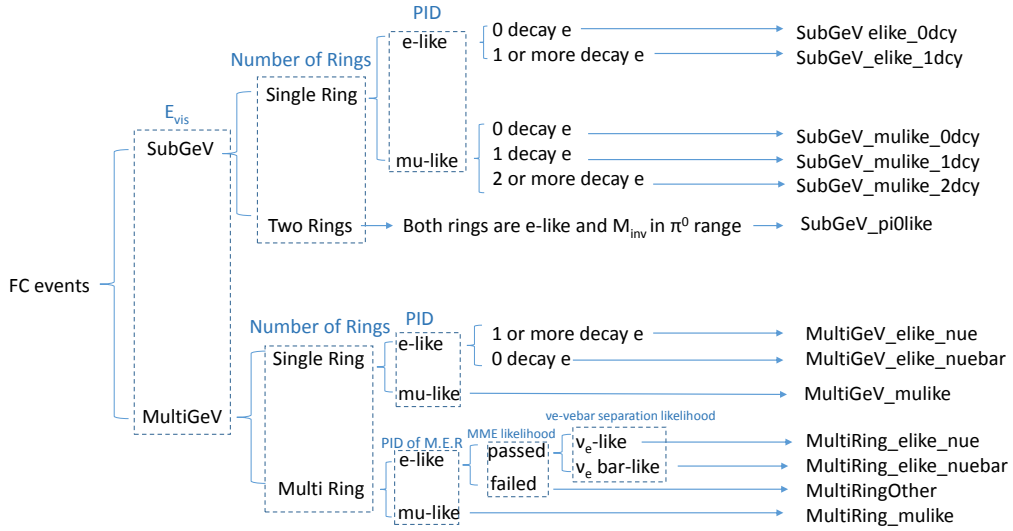

FIGURE 7.1: Summary of event categories for FC samples. The texts in the dashed line boxes shows the result classified by the variables which is on the boxes.

PC and Up-μ events can be found in [111]. After all selections, there are a total of 13 FC analysis samples, 2 PC samples and 3 Up-μ samples.

The binning is defined by momentum and zenith angle as shown in Figure 7.2. All samples in the sub-GeV region are divided into 5 momentum bins. Among them, e-like sample without decay electron and μ-like sample with 0 or 1 decay electron are divided into 10 zenith angle bins. All multi-GeV samples, including FC, PC and Up-μ samples, are divided into 10 zenith angle bins. There are 515 bins in total in current analysis. The expected contribution to the atmospheric neutrino oscillation sensitivity, including mass hierarchy and CP violation, of each sample will be discussed in Section 7.2. Briefly speaking, the largest contribution comes from the FC sample, while the PC and Up-μ samples also contribute.

7.1.2 Selection for Multi-GeV e-like Sample

The key to distinguish the normal from the inverted mass hierarchy is to determine whether the excess of upward-going e-like events at multi-GeV region is from ν_e or $\bar{\nu}_e$, as has been stated in Section 1.2. It is important to separate neutrino and antineutrino components.

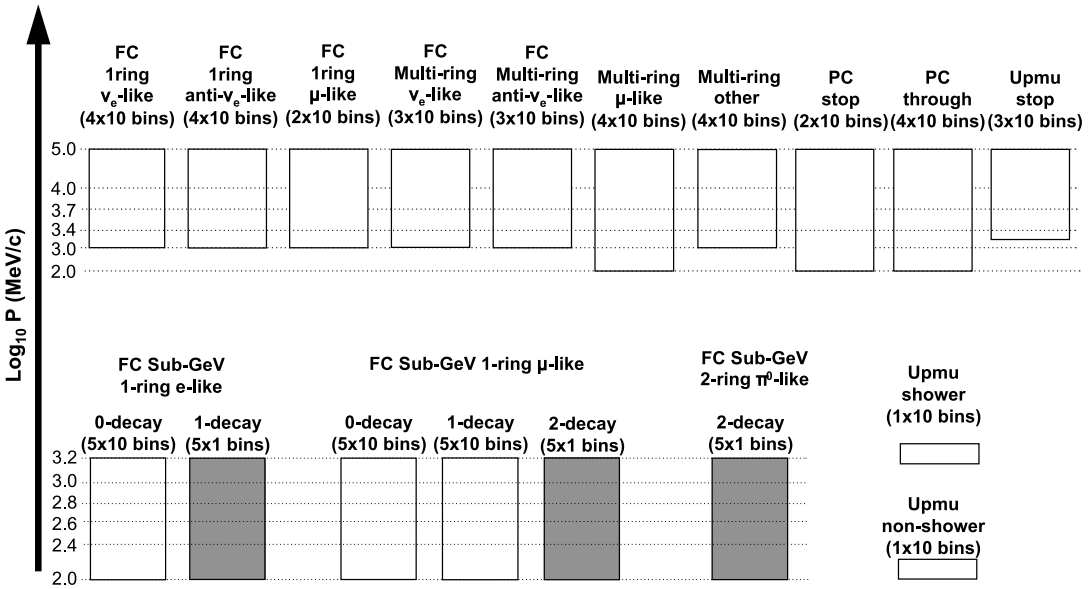

FIGURE 7.2: Definition of the binning used in the neutrino oscillation analysis. FC: 405 bins, PC: 60 bins, Up-μ: 50 bins. The samples which is divided into 10 zenith angle bins between -1 $< \cos\theta <$ 1 for FC and PC, -1 $< \cos\theta <$ 0 for UPMU are denoted by white boxes, while no zenith angle bins are divided for the samples represented by shaded boxes.

Multi-GeV Single-Ring e-like Sample

The multi-GeV single-ring e-like sample is divided into ν_e-like and $\overline{\nu}_e$-like samples by considering the difference between the interactions of ν_e and $\overline{\nu}_e$ in water:

For CC ν_e interaction:

$$\begin{aligned} \nu_e + N \rightarrow e^- + N' + \quad & \pi^+ \\ & \hookrightarrow \quad \mu^+ + \nu_\mu \\ & \quad\ \hookrightarrow e^+ + \nu_e + \overline{\nu}_\mu \end{aligned}$$

An decay electron (actually a positron) is produced finally.

For CC$\overline{\nu}_e$:

$$\overline{\nu}_e + N \rightarrow e^+ + N' + \pi^- \tag{7.1}$$

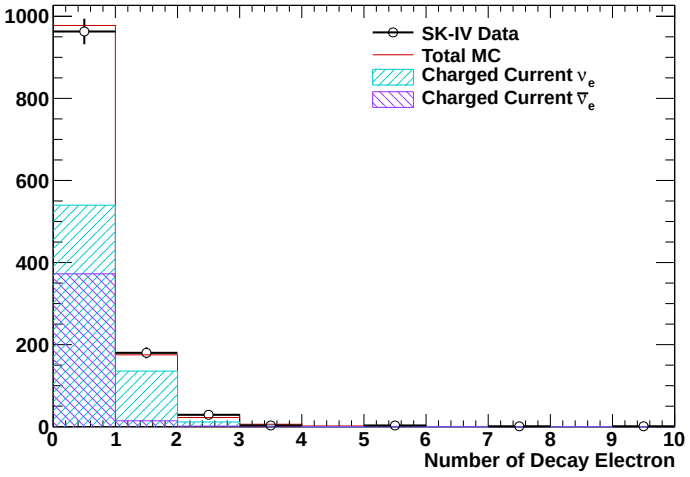

FIGURE 7.3: Distribution of number of decay electrons in both data and MC for SK-IV multi-GeV single-ring e-like sample. Cyan (magenta) shaded histogram represent the distribution of CCν_e (CC$\bar{\nu}_e$) events, red solid line represents total atmospheric neutrino MC and open circle indicates the distribution of data. Error bars show the statistical uncertainty of data.

where π^- is more easy to be absorbed by oxygen nuclei and no decay electron is observed. Therefore multi-GeV single-ring e-like sample can be separated based the number of decay electrons as follows:

$$\text{Number of decay electrons} > 0 \rightarrow \nu_e\text{-like},$$
$$\text{Number of decay electrons} = 0 \rightarrow \overline{\nu}_e\text{-like}.$$

The distribution of number of decay electrons for multi-GeV single-ring e-like sample is shown in Figure 7.3. The fractions for different interaction modes after separating multi-GeV single-ring ν_e-like sample and $\overline{\nu}_e$-like sample are summarized in Table 7.1.

Interaction mode	ν_e-like	$\overline{\nu}_e$-like
CC ν_e	72.6%	55.3%
CC $\overline{\nu}_e$	7.7%	37.9%
CCν_x	8.4%	1.2%
NC	11.3%	5.6%
Total	208.1	975.2

TABLE 7.1: Interaction mode composition of multi-GeV single-ring ν_e-like and $\overline{\nu}_e$-like samples. MC is normalized to data livetime 3118.5 days. The fiducial volume is $D_{\text{wall}} > 200$ cm.

Multi-GeV Multi-Ring e-like Sample

As the fraction of multi-ring events increases at higher energy, the multi-ring event samples are also included in the analysis in multi-GeV region. Due to the complexity of multi-ring events, it is more difficult to achieve high purity of the targeted event types compared to the single-ring case generally. The multi-ring e-like sample, which is selected by requiring the most energetic ring to be e-like, has rather high contamination of CCν_μ and NC events.

A two-stage method based on likelihood functions was developed to reject the $\nu_\mu/\bar{\mu}_\mu$ backgrounds and purify the ν_e and $\bar{\nu}_e$ components for multi-ring e-like events. In the first stage of the separation (Multi-GeV Multi-ring separation, MME separation), CC $\nu_e + \bar{\nu}_e$ interactions is extracted with the method introduced in [118]. However, here the input variables for the likelihood function are reconstructed by fiTQun.

The key to select the CCν_e events from CCν_μ and NC backgrounds is to confirm that the most energetic ring, which is also e-like ring, is from the electron generated by neutrino CCν_e interaction rather than the γ ring from π^0 decay in the hadronic system. Four variables are used in this likelihood: visible energy fraction of the most energetic ring, visible energy fraction of the most energetic charged pion like ring, number of decay electrons and the distance between the event vertex and the farthest decay electrons. The energy fraction of the most energetic ring tends to be small for the background events since larger energy is carried by the hadrons for CCν_μ or NC. The reason to choose the visible energy fraction of the most energetic charged pion like ring is also based on the similar reason. For the last two variables about the decay electron, it is due to the fact that the hadronic system carrying large energy produces more pions, whose decays produce electrons, and the travel length of muon from CCν_μ is longer than the charged pion from CCν_e.

Figure 7.4 shows the distributions of these variables. The likelihood function is defined as the logarithm value of the ratio between the possibility distribution function (p.d.f.) for the target (CCν_e and CC$\bar{\nu}_e$), $\Gamma_i^S(x_i)$, and the p.d.f. for the background (CCν_μ and NC), $\Gamma_i^B(x_i)$:

$$L_{\mathrm{MME}} = \sum_{x_i} \log(\Gamma_i^S(x_i)/\Gamma_i^B(x_i)). \tag{7.2}$$

Here, the four variables used in the likelihood are represented by x_i. The likelihood distribution of the first stage separation is shown in Figure 7.5. Events that fail this

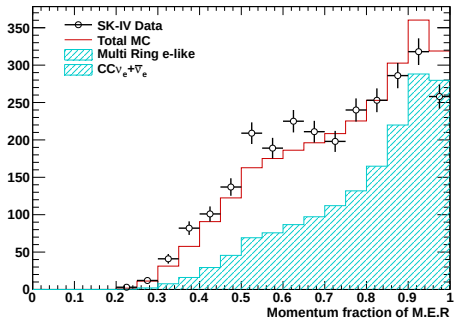

(a) Visible energy fraction of most energetic ring (M.E.R)

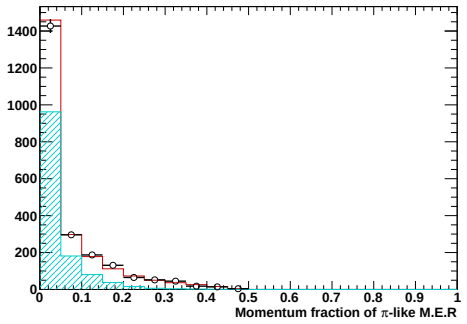

(b) Visible energy fraction of charged pion-like M.E.R

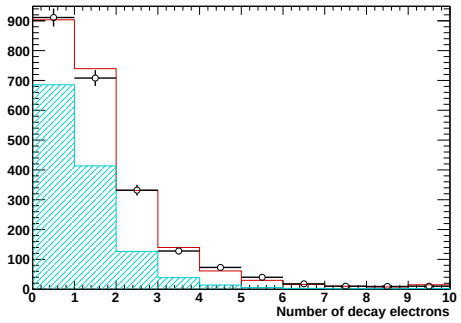

(c) Number of decay electrons

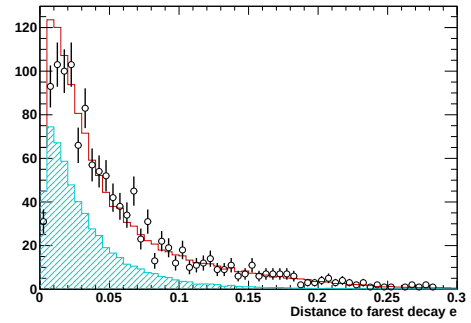

(d) Distance to the farthest decay electron divided by total visible energy

FIGURE 7.4: Distributions of the variables used in the multi-GeV multi-ring e-like (MME) likelihood for SK-IV. Shaded histogram represents CC$\nu_e + \overline{\nu}_e$, red solid line represents total atmospheric neutrino MC and open circle indicates the distribution of data. Error bars represent the statistical uncertainty of the data.

selection are classified as "multi-ring other" and the remains are termed as "multi-ring e-like".

The second stage of the separation process focuses on separating neutrino and antineutrino interactions from the multi-ring e-like data. Unlike the multi-GeV single-ring e-like sample, which is separated with a simple cut on the number of decay electrons, a likelihood method presented in [6] is used, while the variables reconstructed by fiTQun are used.

It is known that ν_e scattering tends to be less forward peaked and have larger energy transferred to the hadronic system compared to $\bar{\nu}_e$ since CCν_e interaction has a wider inelasticity $y := (E' - E)/E$ distribution due to the nature of the weak interaction. Here E and E' represent the initial energy of neutrino and the energy of outgoing electron, respectively. This implies, comparing with CC$\bar{\nu}_e$, :

- Transverse momentum tends to be larger for CCν_e.

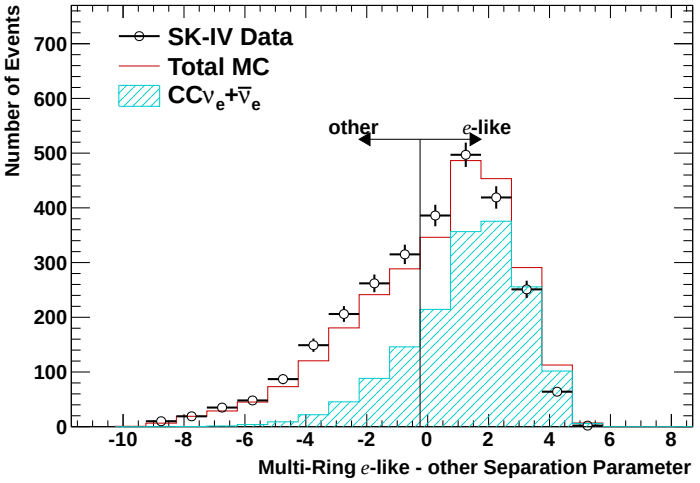

FIGURE 7.5: Likelihood distribution for the first stage of SK-IV multi-GeV multi-ring e-like events separation. The statistical error are denoted by error bars. The cut is determined at -0.25 according to the result of MC study.

- Momentum fraction for the most energetic ring tends to be smaller for CCν_e.
- More rings are expected to be observed for CCν_e.
- More decay electrons are expected to be observed for CCν_e.

A likelihood with parameters including the number of decay electrons, number of rings and transverse momentum of the most energetic ring are used to separate ν_e-like and $\overline{\nu}_e$-like samples. The distributions of those variables are shown in Figure 7.6. The likelihood function is similar to Equation 7.2, which is made by just replacing the variable used and the definition of signal and background to CCν_e and CC$\bar{\nu}_e$. Table 7.2 shows the efficiency and purity for selecting $\nu_e/\bar{\nu}_e$ events in the multi-ring e-like samples, and identifying true CC $\nu_e(\bar{\nu}_e)$ events.

7.2 Oscillation Effect

As discussed in Section 1.5, the electron neutrino oscillation is observable by sub-dominant oscillation. For the electron neutrino, the oscillation effect due to θ_{13} is dominant from a few GeV to 10 GeV, as shown in Figure 1.5.

The amplitude of neutrino oscillation is resonantly enhanced when $A_{CC}/\Delta m^2_{32} = \cos 2\theta_{13}$. Considering that $\cos 2\theta_{13}$ is positive, the enhancement only happens when the sign of A_{CC} and Δm^2_{32} are the same: neutrinos for the normal hierarchy (both of A_{CC} and Δm^2_{32} larger than 0) or antineutrinos for the inverted hierarchy (both of A_{CC} and Δm^2_{32}

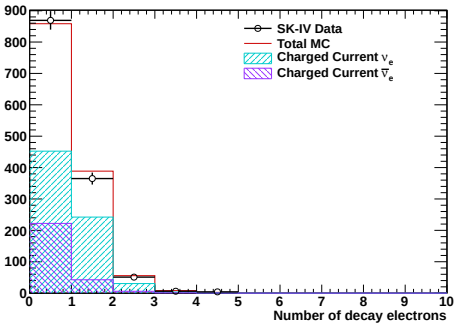

(a) Number of decay electron

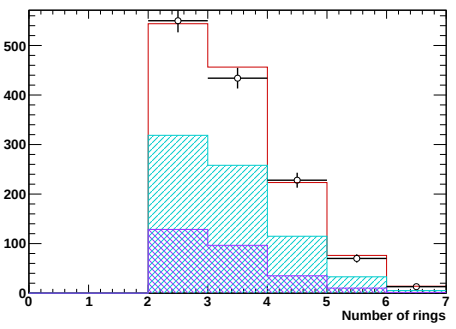

(b) Number of rings

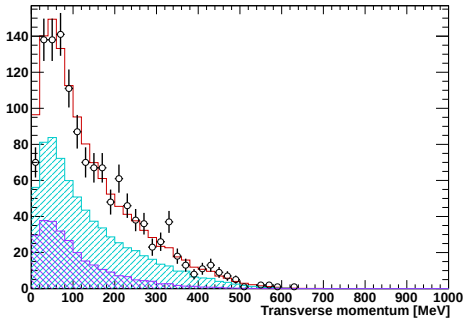

(c) Transverse momentum (MeV)

FIGURE 7.6: Distributions of the variables used in the MME ν_e and $\overline{\nu}_e$ separation likelihood for SK-IV passed the first selection. Cyan (magenta) shaded histogram represent the distribution of CCν_e (CC$\bar{\nu}_e$) events, red solid line represents total atmospheric neutrino MC and open circle indicates the distribution of data. Error bars show the statistical uncertainty of data.

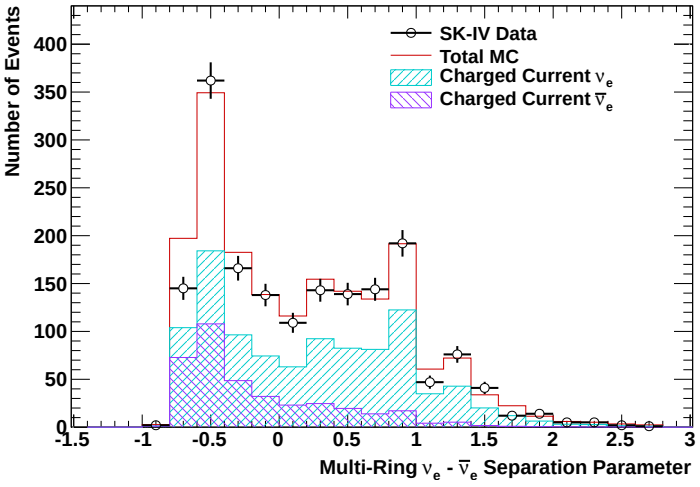

FIGURE 7.7: Likelihood distribution for the second stage of SK-IV multi-GeV multi-ring e-like events separation. The statistical error are denoted by error bars. Events with likelihood values larger (less) than 0 are selected as $\bar{\nu}_e$-like (ν_e-like).

	fiTQun	APFit
First stage		
Multi-ring e-like events		
Efficiency	75.7%	69.7%
Purity	77.8%	69.5%
Second stage		
Multi-ring True CCν_e events		
Efficiency	56.8%	53.6%
Purity	58.8%	52.6%
Multi-ring True CC$\bar{\nu}_e$ events		
Efficiency	68.4%	70.9%
Purity	30.0%	25.9%

TABLE 7.2: Performance of multi-ring e-like events selection. The definition of efficiency is the fraction of the selected events among all true ν_e or $\bar{\nu}_e$ events. The fraction of the true ν_e or $\bar{\nu}_e$ events over all selected events is defined as the purity.

are less than 0). Therefore, the mass hierarchy can be determined by observing the increase in number of upward events in ν_e-like and $\bar{\nu}_e$-like samples. Figure 7.8 shows the sensitivity to the mass hierarchy of each sample. The largest contribution comes from the multi-GeV sample, including multi-GeV FC sample, PC sample and Up-μ sample. Figure 7.9 shows the zenith angle distribution of ratio of number of events with oscillation at (Δm^2_{12}, Δm^2_{32}, $\sin^2\theta_{12}$, $\sin^2\theta_{13}$, δ_{CP}) = (7.49 $\times$ 10^{-5} eV^2, 2.5$\times$ 10^{-3} eV^2, 0.309, 0.021, 200°), to that without oscillation. The enhancement in the upward direction ($\cos\theta < 0$) for ν_e sample can be seen while a deficit is seen in the ν_μ sample, whose size depends on the value of $\sin^2\theta_{23}$. A sizable difference can be seen between the normal hierarchy, which is denoted by dashed line, and the inverted hierarchy, which is denoted by solid line. The reason of larger electron neutrino appearance observed in upward direction in the normal hierarchy than that in the inverted hierarchy is due to more neutrinos from the primary flux and larger absolute cross section of neutrinos than that of antineutrinos as discussed in Chapter 3.

The CP phase also has effect on the oscillation possibility via the interference between θ_{13}-dependent oscillation and the oscillation discussed in Equation 1.25 [68]. Figure 7.10 shows the expected sensitivity to different δ_{CP} of each sample. The largest contribution comes from the sub-GeV FC sample. The ratio between number of events with and that without oscillations as a function of zenith angle at three different CP phase values is shown in Figure 7.11. Besides the excess in upward direction for multi-GeV e-like samples, the interference gives an overall $\sim 2\%$ effect on sub-GeV e-like samples.

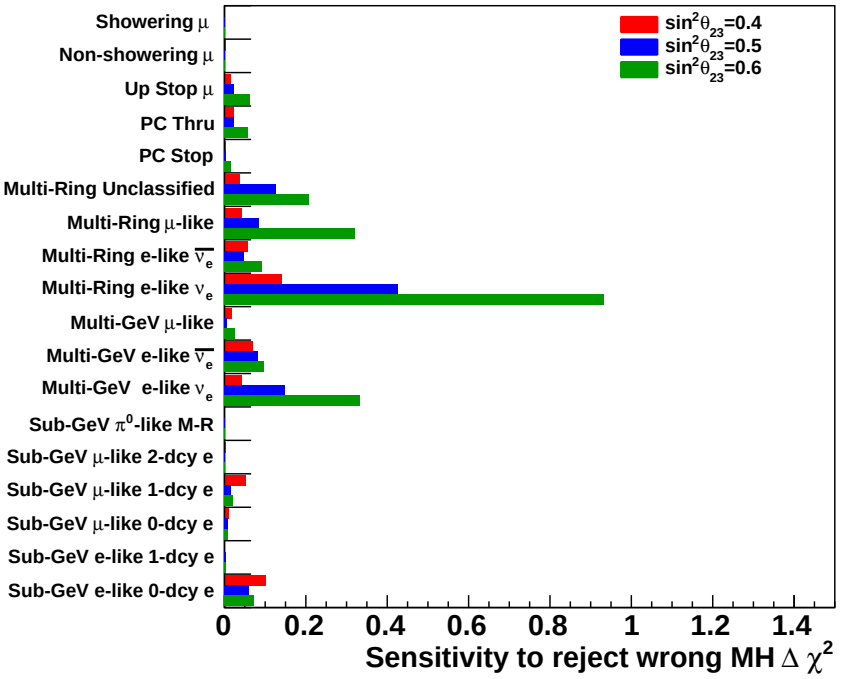

FIGURE 7.8: Sensitivity to reject wrong mass hierarchy (MH) of each sample for atmospheric neutrino. The vertical axis shows the $\Delta\chi^2$ value between the true oscillation point at normal hierarchy and the best fit point at inverted hierarchy. The true oscillation paramters are (Δm^2_{12}, Δm^2_{32}, $\sin^2\theta_{12}$, $\sin^2\theta_{13}$, δ_{CP}) = (7.49 $\times$ 10^{-5} eV^2, 2.5$\times$ 10^{-3} eV^2, 0.309, 0.021, 200°). True MH is assumed to be normal hierarchy. Oscillations at different values of $\sin^2\theta_{23}$ = 0.4 (red), 0.5 (blue), 0.6 (magenta) are shown.

7.3 Fiducial Volume Expansion

The fiducial volume (FV) in previous analyses with APFit was defined as the region where the distance to the nearest wall in the inner detector is larger than 200 cm ($D_{\text{wall}} > 200$ cm), which results that approximately 30% loss of the Super-K inner detector mass. Nevertheless, statistics of the observation still constrains the physical sensitivity. Therefore, by making use of the improved reconstruction performance of fiTQun, the fiducial volume is able to be expanded while keeping a high signal purity and low background to increase the sensitivity.

7.3.1 MC Study for Fiducial Volume Expansion

A larger fiducial volume doesn't only provide more statistics, but also risk for lower purity of signal interactions in neutrino sample. The reconstruction performance might deteriorate for events close to the ID wall since some particles that travel toward the

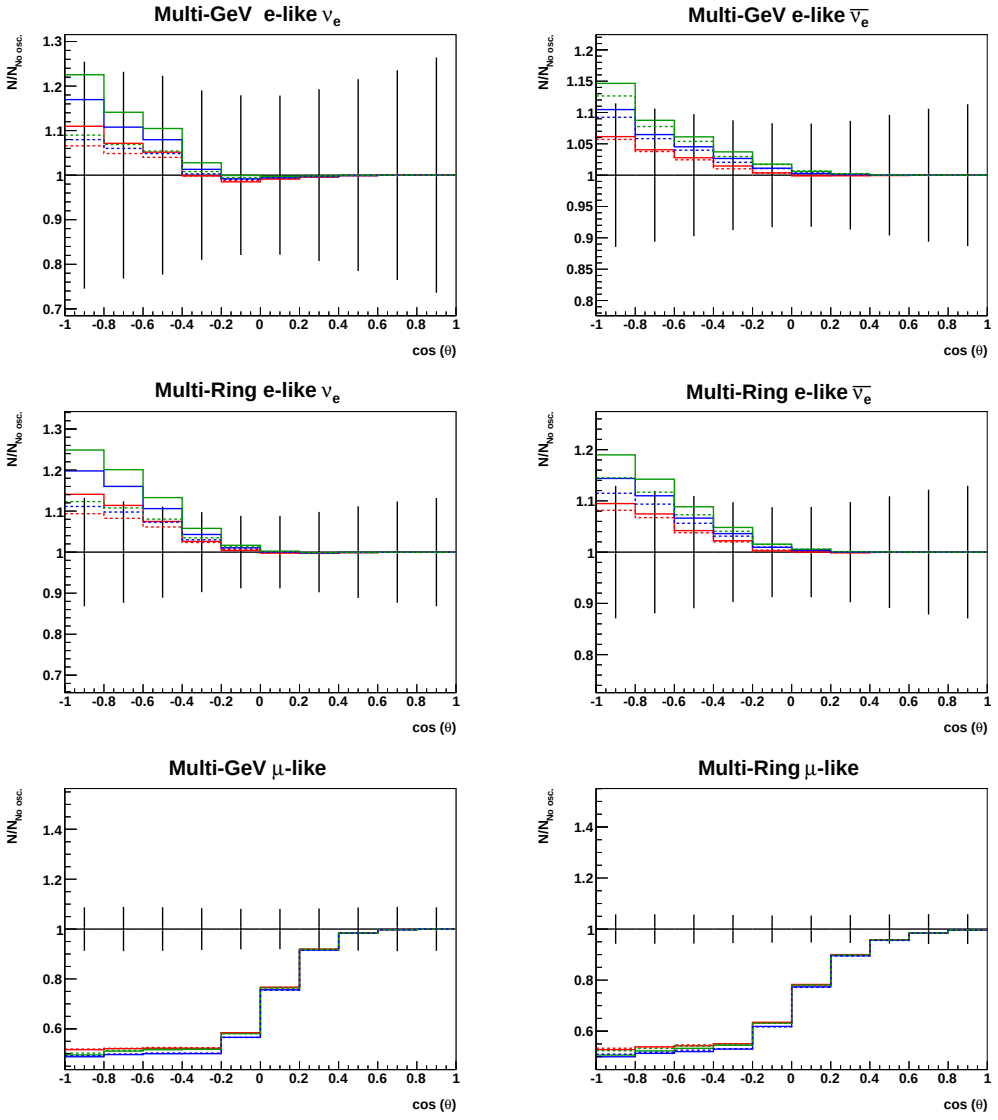

FIGURE 7.9: Oscillation effect on zenith angle distribution for multi-GeV samples. The vertical axis shows the ratio between the number of events with oscillations and the ones without oscillations. Oscillation parameters are (Δm^2_{12}, Δm^2_{32}, $\sin^2\theta_{12}$, $\sin^2\theta_{13}$, δ_{CP}) = (7.49 $\times$ 10^{-5} eV^2, 2.5$\times$ 10^{-3} eV^2, 0.309, 0.021, 200°). Oscillations at different values of $\sin^2\theta_{23}$ = 0.4 (red), 0.5 (blue), 0.6 (green) for normal hierarchy are shown.

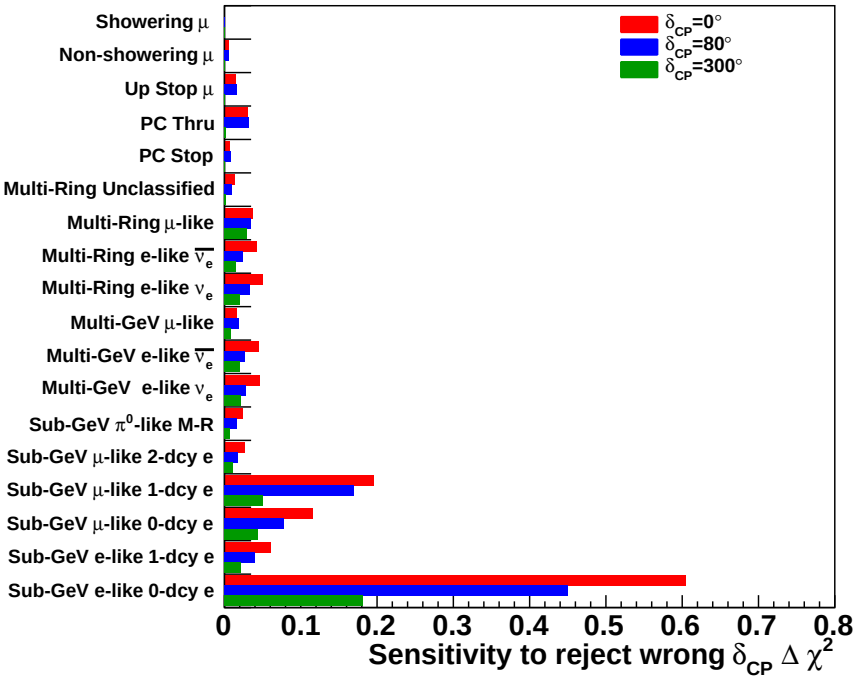

FIGURE 7.10: Sensitivity to $\delta_{\rm CP}$ of each sample for atmospheric neutrino. The y-axis shows the $\Delta\chi^2$ value between the true oscillation point and the best fit point. The true oscillation parameters are (Δm^2_{12}, Δm^2_{32}, $\sin^2\theta_{12}$, $\sin^2\theta_{13}$, $\sin^2\theta_{23}$, δ_{CP}) = (7.49 $\times$ 10^{-5} eV^2, 2.5$\times$ 10^{-3} eV^2, 0.309, 0.021,0.425, 200°). True MH is assumed to be normal hierarchy. Oscillations at different values of δ_{CP} = 0° (red), 80° (blue), 300° (magenta) are shown.

wall in those events will only hits a few PMTs and results in poorly imaged Cherenkov rings. Furthermore, the possibility of that events with interaction vertices outside of the ID wall being reconstructed within the FV increases as the FV cut is moved closer to the wall, due to the vertex resolution. Although most of those events are rejected by the OD cut, some events may generate too few photons to be rejected and contaminate the analysis sample if they originate in the 55 cm insensitive region between the wall of ID and OD or very near the OD wall. Due to the low precision of the detector modeling in those region, large systematic errors might be introduced by those "entering events".

The fraction of signal and backgrounds of the FC sub-GeV μ-like 0 decay-e events changes as a function of the distance from the reconstructed vertex to the nearest ID wall ($D_{\rm wall}$) as shown in Figure 7.12. Until 50 cm, the purity of signal events, including ν_μCC and $\bar{\nu}_\mu$CC interactions (red) for this sample, keeps stable. The component fractions for other samples can be found in Appendix B. Similar behavior is observed in all of 13 FC event categories, which shows that the fiducial volume cannot be expanded to the region with $D_{\rm wall}$ less than 50 cm due to the entering ν events. Table 7.3 shows the

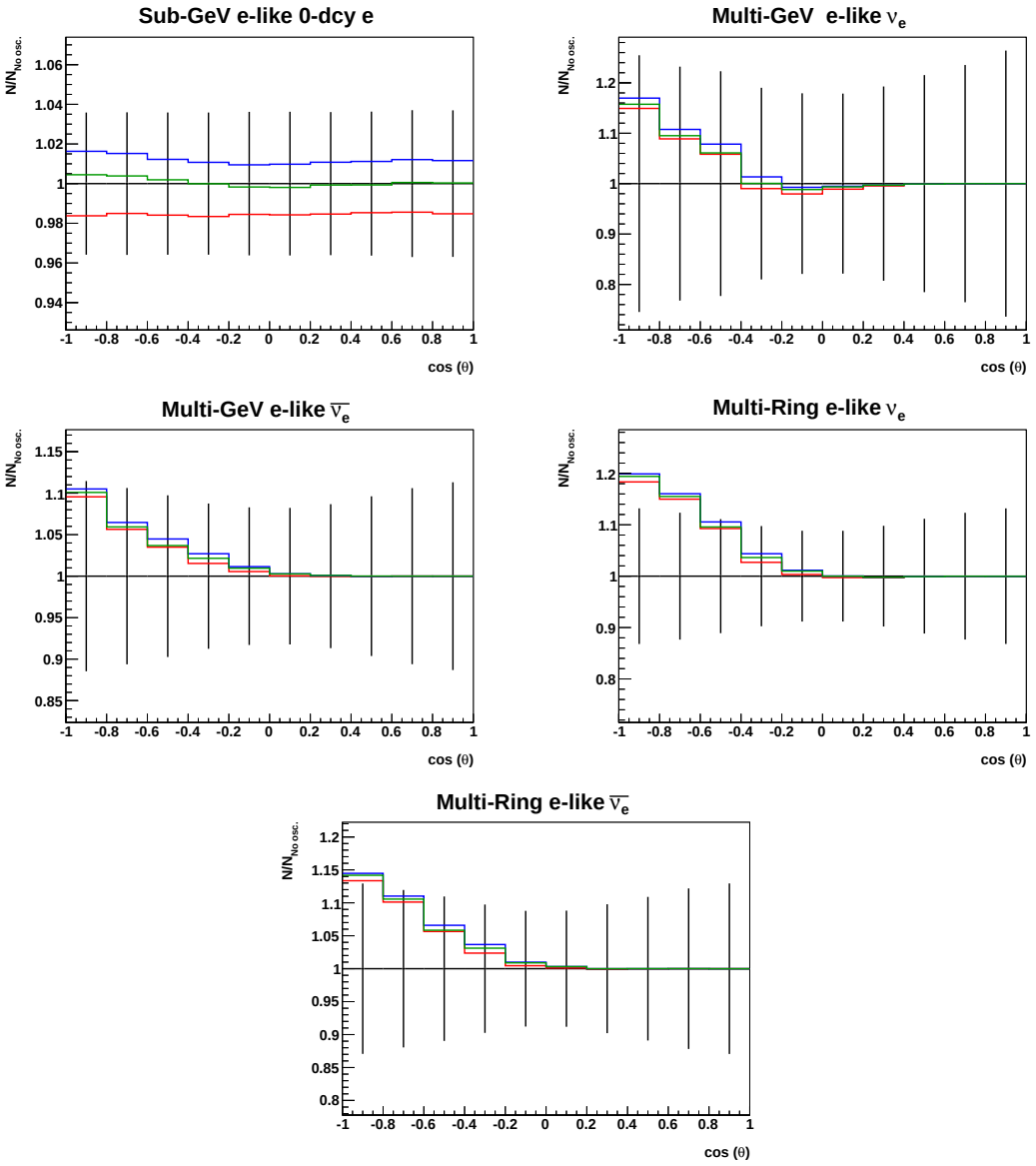

FIGURE 7.11: Zenith angle distributions of the ratio of number of events with oscillation to that without oscillation, assuming oscillation parameters (Δm^2_{12}, Δm^2_{32}, $\sin^2\theta_{12}$, $\sin^2\theta_{23}$) = (7.49×10^{-5}, 2.5×10^{-3}, 0.309, 0.5) in normal hierarchy case for SK-IV. Cases with $\delta_{\text{CP}} = 80°$ (red), 220° (blue) and 300° (green) are shown. The error bars represents statistical uncertainty.

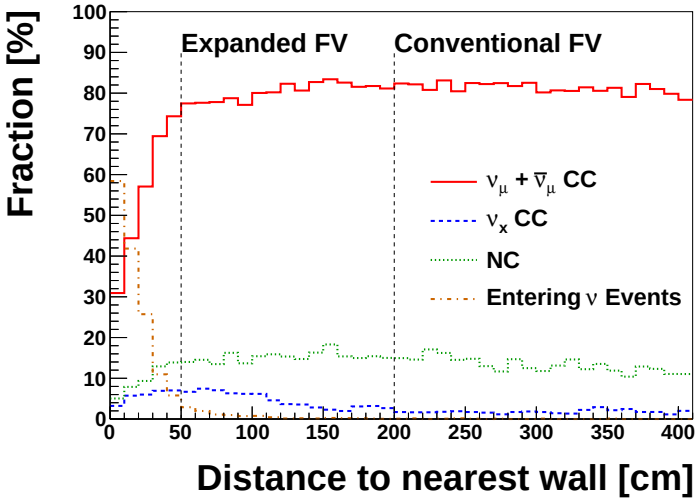

FIGURE 7.12: The composition of the FC sub-GeV μ-like sample without decay electron. Horizontal axis shows the distance between the reconstructed vertex and the nearest ID wall.

purity of the 13 FC samples within the new region (50 cm $< D_{\rm wall} <$ 200 cm) and the conventional FV definition ($D_{\rm wall} >$ 200 cm).

To investigate the effect of the FV expansion, including both of the purity decrease and statistics increase, a study based on MC sample was performed. The sensitivity to reject the inverted mass hierarchy assuming the true mass hierarchy is normal with different FV cut values is shown in Figure 7.13. Systematic errors used in this figure are assumed to be unchanged from the values obtained in the conventional FV region. From this figure it can be expected for a FV cut at 50 cm to bring an improved mass hierarchy sensitivity if the systematic errors keep stable even in the new region (50 cm$< D_{\rm wall} <$ 200 cm). The effect of the FV expansion on the systematic errors and a more precise sensitivity study is presented below.

In fact, besides the $D_{\rm wall}$ value, a cut on "towall" value, which means the distance from the vertex to the wall along the direction of the particle as shown in Fig 7.14, is also considered. Events that are close to the ID wall, but point away from the wall (small $D_{\rm wall}$ but large towall), generally hit enough PMTs to have a well-imaged Cherenkov ring. On the other hand, events that are close to the ID wall but point towards the wall (small $D_{\rm wall}$ and small towall), generally hit too few PMTs, and as a result have poorly imaged Cherenkov rings. Figure 7.15 shows the purity of each component for sub-GeV single ring e-like 1 decay electron as function of the towall value. The fraction of ν_e CC events is lower than 20% since too many background events from ν_μ CC are contaminated.

Sample	CC ν_e	CC $\bar{\nu}_e$	CC $\nu_\mu + \bar{\nu}_\mu$	CC ν_τ	NC
Fully Contained (FC) Sub-GeV					
e-like, Single-ring					
0 decay-e	0.728	0.242	0.001	0.000	0.028
	(0.702)	(0.227)	(0.025)	(0.001)	(0.045)
1 decay-e	0.907	0.020	0.033	0.001	0.040
	(0.712)	(0.015)	(0.208)	(0.001)	(0.063)
μ-like, Single-ring					
0 decay-e	0.010	0.004	0.795	0.001	0.191
	(0.034)	(0.011)	(0.805)	(0.001)	(0.150)
1 decay-e	0.000	0.000	0.974	0.000	0.026
	(0.001)	(0.000)	(0.968)	(0.000)	(0.031)
2 decay-e	0.000	0.000	0.984	0.000	0.016
	(0.000)	(0.000)	(0.980)	(0.000)	(0.019)
π^0-like					
Two-ring	0.051	0.016	0.011	0.000	0.922
	(0.109)	(0.036)	(0.018)	(0.000)	(0.837)
Fully Contained (FC) Multi-GeV					
Single-ring					
ν_e-like	0.726	0.077	0.058	0.027	0.113
	(0.748)	(0.066)	(0.064)	(0.016)	(0.105)
$\bar{\nu}_e$-like	0.553	0.379	0.003	0.008	0.056
	(0.566)	(0.371)	(0.003)	(0.007)	(0.053)
μ-like	0.000	0.000	0.996	0.003	0.001
	(0.000)	(0.000)	(0.995)	(0.004)	(0.001)
Multi-ring					
ν_e-like	0.588	0.117	0.054	0.036	0.204
	(0.609)	(0.112)	(0.059)	(0.032)	(0.188)
$\bar{\nu}_e$-like	0.526	0.300	0.021	0.020	0.134
	(0.541)	(0.301)	(0.023)	(0.016)	(0.118)
μ-like	0.010	0.001	0.959	0.004	0.026
	(0.016)	(0.002)	(0.946)	(0.005)	(0.031)
Other	0.283	0.026	0.342	0.053	0.295
	(0.302)	(0.032)	(0.342)	(0.051)	(0.274)

TABLE 7.3: Purity of different neutrino flavor of each samples with a FV cut of 200 cm. The neutrino oscillations with $\Delta m^2_{32} = 2.52 \times 10^{-3}\text{eV}^2$ and $\sin^2\theta_{23} = 0.51$ has been considered. The result within new region (50 cm ¡ D_{wall} ¡ 200 cm) is shown by the number in the parentheses.

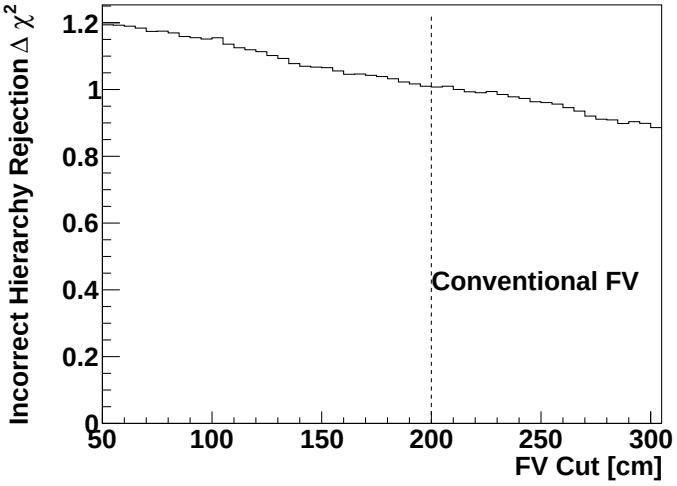

FIGURE 7.13: Sensitivity for incorrect mass hierarchy rejection. The exposure time is 3118.5 days. Horizontal axis shows different FV cut position. The true hierarchy is assumed to be normal hierarchy. The true oscillation parameters are taken as: $\sin^2\theta_{13} = 0.0210$, $\sin^2\theta_{23} = 0.5$, $\Delta m^2_{23} = 2.4 \times 10^{-3}\text{eV}^2$, and $\delta_{CP} = 0$. The systematic error for the analysis with a FV cut at 200 cm is used for all sensitivity calculation with different FV cut.

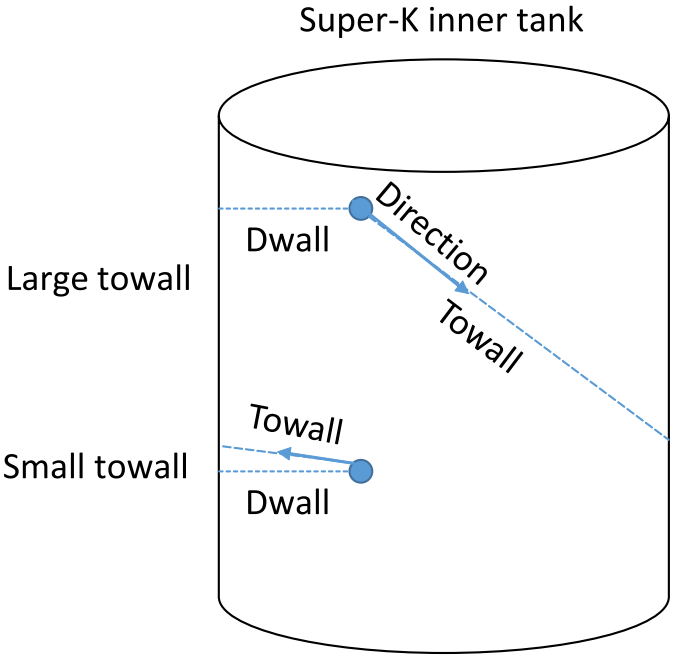

FIGURE 7.14: Defination of "D_{wall}" and "Towall".

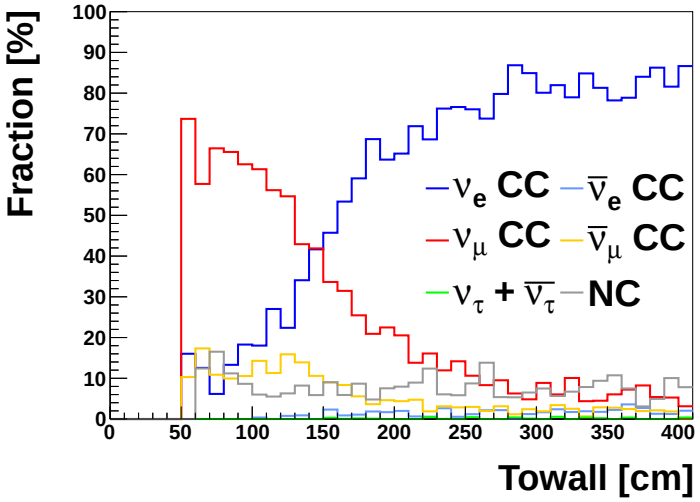

FIGURE 7.15: Purity of each component for sub-GeV single ring e-like 1 decay electron as function of towall value. A D_{wall} cut at 50 cm has been applied.

To investigate the necessity of a cut on towall, the MC sensitivities are also studied for each towall cut value. Figure 7.16 shows the sensitivity as the function of both D_{wall} cut and towall cut. Left figure shows the contribution from the sub-GeV single-ring e-like 1 decay sample. Obviously, the best point for this sample is not near (50, 50) due to too many ν_μ CC background events. However, the contribution from this sample is small. On the other hand, those samples with higher sensitivity such as multi-GeV e-like events, the statistics of events with small towall is low, as shown in Figure 7.17. A high energy event with small towall will easily penetrate the ID wall, enter the OD and then be categorized as a PC event. Therefore, the total sensitivity from all samples indicates that the towall cut is not critical to change the sensitivity. The cut on the towall value is not used for simplicity.

7.3.2 OD Hits

OD hits in the atmospheric neutrino analysis are used to reject cosmic ray muon backgrounds and separate PC from FC events. The selection efficiency of FC events might be affected if we extend the FV to $D_{\text{wall}} > 50$ cm due to the poor modeling of the response of the OD. This can thereby potentially introduce biases and relative inefficiencies in the FC sample. The distributions of the number of OD hits in both region have been studied (Figure 7.18). Data and MC are in good agreements near the FC cut, which requires that the number of OD hits in cluster with the largest charge (nhitac) less than

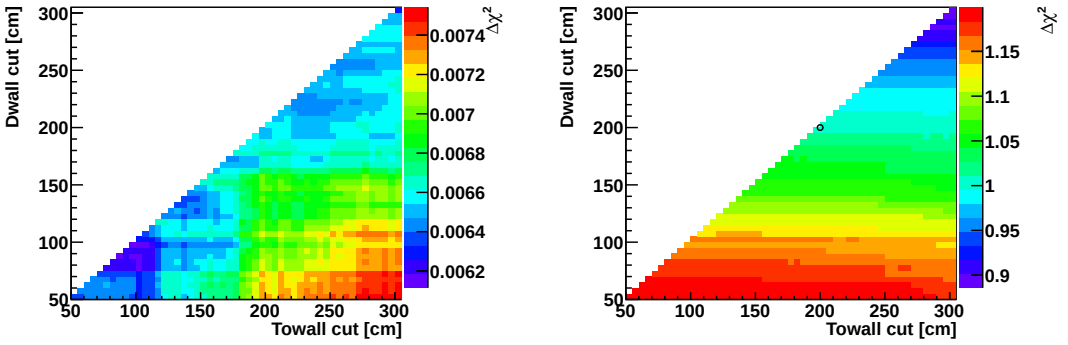

FIGURE 7.16: Sensitivity to reject wrong mass hierarchy. True mass hierarchy is NH. The left figure shows the contribution from sub-GeV single-ring e-like 1 decay sample, while the right figure shows the total sensitivity from all samples. The open circle at (200,200) in right figure represents the sensitivity at the FV cut used in previous APFit analysis.

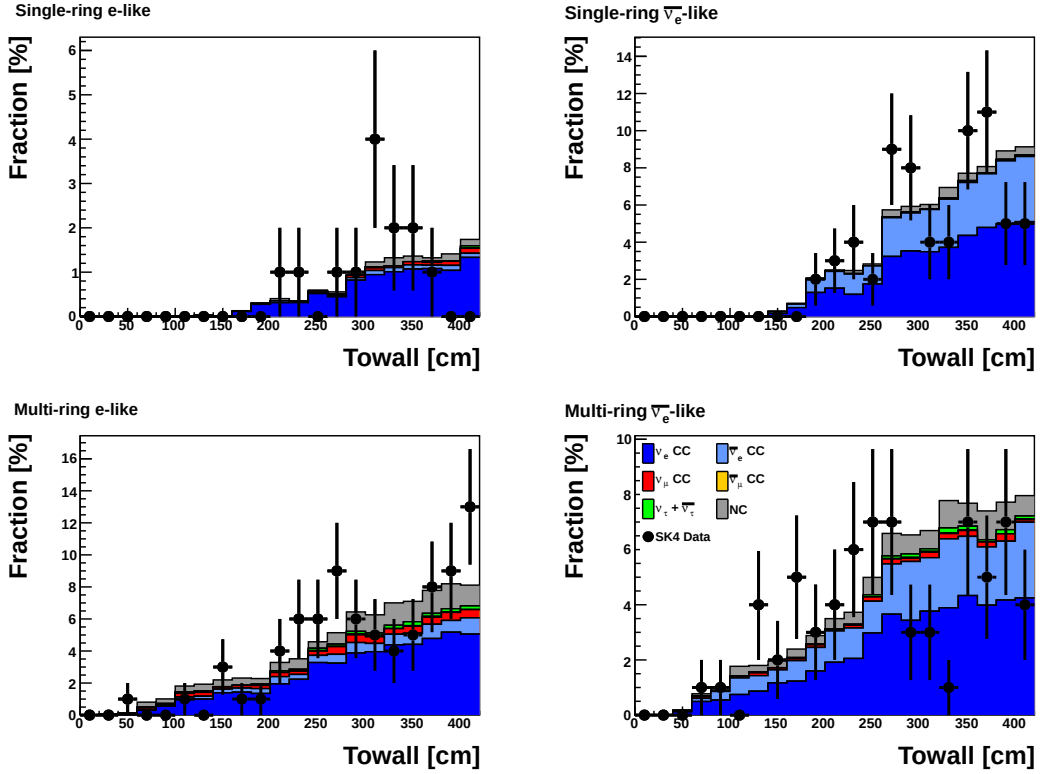

FIGURE 7.17: Towall distribution for multi-Gev e-like events. The statistics with small towall value is low.

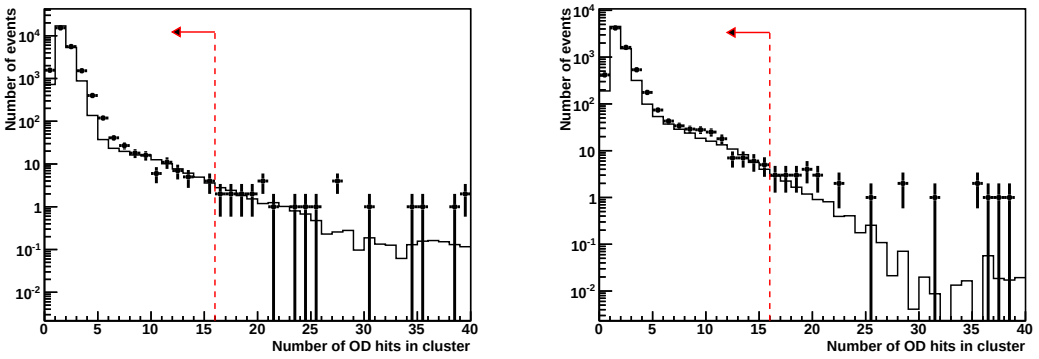

FIGURE 7.18: Distribution of the number of OD hits in cluster. Left figure shows the distribution for data with in conventional FV ($D_{\mathrm{wall}} > 200$ cm). Right figure shows the result in new region (50 cm $< D_{\mathrm{wall}} <$ 200 cm). The peak around 20 in right figure is due to cosmic ray muon events, which is confirmed by eye-scanning. The threshold line to select FC events is denoted by the red dashed line.

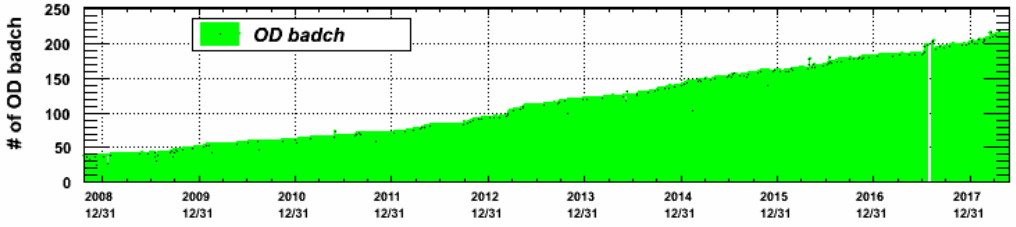

FIGURE 7.19: Number of OD bad channels.

16. After removing the non-neutrino backgrounds confirmed by eye-scanning, the number of FC events with nhitac larger than 16 for data is 8, which is in consistent with the number from MC, 11.5.

Another thing that needs to be noted is that the FC event rate in the region near wall might depend on OD hits or status of OD PMTs highly, since more entering background events might be contaminated due to inactive channels.

As shown in Figure 7.19, the number of bad OD channels increased significantly since SK-IV start. Fortunately, no large change is observed in the event rate of atmospheric neutrino samples as in Table 7.4 and Table 7.5, which show the time variation of the atmospheric neutrino event rate within different detector regions. Therefore, the effect of OD bad channel on rejection efficiency is limited.

7.3.3 Data/MC Comparison and Background Estimation

In addition to the entering neutrino and event mis-categorization, there may be other backgrounds from non-neutrino (non-ν) sources such as cosmic ray muons and flashing PMTs due to the FV expansion.

Livetime [days]	0∼1000	1000∼2000	2000∼3118.5	MC
$D_{\mathrm{wall}} > 200$ cm	8.06±0.09	8.07±0.09	8.17±0.10	8.29
50 cm $< D_{\mathrm{wall}} <$ 200 cm	2.21±0.05	2.17±0.05	2.25±0.05	2.15
$D_{\mathrm{wall}} <$ 50 cm	1.22±0.03	1.16±0.03	1.22±0.04	0.96

TABLE 7.4: Time variation of atmospheric neutrino event rate in different detector region. number of OD hits in cluster with the largest charge is required to be less than 16, and visible energy is required to be larger than 30 MeV. For the last row, Dwall < 50 cm , there are many cosmic ray muon background events contaminated therefore the event rate is much higher than the expected value of MC.

Livetime [days]	0∼1000	1000∼2000	2000∼3118.5	MC
1810 cm > Z > 900 cm	2.95±0.05	2.85±0.05	3.03±0.06	2.83
900 cm > Z > 0 cm	2.93±0.05	2.93±0.05	2.92±0.06	2.88
0 cm > Z > -900 cm	2.86±0.05	2.88±0.05	2.85±0.06	2.88
-900 cm > Z > -1810 cm	2.75±0.05	2.73±0.05	2.83±0.06	2.76

TABLE 7.5: Time variation of atmospheric neutrino event rate in different detector region. number of OD hits with the largest charge in cluster is required to be less than 16, and visible energy is required to be larger than 30 MeV.

Before being observed in the ID, cosmic ray muons must pass through the OD, therefore most of them are rejected by cuts on OD activity. The true vertex of cosmic ray muons events observed in ID is the entrance point on the wall, meaning that the FV cut can help to reject any events remaining after OD cuts are applied. However, due to the vertex resolution of the reconstruction algorithm, which is around 15 cm $\sim$ 20 cm, cosmic ray background events might contaminate the FC sample when the FV cut is near the wall.

Another kind of non-neutrino background is flasher events, which are caused by the internal electrical discharge of a PMT. The reconstructed vertex for flasher event is also expected to be on the wall, more specifically, the position of discharged PMT. Due to the same reason as the cosmic ray muon case, more flasher backgrounds might be introduced into the FC sample when the FV cut is near the wall.

The distribution of the distance from the reconstructed vertex to the nearest wall of FC events is shown in Figure 7.20. Several distributions, including the events' momentum, direction, particle ID, ring counting likelihood of the FC sample have also been checked for both the conventional FV region ($D_{\mathrm{wall}} > 200$ cm) and new region (50 cm $< D_{\mathrm{wall}} <$ 200 cm), respectively. The observations are in good agreement with the expectation.

In fact, all FC events within the fiducial volume ($D_{\mathrm{wall}} >$50 cm in this analysis) were checked by eye with a graphical event display program to evaluate the background rate more precisely. The eye-scanning result shows that one flasher event and 24 cosmic ray muon events were contaminated in the FC sample within the expanded FV ($D_{\mathrm{wall}} >$

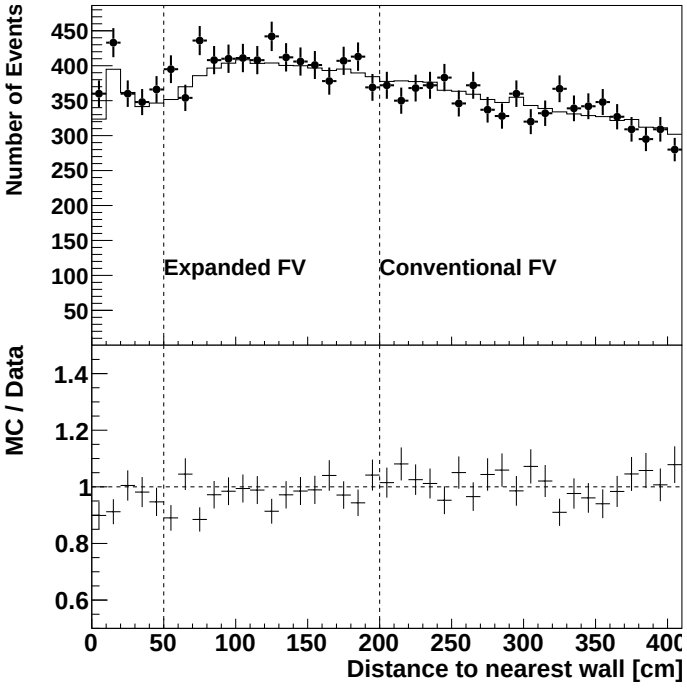

FIGURE 7.20: Number of events as the function of the distance between the reconstructed event vertex and the nearest ID wall for FC samples. Points represent the result of data and solid line is for MC. The ratio between MC and data is shown in bottom figure.

50 cm). Most of the cosmic ray muon backgrounds were categorized as multi-ring μ-like events with downward direction and momentum which is larger than 5 GeV/c. Due to the presence of the fake ring found by fiTQun, their vertices were reconstructed within the expanded fiducial volume. Independent cosmic ray muon samples also show consistent result for both the rate and type of such mis-reconstructions, which enable us to remove the expected cosmic ray background in the final analysis sample statistically based on the D_{wall} distribution of the cosmic ray muon events. By comparison of the event classification of this control sample with those observed in the eye-scanned background, it is shown that the FC event reduction process does not depend strongly on the muon's direction and momentum. Figure 7.21 and Figure 7.22 show the distribution of D_{wall}, the momentum and zenith angle distribution respectively. The shape of the cosmic ray muon sample (solid line) and the eye-scanned background events (points) in the FC sample are in good agreement.

As has been stated above, only one flasher event is observed within the expanded FV ($D_{\mathrm{wall}} > 50$ cm) by eye-scanning. This contamination is expected to have a limited impact on the final FC sample. Therefore, the effect of the flasher event is considered by a systematic error on the event rate in the oscillation analysis presented below.

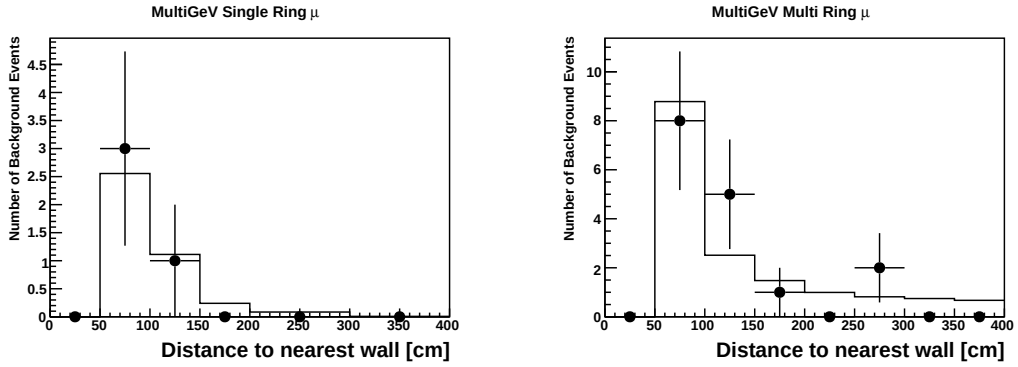

FIGURE 7.21: The distribution of the distance from the reconstructed vertex to the nearest ID wall of μ-like samples. Left figure shows the distribution of single-ring events while right figure shows the one of multi-ring events. Both of the independent cosmic ray muon sample (solid line) and eye-scanned background events in FC sample (points) are shown. Histograms are normalized by the total number of backgrounds events seen in the FC sample.

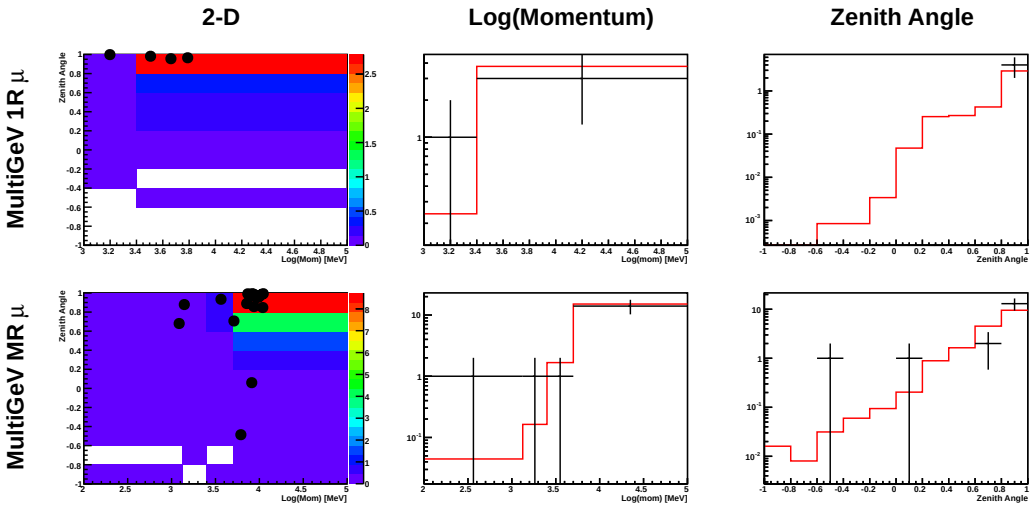

FIGURE 7.22: The distribution of the momentum and zenith angle of single-ring (top) and multi-ring (bottom) μ-like samples. The left two figures show the 2-d distribution, where points represent the background events identified by eye scanning in FC and color box indicate the distribution of cosmic ray muon sample. In right four figures, solid line represents the result of cosmic ray muon sample and the cross shows the distribution of the eye-scanned background events in FC. Histograms are normalized by the total number of events.

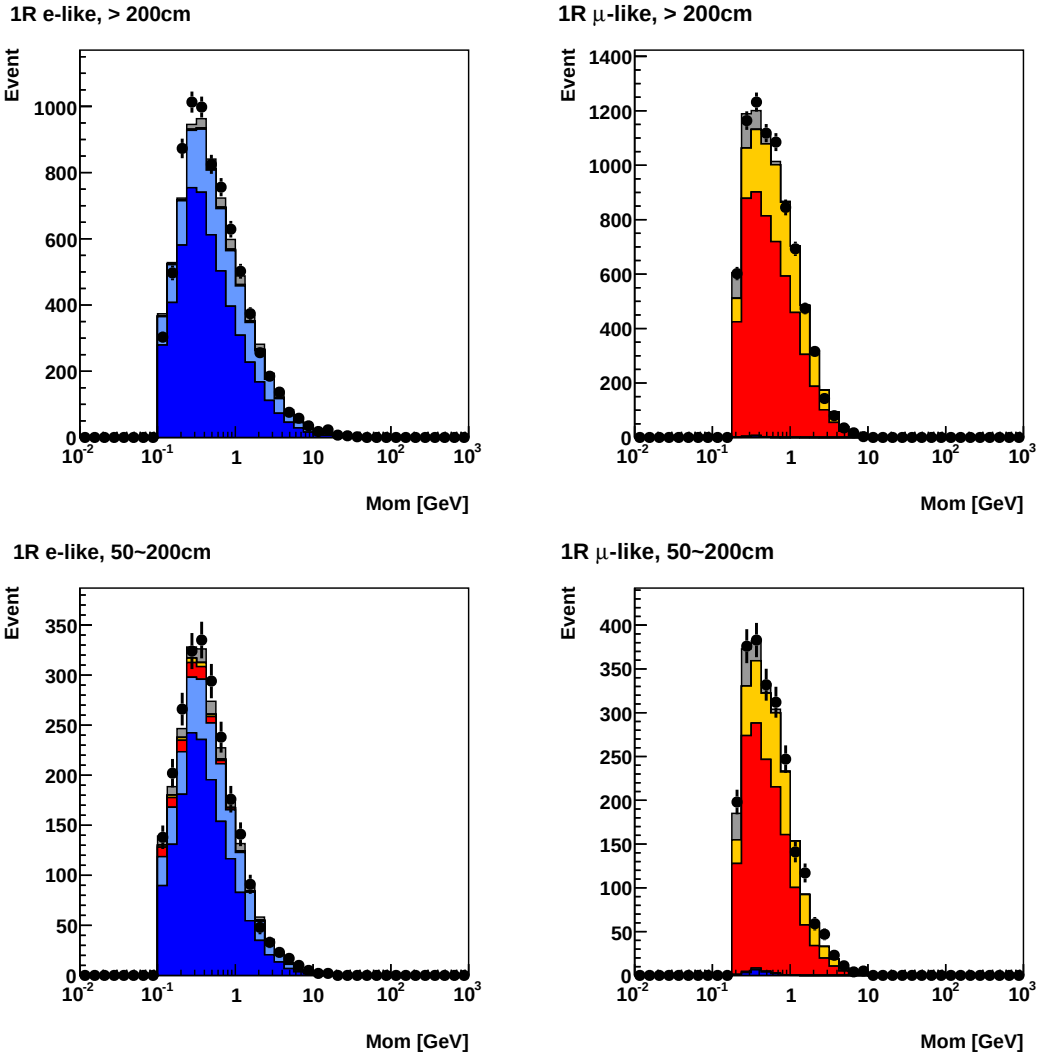

FIGURE 7.23: Momentum distribution of single ring event in different detector region. Samples are divided based on the reconstructed particle ID. Upper two plots show the events within conventional FV, $D_{\text{wall}} > 200$ cm, while the lower two plots show the events within new region, 50 cm $< D_{\text{wall}} <$ 200 cm. Good agreement between data and MC can be observed.

Another possible issue is momentum reconstruction. The influence of reflection and scattering would be stronger when the particle vertex is near to the wall. The decrease of number of hit PMTs might enhance this influence further. Furthermore, part of the track might penetrate the ID wall and enter the 55 cm insensitive region between ID and OD, which might cause bias in momentum reconstruction. Figure 7.23 shows that the momentum distribution of single-ring events of MC is in good agreement with data, which means that those effects have been simulated in the MC and will not result in additional systematic uncertainty. The other detailed basic distribution of each event category in both FV regions can be found in Appendix B.

Figure 7.24 shows the distributions of reconstructed direction for each analysis sample

within the expanded FV. As indicated in Figure 7.25, the event rate of FC sample is stable at 8.3(2.2) per day for the conventional FV (new region) since the start of SK-IV, with 0.73 events per day for PC sample and 1.49 events per day for Up-μ sample.

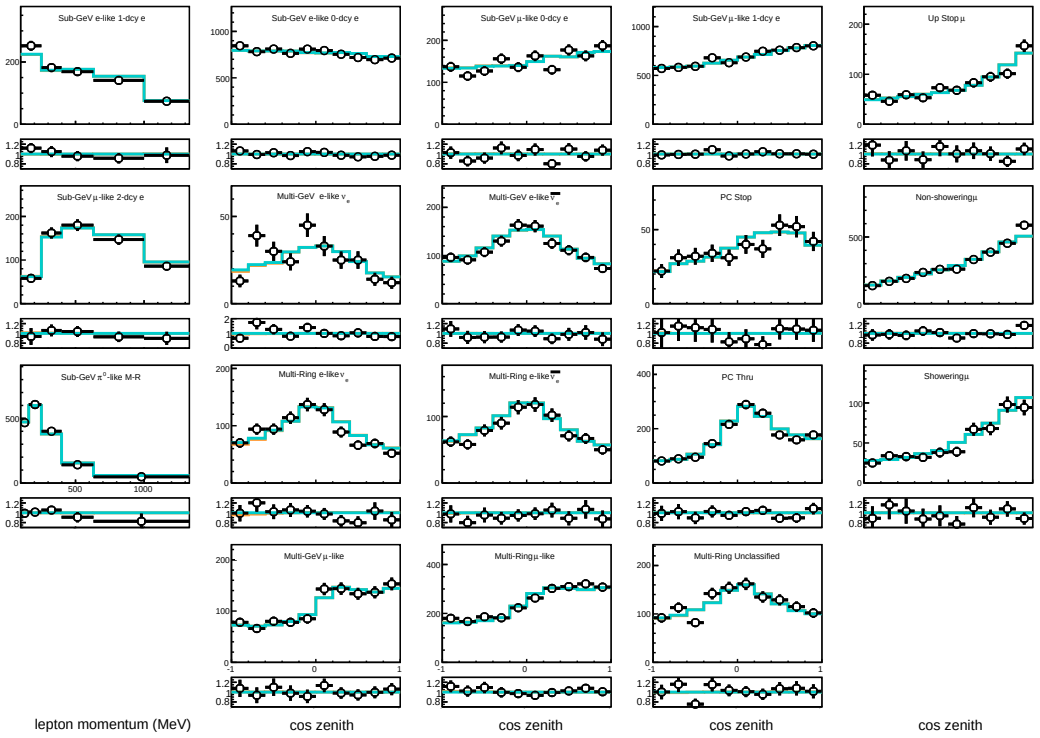

FIGURE 7.24: Comparisons between SK-IV data and MC within expanded FV ($D_{\text{wall}} > 50$ cm). The sample has been divided into 18 categories. The reconstructed momentum distributions for the samples with only one zenith angle bin are shown in the first column. The other samples are shown as zenith angle distributions from second to fifth column. The best-fit MC assuming the normal hierarchy is denoted by solid lines. The ratio between MC to data is shown in the narrow panels below each distribution. The error bars in each panels represent the statistical error.

7.4 Analysis Method

Atmospheric neutrino data are fit to the MC prediction under different oscillation parameter sets with a binned χ^2 method assuming Poisson statistics to find the most preferred one. Different error sources are assumed to be uncorrelated and scaling factors on the MC in each bin are assigned for each error to reflect their effects [119]. The χ^2 is defined as:

$$\chi^2 = 2\sum_n \left(E_n - \mathcal{O}_n + \mathcal{O}_n \ln \frac{\mathcal{O}_n}{E_n} \right) + \sum_i \left(\frac{\epsilon_i}{\sigma_i} \right)^2, \tag{7.3}$$

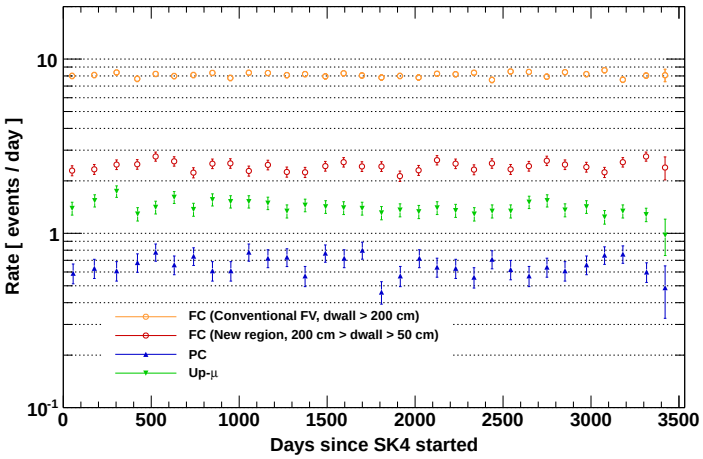

FIGURE 7.25: Final event rates variation with respect to running time since SK-IV launch. The error bars represent the statistical error. The fully contained event rate is denoted by circle and the partially contained (upward-going muon) event rates are denoted by upward-facing (downward-facing) triangles. The fiducial volume cut value for FC events are shown in the parentheses.

where

$$E_n \quad = \quad E_{n,0}(1 + \sum_i f_n^i \epsilon_i). \tag{7.4}$$

In this equation the observed number of events in the n-th analysis bin is represented by $\mathcal{O}_n$, the nominal MC expectation and the one after considering systematic errors in that bin are denoted by $E_{n,0}$ and E_n, respectively. The fractional change of the event rate under a 1σ variation of the systematic error source is described as f_n^i, where index n and i represent the number of bin and systematic error, respectively. The penalty term from the systematic errors adjustment for a better agreement between MC and data is defined as the sum of $(\epsilon_i/\sigma_i)^2$. MC is fit to the data by finding the error parameters set ϵ_i which has minimum χ^2 for each oscillation parameter set.

Two fits, including a θ_{13}-free fit, in which θ_{13} is a free parameter, and a θ_{13}-constrained fit, in which it is constrained to its global best fit value, are performed over 515 analysis bins in SK-IV. Besides the expanded FV ($D_{\text{wall}} > 50$ cm), the fits are also done within the conventional FV ($D_{\text{wall}} > 200$ cm) for comparison. The fit with θ_{13}-constrained is performed over three parameters, $|\Delta m^2_{32,31}|$, $\sin^2\theta_{23}$ and δ_{CP} with a total of 72 systematic errors and $\sin^2\theta_{13}$ is constrained to 0.0210 ± 0.0011 [27]. The number of oscillation parameters for fit with θ_{13}-free is increased to four to include $\sin^2\theta_{13}$ and the number of the systematic errors is reduced to 71: the error from θ_{13} uncertainty is removed in this fit. Although the $\sin^2\theta_{13}$ has been measured very precisely by other experiments already, measurements with atmospheric neutrinos can test the validity of the analysis'

Parameter	Value
Δm^2_{21}	$(7.53 \pm 0.18) \times 10^{-5}\text{eV}^2$
$\sin^2\theta_{12}$	0.307 ± 0.013
$\sin^2\theta_{13}$	0.0210 ± 0.0011

TABLE 7.6: Summary of the oscillation parameters fixed in the analysis. Both of the value and associated uncertainty are shown. It should be noted that $\sin^2\theta_{13}$ is not fixed in the "θ_{13}-free"analyses.

Parameter	Range	Scan points
$\lvert\Delta m^2_{32,31}\rvert$	$1.5 \times 10^{-3} \sim 3.5 \times 10^{-3}\text{eV}^2$	40 points
$\sin^2\theta_{13}$	$0.0 \sim 0.06$	25 points
$\sin^2\theta_{23}$	$0.3 \sim 0.725$	35 points
δ_{CP}	$0.0 \sim 2\pi$	19 points

TABLE 7.7: Oscillation parameter points scanned in this analysis.

hierarchy preference since θ_{13} drives the appearance of upward-going electron events expected for a mass hierarchy signal. During the fitting, the solar mixing parameters, Δm^2_{21} and $\sin^2\theta_{12}$, are fixed to the values in Table 7.6. The uncertainty in the fixed oscillation parameters are considered with the corresponding systematic errors in the analysis. Each combination of the oscillation parameter shown in Table 7.7 is used to find the best-fit parameter set which minimizes the χ^2 as defined in Equation 7.3. The normal and inverted hierarchy are fitted separately. The value of Δm^2_{32} is used during the fits to the normal hierarchy, while Δm^2_{31} value is used for the inverted hierarchy fitting. The one with smaller minimum χ^2 value among the two hierarchy fits is taken as the global best-fit. The difference between the two hierarchies is used to evaluate the mass hierarchy preference.

7.5 Systematic Errors

The same systematic errors as those introduced in [6] are used for those related to the flux of atmospheric neutrino and cross section of interaction. The errors for PC or Up-μ events are also the same as in the reference, but the systematic errors related to FC event reconstruction are evaluated with the fiTQun reconstructed samples for both conventional fiducial volume and expanded fiducial volume. The detailed description for other error sources and evaluation method can be found in [28, 120].

7.5.1 Energy Calibration

The systematic from the energy calibration is obtained by comparing of the energy scales between data and MC. To cover the whole energy range of the neutrino sample, three calibration samples: decay electrons, π^0 from atmospheric neutrino neutral current interaction and stopping cosmic ray muons are used to evaluate the absolute energy scale error. The value of the most discrepant sample is taken as the uncertainty on the absolute energy scale in the oscillation analysis. The total systematic error from the energy calibration is the quadrature-sum of absolute energy scale error and the time variation of the absolute energy scale. The total energy scale uncertainty for fiTQun within conventional FV (expanded FV) is 2.17% (2.02%), which is at the same level of that for APFit, 2.1% [6].

In addition, the uncertainty from the up/down asymmetry of the detector is also considered. It is evaluated by studying the difference on momentum distribution between data and MC of Michel electrons from cosmic ray muons with different zenith angle. The difference at the most deviated direction is taken as the uncertainty from the detector asymmetry. The uncertainty from up/down asymmetry for fiTQun within conventional FV (expanded FV) is 0.67% (0.58%), which is at the same level of that for APFit, 0.4% [6].

The detailed information can be found in Section 4.2.

7.5.2 Ring Counting, Particle Identification and Multi-GeV Multi-ring e-like Event Separation

Systematic errors on the event selection including the particle identification (PID), number of rings (ring counting), and the two-stage separation of the multi-GeV multi-ring e-like event samples are evaluated using the atmospheric neutrino data itself since no other control samples span the same energies and event topologies as the atmospheric neutrinos.

The likelihood distribution of MC is fitted to the data by shifting and smearing as:

$$L'_m = \beta^1 L_m + \beta^0, \tag{7.5}$$

where β^0 is a shift parameter that shifts the L_m distribution, while β^1 is a scale parameter that adjusts the L_m distribution to be wider (for $\beta^1 > 1$) or narrower (for $\beta^1 < 1$). The original distribution of MC is further divided into several subsamples based on MC truth information. The categorization of the subsamples is summarized in Table 7.8. An

Likelihood distribution	Subsample
Ring counting	True single-ring events, true multi-ring events
Particle ID	True $\nu_e/\bar{\nu}_e$ events, true $\nu_\mu/\bar{\nu}_\mu$ events
Multi-GeV multi-ring separation	True ν_e events, true $\bar{\nu}_e$ events, other

TABLE 7.8: Summary table of subsample categorization for different MC likelihood distribution. The true number of rings is counted using only particles with energy more than 30 MeV above Cherenkov threshold in the final states.

example of fitting the ring counting likelihood within the new region (50 cm $< D_{\text{wall}} <$ 200 cm) for the associated systematic error using true single- and multi-ring events is shown in Figure 7.26. The dashed lines represent the distribution of the subsample while the solid lines represent the overall distribution. The blue and red colors denote the distribution before and after fitting, respectively. The final fractional change in the total sample content across the threshold between before and after fitting is used as the systematic error, as shown in Figure 7.27.

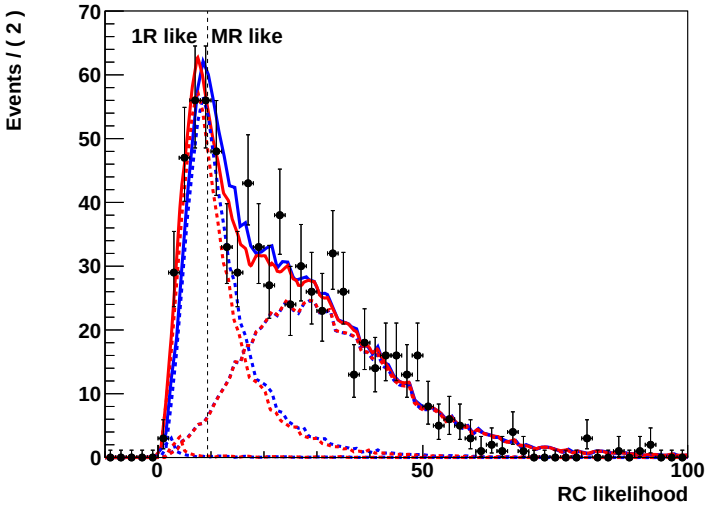

FIGURE 7.26: Ring counting likelihood distribution for multi-GeV e-like events in the new region (Dwall from 50 cm to 200 cm). The original p.d.f constructed from MC (blue line), the fitted p.d.f. (red line) and the data (points) are shown. The dashed lines show the contribution from different components: true single-ring subsample and true multi-ring sample. The true number of rings is counted using only particles with energy more than 30 MeV above Cherenkov threshold in the final states. Error bars represent the statistical error.

A Markov chain Monte Carlo method based on Metropolis-Hastings algorithm [121] is used to estimate the effect of the fitting error. The fit result in the previous step is chosen as the start point, and the $\Delta\chi^2$ from a random move is used to determine whether we accept this move. The 68.7% percentile points with larger absolute $\Delta\chi^2$ value is used as the final systematic error value (Figure 7.28).

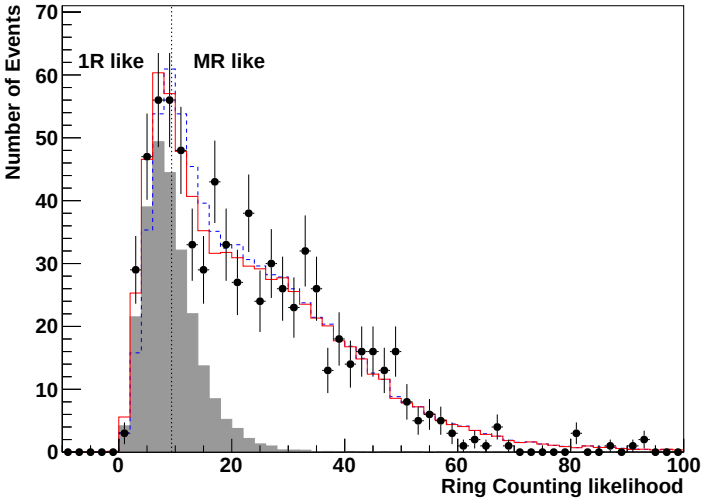

FIGURE 7.27: Ring counting likelihood distribution for multi-GeV e-like events in the new region. (dwall from 50 cm to 200 cm.) Point shows the data, and solid (dashed) line shows fitted (nominal) distribution. The dotted line is the cut line for single-ring/multi-ring event separation. The shaded histograms show the after fitting distribution for true single-ring events in final state. The term "1R" and "MR" represent "single-ring" and "multi-ring" respectively.

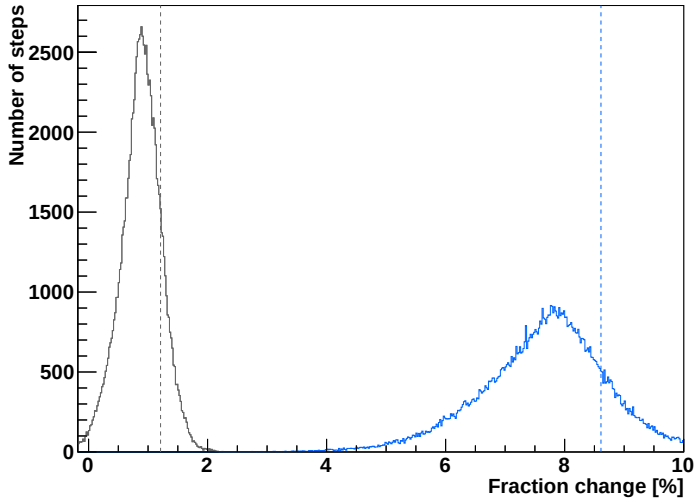

FIGURE 7.28: Fractional change of the single ring component distribution of multi-GeV e-like ring counting likelihood systematic error evaluation for conventional FV ($D_{\mathrm{wall}} > 200$ cm, black) and new region (50 cm $< D_{\mathrm{wall}} <$ 200 cm, blue). The dashed lines show the final systematic error value, which is defined as the 68.7% percentile points with larger absolute value. The systematic error in new region is larger than the one in conventional FV.

The result of systematic error evaluation of each of the FC analysis samples for both the conventional fiducial volume ($D_{\text{wall}} > 200$ cm) and the new region (50 cm $< D_{\text{wall}} < 200$ cm) are summarized in Table 7.9. The related distributions can be found in Appendix C. Errors from a particular uncertainty are assumed to be fully correlated or fully anti-correlated among all of the analysis samples. The sign of numbers in the table indicates the correlation. The systematic error from different sources is assumed to be independent from each other. In the conventional fiducial volume, the sizes of the systematic errors evaluated by fiTQun is similar or better than that for APFit. FiTQun reconstruction also shows consistent errors between the conventional fiducial volume and the new region (50 cm $< D_{\text{wall}} < 200$ cm) for many error categories, although larger systematic errors are observed for the new region in some cases: such as the ring counting uncertainty for multi-GeV single-ring events. However, the benefit to the sensitivity of neutrino oscillation by including events in the new region into the analyses outweighs this slight downside. The final coefficient (f_n^i) used in the analysis within the expanded FV is obtained by merging the numbers for the different FV regions. The sensitivity with the expanded FV and updated systematic errors is presented in Section 7.6.

7.5.3 Other Systematic Error related to Event Reconstruction

Two-ring π^0 selection

The uncertainty from two-ring π^0 events selection is estimated by considering the uncertainty from ring counting and PID for both first ring and second ring. The evaluation method for each ring is similar to the one introduced in previous section. The ring counting and PID likelihood distributions for data and MC for both rings within the expanded FV are shown in Figure 7.29. The errors for each item are summarized in Table 7.10. The final uncertainty from two-ring π^0 selection is 1.03%, which is used for both analyses within the conventional FV and the expanded FV due to the similar ring counting and PID performance within the conventional FV and the new region for sub-GeV events (Table 7.9).

Decay electron tagging

Decay electron tagging is important for the atmospheric neutrino oscillation since it is crucial for the classification between ν_e-like events and $\bar{\nu}_e$-like events, as discussed in Section 7.1.2: an event with no decay electrons would be easier to be reconstructed as $\bar{\nu}_e$-like events. The systematic error in decay electron detection efficiency is estimated

Reconstruction	fiTQun	fiTQun	APFit[6]
Dwall range	50 cm∼200 cm	> 200 cm	> 200 cm
Ring counting			
Sub-GeV , Single-ring			
e-like, p < 400 MeV	1.94%	1.20%	1.6%
e-like, p > 400 MeV	0.59%	0.48%	1.0%
μ-like, p < 400 MeV	1.08%	0.42%	-3.0%
μ-like, p > 400 MeV	1.25%	1.21%	0.6%
Sub-GeV, Multi-ring			
e-like	-3.58%	-2.39%	-1.9%
μ-like, $E_{\rm vis}$ > 600MeV	-2.32%	-1.66%	2.3%
Multi-GeV Single-ring			
e-like	8.61%	1.21%	1.0%
μ-like	2.65%	-2.33%	-1.2%
Multi-GeV Multi-ring			
e-like	-4.21%	-0.62%	-0.9%
μ-like	-3.07%	0.72%	2.4%
Particle ID of single-ring events			
Sub-GeV			
e-like	0.99%	0.36%	-0.28%
μ-like	-0.89%	-0.37%	0.22%
Multi-GeV			
e-like	0.23%	0.06%	-0.35%
μ-like	-0.21%	-0.06%	0.35%
Particle ID of the brightest ring in multi-ring events			
Sub-GeV			
e-like	-3.19%	-0.72%	4.19%
μ-like	1.31%	0.31%	-1.56%
Multi-GeV			
e-like	1.94%	1.10%	3.33%
μ-like	-1.06%	-0.66%	-1.56%
Multi-GeV Multi-ring e-like - other separation			
e-like	-0.88%	-0.67%	3.0%
other	0.50%	0.53%	-3.4%
Multi-GeV Multi-ring ν_e-like - $\bar{\nu}_e$-like separation			
ν_e-like	-3.64%	-2.33%	6.82%
$\bar{\nu}_e$-like	4.51%	2.10%	-6.04%

TABLE 7.9: Systematic errors related to the ring counting, particle identification and multi-GeV multi-ring e-like separation. The related distribution can be found in Appendix C. Errors from a particular uncertainty are assumed to be fully correlated or fully anti-correlated among all of the analysis samples. The sign of numbers in the table indicates the correlation. The systematic error from different sources is assumed to be independent from each other.

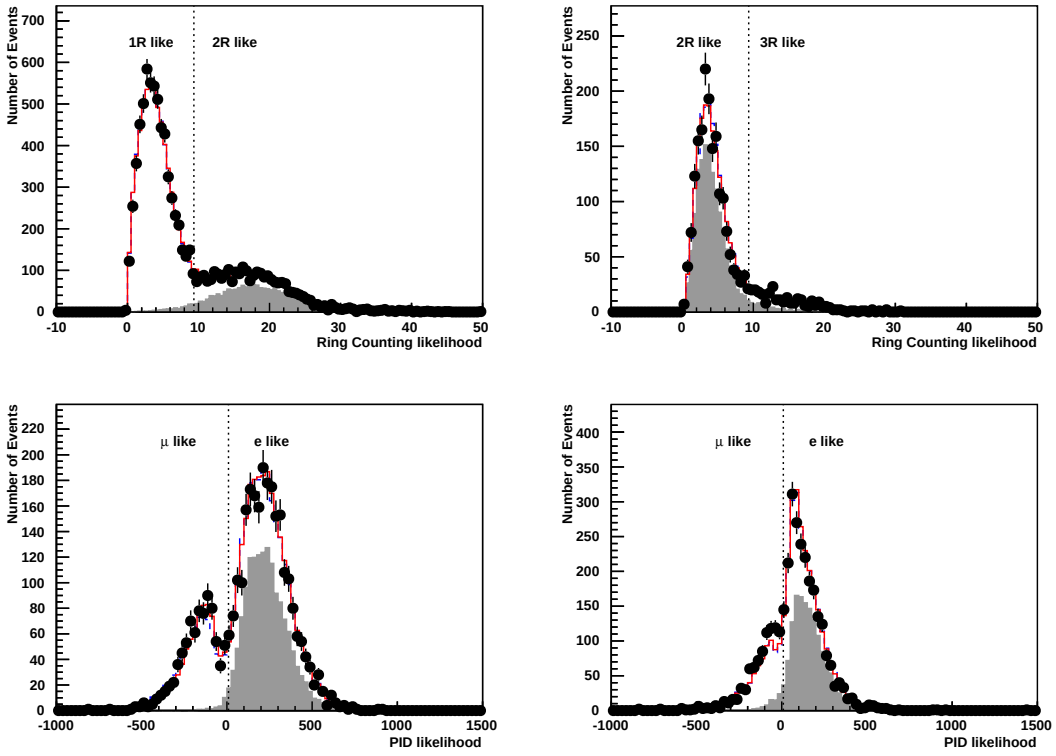

FIGURE 7.29: Likelihood distribution of ring counting (top) and PID (bottom) for both first ring (left two plots) and second ring (right two plots). Fiducial volume cut is $D_{\text{wall}} > 50$ cm. The shaded histogram show the distribution of CC $1\pi^0$ events. The solid red (dashed blue) line denote the fitted MC (nominal) while the points are for data. Error bars show the statistical uncertainty of data.

	First ring	Second ring
Ring counting	0.43%	0.12%
PID	0.27%	0.89%

TABLE 7.10: Uncertainty from two-ring π^0 event selection.

	Sub-GeV	Multi-GeV
Conventional FV ($D_{\text{wall}} > 200$ cm)	0.7%	0.7%
New region (50 cm $< D_{\text{wall}} <$ 200 cm)	0.7%	2.1%

TABLE 7.11: Uncertainty from decay electron tagging.

by comparing the number of tagged Michel electrons from cosmic ray muons data and MC. The error is summarized in Table 7.11.

Furthermore, the uncertainty from decay probability of π^+ is also considered, since it also affects the number of detected decay electrons. The decay probability of π^+ depends on whether it is scattered or not and how it is scattered, which varies as a function of its momentum. The uncertainty from π^+ interaction is estimated from the difference between experimental data and the Monte Carlo prediction, as shown in Figure 3.7.

The uncertainty of π^+ decay probability is then evaluated by generating π^+ MC with increased or decreased mean free path based on the interaction uncertainties [122]. The final uncertainty for π^+ decay electron tagging varies from 0.3% to 0.6% for FC sub-GeV single-ring e-like 0-decay sample.

7.6 Results and Discussion

7.6.1 Fit Results and Discussion with Free θ_{13}

The measurements with atmospheric neutrinos on θ_{13} represent an important test of the analysis' hierarchy preference since the appearance of upward-going electron events expected for the mass hierarchy signal is driven by θ_{13}. Due to the limited impact of the solar mixing parameters, Δm^2_{21} and $\sin^2\theta_{12}$ on the oscillations of neutrinos in the energy range considered in the analysis, they are fixed in this analysis, while their associated uncertainties are considered as systematic errors.

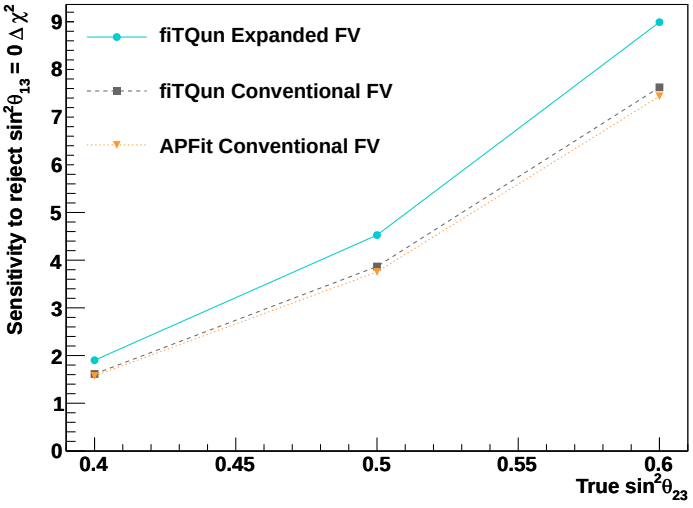

FIGURE 7.30: Expected median sensitivity of the atmospheric neutrino sample to reject a zero value of $\sin^2\theta_{13}$ with a livetime of 3118.5 days. Horizontal axis shows the assumed true value of $\sin^2\theta_{23}$. The result of the events reconstructed by fiTQun within the conventional FV and expanded FV are denoted by grey and blue lines, respectively. The sensitivity with events reconstructed by APFit and conventional FV is denoted by orange line.

The expected sensitivity to reject a zero value of $\sin^2\theta_{13}$ as a function of the true value of $\sin^2\theta_{23}$ is shown in Figure 7.30. The fiTQun-based analysis samples with both the conventional (grey dashed line) and expanded FV (blue solid line) as well as an analysis with APFit-reconstructed samples with the conventional FV (orange dotted line) are shown. Similar sensitivities for the two algorithms within the same FV are due to

Reconstruction	fiTQun	fiTQun	APFit
Dwall range	50 ∼ 200 cm	> 200 cm	> 200 cm
Single-ring			
ν_e-like	0.064	0.058	0.109
$\bar{\nu}_e$-like	0.003	0.003	0.009
Multi-ring			
ν_e-like	0.059	0.054	0.121
$\bar{\nu}_e$-like	0.023	0.021	0.040

TABLE 7.12: CC backgrounds, including CCν_μ and CC$\bar{\nu}_\mu$, in multi-GeV e-like sample.

the large fraction of common events between them: $> 97\%$ and consistency of their systematic errors. The remaining 3% difference comes from the vertex resolution near the boundary of FV. The slight boost in the sensitivity for the fiTQun-selected sample within the conventional FV, is due to the lower contamination of ν_μ events in the e-like samples, which is the most sensitive to θ_{13}, as shown in Table 7.12. More signal events are incorporated naturally by expanding the FV in the analysis and the improvement of sensitivity is therefore more significant.

Figure 7.31 and Figure 7.32 show one dimensional allowed regions for θ_{13}, $|\Delta m^2_{32,31}|$, $\sin^2\theta_{23}$ and δ_{CP} within the conventional FV and the expanded FV, respectively. A smaller χ^2 can be obtained for the normal hierarchy hypothesis than that for the inverted hierarchy hypothesis with $\chi^2_{\mathrm{NH,min}} - \chi^2_{\mathrm{IH,min}} = -1.81(-1.41)$ for the expanded (conventional) FV. The value of $\sin^2\theta_{13}$ is preferred from 0.003 to 0.033 (from 0.001 to 0.023) for the normal (inverted) hierarchy fit within 1σ. This result also disfavors a zero-value of $\sin^2\theta_{13}$ at $\sim 1.8\sigma$ ($1.2\ \sigma$) for the normal (inverted) hierarchy fit, which is consistent with the value preferred globally. Table 7.13 summarizes the best-fit information and constraints on the oscillation parameter.

As discussed in Section 1.2, upward-going electron neutrino appearance at multi-GeV energies determines both $\sin^2\theta_{13}$ and the mass hierarchy. The up-down asymmetry of the multi-GeV single- and multi-ring electron-like samples is shown in Figure 7.33. Here, the asymmetry is defined as the ratio of the difference of the number of upward-going ($\cos\theta_{\mathrm{zenith}} < -0.4$) and downward-going ($\cos\theta_{\mathrm{zenith}} > 0.4$) events relative to their sum. The normal hierarchy preference is mainly contributed by the excesses between a few and ten GeV in the multi-GeV single-ring e-like ν_e and the multi-ring e-like ν_e samples, as shown in Figure 7.34.

The best-fit atmospheric mixing parameters from the normal hierarchy fit are $\sin^2\theta_{23} = 0.588^{+0.030}_{-0.062}$ for second octant (best-fit), $0.425^{+0.051}_{-0.034}$ for first octant and $\Delta m^2_{32} = 2.63^{+0.10}_{-0.21}\times 10^{-3}\mathrm{eV}^2$. The result disfavors the maximal mixing ($\sin^2\theta_{23} = 0.5$) weakly at $\sim 1\sigma$. This

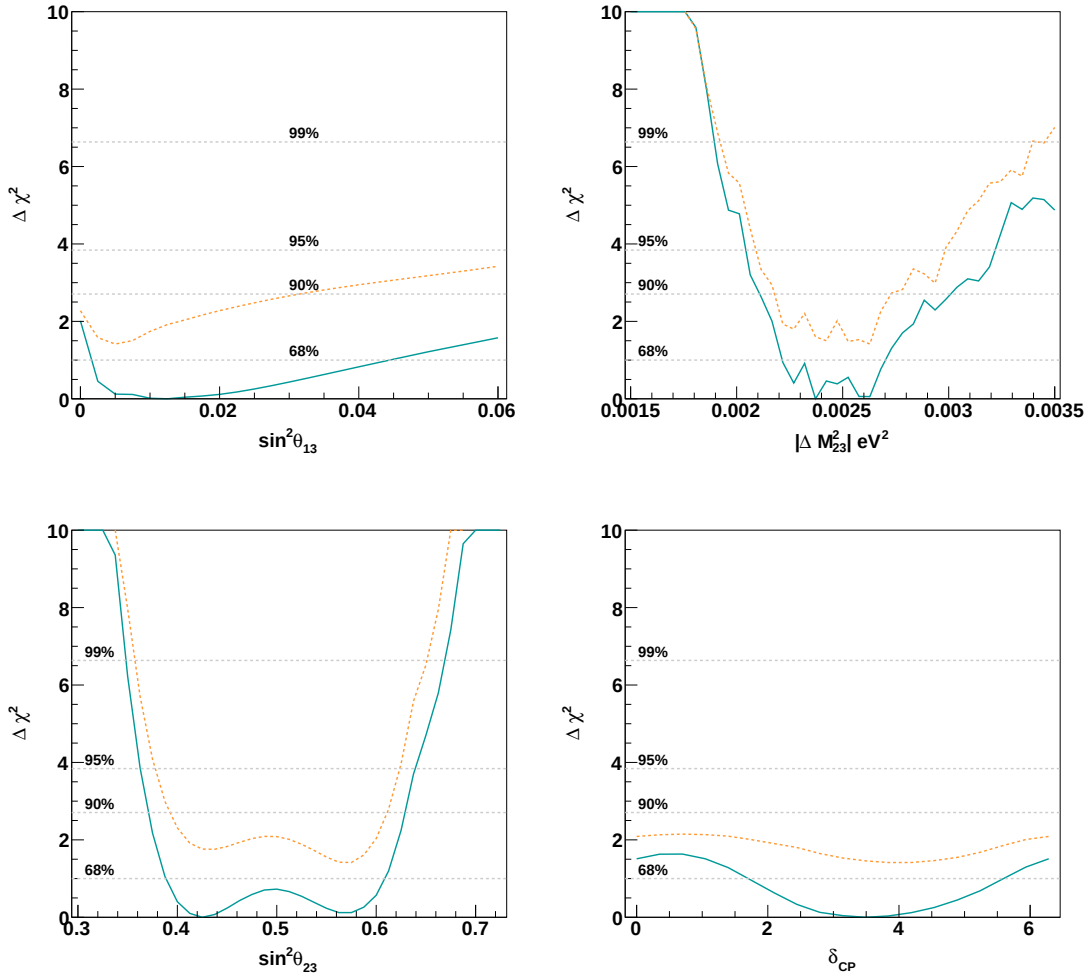

FIGURE 7.31: Difference of χ^2 value between global best fit result in this analysis and the result with the oscillation parameter shown in the horizontal axis. In these plots, no external constraints are applied and the events within conventional FV ($D_{\text{wall}} >$ 200 cm) are used. The normal hierarchy result is denoted by blue solid lines. The result of inverted hierarchy is denoted by orange dashed lines and has been offset from the normal hierarchy result by the difference of minimum χ^2 values between them.

preference is driven by the data deficits of the multi-GeV μ-like sample as well as the data excesses in the upward-going regions of the single-ring e-like $\bar{\nu}_e$ sample and multi-ring e-like ν_e sample. Since both $\sin^2\theta_{23}$ and $\sin^2\theta_{13}$ measurements feature in the $\nu_\mu \to \nu_e$ oscillation probability, as shown in Equation 1.25, the preference for these two parameters are coupled. As we will see in the next section, this coupling will affect the result of the θ_{13}-constrained analysis.

The normal (inverted) hierarchy fits show the best-fit value of δ_{CP} at 3.84 (4.19) radians. It is expected to observe more electron neutrino appearance in the sub-GeV e-like samples due to $\nu_\mu \to \nu_e$ oscillations for $\delta_{CP} = 3.84$ comparing with the least preferred δ_{CP} value of 0.8 radians. It should be noted that δ_{CP} similarly influences the amount of

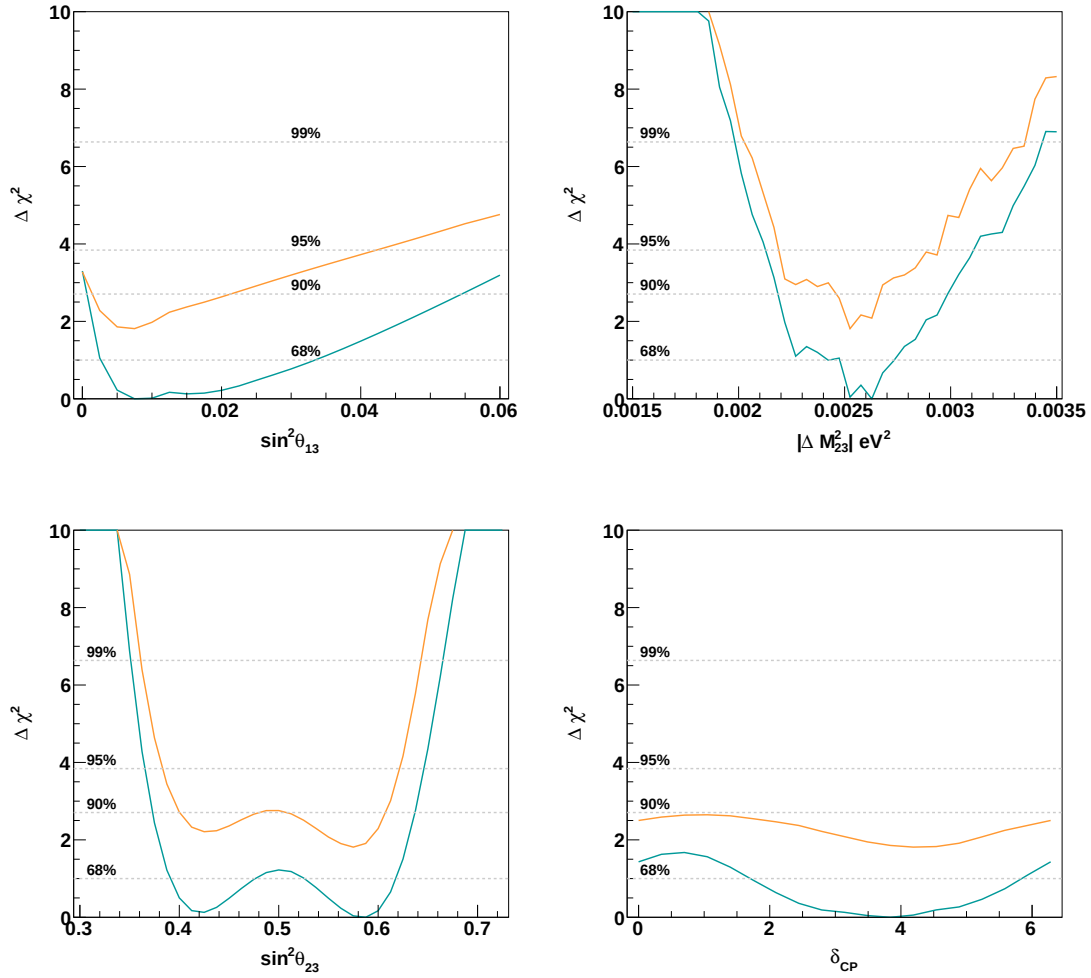

FIGURE 7.32: Difference of χ^2 value between global best fit result in this analysis and the result with the oscillation parameter shown in the horizontal axis. In these plots, no external constraints are applied and the events within expanded FV ($D_{\mathrm{wall}} > 50$ cm) are used. The normal hierarchy result is denoted by blue solid lines. The result of inverted hierarchy is denoted by orange dashed lines and has been offset from the normal hierarchy result by the difference of minimum χ^2 values between them.

electron neutrino appearance in the multi-GeV region, but its effect is subdominant to that of θ_{13}. Considering the fact that neutrinos have higher flux and interaction cross section than those of antineutrinos in the atmospheric sample, the predicted excess of upward-going e-like events is smaller for the inverted hierarchy since matter effects only influence antineutrino events in that case. The value of θ_{13} can be therefore adjusted for a better agreement between data and MC more easily, which results in a weaker constraint on δ_{CP} for the inverted hierarchy fit.

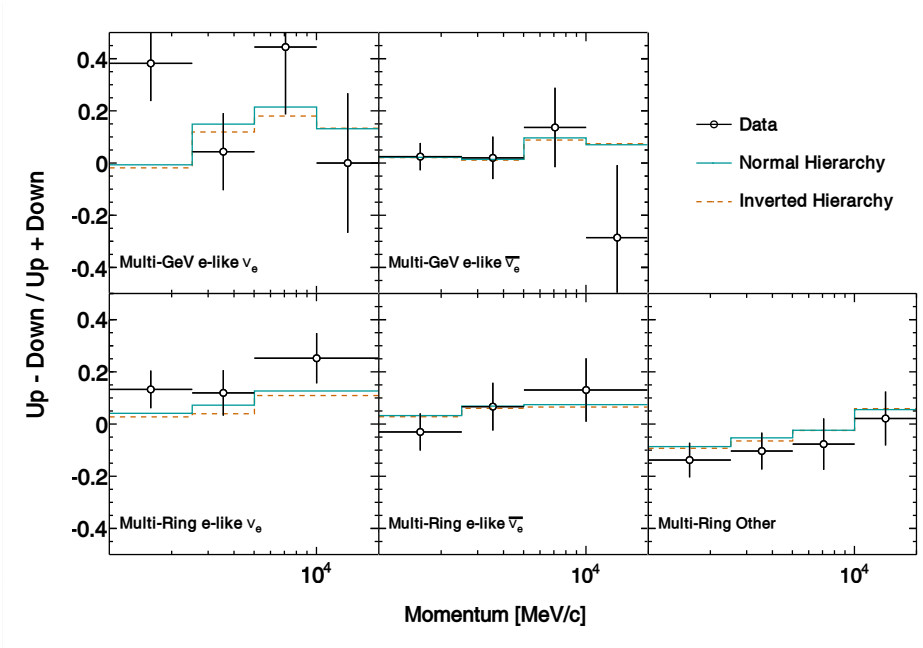

FIGURE 7.33: Upward- ($\cos\theta < -0.4$) to downward-going ($\cos\theta > 0.4$) event ratio for different momentum within expanded FV. The momentum for multi-ring event is defined as the sum of the momentum of each ring. Statistical uncertainties are denoted by the error bars. The cyan line denotes the best fit from the normal hierarchy hypothesis, and the orange line the best fit from the inverted hierarchy hypothesis.

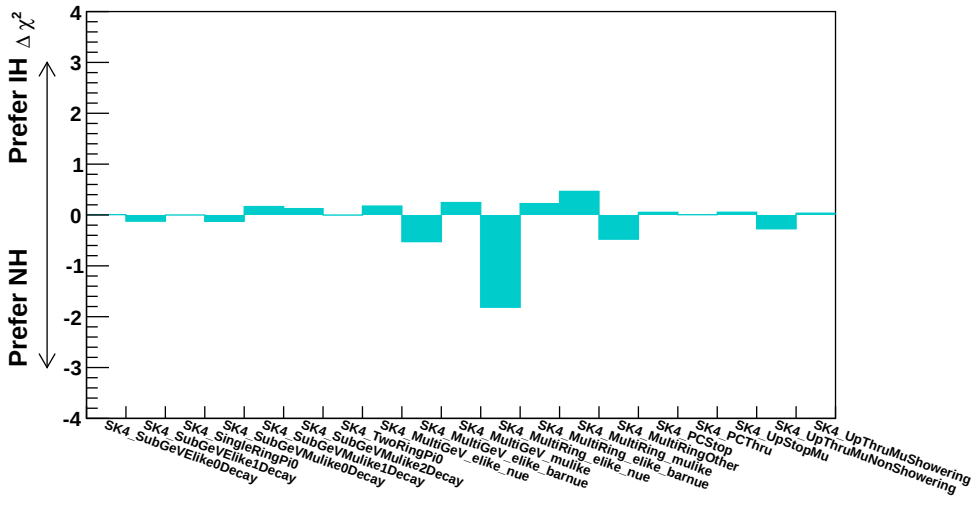

FIGURE 7.34: The preference for MH for each event types within expanded FV. The y-axis shows the difference of χ^2 between normal hierarchy (NH) and inverted hierarchy (IH) contributed by each event sample at the best-fit oscillation parameters. The definition of the vertical axis is $\Delta\chi^2 = \chi^2_{\mathrm{NH}} - \chi^2_{\mathrm{IH}}$, which means that the negative value represent the preference for the normal hierarchy.

7.6.2 Fit Results and Discussion with Constrained θ_{13}

In general, it is hard for Super-K to reconstruct the neutrino kinematics fully since atmospheric neutrinos come from all directions with a wide range of energies, and often produce particles without Cherenkov radiations. As a result, the neutrino mixing parameter sensitivity from atmospheric neutrino experiments is not at the same level as that from experiments which utilize artificial neutrino sources, such as in accelerator or reactor. As shown in Equation 1.26, the size of MSW effect directly relies on the value of $\sin^2\theta_{13}$, which is constrained by reactor neutrino experiments with high precision: $\sin^2\theta_{13} = 0.0210 \pm 0.0011$ [27]. The sensitivity to the mass hierarchy and δ_{CP} can be expected to be increased by introducing such a constraint. During the θ_{13}-constrained fit, the value of $\sin^2\theta_{13}$ is fixed at its central value 0.0210. A systematic error to reflect the impact of the uncertainty of $\sin^2\theta_{13}$ is added to the analysis. The same data samples, binning, and parameter grid for all other oscillation parameters as the analysis presented above are used in this fit.

Besides the constraint on $\sin^2\theta_{13}$ from reactor experiments, the constraint on $\sin^2\theta_{23}$ from accelerator neutrinos could also help increase the sensitivity. More details will be discussed in Chapter 8.

As shown in the Figure 7.35, the expected sensitivity to the mass hierarchy with events reconstructed by fiTQun is higher than the one with events reconstructed by APFit for all assumed values of $\sin^2\theta_{23}$. The sensitivity strengthens further after expanding FV.

The χ^2 value as a function of the atmospheric neutrino mixing parameters and δ_{CP} in the θ_{13}-constrained fit to the data is illustrated in Figure 7.36. Similar to the result of the unconstrained fit, the normal mass hierarchy is preferred with $\Delta\chi^2 = -2.45(-2.18)$ by the Super-K IV data for the expanded (conventional) FV. The fit result with the expanded FV is in good agreement with the one with the conventional FV, but shows higher significance to reject inverted hierarchy, which is consistent with the expectation from the sensitivity.

The preferred region at 1σ for $|\Delta m^2_{32}|$ is [2.41,2.75] $\times 10^{-3}\text{eV}^2$ ([2.36, 2.67] $\times 10^{-3}\text{eV}^2$) when the true mass hierarchy is assumed to be normal (inverted). This result is consistent with the one from the unconstrained fit. The jagged nature of the $|\Delta m^2_{32}|$ comes from the limited data and MC statistics in the low energy region. As shown in Equation 1.25, the oscillation probability is proportional to $\sin^2(1.27\Delta m^2_{32}L/E)$, which means that it will change drastically for a large L/E value and is therefore very sensitive to Δm^2_{32}. Therefore, without sufficient data and MC to average over these oscillations, small changes in Δm^2_{32} result in the rapid change of the χ^2, as seen in the figure.

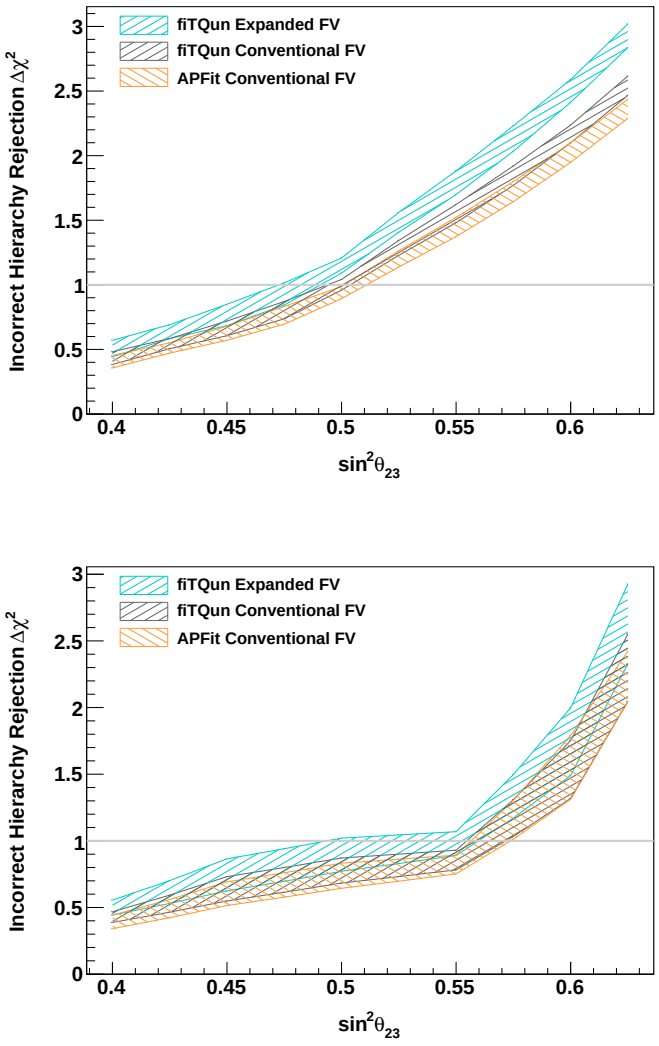

FIGURE 7.35: Expected median sensitivity with a livetime of 3118.5 days to mass hierarchy. Top figure shows the sensitivity to normal mass hierarchy and bottom figure shows the sensitivity to inverted hierarchy. Horizontal axis shows the assumed true value of $\sin^2\theta_{23}$. Here the value of $\sin^2\theta_{13}$ is fixed to 0.0210. The result of the events reconstructed by fiTQun within the conventional FV and expanded FV are denoted by the gray and blue bands. The sensitivity with events reconstructed by APFit algorithm and the conventional FV is denoted by the orange band. The bands represents the effect of the uncertainty from δ_{CP}.

Figure 7.37 shows the two-dimensional atmospheric mixing contour for the preferred regions at 90% C.L.. While the best fit value of $\sin^2\theta_{23}$ is changed to the first octant compared to both the previous Super-K analysis with APFit [6] and the unconstrained fit with fiTQun, it is within errors of the unconstrained fit and in good agreement with other measurements, as shown in Figure 7.38. Comparing with the fitting result with θ_{13}-free, the preferred value of θ_{23} shifts from the second to first octant after adding the constraint on $\sin^2\theta_{13}$, though both octants are allowed at 1σ. It is due to the degeneracy on the appearance probability for certain combinations of $\sin^2 2\theta_{13}$ and $\sin^2\theta_{23}$, as shown

in Equation 1.25. Figure 7.39 shows the preference for the $\sin^2\theta_{23}$ octant of each sample for the constrained $\sin\theta_{13}$ fit (0.02, red triangles) and the unconstrained $\sin\theta_{13}$ fit (whose best fit value is 0.0075, blue boxes). Although the preference for the second octant from multi-ring ν_e-like events is stronger for a larger $\sin\theta_{13}$ value due to the upward-going event excesses that drive the mass hierarchy preference (c.f. Figure 7.9), the multi-ring $\bar{\nu}_e$-like and μ-like samples prefer the first octant more significantly. This is because the θ_{13} and octant preferences in the unconstrained analysis cannot be supported simultaneously by the excess of ν_e and deficits of ν_μ, as shown in Figure 7.40. The data is accommodated for a larger $\sin\theta_{13}$ value by reducing the amplitude for both the excess of e-like events and the deficit of μ-like events by moving θ_{23} to the first octant. In fact, the difference in χ^2 between the minimum value of each octant is $\Delta\chi^2_{1^{st}-2^{nd}}$ = -0.73 (0.13) for the constrained (unconstrained) fit. The preference for both octant is weak, as we will discuss below.

The fit result of δ_{CP} is consistent with the result of the unconstrained fit but a tighter constraint is obtained: the 1σ allowed region is [1.79, 5.81] ([0, 0.12] $\cup$ [1.43, 6.28]) for the normal (inverted) hierarchy. Table 7.13 shows the best-fit oscillation parameter values and their 1σ errors.

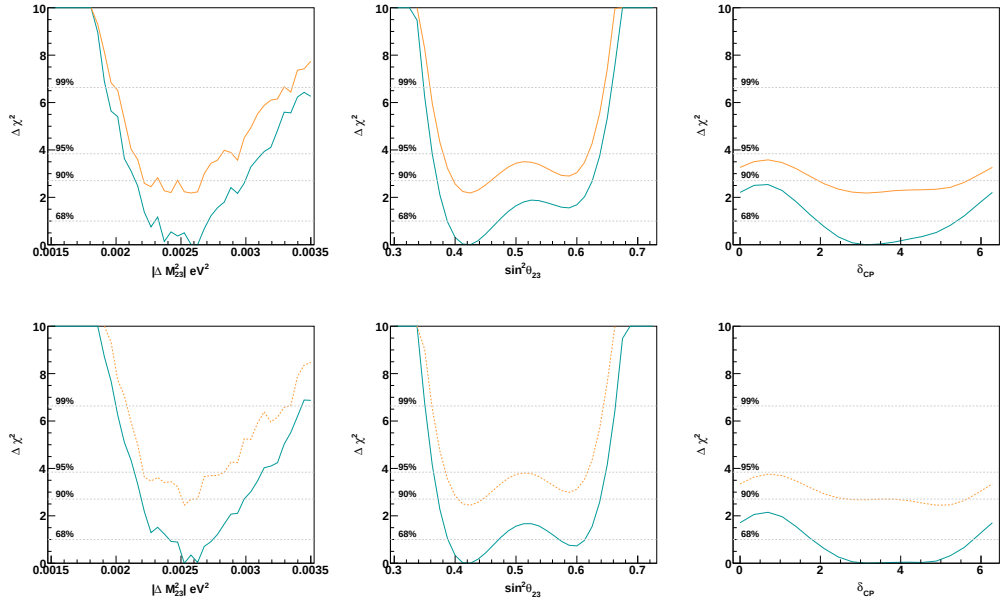

FIGURE 7.36: Difference of χ^2 value between global best fit result in this analysis and the result with the oscillation parameter shown in the horizontal axis. In these plots, no external constraints are applied. Top three figures show the result within conventional FV ($D_{\text{wall}} > 200$ cm) and bottom three figures show the result within expanded FV ($D_{\text{wall}} > 50$ cm). The normal hierarchy result is denoted by blue solid lines. The result of inverted hierarchy is denoted by orange dashed lines and has been offset from the normal hierarchy result by the difference of minimum χ^2 values between them.

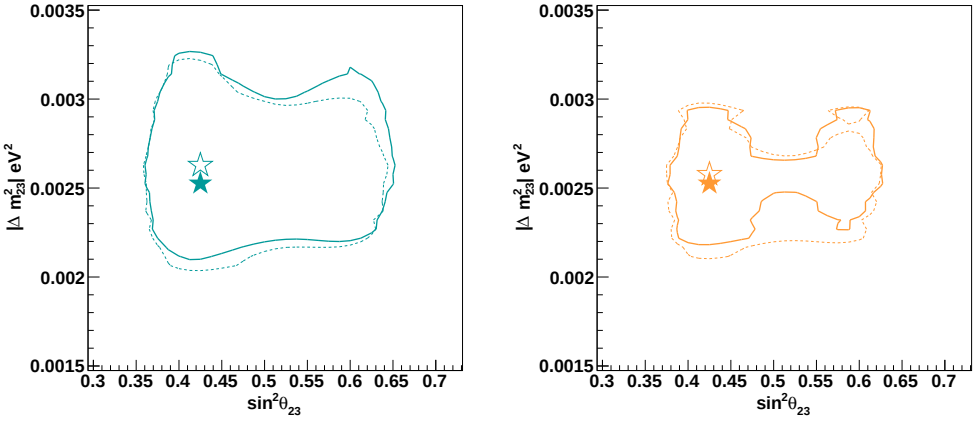

FIGURE 7.37: Two-dimensional atmospheric mixing contour for the preferred regions at 90% C.L.. The left (right) figure shows 90% C.L. for the normal (inverted) hierarchy. The solid line denotes the fit result within expanded FV while the dashed line is for the result within conventional FV. The full (open) star denotes the best-fit value for expanded FV (conventional FV). In each contour $\sin^2\theta_{13}$ is fixed to 0.0210. Both contours have been drawn with respect to the global best-fit for each FV.

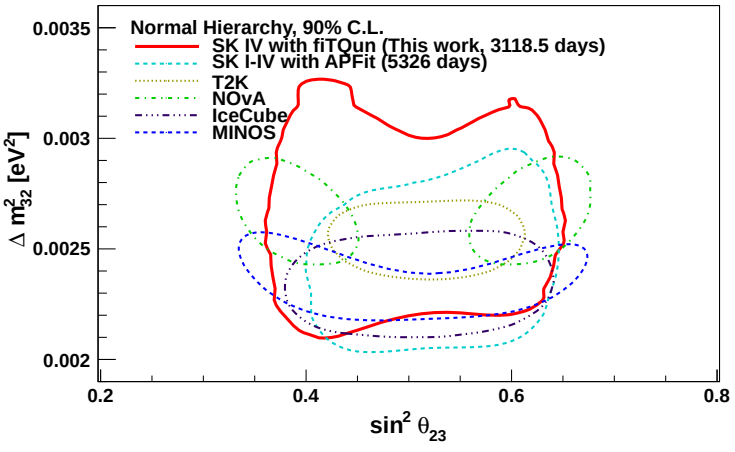

FIGURE 7.38: Constraints on neutrino oscillation contours at the 90% C.L. from analyses assuming the normal mass hierarchy. The contour from Super-K IV with fiTQun (red) is taken from the analysis with $\sin^2\theta_{13}$ constrained to be 0.0210 ± 0.0011. Contours from the Super-K I-IV with APFit (dashed cyan) [6], T2K (dotted yellow) [22], NOvA (dashed green) [23], IceCube (dashed black) [24] and MINOS+ (dashed blue) [25] experiments are also shown.

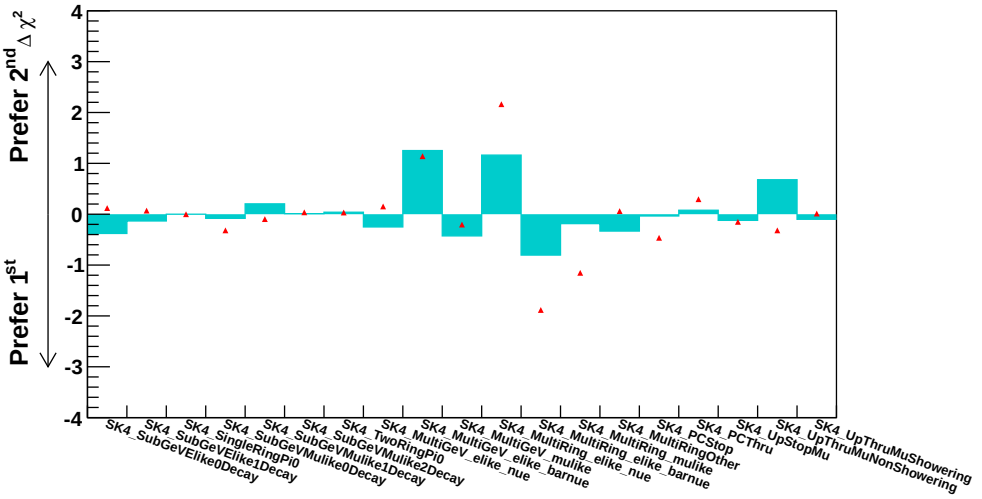

FIGURE 7.39: Distributions of the $\Delta\chi^2$ for octant preference $(\chi^2_{\sin^2\theta_{23}=0.4} - \chi^2_{\sin^2\theta_{23}=0.6})$ for each sample. Blue boxes represents the fit result with $\sin\theta_{13}$ free, whose the best-fit value is 0.0075, while the red triangles show the fit result with $\sin\theta_{13}$ fixed to 0.02.

Fit within conventional FV Hierarchy	θ_{13} Free NH	θ_{13} Free IH	θ_{13} Constrained NH	θ_{13} Constrained IH
χ^2	540.9	542.3	541.0	543.2
$\sin^2\theta_{13}$	$0.013^{+0.032}_{-0.011}$	$0.005^{+0.018}_{-0.005}$	–	–
$\sin^2\theta_{23}$ (1^{st} oct.)	$\boxed{0.425^{+0.075}_{-0.036}}$	$0.438^{+0.062}_{-0.040}$	$\boxed{0.425^{+0.046}_{-0.038}}$	$\boxed{0.425^{+0.057}_{-0.037}}$
$\sin^2\theta_{23}$ (2^{nd} oct.)	$0.563^{+0.046}_{-0.063}$	$\boxed{0.575^{+0.031}_{-0.075}}$	Excluded in 1σ	$0.588^{+0.016}_{-0.034}$
$\lvert\Delta m^2_{32,31}\rvert$ [$\times 10^{-3}$ eV^2]	$2.37^{+0.33}_{-0.16}$	$2.63^{+0.07}_{-0.44}$	$2.63^{+0.08}_{-0.38}$	$2.58^{+0.12}_{-0.39}$
δ_{CP}	$3.49^{+1.80}_{-1.79}$	$3.84^{+2.44}_{-3.84}$	$3.14^{+2.25}_{-1.21}$	$3.14^{+3.05}_{-1.71}$
Fit within expanded FV Hierarchy	θ_{13} Free NH	θ_{13} Free IH	θ_{13} Constrained NH	θ_{13} Constrained IH
χ^2	576.3	578.1	576.5	579.0
$\sin^2\theta_{13}$	$0.008^{+0.025}_{-0.005}$	$0.008^{+0.015}_{-0.007}$	–	–
$\sin^2\theta_{23}$ (1^{st} oct.)	$0.425^{+0.051}_{-0.034}$	$0.425^{+0.075}_{-0.027}$	$\boxed{0.425^{+0.046}_{-0.037}}$	$\boxed{0.425^{+0.055}_{-0.036}}$
$\sin^2\theta_{23}$ (2^{nd} oct.)	$\boxed{0.588^{+0.030}_{-0.062}}$	$\boxed{0.575^{+0.034}_{-0.075}}$	$0.600^{+0.013}_{-0.030}$	$0.588^{+0.022}_{-0.037}$
$\lvert\Delta m^2_{32,31}\rvert$ [$\times 10^{-3}$ eV^2]	$2.63^{+0.10}_{-0.21}$	$2.53^{+0.14}_{-0.08}$	$2.53^{+0.22}_{-0.12}$	$2.53^{+0.14}_{-0.31}$
δ_{CP}	$3.84^{+2.00}_{-2.14}$	$4.19^{+2.09}_{-4.19}$	$3.14^{+2.67}_{-1.35}$	$4.89^{+1.51}_{-3.46}$

TABLE 7.13: Best-fit result of oscillation parameter for each analysis. The term "NH" ("IH") refers to the fit assuming normal (inverted) hierarchy. The fits without and with a constraint on $\sin^2\theta_{13}$ are termed as "Free" and "Constrained", respectively. The best-fit result of $\sin^2\theta_{23}$ in both octants are shown, with the best-fit octant enclosed in a box.

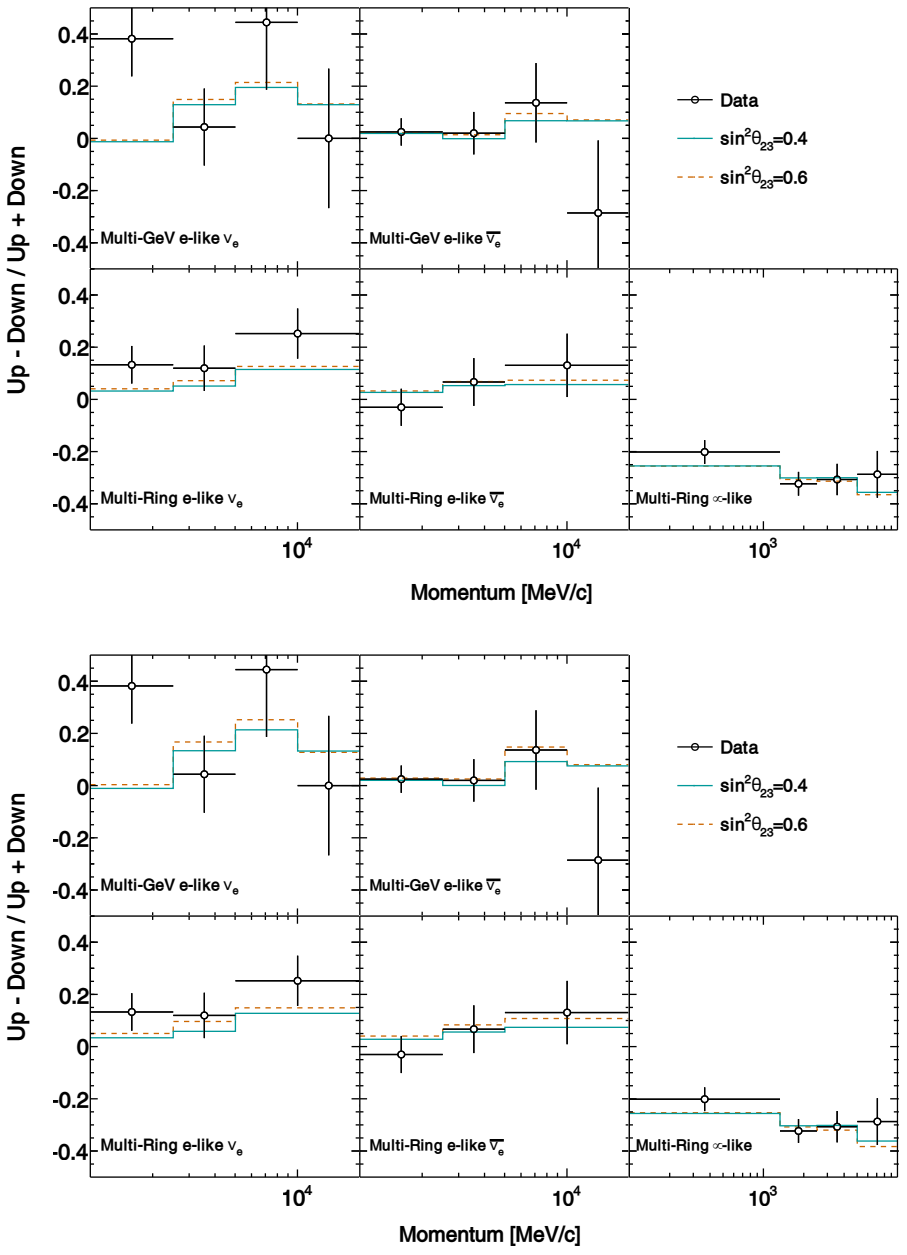

FIGURE 7.40: Upward- ($\cos\theta < -0.4$) to downward-going ($\cos\theta > 0.4$) event ratio as a function of energy for expanded FV. Statistical error are denoted by the error bars. For the multi-ring samples the momentum is defined as the sum of each ring's momentum. The cyan line denotes the best fit when $\sin^2\theta_{23} = 0.4$, and the orange line the best fit when $\sin^2\theta_{23} = 0.6$. Top five plots show the result when $\sin^2\theta_{13} = 0.0075$, which is the best-fit value in the $\sin^2\theta_{13}$-free analysis, while the bottom ones show the result when $\sin^2\theta_{13} = 0.02$, which is the global best-fit value.

Note that the absolute χ^2 value increased from around 540 to 576 after expanding the fiducial volume, which means worse agreement between data and best-fit MC since the number of degrees of freedom in the fit have not changed. To validate the fit result, MC ensembles were generated at the best-fit point with statistical and systematic error variations applied. Statistical variations is estimated based on the current detector exposure, and systematic errors have been varied according to Gaussian distribution with the deviation parameter specified by their uncertainties (σ in Equation 7.3).

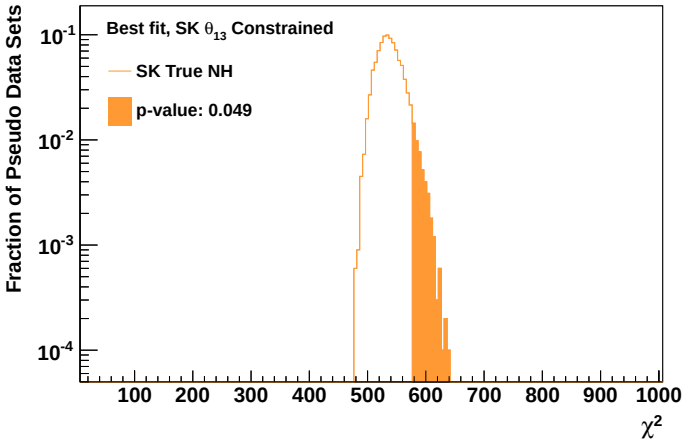

FIGURE 7.41: Distributions of the best-fit χ^2 values fits to pseudo data sets. The pseudo data have been generated with the best-fit value in NH expanded FV θ_{13} constrained fit shown in Table 7.13. Shaded portions of the histograms denote the fraction of pseudo data sets with more extreme values than that observed in the data, $\chi^2_{NH} = 576.5$.

Figure 7.41 shows the distribution of the best-fit χ^2 values fit to MC ensembles. During the pseudo data generation, only the events in the new region (50 cm $< D_{\text{wall}} <$ 200 cm) were generated with fluctuations and then merged with the observed data within the conventional FV ($D_{\text{wall}} > 200$ cm). The p-value for observing a χ^2 greater than that seen in the data, 576.5, is 0.049. Figure 7.42 shows the absolute χ^2 distribution for each event category. The error bar of pseudo data (blue box) represents one σ uncertainty from statistical fluctuations and systematic error. The observed data in this analysis is shown by red triangle. The top two categories which have the largest deviation from pseudo data center value are sub-GeV e-like 0 decay sample and multi-GeV single-ring ν_e-like sample. The zenith angle distributions for both two samples are shown in Figure 7.43 and Figure 7.44. Those events were also checked by eye-scanning and no abnormal was observed. As a conclusion, there is no issue observed in the oscillation analysis with the expand FV. More statistical validation can be found in Appendix D.

The systematic errors used and their best-fit values in the $\sin^2\theta_{13}$-constrained analysis have been discussed in Section 7.5 and summarized in Table 7.14. The best-fit values of

the systematic parameters are within 1.5 standard deviations of their priors.

TABLE 7.14: Summary of the systematic error used in this analysis. The best-fit value of the systematic error parameter in percent is shown in second column. The estimated 1σ error size in percent is shown in third column. The result of the $\theta_{13}-$*constrained* fit within expanded FV is shown here.

Systematic Error			Fit Value (%)	σ (%)
Flux normalization	$E_\nu < 1$ GeV[1]		7.3	25
	$E_\nu > 1$ GeV[2]		9.6	15
$(\nu_\mu + \bar{\nu}_\mu)/(\nu_e + \bar{\nu}_e)$	$E_\nu < 1$ GeV		1.3	2
	$1 < E_\nu < 10$ GeV		2.7	3
	$E_\nu > 10$ GeV[3]		6.6	5
$\bar{\nu}_e/\nu_e$	$E_\nu < 1$ GeV		−1.1	5
	$1 < E_\nu < 10$ GeV		−2.7	5
	$E_\nu > 10$ GeV[4]		−0.34	8
$\bar{\nu}_\mu/\nu_\mu$	$E_\nu < 1$ GeV		0.36	2
	$1 < E_\nu < 10$ GeV		3.24	6
	$E_\nu > 10$ GeV[5]		9.2	15
Up/down ratio	< 400 MeV	e-like	0.079	0.1
		μ-like	0.24	0.3
		0-decay μ-like	0.87	1.1
	> 400 MeV	e-like	0.63	0.8
		μ-like	0.40	0.5
		0-decay μ-like	1.34	1.7
	Multi-GeV	e-like	0.55	0.7
		μ-like	0.16	0.2
	Multi-ring Sub-GeV	e-like	0.32	0.4
		μ-like	0.16	0.2
	Multi-ring Multi-GeV	e-like	0.24	0.3
		μ-like	0.16	0.2
	PC		0.16	0.2
Horizontal/vertical ratio	< 400 MeV	e-like	−0.023	0.1
		μ-like	−0.023	0.1
		0-decay μ-like	−0.069	0.3
	> 400 MeV	e-like	−0.32	1.4
		μ-like	−0.44	1.9
		0-decay μ-like	−0.32	1.4
	Multi-GeV	e-like	−0.74	3.2

Continued on next page

Table 7.14 – *Continued from previous page*

Systematic Error			Fit Value (%)	σ (%)
		μ-like	−0.53	2.3
	Multi-ring Sub-GeV	e-like	−0.32	1.4
		μ-like	−0.30	1.3
	Multi-ring Multi-GeV	e-like	−0.64	2.8
		μ-like	−0.35	1.5
	PC		−0.39	1.7
K/π ratio in flux calculation[6]			−5.3	10
Neutrino path length			−2.3	10
Sample-by-sample	FC Multi-GeV		−0.22	5
	PC + Stopping UP-μ		2.46	5
Matter effects			0.06	6.8
Solar Activity			0.31	7
M_A in QE			−4.79	10
Single π Production, Axial Coupling			−7.03	10
Single π Production, C_{A5}			9.33	10
Single π Production, BKG			−3.03	10
CCQE cross section[7]			7.37	10
CCQE $\bar{\nu}/\nu$ ratio[7]			4.81	10
CCQE μ/e ratio[7]			−2.74	10
DIS cross section			5.72	10
DIS model comparisons[8]			4.84	10
DIS Q^2 distribution (high W)[9]			−5.70	10
DIS Q^2 distribution (low W)[9]			−9.21	10
Coherent π production			−9.41	100
NC/CC			−0.10	20
ν_τ cross section			9.08	25
Single π production, $\pi^0/\pi^\pm$			1.75	40
Single π production, $\bar{\nu}_i/\nu_i$ (i=e, μ)[10]			2.30	10
NC fraction from hadron simulation			−5.07	10
π^+ decay uncertainty Sub-GeV 1-ring				
	e-like 0-decay		−0.050	0.6
	μ-like 0-decay		−0.066	0.8
	e-like 1-decay		−0.34	4.1
	μ-like 1-decay		−0.025	0.3
	μ-like 2-decay		−0.47	5.7
Final state and secondary interactions[11]				

Continued on next page

Table 7.14 – *Continued from previous page*

Systematic Error			Fit Value (%)	σ (%)
	1-ring		−6.83	10
	Multi-ring		6.93	10
Meson exchange current[12]			1.08	10
Δm^2_{21} [27]			0.0	0.0002
$\sin^2(\theta_{12})$ [27]			0.05	1.3
$\sin^2(\theta_{13})$ [27]			0.00	0.11
FC reduction			0.27	1.3
PC reduction			−0.26	1
FC/PC separation			0.000	0.02
PC stopping/through-going separation (bottom)			−1.75	6.8
PC stopping/through-going separation (barrel)			1.13	8.5
PC stopping/through-going separation (top)			−29.0	40
Non-ν background	Sub-GeV μ-like		−0.001	0.02
	Multi-GeV μ-like		−0.002	0.07
	Sub-GeV 1-ring 0-decay μ-like		−0.001	0.02
	PC		−0.015	0.49
	Sub-GeV e-like (flasher event)		−0.000	0.03
	Multi-GeV e-like (flasher event)		−0.001	0.07
Fiducial Volume			−0.40	2.00
Ring separation	$<$ 400 MeV	e-like	−0.44	−0.86
		μ-like	0.43	0.84
	$>$ 400 MeV	e-like	0.19	0.37
		μ-like	1.03	2
	Multi-GeV	e-like	1.32	2.57
		μ-like	−0.74	−1.44
	Multi-ring Sub-GeV	e-like	−0.42	−0.82
		μ-like	0.42	0.82
	Multi-ring Multi-GeV	e-like	−0.66	−1.28
		μ-like	0.59	1.14
Particle identification (1 ring)				
	Sub-GeV	e-like	−0.11	0.52
		μ-like	0.10	−0.49
	Multi-GeV	e-like	−0.02	0.09
		μ-like	0.02	−0.09
Particle identification (multi-ring)				
	Sub-GeV	e-like	0.29	−1.33

Continued on next page

Table 7.14 – *Continued from previous page*

Systematic Error			Fit Value (%)	σ (%)
		μ-like	−0.12	0.53
	Multi-GeV	e-like	−0.27	1.25
		μ-like	0.16	−0.73
Multi-ring likelihood selection	Multi-ring e-like	ν_e,$\bar{\nu}_e$	−0.42	−0.71
	Multi-ring Other		0.32	0.52
Energy calibration			−0.24	2.02
Up/down asymmetry energy calibration			−0.53	0.67
UP-μ reduction	Stopping		0.048	0.5
	Through-going		0.029	0.3
UP-μ stopping/through-going separation			0.018	0.6
Energy cut for stopping UP-μ			0.30	1.7
Path length cut for through-going UP-μ			−0.33	1.5
Through-going UP-μ showering separation			3.26	3
Background subtraction for UP-μ				
	Stopping[13]		−4.9	11
	Non-showering[13]		2.3	17
	Showering[13]		−6.55	24
$\nu_e/\bar{\nu}_e$ Separation			1.89	2.57
Sub-GeV 2-ring π^0			−0.039	1.03
Decay-e tagging			0.29	0.7
FC stopping muon subtraction			89.2	67

The significance of the preferences for the θ_{23} octant and the mass hierarchy in this analysis is addressed with the CL_s method [128]. The definition of the CL_s^O for the θ_{23}

[1] Uncertainty decreases linearly with $\log E_\nu$ from 25 %(0.1 GeV) to 7 %(1 GeV).
[2] Uncertainty is 7 % up to 10 GeV, linearly increases with $\log E_\nu$ from 7 %(10 GeV) to 12 %(100 GeV) and then to 20 %(1 TeV)
[3] Uncertainty linearly increases with $\log E_\nu$ from 5 %(30 GeV) to 30 %(1 TeV).
[4] Uncertainty linearly increases with $\log E_\nu$ from 8 %(100 GeV) to 20 %(1 TeV).
[5] Uncertainty linearly increases with $\log E_\nu$ from 6 %(50 GeV) to 40 %(1 TeV).
[6] Uncertainty increases linearly from 5% to 20% between 100GeV and 1TeV.
[7] Difference from the Nieves [123] model is set to 1.0
[8] Difference from CKMT [124] parametrization is set to 1.0
[9] Difference from GRV98 [125] is set to 1.0
[10] Difference from the Hernandez[126] model is set to 1.0
[11] Ref. [127]
[12] Difference from NEUT without model from [123] is set to 1.0
[13] The uncertainties in BG subtraction for upward-going muons are only for the most horizontal bin, $-0.1 < \cos\theta < 0$.

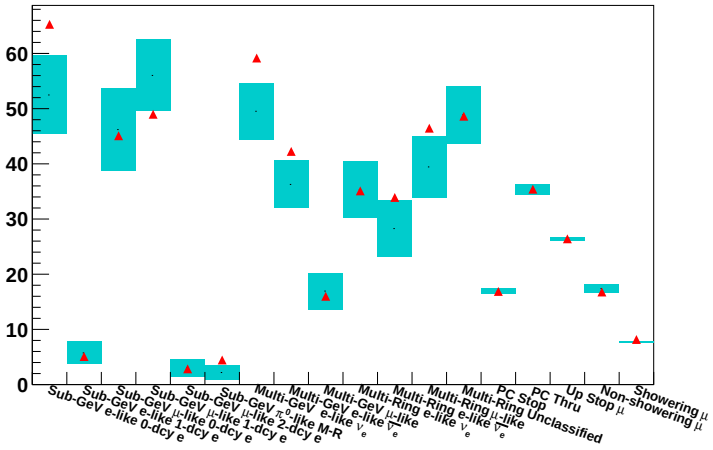

FIGURE 7.42: Distributions of the best-fit χ^2 of observed data (red triangle) and pseudo data sets (blue box). The error bar of pseudo data sets result represents the 1σ uncertainty from statistical fluctuations and systematic errors. The pseudo data have been generated with the best-fit value in NH expanded FV θ_{13} constrained fit shown in Table 7.13. The variation shows the effect of the statistical fluctuations of the new region (50 cm $< D_{\text{wall}} <$ 200 cm).

octant study is as:

$$\text{CL}_s^{\text{O}} = \frac{p_0(O_2)}{1 - p_0(O_1)}, \tag{7.6}$$

Here, O_1 and O_2 represent the hypotheses with the first octant ($\sin^2\theta_{23} = 0.4$) and the second octant ($\sin^2\theta_{23} = 0.6$), respectively. The χ^2 values of the best-fit result with the first octant hypothesis (O_1) and the second octant hypothesis (O_2) are defined as $\chi^2_{O_1}$ and $\chi^2_{O_2}$, respectively. The value of $p_0(O_1)$ represents p-value with respect to obtaining a value of $\Delta\chi^2_{O_1-O_2} := \chi^2_{O_1} - \chi^2_{O_2}$ larger than the value of data under the hypothesis with the first octant. The definition of $p_0(O_2)$ is similar, but the p-value is calculated with respected to obtaining a smaller value than the observation. Figure 7.45 shows the pseudo MC distributions of both octant and both hierarchies hypotheses. The shaded histograms show the definition of $p_0(O_i)$. The second octant is disfavored at 90.2% and 69.5% for the normal and inverted hierarchies, respectively, which means that no strong preference for the octant is observed.

The parameter CL_s^{H} for the mass hierarchy is defined in the same way, as

$$\text{CL}_s^{\text{H}} = \frac{p_0(\text{IH})}{1 - p_0(\text{NH})}, \tag{7.7}$$

which just replaces the hypothesis of the first octant (O_1) and the second octant (O_2) used in Equation 7.6 with the normal hierarchy (NH) and the inverted hierarchy (IH).

The distribution for the mass hierarchy CL_s^{H} calculation is shown in Figure 7.46. As

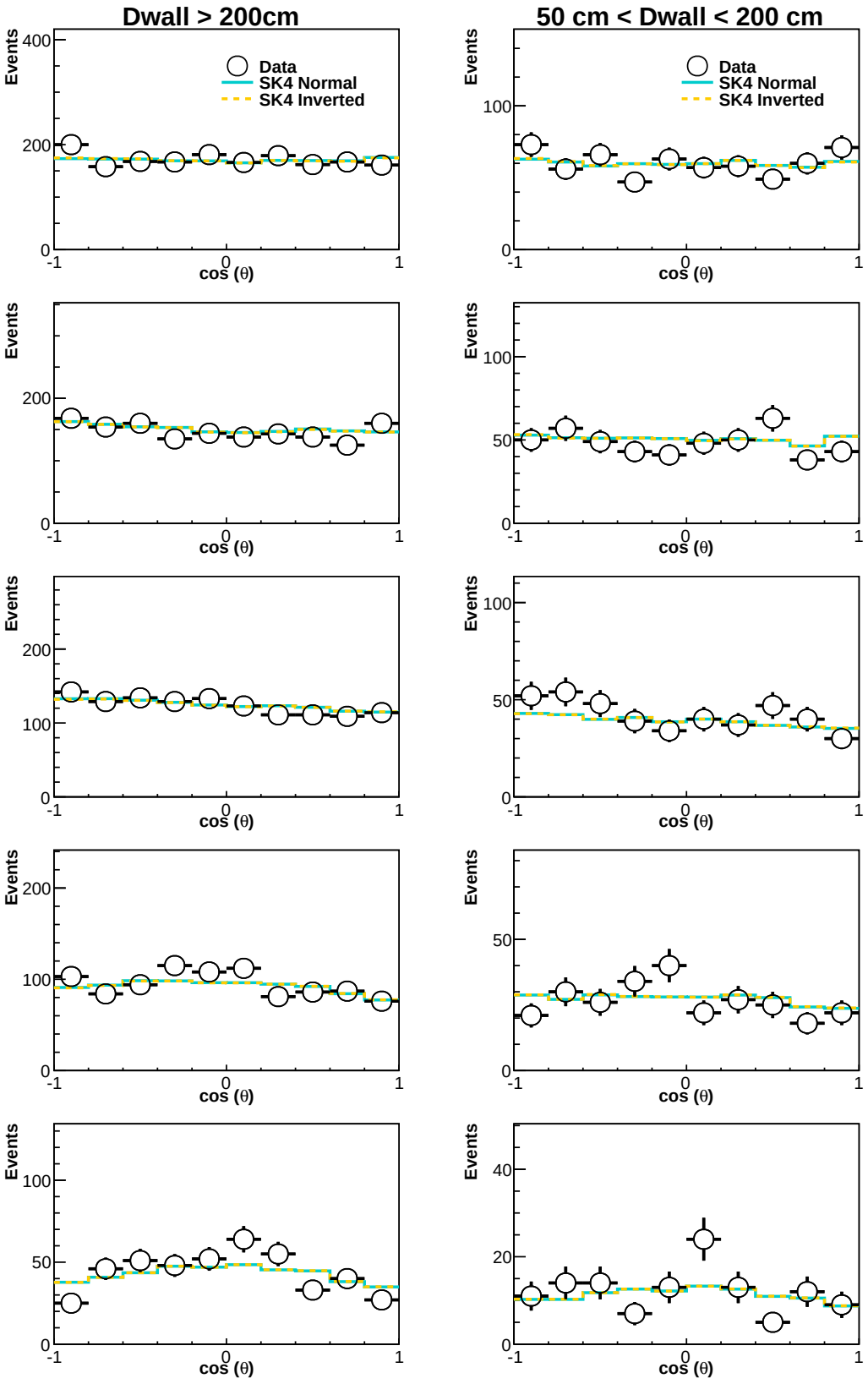

FIGURE 7.43: Zenith angle distributions for of data (open circle) and best-fit MC for both NH (blue solid line) and IH (orange dashed line). Sub-GeV single ring e-like 0-decay electron events are shown here. Left figures are for conventional FV ($D_{\mathrm{wall}} >$ 200) cm, while right figures are for new region (50 cm $< D_{\mathrm{wall}} <$ 200 cm). The momentum range are 100 MeV $\sim$ 200 MeV, 200 MeV $\sim$ 300 MeV, 300 MeV $\sim$ 600 MeV, 600 MeV $\sim$ 1000 MeV, 1000 MeV $\sim$ 1330 MeV from most top figures, respectively.

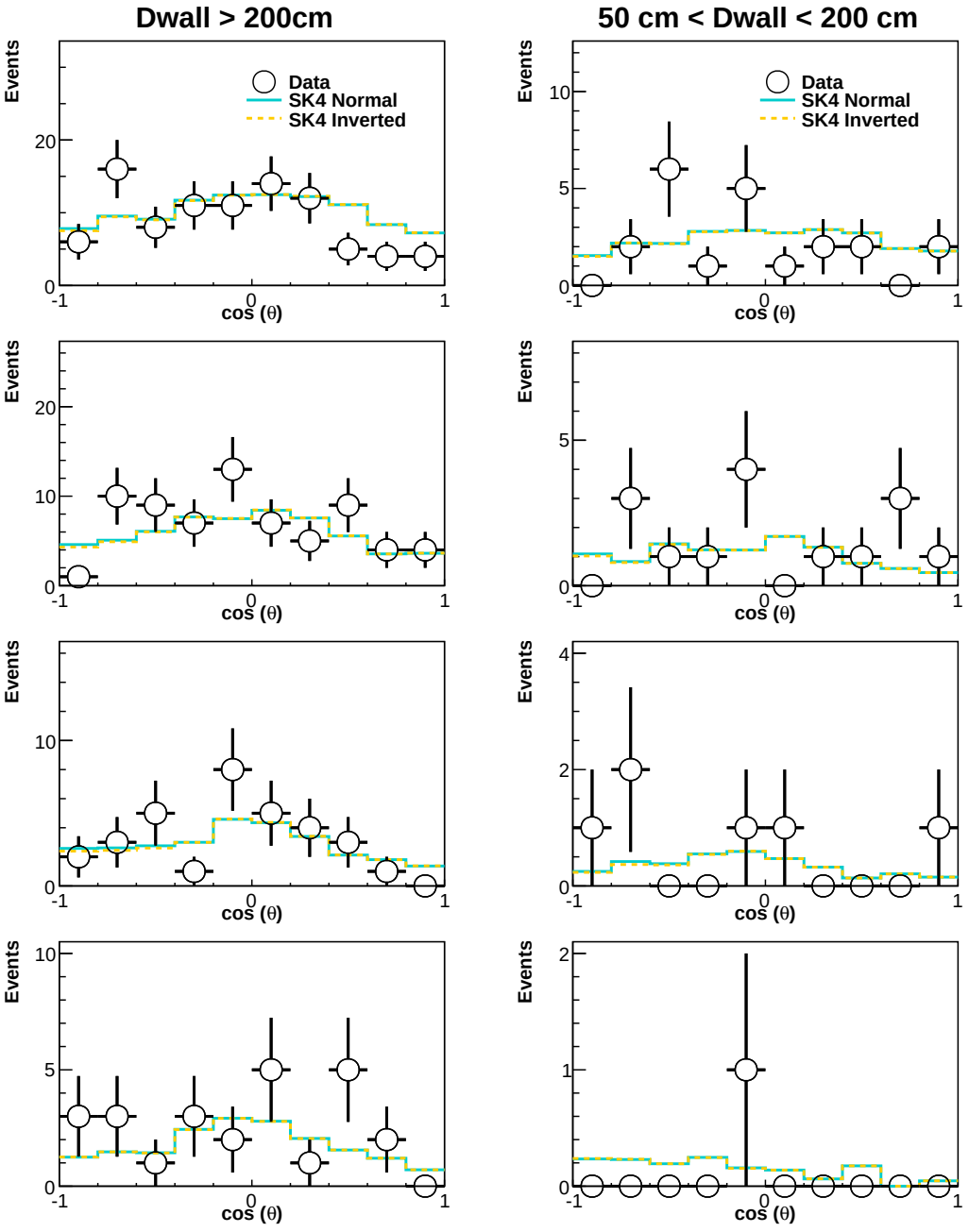

FIGURE 7.44: Zenith angle distributions for of data (open circle) and best-fit MC for both NH (blue solid line) and IH (orange dashed line). Multi-GeV single ring ν_e-like events are shown here. Left figures are for conventional FV ($D_{\rm wall} > 200$) cm, while right figures are for new region (50 cm $< D_{\rm wall} <$ 200 cm). The momentum range are 1000 MeV $\sim$ 2500 MeV, 2500 MeV $\sim$ 5000 MeV, 5000 MeV $\sim$ 10000 MeV, >10000 MeV from most top figures, respectively.

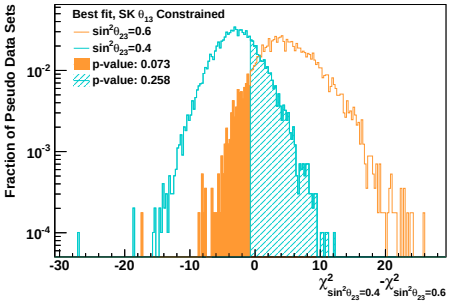

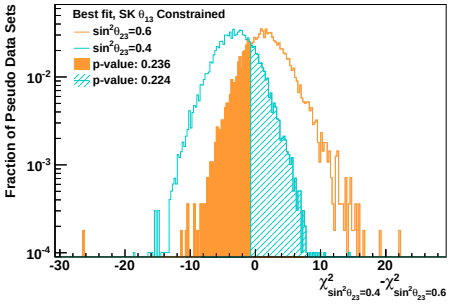

FIGURE 7.45: Distributions of the difference in best-fit χ^2 values assuming the first octant ($\sin^2\theta_{23} = 0.4$) and second octant ($\sin^2\theta_{23} = 0.6$). The value of $\sin^2\theta_{13}$ is fixed to 0.0210 and expanded FV are used. The result of pseudo data generated assuming $\sin^2\theta_{23} = 0.4$ ($\sin^2\theta_{23} = 0.6$) is shown as the cyan (orange) histogram. The left figure shows the true NH case, while the right figure show the true IH case. The calculation of p-value to obtain a value of $\Delta\chi^2$ more extreme than the observed value, $\Delta\chi^2_{data} = -0.73$, is according to the shaded histogram.

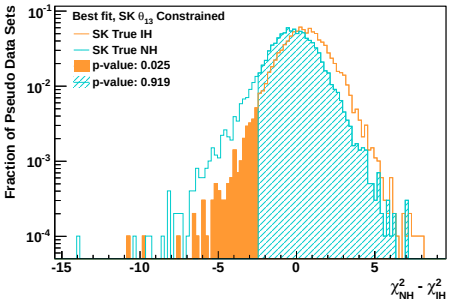

(a) True $\sin^2\theta_{23} = 0.4$

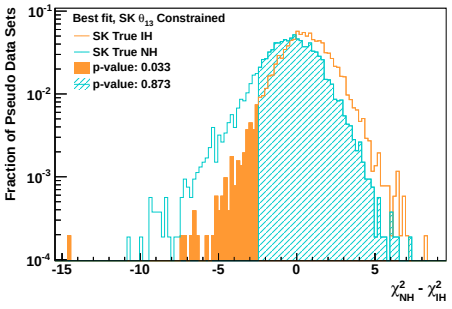

(b) True $\sin^2\theta_{23} = 0.425$ (best fit)

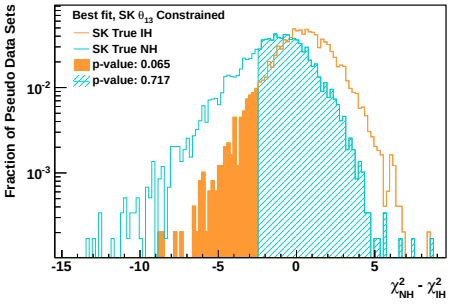

(c) True $\sin^2\theta_{23} = 0.5$

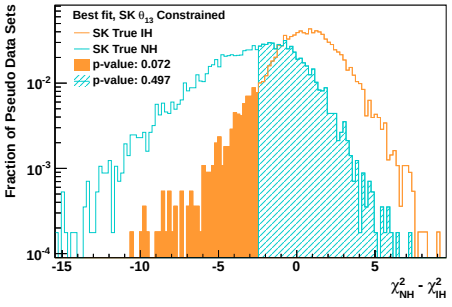

(d) True $\sin^2\theta_{23} = 0.6$

FIGURE 7.46: Distributions of the difference in best-fit χ^2 values assuming the normal hierarchy and inverted hierarchy. The value of $\sin^2\theta_{13}$ is fixed to 0.0210 and expanded FV are used. The result of pseudo data generated assuming normal (inverted) hierarchy is shown as the cyan (orange) histogram. The results with different assumed true $\sin^2\theta_{23}$ are shown. The calculation of p-value to obtain a value of $\Delta\chi^2$ more extreme than the observed value, $\Delta\chi^2_{data} = -2.45$, is according to the shaded histogram.

SK θ_{13} Constrained Fit				
True $\sin^2\theta_{23}$	0.4	0.425	0.5	0.6
p_0(IH)	0.025	0.033	0.065	0.072
CL_s^H	0.308	0.260	0.229	0.143

TABLE 7.15: Normal hierarchy significance summarized in terms of the probability of observing a χ^2 preference for the NH more extreme than that observed in the data assuming an IH, p_0(IH) , and CL_s^H values for a range of assumed parameters. The first row shows the true θ_{23} used to generate MC ensembles used in the calculations. Other oscillation parameters are taken from the analysis' best-fit.

shown in Figure 7.35, the sensitivity to the mass hierarchy changes significantly for different value of θ_{23}. The result of this analysis doesn't show strong constraint on this parameter. MC ensembles therefore have been generated with different θ_{23} values. The other oscillation parameters are fixed to their best-fit values during the MC generation process. The p-values and CL_s^H values for the hierarchy test are summarized in Table 7.15. The observed CL_s^H values vary from a 30.8% C.L. preference for the inverted mass hierarchy to 14.3% as $\sin^2\theta_{23}$ increases from 0.4 to 0.6. Less electron neutrino appearance is expected for a smaller value of $\sin^2\theta_{23}$, which results in a smaller p_0(IH) values and larger CL_s^H. The preference at the analysis best-fit value is 26.0%, which means that the inverted hierarchy is disfavored at 74.0% by SK-IV data with fiTQun reconstruction and the expanded FV. Comparing with the result of NH from the full SK I-IV analysis based on APFit: 93.0% [6], the preference from this analysis is smaller since only data from SK-IV is used. Full analysis with fiTQun will be done in the near future.

Chapter 8

Conclusions and Outlook

We have developed a new algorithm based on a maximum likelihood method for reconstruction of atmospheric neutrino events observed by Super-K. The new algorithm has improved performance with various metrics including resolution of event vertex and momentum, ring counting and particle identification compared with those of the conventional reconstruction algorithm. Reliable performance is also demonstrated by the new algorithm over a larger fiducial volume of the detector. The fiducial volume definition has been therefore expanded to include all events whose distance to the nearest ID wall is larger than 50 cm for the first time in this analysis, which means a 32% increase in the number of events used in analysis comparing with the previous SK analyses, whose cut is 200 cm. An analysis of a 253.9 kton-year exposure of the SK-IV atmospheric data reconstructed by the new algorithm within the expanded fiducial volume definition has been performed. The result is consistent with both previous Super-K measurements and the ones from other experiments. The best-fit value and 1σ error on the atmospheric mixing parameters are $\Delta m^2_{32} = 2.53^{+0.22}_{-0.12}$, $\sin^2\theta_{23} = 0.425^{+0.046}_{-0.037}$ $(0.600^{+0.013}_{-0.030})$ for first (second) octant and $\delta_{CP} = 3.14^{+2.67}_{-1.35}$ for the normal mass hierarchy assumption. A weak preference for the normal mass hierarchy is indicated by the data. The inverted mass hierarchy is disfavored at 74.0% assuming the oscillation parameters at the best-fit point in the analysis. Such a preference varies from 69.2% to 85.7% as the value of $\sin^2\theta_{23}$ changes from 0.4 to 0.6. For the θ_{23} octant, the second octant is disfavored at 90.2% and 69.5% assuming the normal and inverted hierarchy, respectively, which means that current data doesn't indicate strong preference.

The analysis presented here has demonstrated the potential of the new reconstruction algorithm to improve our understanding of the neutrino oscillations with only a subset of the Super-Kamiokande data. The improvement on the expected median sensitivity with the new algorithm becomes more significant when more data is used, as shown in

Figure 8.1. Currently the new reconstruction has only been applied to the 3118.5-day SK-IV fully contained data set, but further studies are ongoing to include other Super-K samples and run periods, which brings an additional 2,800 days of livetime. Some work to achieve this goal has already started such as the work shown in Appendix A.

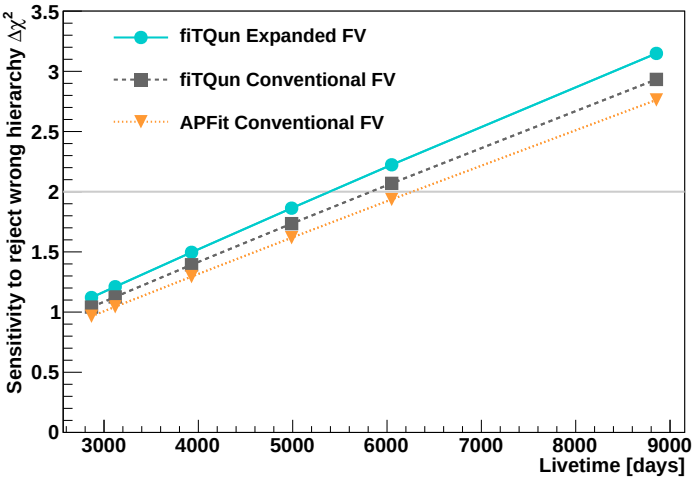

FIGURE 8.1: Median expected sensitivity to mass hierarchy for different livetime. Normal hierarchy is assumed to be true and the true value of $\sin^2\theta_{23}$ is assumed to be 0.5. Here the value of $\sin^2\theta_{13}$ is fixed to 0.0210. The result of the events reconstructed by fiTQun within the conventional FV and expanded FV are denoted by the gray and blue lines. The sensitivity with events reconstructed by APFit algorithm and the conventional FV is denoted by the orange line.

Furthermore, the size of the mass hierarchy signal depends on oscillation parameters including θ_{13}, θ_{23} and $|\Delta m^2_{32}|$ as shown in Equation 1.25, 1.26 and 1.27. As a result the large uncertainties on them translate directly into reduced hierarchy sensitivity. Besides the value of θ_{13}, which is constrained by reactor experiments as discussed in Section 7.6.2, the value of θ_{23} and $|\Delta m^2_{32}|$ can also be constrained by accelerator experiments, such as the T2K experiment [6]. For this reason, the sensitivity to the mass hierarchy, $\sin^2\theta_{23}$ octant and δ_{CP} of the joint analysis of atmospheric neutrinos and accelerator neutrinos for both present and future experiments will be discussed below.

Combination with accelerator neutrinos of T2K experiment

In the T2K experiment, the neutrino beam produced at the Japan Proton Accelerator Research Complex (J-PARC) is directed 2.5 degrees away from the Super-K detector for a narrow band beam with a spectrum peaked at 600 MeV, the first oscillation maximum for the 295 km, which is the baseline length from neutrino production point to Super-K detector. A near detector located 280 m downstream of the neutrino production point

and at the same off-axis angle is used to measure the unoscillated beam spectrum and to thereby constrain the expected spectrum at Super-K, the far detector (Figure 8.2).

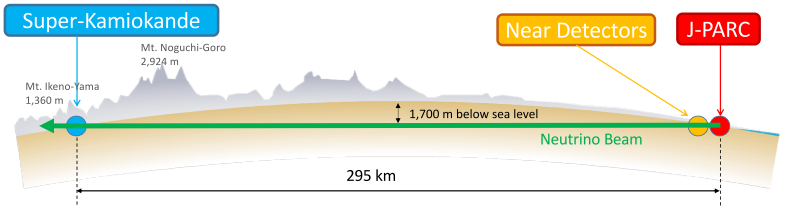

FIGURE 8.2: A schematic of a neutrino's journey from the neutrino beamline at J-PARC, through the near detectors (green dot) which are used to determine the properties of the neutrino beam, and then 295 km underneath the main island of Japan to Super-Kamiokande. Taken from [26]

Currently the constraint on θ_{23} and $|\Delta m^2_{32}|$ from T2K [34] is tighter than that from Super-K and is statistically independent from the Super-K result. Therefore the sensitivity of the analysis in this thesis can be expected to be increased by taking the T2K measurements and its systematic error sources into consideration during oscillation analysis.

Indeed, the observable of the atmospheric neutrinos from Super-K and the accelerator neutrinos from T2K are the same since Super-K serves as the far detector for the latter experiment. Therefore, the simulated T2K ν_e appearance and ν_μ disappearance samples and associated systematic errors, rather than the effective model used in [6], can be integrated into the atmospheric analysis directly to incorporate T2K's measurement.

The sensitivity analysis specifies a set of oscillation parameters for the MC, which is oscillated accordingly to calculate the expected number of events in each bins. Similar to the analysis described in Section 7.4, a binned χ^2 method assuming Poisson statistics is used to judge the agreement between the oscillated MC with true parameter and test parameter. Since the systematic errors associated to the accelerator neutrino sample provided by the T2K experiments are correlated, the definition of χ^2 function modified from Equation 7.3 to :

$$\chi^2 = 2\sum_n \left(E_n - \mathcal{O}_n + \mathcal{O}_n \ln \frac{\mathcal{O}_n}{E_n} \right) + \sum_i \sum_j \epsilon_i [\sigma^2_{ij}]^{-1} \epsilon_j \tag{8.1}$$

where $[\sigma^2_{ij}]^{-1}$ is the covariance matrix representing the correlation between i-th and j-th systematic errors. The definition of the penalty term for adjusting the systematic errors is consistent with the previous one defined in Equation 7.3 as $[\sigma^2_{ij}]^{-1}$ becomes a diagonal matrix if there is no uncertainty correlation.

Another difference between accelerator neutrino sample and atmospheric neutrino sample is that the effect of systematic errors, which are parameterized by different methods.

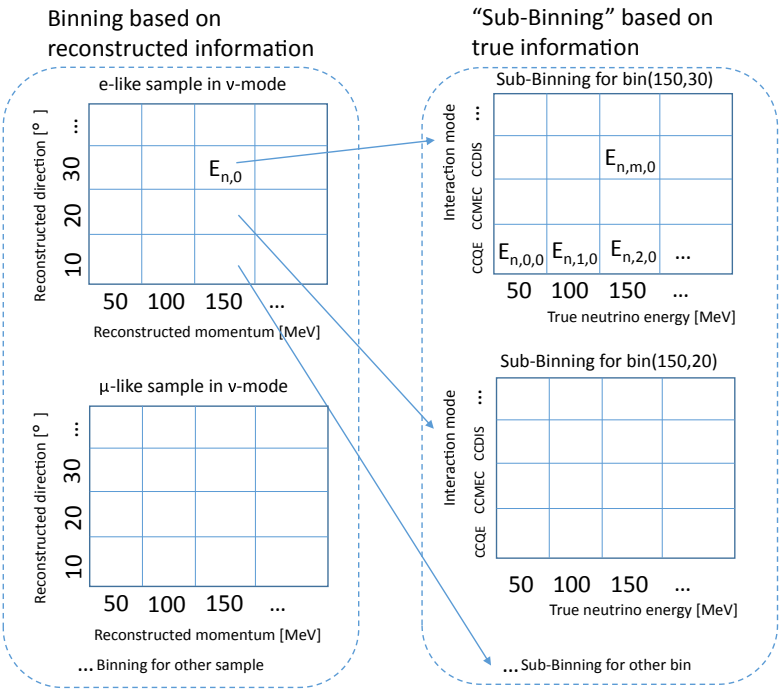

FIGURE 8.3: Sub-binning structure for the T2K systematic uncertainty parameterization. The binnings shown on the left are based on reconstructed information, while the ones shown on the right are based on true information. $E_{n,0}$ represents the number of events of nominal MC prediction in n-th bin based on reconstructed information, while $E_{n,m,0}$ denotes the number of events in the m-th sub-bin for n-th bin.

In the Super-K analysis, the original definition of the expectation of the number of events in n-th bin based on reconstructed information after incorporating the systematic error E_n in Equation 7.4:

$$E_n \quad = \quad E_{n,0}(1 + \sum_i f_n^i \epsilon_i)$$

assumes that the systematic uncertainty affects the number of events in each bin of reconstructed energy directly. However, in the T2K experiment, a more detailed parameterization method is used: the systematic uncertainties of the neutrino flux or interaction cross-section also depend on the true neutrino energy or interaction mode (i.e. charged-current or neutral-current) besides the reconstructed energy and direction. To emulate the parameterization of T2K in Super-K structure, each reconstruction energy bin E_n is further divided into several "sub-bin", which considers the true neutrino energy and interaction mode for MC (c.f Figure 8.3).

The definition of $E_{n,0}$, which represents the nominal MC expectation in n-th bin and E_n is also updated to:

$$\begin{aligned} E_{n,0} &= \sum_m E_{n,m,0} \\ E_n &= \sum_m E_{n,m,0}(1 + \sum_i f^i_{n,m}\epsilon_i) \end{aligned}$$

where m is the sub-binning number in each bin n based on reconstructed bin, $f^i_{n,m}$ represents the coefficient for the i-th systematic uncertainty on the m-th sub-bin of n-th bin. Such a "sub-bin" definition of E_n is only used for accelerator neutrinos since the effect of the dependency on true neutrino energy and interaction mode is not considered during the systematic error evaluation process for atmospheric neutrinos. The error values are the same as the one in [129].

Currently, the correlation between the systematics of the two kinds of neutrino sources is not considered except the energy scale since the evaluation method is different for these two experiments. Further efforts are needed to unify the systematic error related to the cross-section and detector.

The expected sensitivities as the function of true $\sin^2\theta_{23}$ with different running time are shown in Figure 8.4. The atmospheric neutrino data collected by all four Super-K phases within the convention FV are considered here.

The sensitivity to neutrino mass hierarchy with joint analysis (dashed line) of the atmospheric neutrino sample and accelerator neutrino sample is expected be $\sqrt{\Delta\chi^2} > 2.5(3.0)$ for $\sin^2\theta_{23} > 0.55$ and true $\delta_{CP} = 0°(270°)$ at the end of 2026, while the result with atmospheric neutrino only (solid line) is $\sqrt{\Delta\chi^2} > 2$ at the same condition. The atmospheric neutrinos show higher sensitivity comparing with accelerator neutrinos since matter effects are strong in the resonance-enhanced oscillation region of the atmospheric neutrino energy spectrum (2-10 GeV). On the other hand, for accelerator neutrinos, their energy is low ($\sim$ 600 MeV) and the baseline for the neutrino oscillation is short (295 km). Furthermore, as shown in Figure 8.4, the sensitivity of accelerator neutrinos depends on the true value of δ_{CP} largely due to the degeneracy between the CP violation and the mass hierarchy caused by its fixed baseline. It is therefore difficult to determine the mass hierarchy by accelerator neutrino measurement only. Anyway, accelerator neutrino data provides a clean measurement of the atmospheric mixing parameters which determines the size of the matter effects, and the sensitivity to the mass hierarchy is therefore improved.

Figure 8.5 shows the sensitivity to the CP violation ($\sin\delta_{CP} \neq 0$) when the true mass hierarchy is assumed to be the normal hierarchy. Although the sensitivity with the

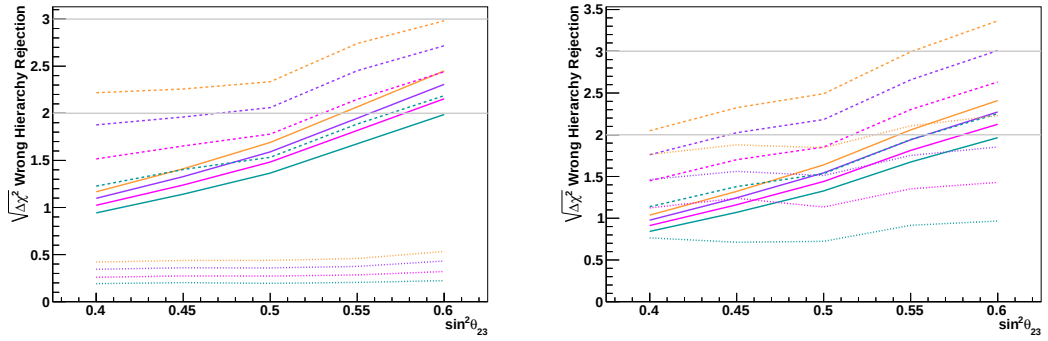

FIGURE 8.4: Sensitivity to mass hierarchy as function of true $\sin^2\theta_{23}$. The solid lines (dotted lines) are the sensitivity with atmospheric neutrino only (accelerator neutrino only), while the dashed lines represent the result of joint analysis. The result shown in left figure assumes true $\delta_{CP} = 0°$, while the right figure is for true $\delta_{CP} = 270°$. The orange, purple, magenta and green lines represent the result at the end of year 2026, 2023, 2020 and 2017, respectively.

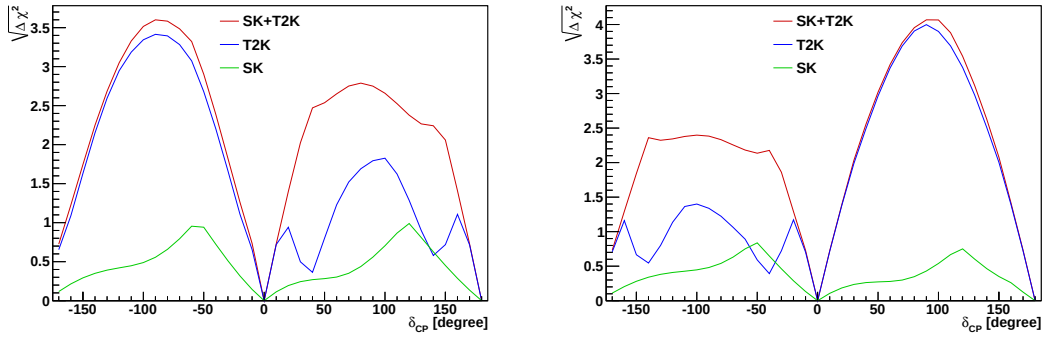

FIGURE 8.5: Sensitivity to CP violation ($\sin\delta_{CP} \neq 0$) as function of true $\sin\delta_{CP}$. The true mass hierarchy of left figure is assumed to be normal hierarchy, while for right figure it is assumed to be inverted hierarchy. The green, blue and red lines represent the sensitivity with atmospheric neutrino only, accelerator neutrino only and combined analysis at the end of year 2026, respectively.

accelerator neutrinos from the T2K experiment (blue line) is higher than that with atmospheric neutrinos (green line) overall, the degeneracy between the mass hierarchy and the CP phase constrains the sensitivity. By combining these two samples, the degeneracy is resolved and the sensitivity is increased more than 1σ in the region where the degeneracy was observed before.

For the $\sin^2\theta_{23}$ octant, as shown in Figure 8.6, although the sensitivity from accelerator neutrino samples is larger than that from atmospheric neutrino samples, the sensitivity can be increased further by combining these two samples.

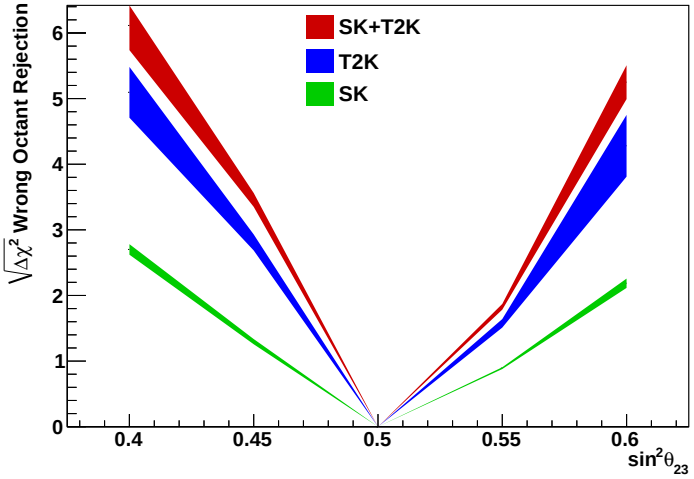

FIGURE 8.6: Sensitivity to $\sin^2\theta_{23}$ octant (> 0.5 or < 0.5) as function of true $\sin^2\theta_{23}$. The green, blue and red lines represent the sensitivity with atmospheric neutrino only, accelerator neutrino only and combined analysis at the end of year 2026, respectively.

Future experiment: Hyper-Kamiokande

It has been shown that current sensitivity to the mass hierarchy has been limited by the lack of statistics. A next generation gigantic underground water Cherenkov ring imaging detector, Hyper-Kamiokande (Hyper-K) is proposed to obtain more statistics. It consists of at least one and possibly two water tanks with the dimensions of the 74 m (D) $\times$ 78 m (H) for each. The total fiducial water mass will be 0.37 million tons, approximately 17 times as large as that of Super-K detector [44]. The first tank is planed to be placed in Japan at 295 km from the J-PARC neutrino beam with 2.5° off-axis angles as the Super-K detector, while the second detector if built, is being considered in Korea, with an off-axis angle of 1.3° and a baseline of 1,088 km[130]. The Hyper-K experiment is expected to start its operation around 2026 [44].

A combined analysis of accelerator beam and atmospheric neutrino data assuming a Hyper-K detector in Japan (JD) and at the Mt. Bisul in Korean (KD) and compare with sensitivities assuming two detectors in Kamioka, Japan (JD $\times$ 2) are shown. The treatment of the atmospheric neutrino samples and their systematic errors follows that of Super-Kamiokande, with no assumed improvements, while the systematic errors for accelerator neutrino samples is estimated based on the T2K experiment taking into account improvements expected in the future T2K data and analysis [44, 130].

The physics sensitivity shown here assumes that one or two 187 kton detectors will be operated over 10 years (10×10^7 sec) at 1.3 MW beam power, corresponding to 27×10^{21}

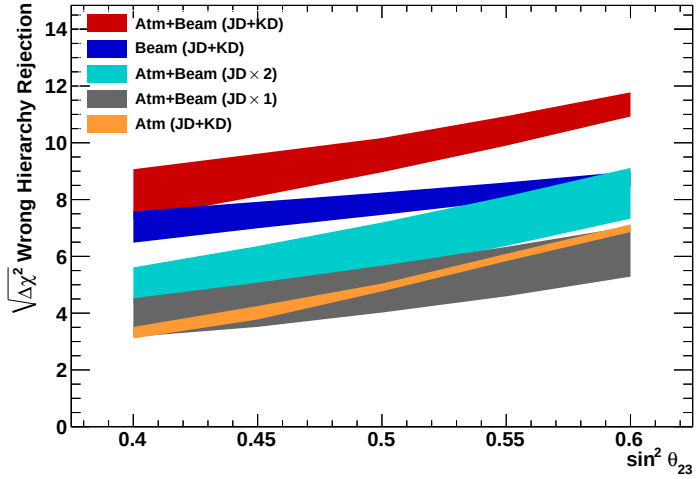

FIGURE 8.7: Sensitivity to the normal mass hierarchy for components of a combined measurement of beam and atmospheric neutrinos for a 10 year exposure. Here JD refers to a single Hyper-K detector in Kamioka, Japan, and JD ×2 refers two to such detectors operating simultaneously. The horizontal axis shows the assumed value of $\sin^2\theta_{23}$ and the width of the bands shows the variation in sensitivity with δ_{CP}.

protons on target. The total exposure for atmospheric neutrinos is expected to be 1.87 Mton·year for one tank (3.74 Mton·year for two tanks).

Figure 8.7 shows the sensitivity to the mass hierarchy for the combined analysis. After 10 years of running the expected ability to determine the mass hierarchy is better than $\sqrt{\Delta\chi^2} = 7$. Though the combined JD and Mt. Bisul beam measurement has better sensitivity than the atmospheric neutrino measurement alone, the sensitivity improves further when all of the samples are combined. The power of this improvement results in an earlier realization of the hierarchy as shown in the left plot of Figure 8.10. The sensitivity is expected to exceed $\sqrt{\Delta\chi^2} = 4$ within two years of operations in this experimental configuration.

Atmospheric neutrinos provide additional constraints on δ_{CP} as shown in the Figure 8.8 although it has less sensitivity than the measurement with accelerator neutrinos. Similarly, the constraint on the CP violation from atmospheric neutrino is weaker than that from the accelerator and provides only a slight improvement in sensitivity shown Figure 8.9. However, as with the other oscillation measurements, the power of the combined accelerator and atmospheric measurement comes in the early realization of this sensitivity as shown in the right plot of Figure 8.10.

As discussed above, the sensitivity to the mass hierarchy for Super-K can be increased by analyzing the accelerator beam neutrinos and atmospheric neutrinos simultaneously. The sensitivity expected be $\sqrt{\Delta\chi^2} > 2.5(3.0)$ for $\sin^2\theta_{23} > 0.55$ at the end of 2026 for true $\delta_{CP} = 0°(270°)$.

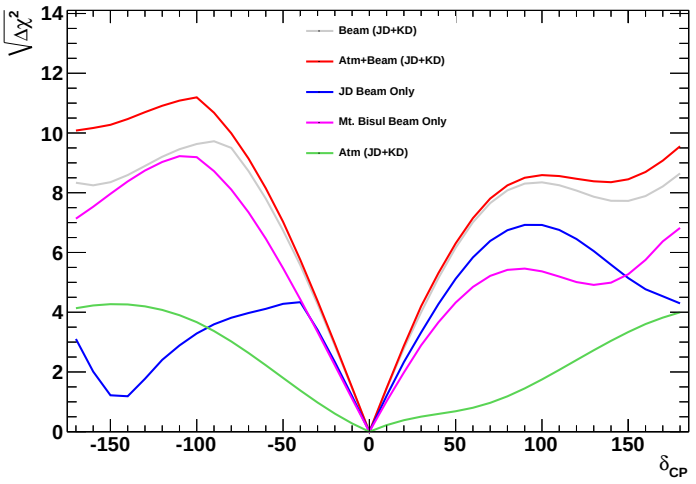

FIGURE 8.8: Sensitivity to $\delta_{CP} = 0$ for components of a combined measurement of beam and atmospheric neutrinos for a 10 year exposure. Here JD refers to a single Hyper-K detector in Kamioka, Japan.

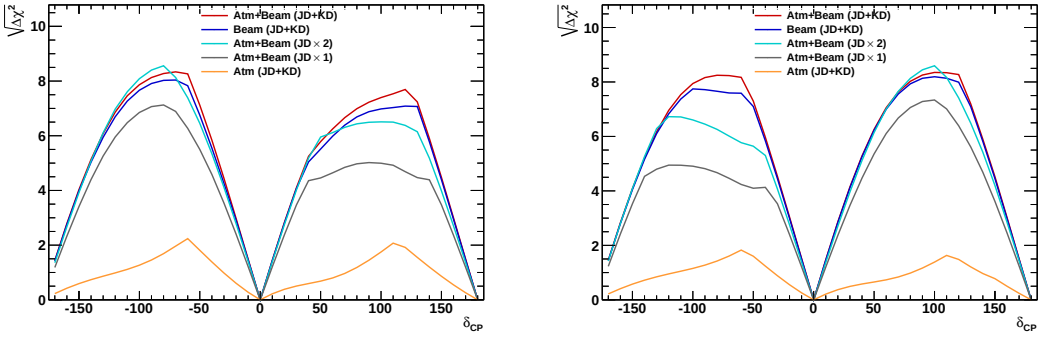

FIGURE 8.9: Sensitivity to CP violation (sin $\delta_{CP} \neq 0$) for components of a combined measurement of beam and atmospheric neutrinos for a 10 year exposure. Here JD refers to a single Hyper-K detector in Kamioka, Japan, and JD × 2 refers two to such detectors operating simultaneously. The horizontal axis shows the assumed true value of δ_{CP}.

On the other hand, Hyper-K has strong potential to determine neutrino mass hierarchy and discover leptonic CP violation by the observation of accelerator and atmospheric neutrino oscillation. Joint analysis of these two kinds of neutrinos at Hyper-K can improve its sensitivity further. After 10 years running, the significance to determine the mass hierarchy is expected to reach 5σ, when $\sin^2\theta_{23} = 0.5$ and a CP violation discovery at 3σ or more can be made for 70% of the δ_{CP} phase space.

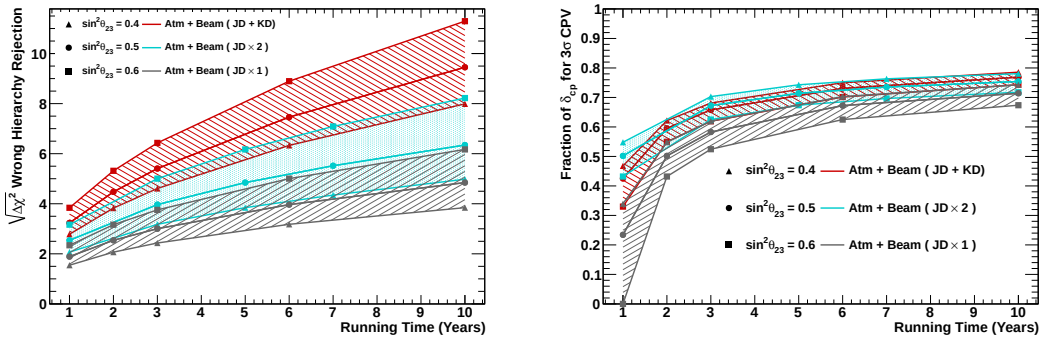

FIGURE 8.10: Sensitivity as a function of year to the mass hierarchy (left) and the fraction of δ_{CP} phase space for which CP violation (sin $\delta_{CP} \neq 0$) can be determined at 3σ or better. Red lines show a combined beam and atmospheric neutrino measurement with one Hyper-K detector in Kamioka, Japan (JD) and one at the Mt. Bisul site in Korea. Cyan lines show the same analysis assuming two detectors in Kamioka (JD × 2) and grey lines assume only one detector in Kamioka (JD × 1). Different symbols show the assumed value of $\sin^2\theta_{23}$.

Appendix A

SK-I retuning

As has been introduced in Section 6.2.3, the new reconstruction tool fiTQun, is expected to be used for ATMPD analysis, but large data/MC discrepancy were found for the PID likelihood of SK-I FC samples, while such discrepancy is not observed for SK-I APFit, as shown in Figure A.1. The distribution of such sample for SK-IV data and MC are also in good agreement, as shown in Figure 6.3.

The key to distinguish e-like events and μ-like events is the difference on charge pattern: rings from electrons tend to have rough edges produced by the light from their electromagnetic showers, while rings from muons or charged pions predominately produce crisp edges. Figure A.2 and Figure A.3 show the charge profile and hit profile with respect to the vertex and direction of particles for sub-GeV single-ring events of SK-I and SK-IV for. The ratio between data and MC is shown in Figure A.4, which indicates a good agreement on the charge profile for both SK-I and SK-IV (left), while a large discrepancy on the hit profile for SK-I between data and MC can be seen clearly. More hits observed for SK-I MC than that of data.

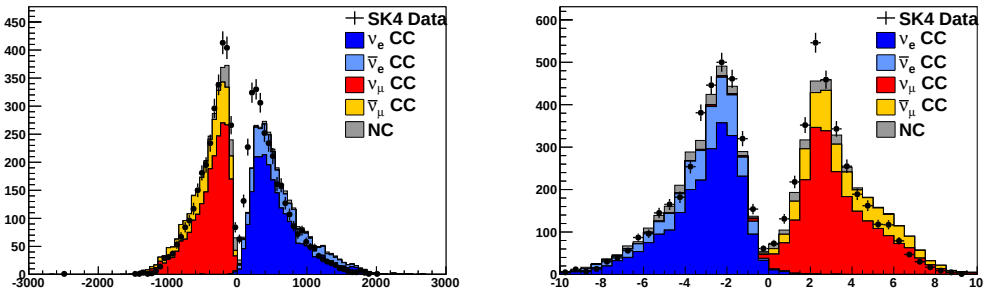

FIGURE A.1: PID likelihood distribution of sub-GeV single-ring events for SK-I. Left (right) figure shows the distribution reconstructed by fiTQun (APFit).

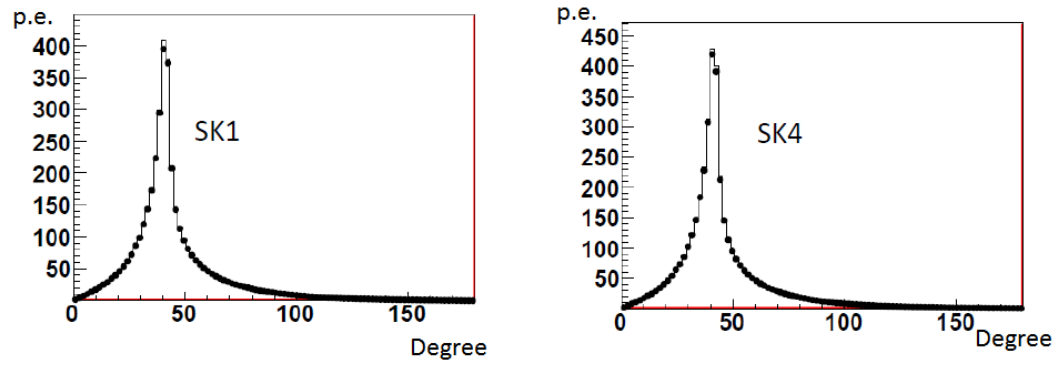

FIGURE A.2: Charge profile with respect to the reconstructed vertex and direction of sub-GeV single-ring events for SK-I (left) and SK-IV (right). Points denote the data and solid line is for MC.

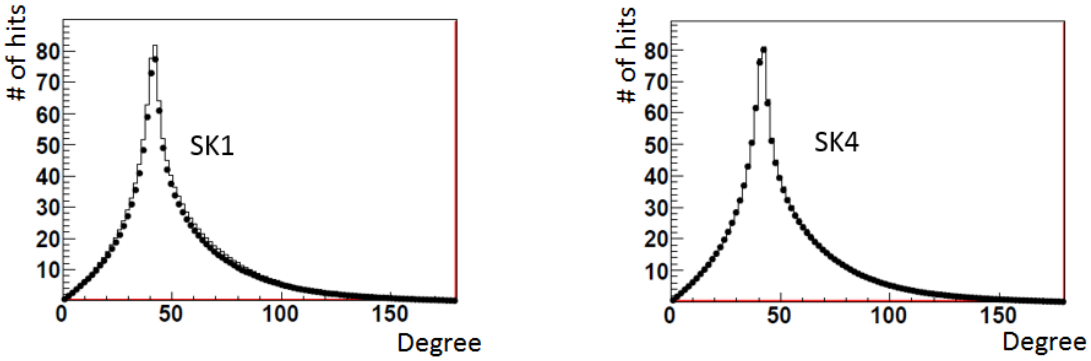

FIGURE A.3: Hit profile with respect to the reconstructed vertex and direction for sub-GeV single-ring events for SK-I (left) and SK-IV (right). Points denote the data and solid line is for MC.

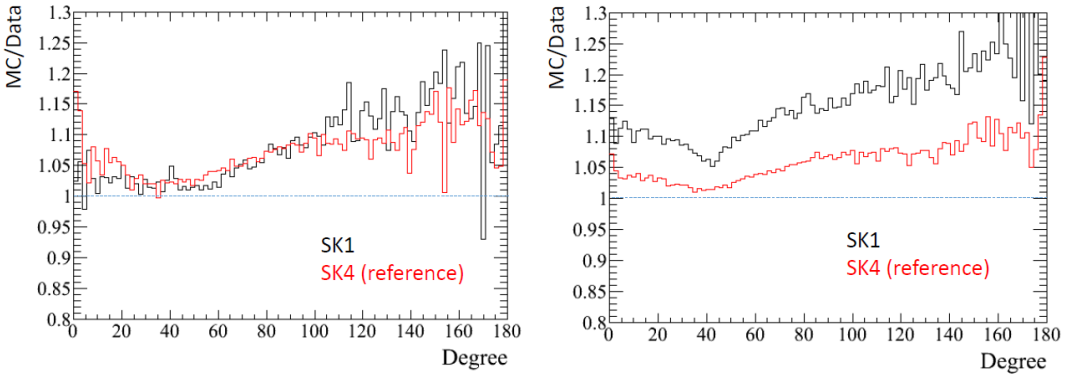

FIGURE A.4: Ratio between data and MC of charge profile (left) and hit profile (right) for sub-GeV single-ring events for SK-I (black) and SK-IV (red).

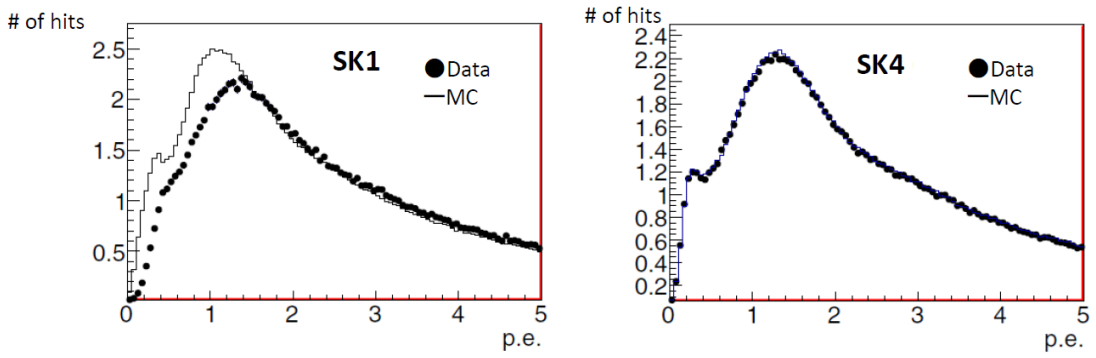

FIGURE A.5: Charge distribution around the Cherenkov angle (42°) for sub-GeV single-ring events of SK-I (left) and SK-IV (right). Points denote the distribution of data, while the solid line is for MC.

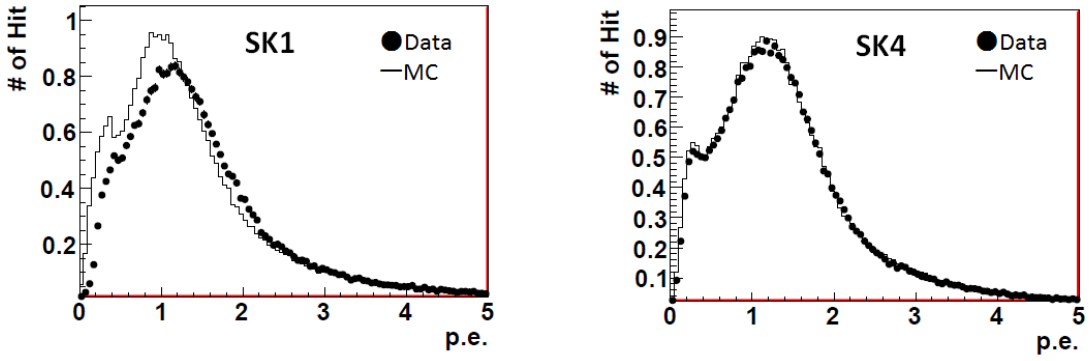

FIGURE A.6: Charge distribution around the Cherenkov angle (42°) for Michel electron from cosmic ray muon of SK-I (left) and SK-IV (right). Points denote the distribution of data, while the solid line is for MC.

Figure A.5 and Figure A.6 show the charge distribution around the Cherenkov angle (42°) for sub-GeV single-ring events and Michel electron from cosmic ray muon, respectively. Large discrepancy is observed in low charge region for SK-I, which results in the disagreement on hit pattern. Such discrepancy has limited effect on the charge pattern since the charge for those hits are small.

The ideal method to resolve issue is to retune the single p.e. distribution for SK-I with the nickel data as introduced in Section 4.1.2. The reason to double the gain of PMT is for the measurement of the shape below the trigger threshold. However, those data is not found yet since they were taken 20 years ago. The retuning of single p.e. distribution is done by adding the observed discrepancy between MC and data with considering the effect from trigger threshold. The distribution under the trigger threshold is tuned to keep the mean value of single p.e. unchanged since the charge pattern agrees well.

The event selection for the nickel data is:

1. $N_{50} > 30$

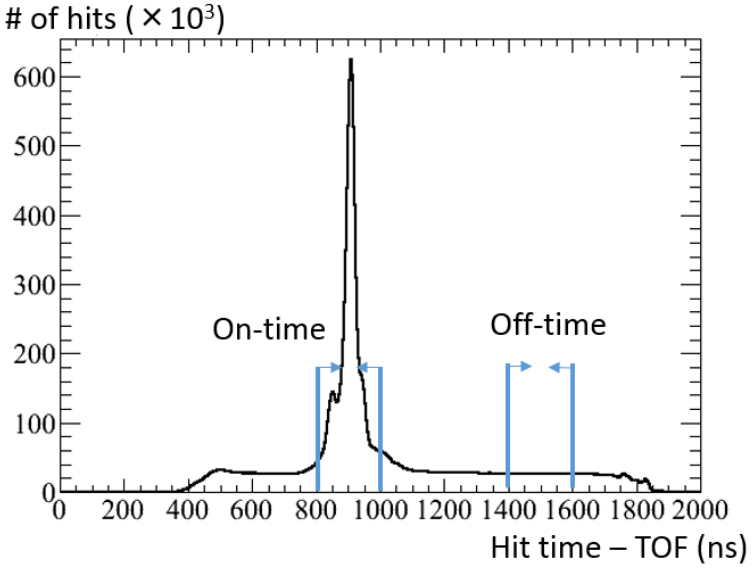

FIGURE A.7: Hit time distribution of each PMT for Nickel source after event selection. The on-time region and off-time region are marked with blue line.

2. Distance between the vertex reconstructed by low energy fitter and the position of nickel source is less than 4 m.

3. Time difference between two events is longer than $10\mu s$.

The data from Nickel source taken on 10, August, 1996 for calibration. The hit time and charge distribution of each PMT are shown in Figure A.7 and Figure A.8. To remove the effect of dark hits caused by electronic noise, the charge distribution were shown for on-time region and off-time region respectively. The final observed single p.e. distribution is obtained from the difference from these two charge distribution.

The tuned single p.e. distribution with and without is shown in Figure A.9. Tuned MC has good agreement with the nickel data.

The charge profile and hit profile after tuning is shown in Figure A.10. The agreement between data and MC on hit profile increased a lot while the charge profile is almost not affected as our expectation.

The momentum and PID of Michel decay electron from cosmic ray muon before and after tuning is shown in Figure A.11 and Figure A.12. The discrepancy between data and MC for the momentum is at the same level ($\sim$ 1.2%, while the agreement on the PID distribution increased.

Similarly, the PID distribution for sub-GeV single-ring event after tuning is shown in Figure A.13. The agreement improved large although some discrepancy remained due to the remaining discrepancy shown in Figure A.14, which need further investigation.

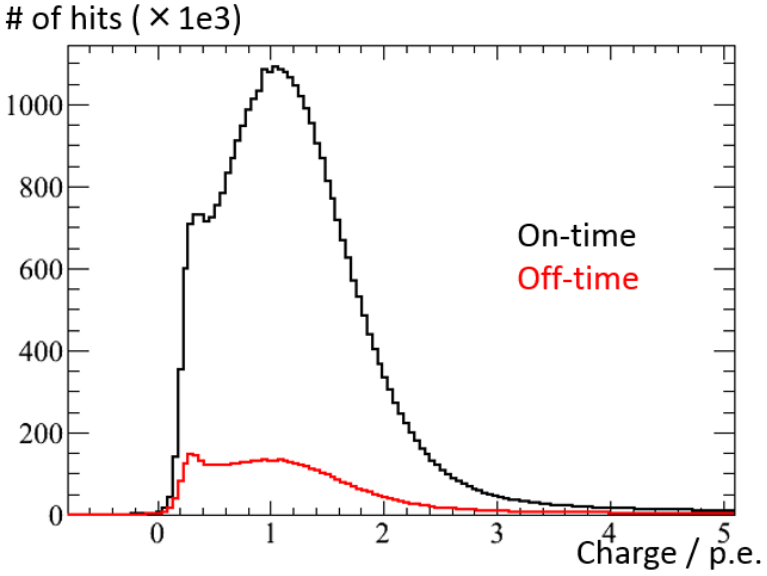

FIGURE A.8: Charge distribution of each PMT for Nickel source. Black (red) line denote the distribution from on-time (off-time) region.

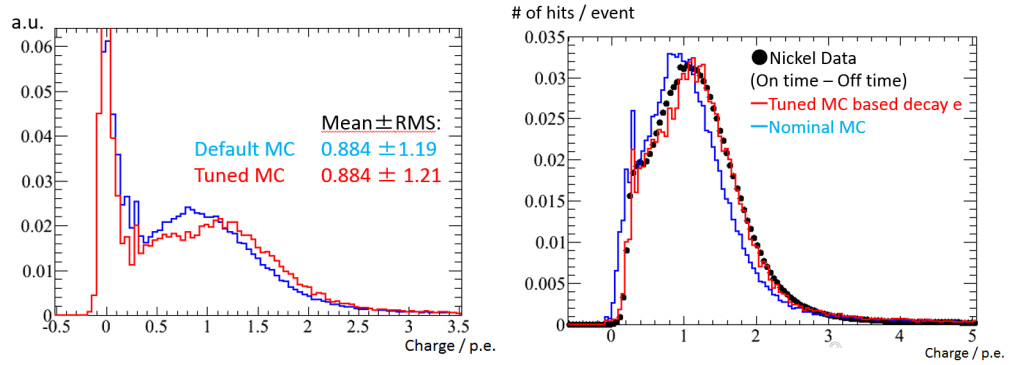

FIGURE A.9: Charge distribution for single p.e. with (left) and without (right) the trigger effect. The points on the right shows the data from Nickel source taken on 10, August, 1996 for calibration.

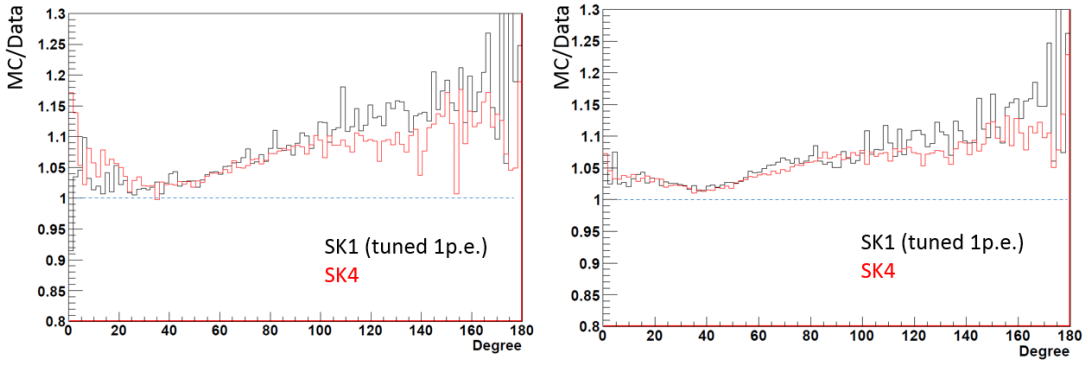

FIGURE A.10: Charge profile (left) and hit profile (right) for sub-GeV single-ring events for SK-I (black) and SK-IV (red).

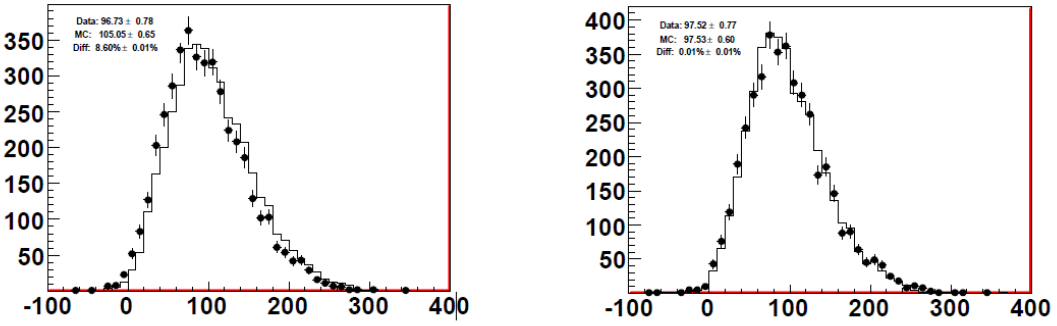

FIGURE A.11: PID likelihood distribution for SK-I Michel electron from cosmic ray muon before (left) and after (right) retuning.

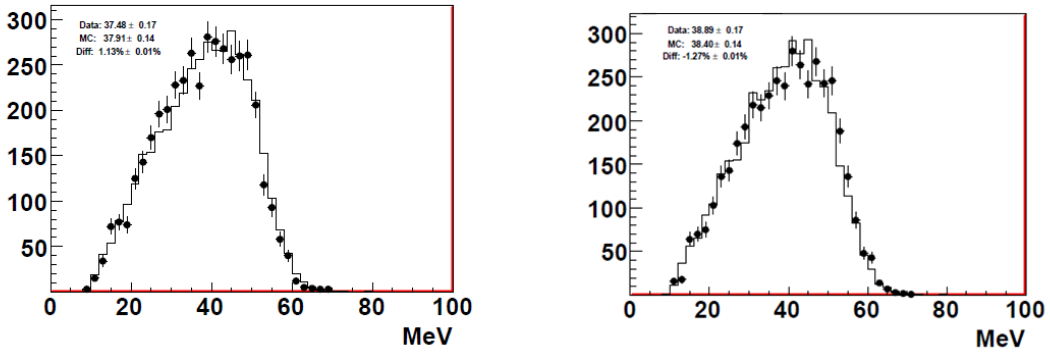

FIGURE A.12: Momentum distribution for SK-I Michel electron from cosmic ray muon before (left) and after (right) retuning.

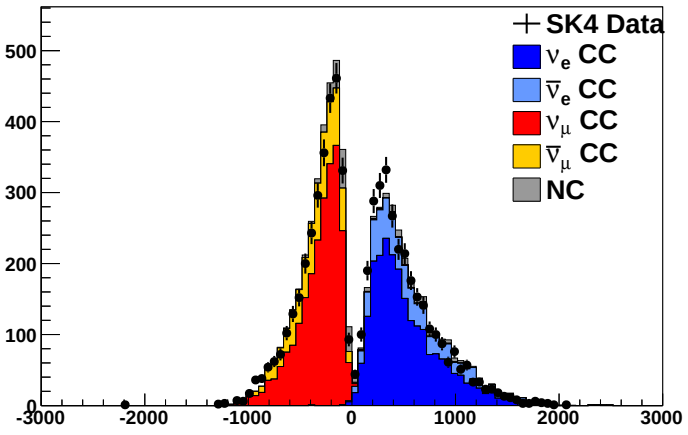

FIGURE A.13: PID likelihood distribution of sub-GeV single-ring events for SK-I after retuning.

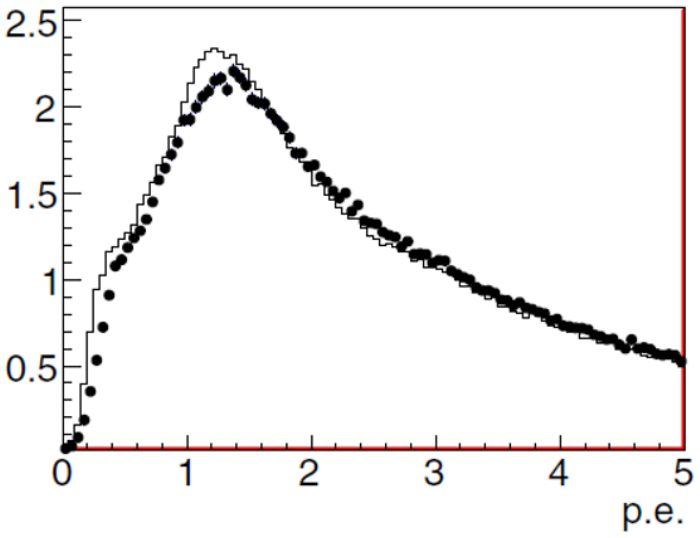

FIGURE A.14: Charge distribution around the Cherenkov angle (42°) for sub-GeV single-ring events of. Points denote the distribution of data, while the solid line is for MC.

Appendix B

Performance check for fiducial volume expansion

Table B.1, B.2, and B.3 show the event rate and component fraction for each analysis sample in conventional FV ($D_{\text{wall}} > 200$ cm), new region (50 cm $< D_{\text{wall}} <$ 200 cm) and expanded FV ($D_{\text{wall}} > 50$ cm) respectively.

Basic distribution, including the event rate, interaction fraction, direction resolution, momentum bias, energy distribution and zenith angle distribution, for all 13 FC event samples are shown here to validate fiducial volume expansion. Different figures share the same legends, which indicate the different interaction mode. The event reconstruction and selection are done by fiTQun.

There are no serious issues observed when expanding the FV to $D_{\text{wall}} > 50$ cm.

Sample	CC ν_e	CC $\bar{\nu}_e$	CC $\nu_\mu + \bar{\nu}_\mu$	CC ν_τ	NC	Data	MC
Fully Contained (FC) Sub-GeV							
e-like, Single-ring							
0 decay-e	0.728	0.242	0.001	0.000	0.028	5796	5422.3
1 decay-e	0.907	0.020	0.033	0.001	0.040	596	559.3
μ-like, Single-ring							
0 decay-e	0.010	0.004	0.795	0.001	0.191	1037	1011.9
1 decay-e	0.000	0.000	0.974	0.000	0.026	5395	5086.3
2 decay-e	0.000	0.000	0.984	0.000	0.016	493	493.5
π^0-like							
Two-ring	0.051	0.016	0.011	0.000	0.922	1346	1304.5
Fully Contained (FC) Multi-GeV							
Single-ring							
ν_e-like	0.726	0.077	0.058	0.027	0.113	217	208.1
$\bar{\nu}_e$-like	0.553	0.379	0.003	0.008	0.056	963	975.2
μ-like	0.000	0.000	0.996	0.003	0.001	882	907.0
Multi-ring							
ν_e-like	0.588	0.117	0.054	0.036	0.204	759	773.4
$\bar{\nu}_e$-like	0.526	0.300	0.021	0.020	0.134	644	654.6
μ-like	0.010	0.001	0.959	0.004	0.026	1982	1943.1
Other	0.283	0.026	0.342	0.053	0.295	1038	1024.5
Partially Contained (PC)							
Stopping	0.084	0.033	0.840	0.000	0.043	374	374.4
Through-going	0.007	0.002	0.985	0.000	0.006	1685	1711.2
Upward-going Muons (Up-μ)							
Stopping	0.008	0.003	0.987	0.000	0.003	843	776.6
Through-going							
Non-showering	0.002	0.001	0.996	0.000	0.001	3013	2956.3
Showering	0.001	0.000	0.998	0.000	0.001	547	550.8

TABLE B.1: Sample purity broken down by neutrino flavor assuming neutrino oscillations with $\Delta m^2_{32} = 2.52 \times 10^{-3}\text{eV}^2$ and $\sin^2\theta_{23} = 0.51$. The right two columns show the sample size of the data and MC for the entire SK data set, respectively. Only fully contained events are reconstructed by fiTQun. Partially contained events and upward-going muon are reconstructed by APFit. All of the samples shown here have a FV cut of 200 cm.

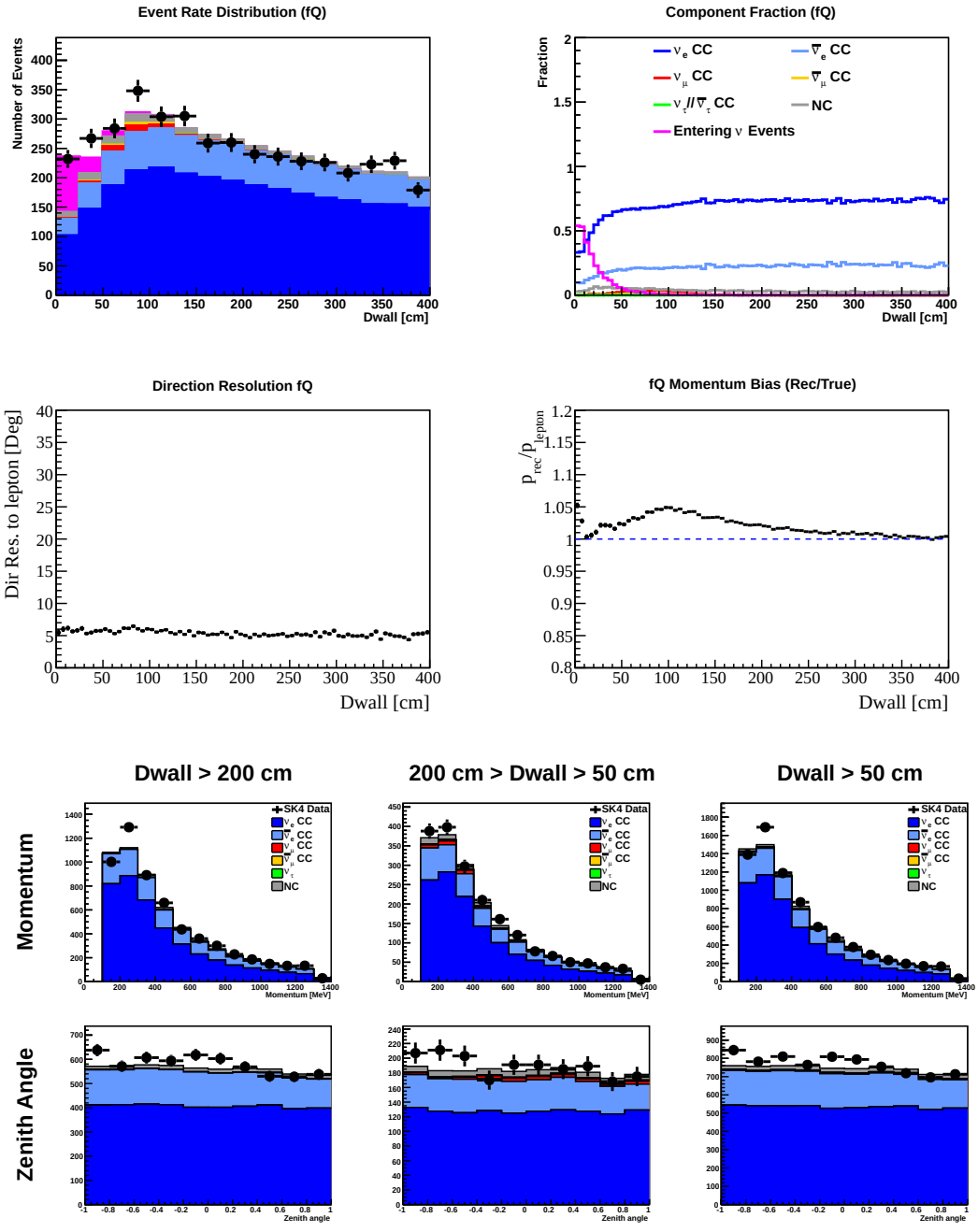

FIGURE B.1: Basic distribution for SubGeV single-ring *e*-like 0 decay-e sample reconstructed and selected by fiTQun. Top four figures shows the event rate, component fraction, direction resolution and momentum bias as the function of the distance to nearest wall (dwall), respectively. The error bar shows the statistical uncertainty. Bottom six figures shows the energy distribution and zenith angle distribution in different detector region. Same plots are shown for next 12 figures.

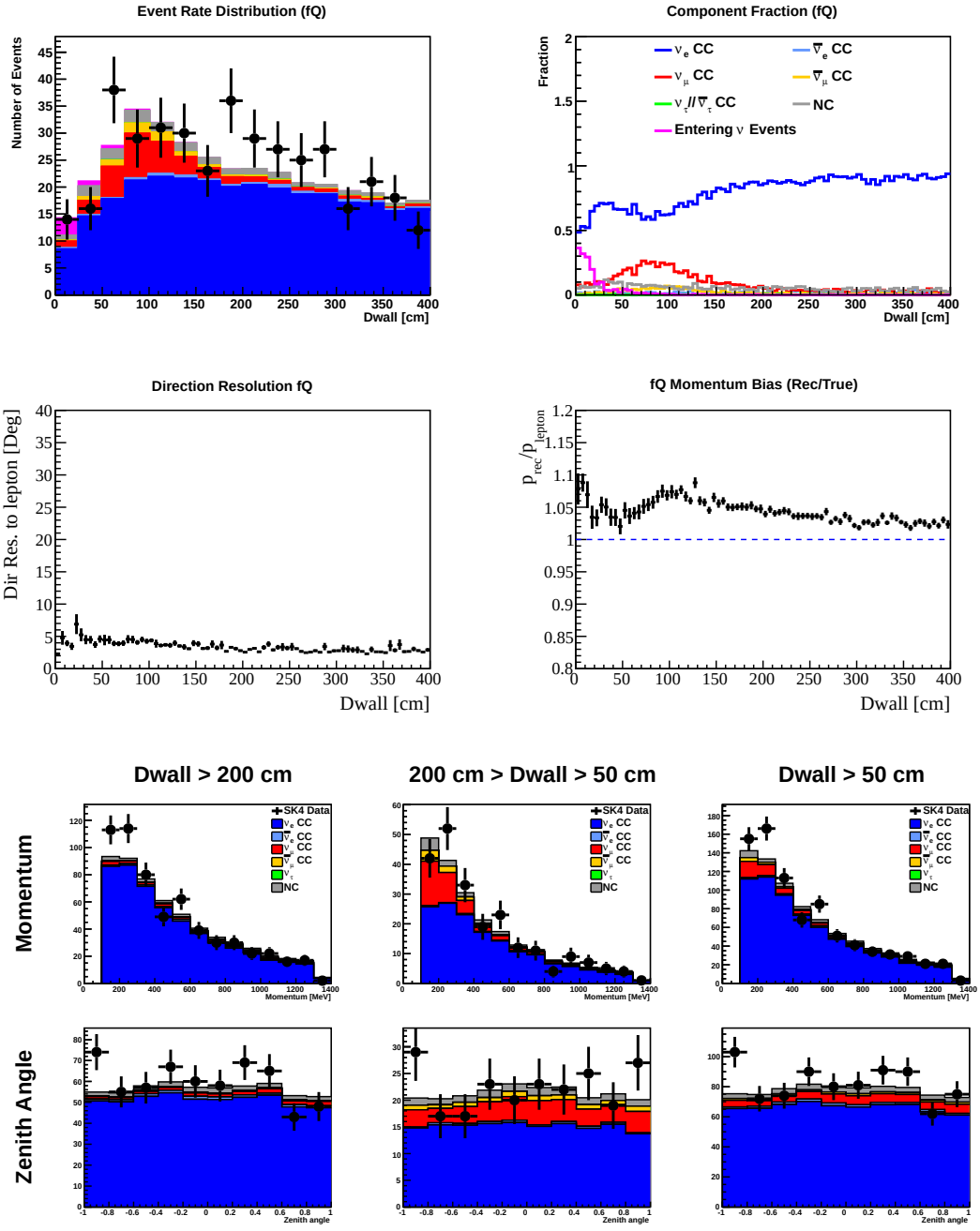

FIGURE B.2: Basic distribution for SubGeV single-ring *e*-like with 1 or more decay-e sample reconstructed and selected by fiTQun.

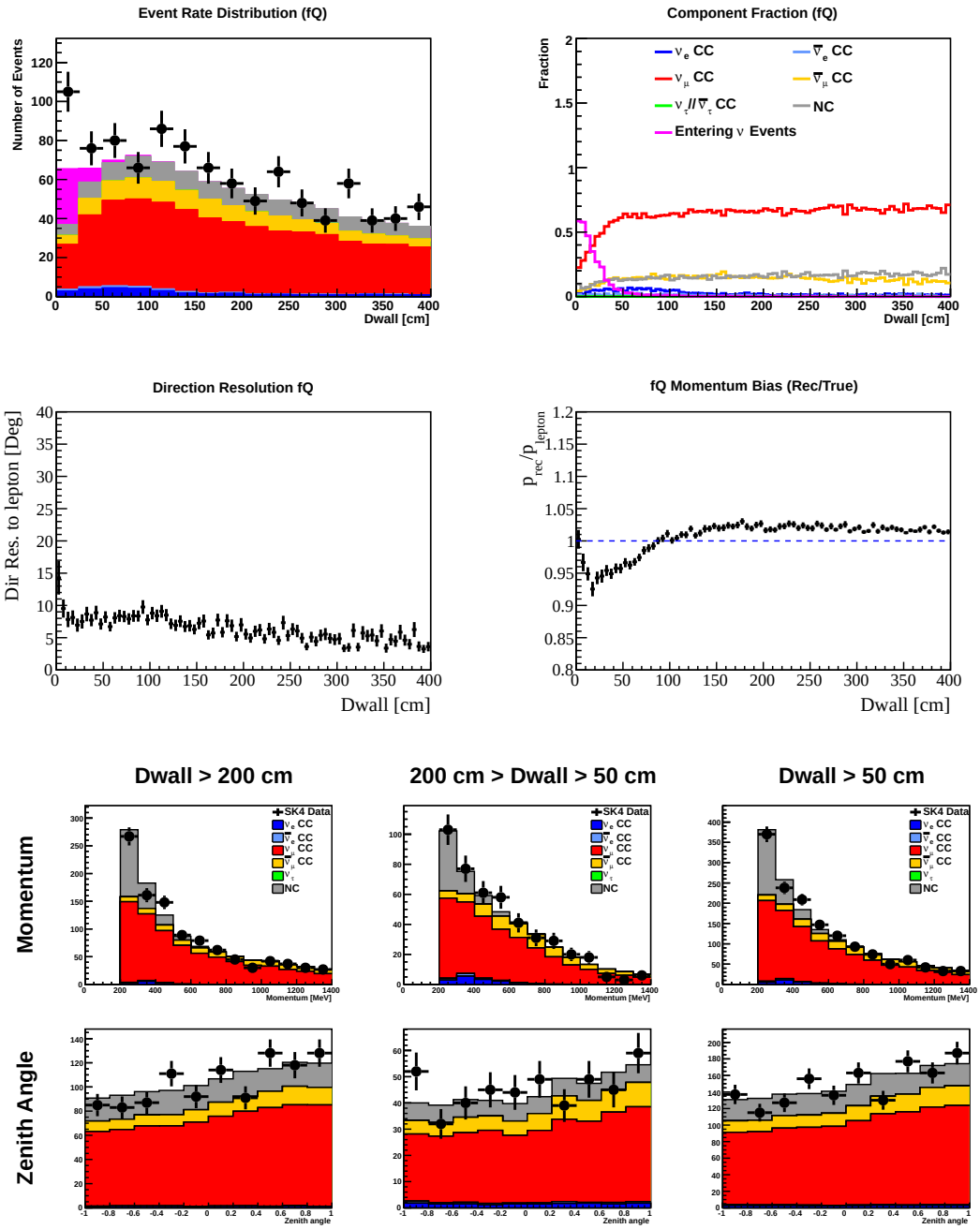

FIGURE B.3: Basic distribution for SubGeV single-ring μ-like 0 decay-e sample reconstructed and selected by fiTQun.

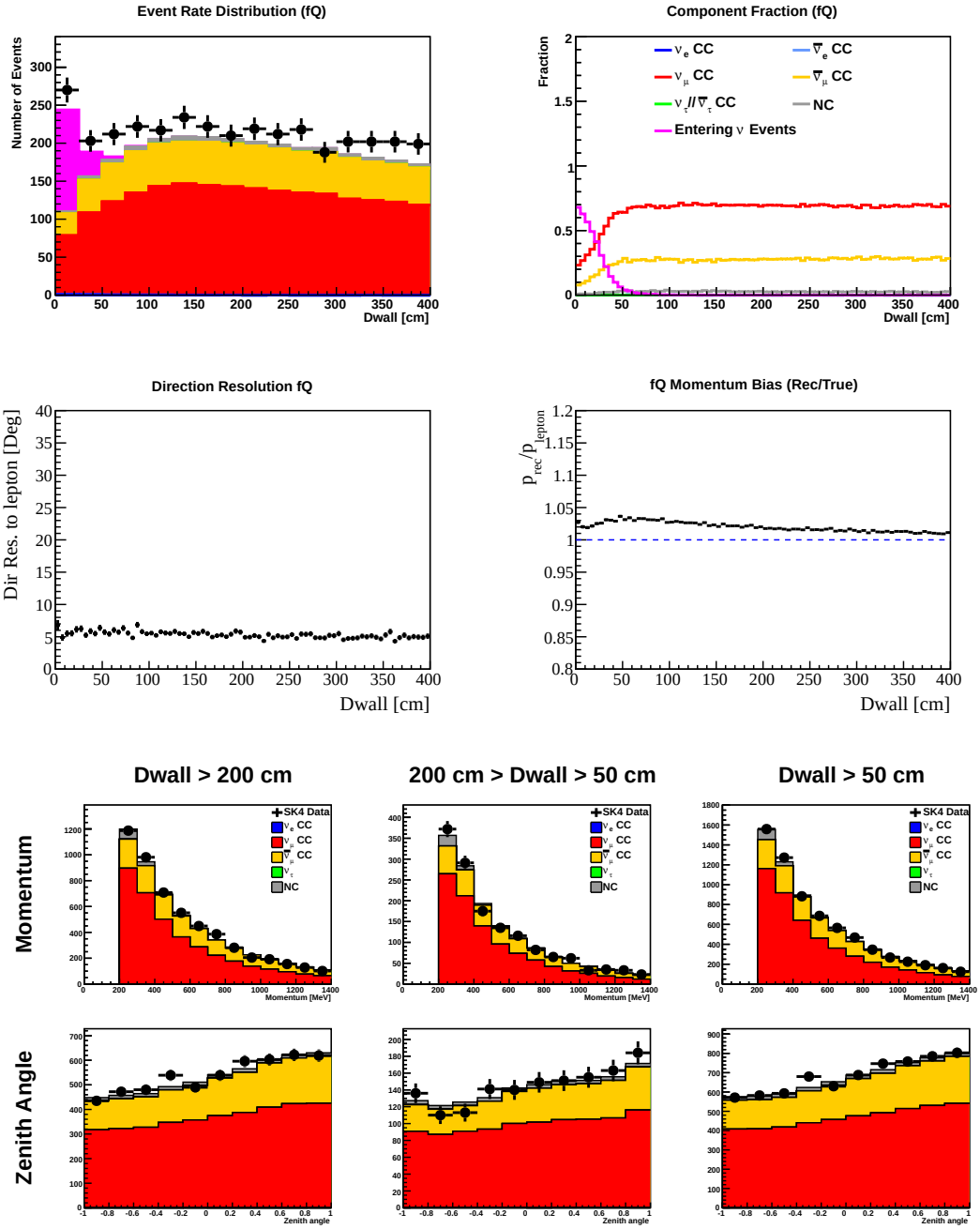

FIGURE B.4: Basic distribution for SubGeV single-ring μ-like 1 decay-e sample reconstructed and selected by fiTQun.

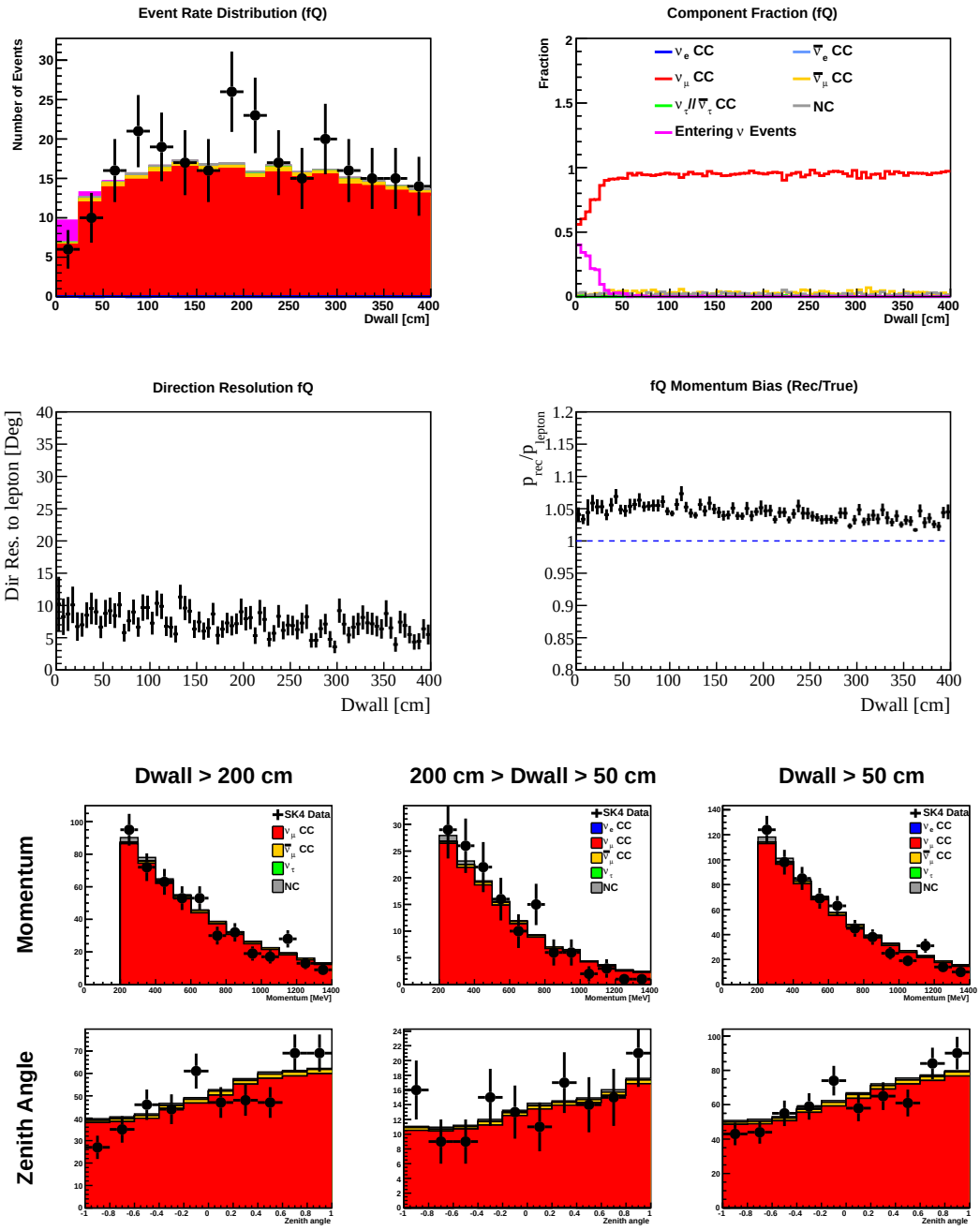

FIGURE B.5: Basic distribution for SubGeV single-ring μ-like with 2 or more decay-e sample reconstructed and selected by fiTQun.

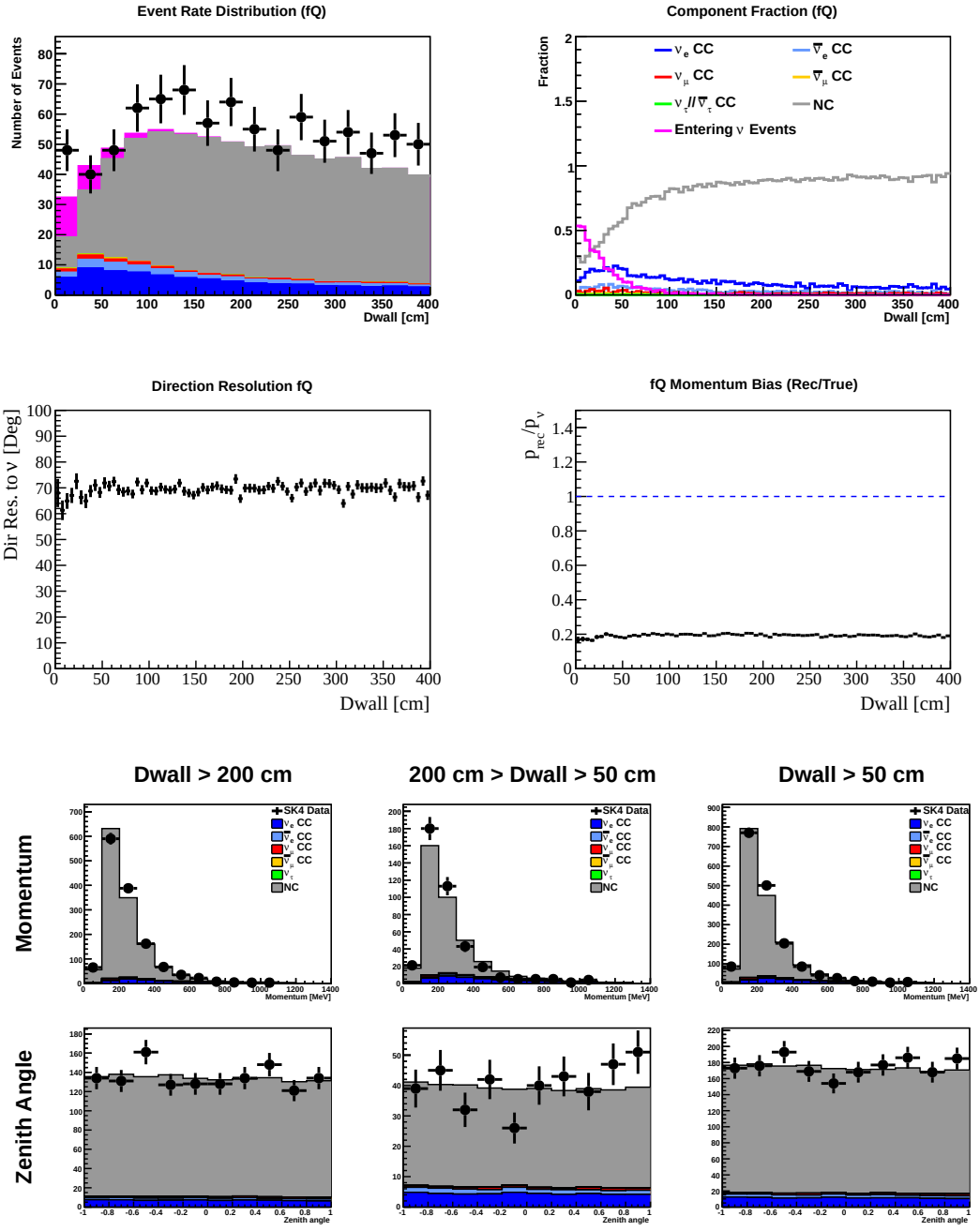

FIGURE B.6: Basic distribution for SubGeV two-ring π^0 sample reconstructed and selected by fiTQun.

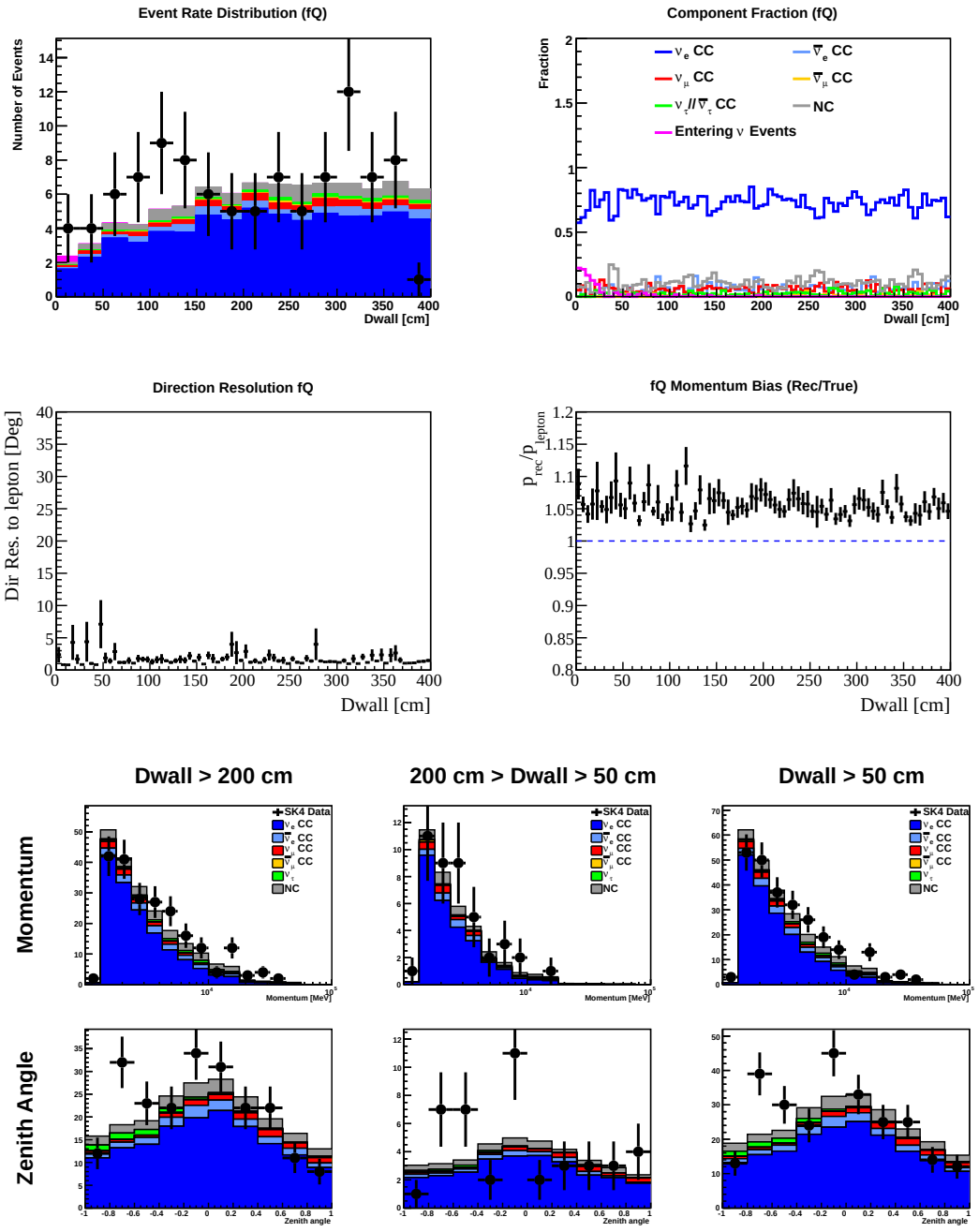

FIGURE B.7: Basic distribution for MultiGeV single-ring ν_e-like sample reconstructed and selected by fiTQun.

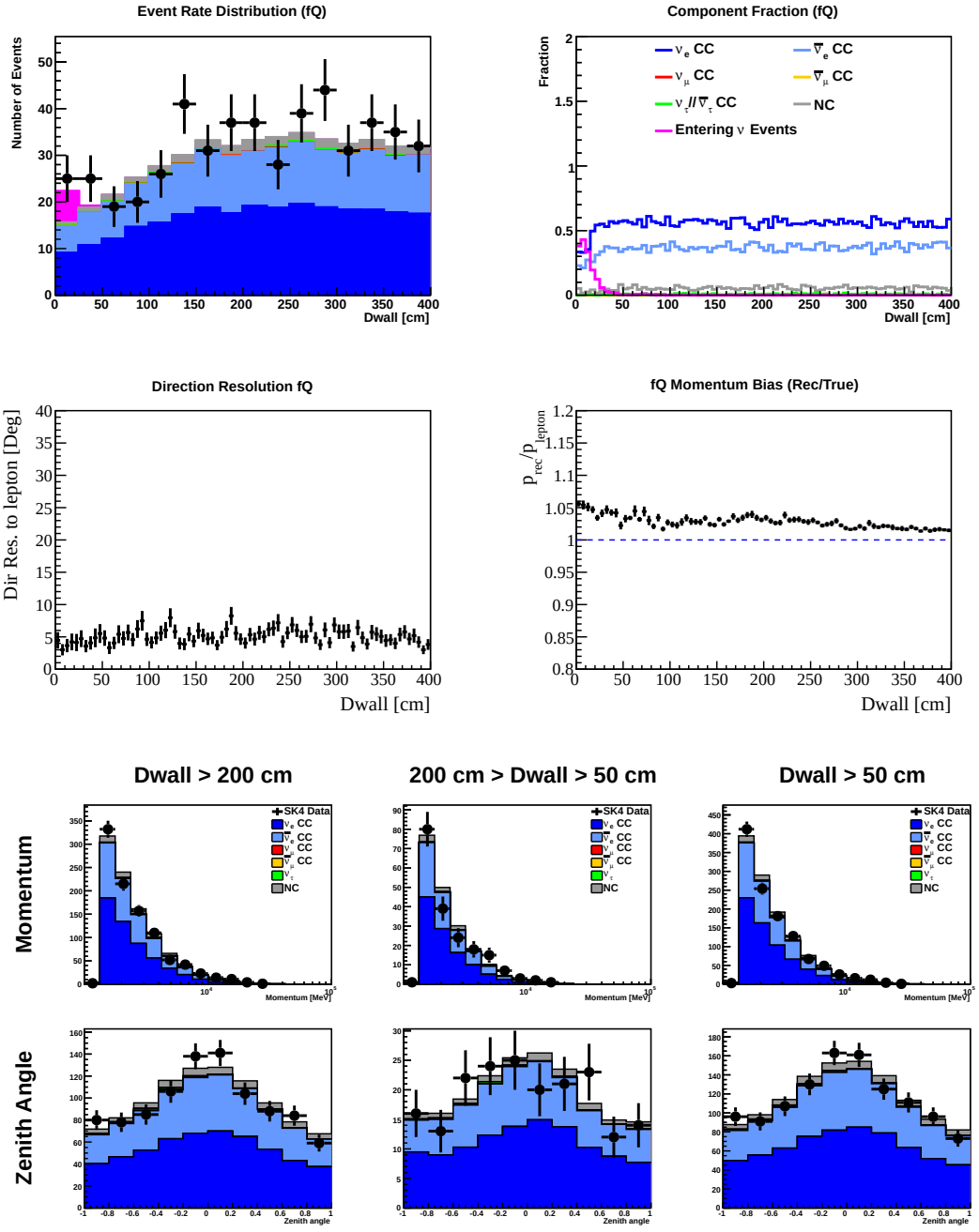

FIGURE B.8: Basic distribution for MultiGeV single-ring $\bar{\nu}_e$-like sample reconstructed and selected by fiTQun.

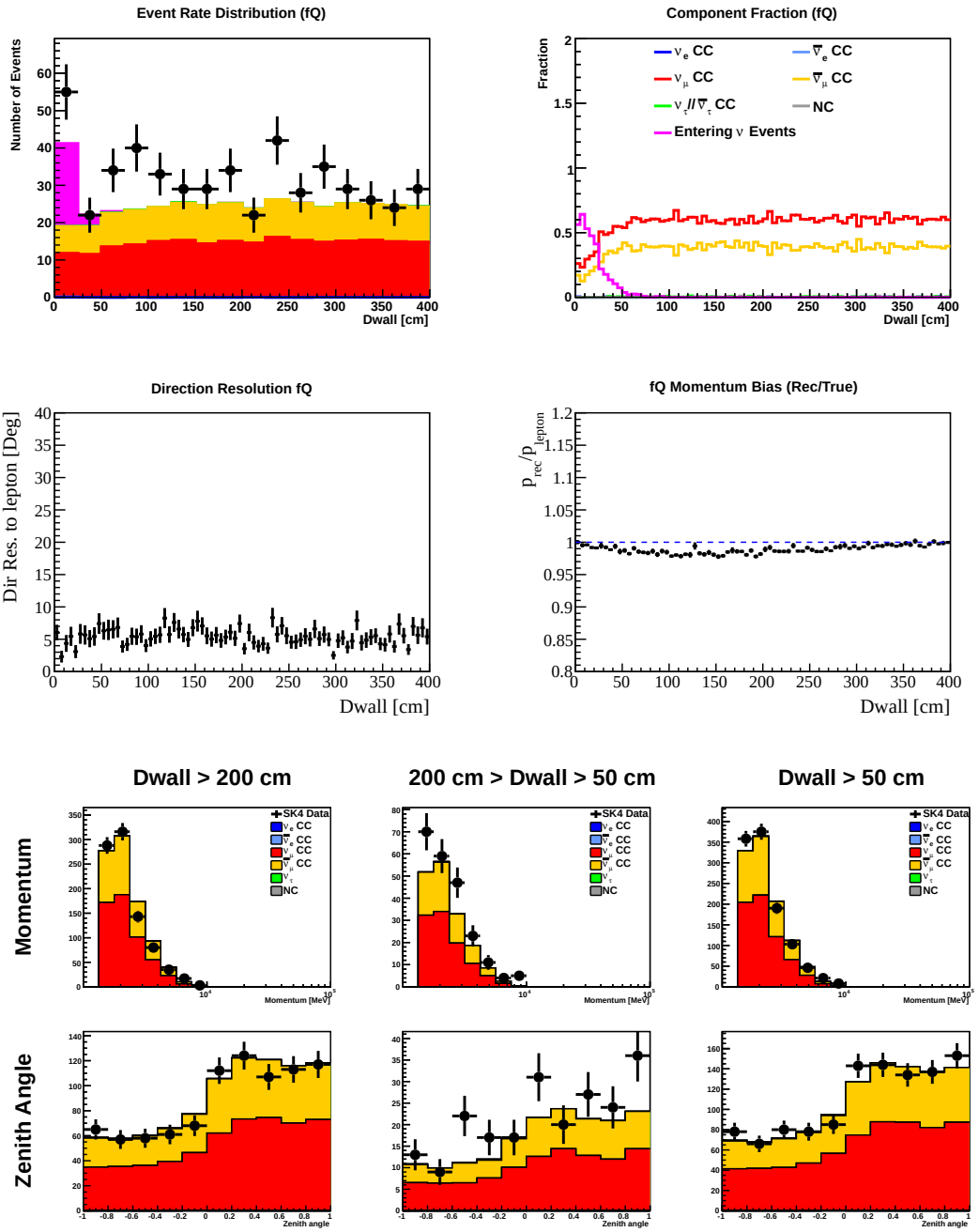

FIGURE B.9: Basic distribution for MultiGeV single-ring ν_μ-like sample reconstructed and selected by fiTQun.

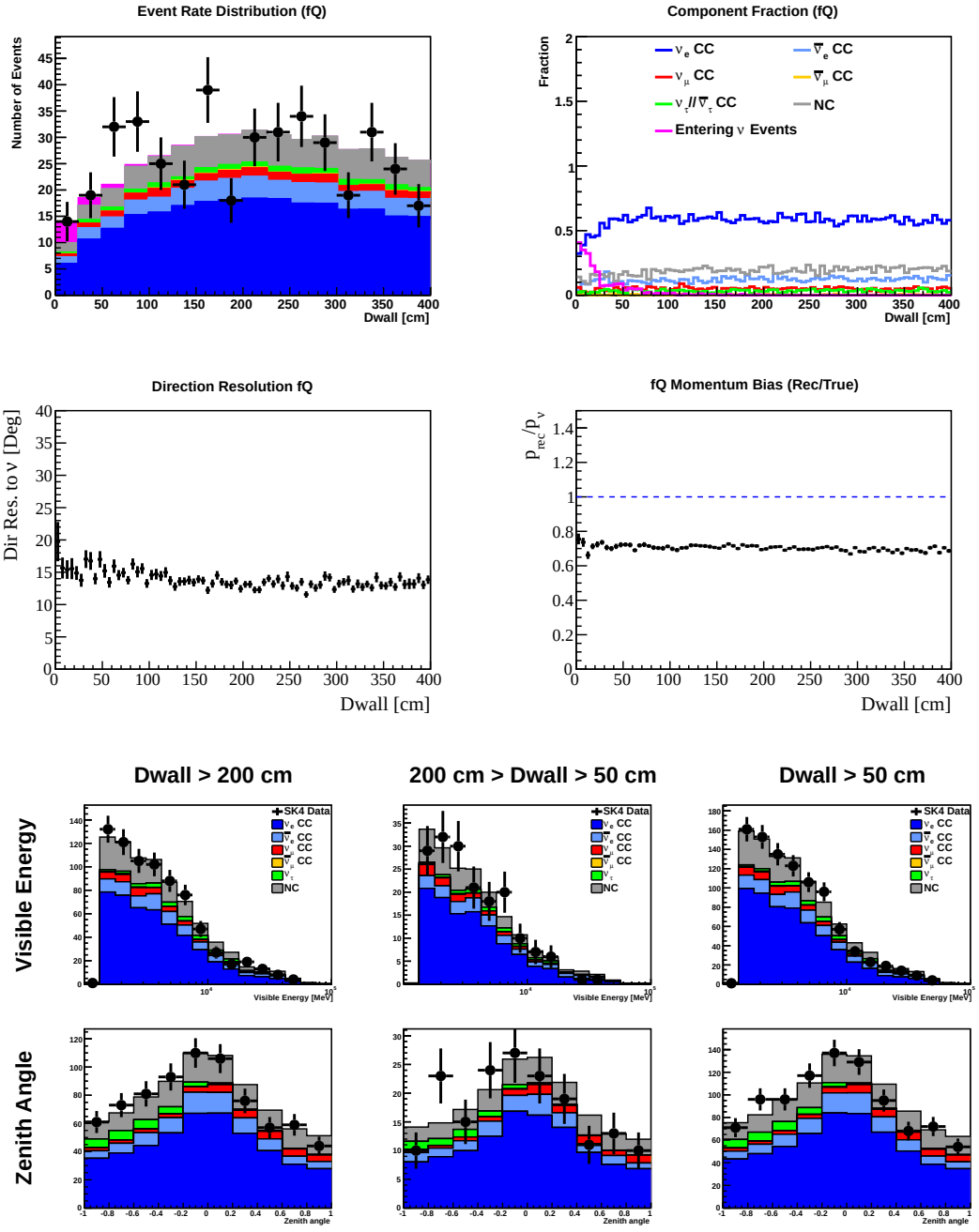

FIGURE B.10: Basic distribution for MultiGeV multi-ring ν_e-like sample reconstructed and selected by fiTQun.

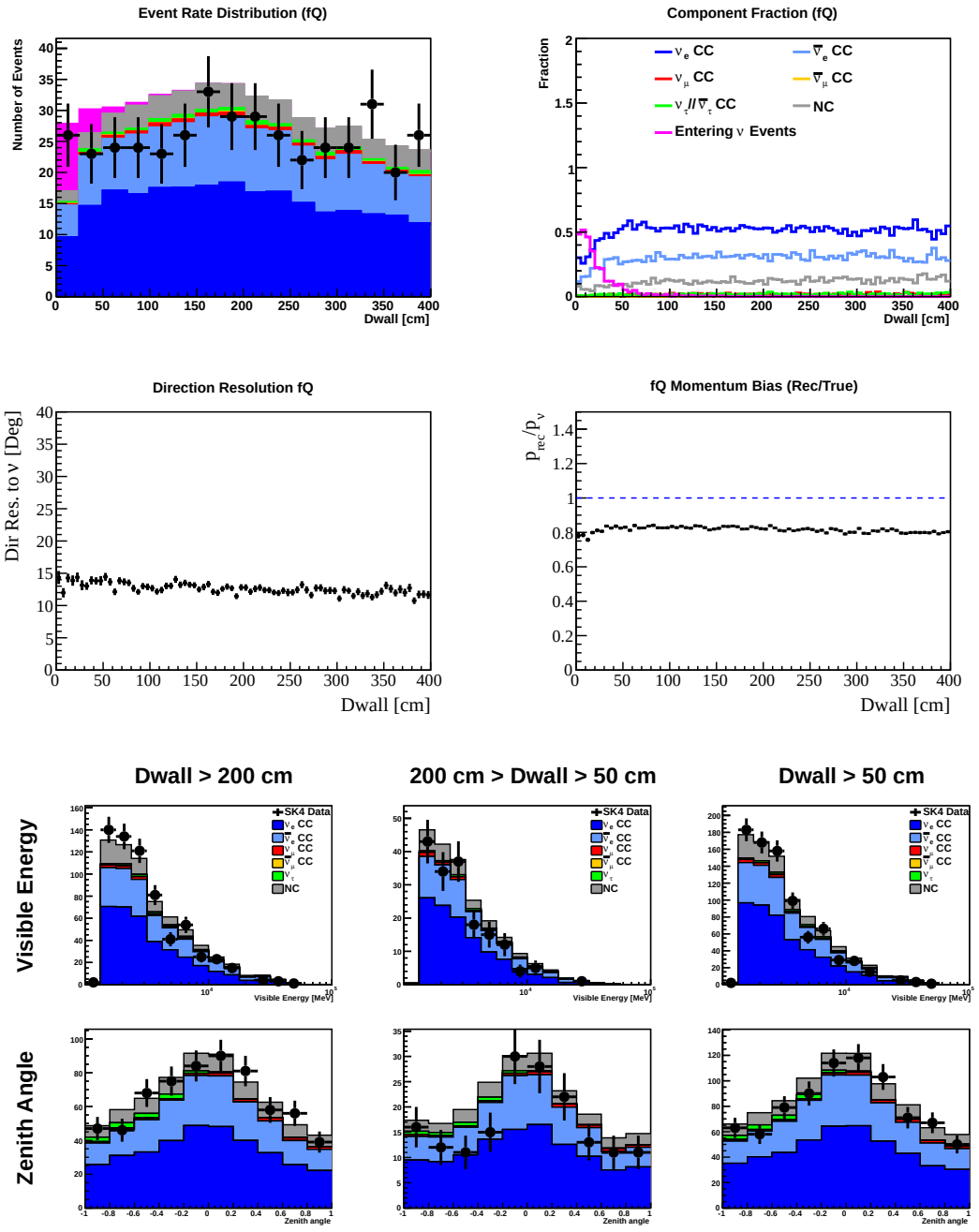

FIGURE B.11: Basic distribution for MultiGeV multi-ring $\bar{\nu}_e$-like sample reconstructed and selected by fiTQun.

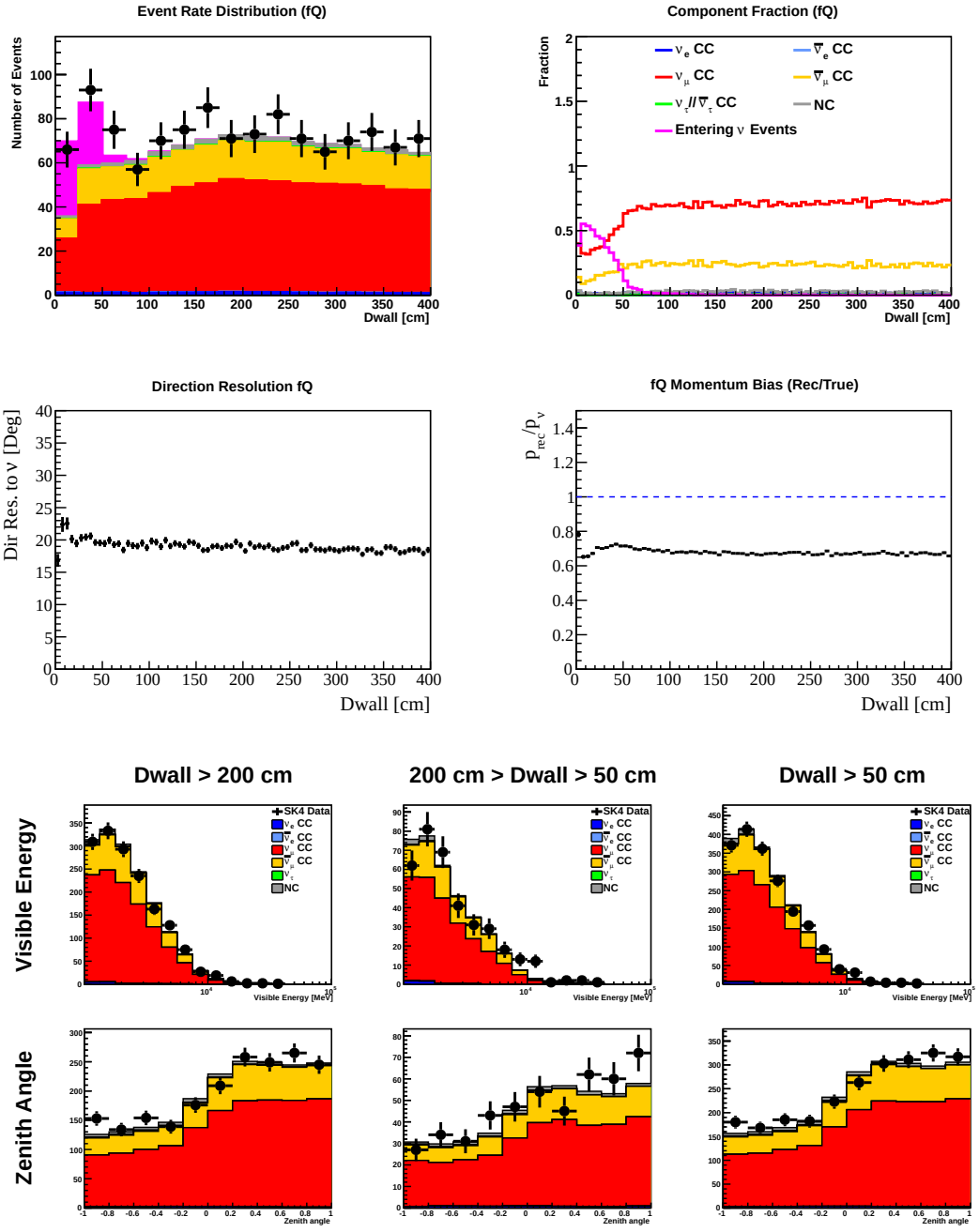

FIGURE B.12: Basic distribution for MultiGeV multi-ring μ-like sample reconstructed and selected by fiTQun.

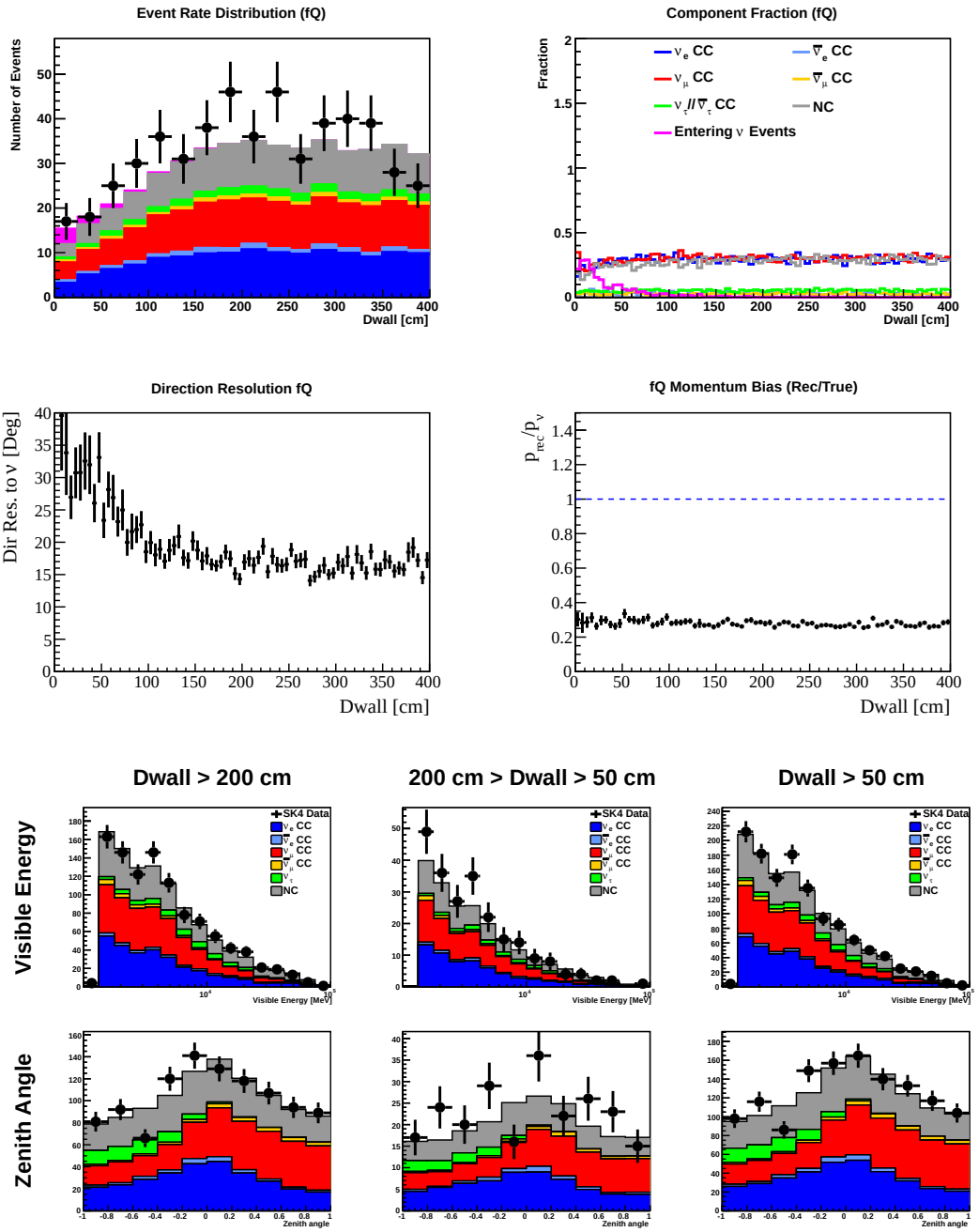

FIGURE B.13: Basic distribution for MultiGeV multi-ring *e*-like other sample reconstructed and selected by fiTQun.

Sample	CC ν_e	CC $\bar{\nu_e}$	CC $\nu_\mu + \bar{\nu_\mu}$	CC ν_τ	NC	Data	MC
Fully Contained (FC) Sub-GeV							
e-like, Single-ring							
0 decay-e	0.702	0.227	0.025	0.001	0.045	1890	1758.0
1 decay-e	0.712	0.015	0.208	0.001	0.063	222	210.2
μ-like, Single-ring							
0 decay-e	0.034	0.011	0.805	0.001	0.150	454	427.2
1 decay-e	0.001	0.000	0.968	0.000	0.031	1442	1351.5
2 decay-e	0.000	0.000	0.980	0.000	0.019	140	130.2
π^0-like							
Two-ring	0.109	0.036	0.018	0.000	0.837	403	379.4
Fully Contained (FC) Multi-GeV							
Single-ring							
ν_e-like	0.748	0.066	0.064	0.016	0.105	43	37.0
$\bar{\nu}_e$-like	0.566	0.371	0.003	0.007	0.053	190	194.1
μ-like	0.000	0.000	0.995	0.004	0.001	219	171.9
Multi-ring							
ν_e-like	0.609	0.112	0.059	0.032	0.188	174	179.6
$\bar{\nu}_e$-like	0.541	0.301	0.023	0.016	0.118	169	206.8
μ-like	0.016	0.002	0.946	0.005	0.031	475	445.1
Other	0.302	0.032	0.342	0.051	0.274	229	199.6

TABLE B.2: Sample purity broken down by neutrino flavor assuming neutrino oscillations with $\Delta m^2_{32} = 2.52 \times 10^{-3}\text{eV}^2$ and $\sin^2\theta_{23} = 0.51$. The right two columns show the sample size of the data and MC for the entire SK data set, respectively. Only fully contained events in the new region, within the range of the distance to the wall from 50cm to 200cm are shown.

Sample	CC ν_e	CC $\bar{\nu}_e$	CC $\nu_\mu + \bar{\nu}_\mu$	CC ν_τ	NC	Data	MC
Fully Contained (FC) Sub-GeV							
e-like, Single-ring							
0 decay-e	0.722	0.238	0.007	0.000	0.032	7686	7180.4
1 decay-e	0.853	0.019	0.081	0.001	0.046	818	769.5
μ-like, Single-ring							
0 decay-e	0.017	0.006	0.798	0.001	0.179	1491	1439.1
1 decay-e	0.000	0.000	0.973	0.000	0.027	6837	6437.8
2 decay-e	0.000	0.000	0.983	0.000	0.017	633	623.8
π^0-like							
Two-ring	0.064	0.020	0.012	0.000	0.903	1749	1683.9
Fully Contained (FC) Multi-GeV							
Single-ring							
ν_e-like	0.729	0.075	0.059	0.026	0.111	260	245.1
$\bar{\nu}_e$-like	0.555	0.378	0.003	0.008	0.056	1153	1169.3
μ-like	0.000	0.000	0.996	0.003	0.001	1101	1079.0
Multi-ring							
ν_e-like	0.592	0.116	0.055	0.036	0.201	933	953.0
$\bar{\nu}_e$-like	0.529	0.300	0.021	0.019	0.130	813	861.4
μ-like	0.011	0.001	0.957	0.004	0.027	2457	2388.2
Other	0.286	0.027	0.342	0.053	0.292	1267	1224.1

TABLE B.3: Sample purity broken down by neutrino flavor assuming neutrino oscillations with $\Delta m^2_{32} = 2.52 \times 10^{-3}\text{eV}^2$ and $\sin^2\theta_{23} = 0.51$. The right two columns show the sample size of the data and MC for the entire SK data set, respectively. Only fully contained events are reconstructed by fiTQun and have a FV cut of 50 cm. PC and Up-μ samples are reconstructed by APFit and no FV cut change for these two samples.

Appendix C

Distribution for systematic error evaluation

This section shows the distribution of ring counting (RC), particle identification (PID) and two staged multi-GeV multi-ring e-like separation, which is introduced in Section 6.2.2. As has been stated in Section 7.5.2, the systematic error is evaluated by fitting MC to data with smearing and shift parameters simultaneously, and this evaluation method is proceed in both of conventional FV (Dwall $>$ 200 cm) and new region (200 cm $>$ Dwall $>$ 50 cm).

Those distributions indicate no issues in the fitting procedure and no abnormal distribution observed in both detector region.

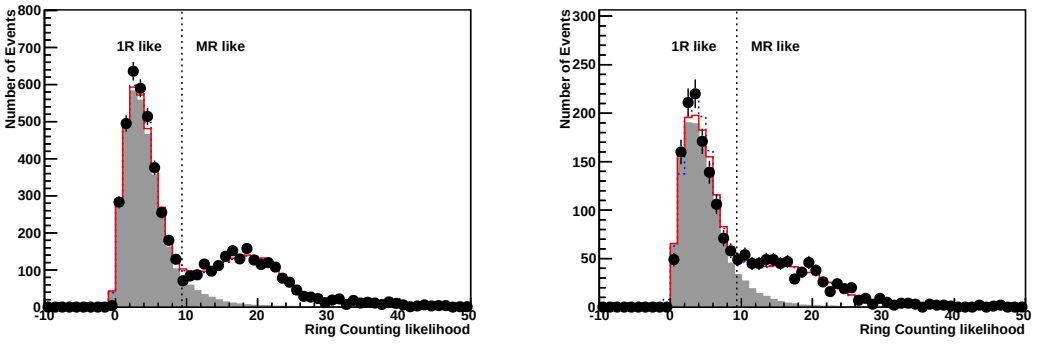

FIGURE C.1: Ring counting likelihood distribution of sub-GeV e-like events with momentum less than 400 MeV. Points show the distribution from data, while the red solid line (blue dashed line) represents the distribution after (before) fitting. The shaded histogram show events with only single-ring in the final states. Left figure shows the distribution for conventional FV (Dwall $>$ 200 cm), while right figure shows the one for new region (200 cm $>$ Dwall $>$ 50 cm). All following figures in this section have the same configuration.

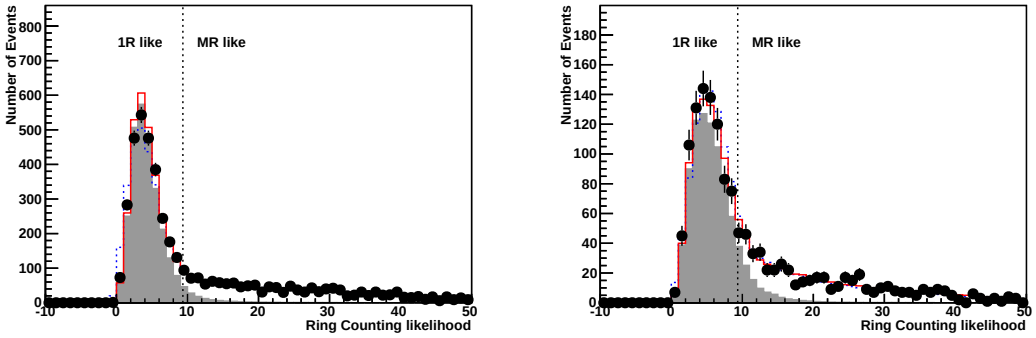

FIGURE C.2: Ring counting likelihood distribution of sub-GeV e-like events with momentum larger than 400 MeV.

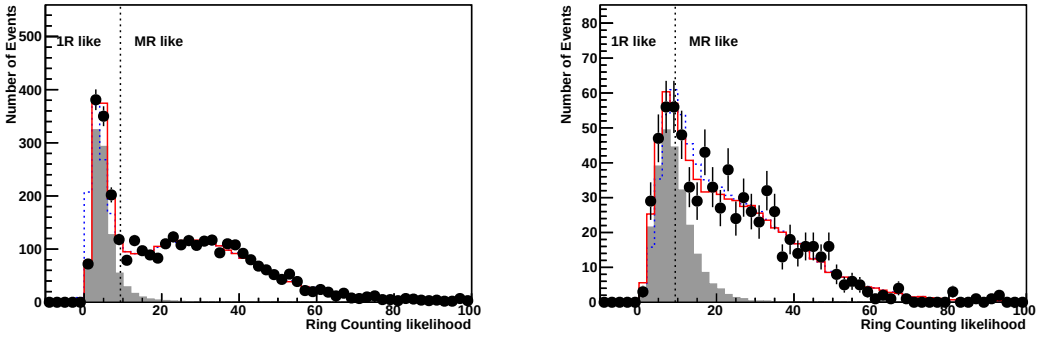

FIGURE C.3: Ring counting likelihood distribution of multi-GeV e-like events.

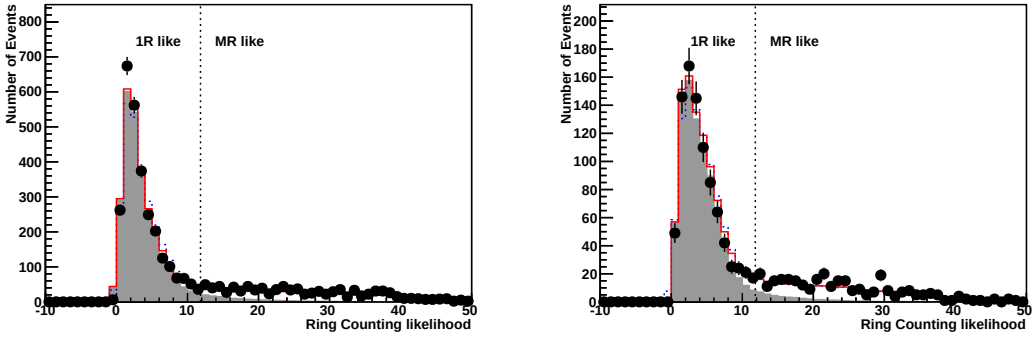

FIGURE C.4: Ring counting likelihood distribution of sub-GeV μ-like events with momentum less than 400 MeV.

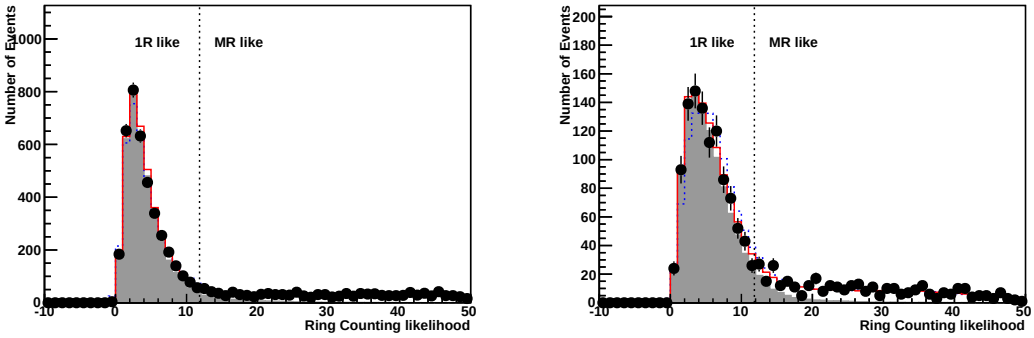

FIGURE C.5: Ring counting likelihood distribution of sub-GeV μ-like events with momentum larger than 400 MeV.

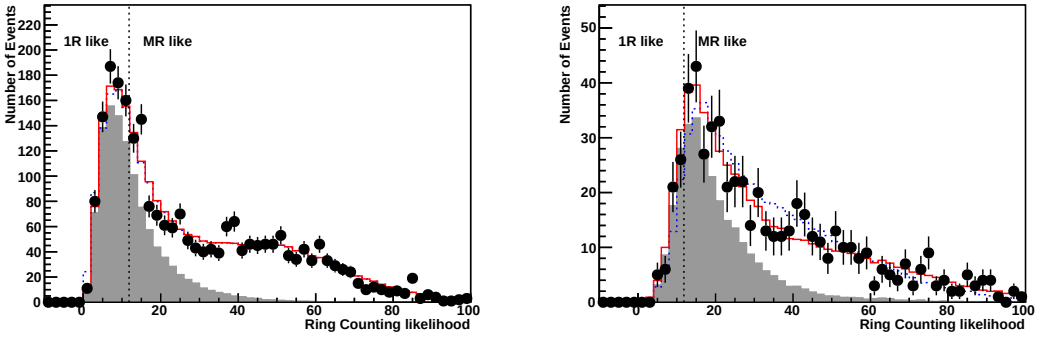

FIGURE C.6: Ring counting likelihood distribution of multi-GeV μ-like events.

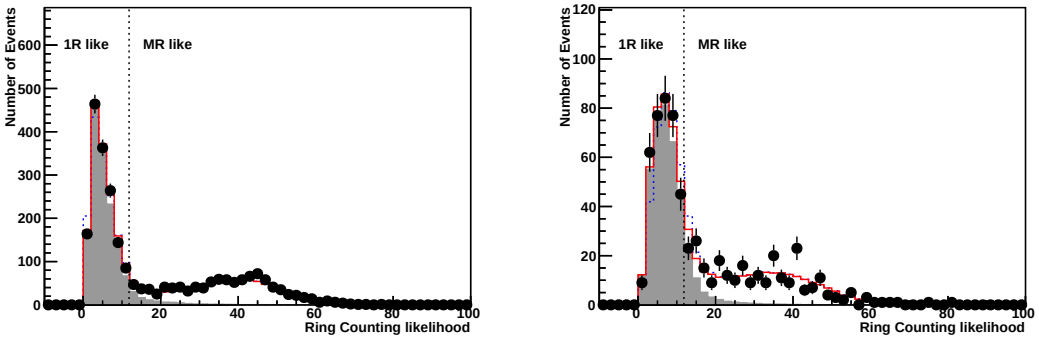

FIGURE C.7: Ring counting likelihood distribution of μ-like events with $E_{\mathrm{vis}} > 600$ MeV. This category has overlap with Figure C.5 and Figure C.6.

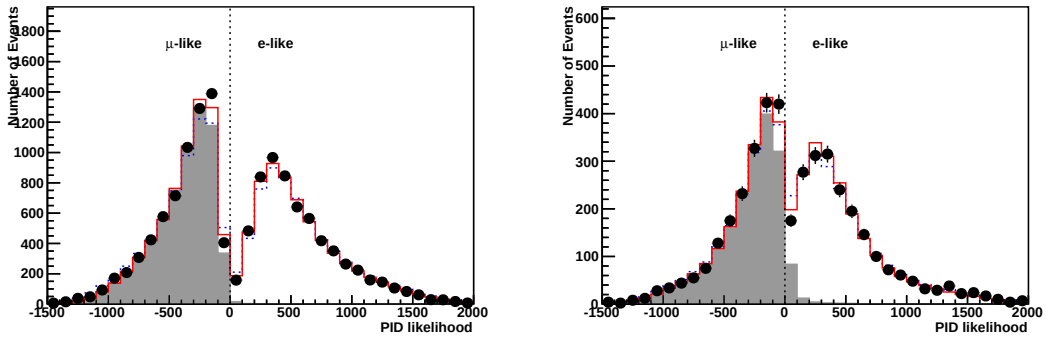

FIGURE C.8: PID likelihood distribution for sub-GeV single-ring events. The shaded histogram show ν_μ charged current interactions.

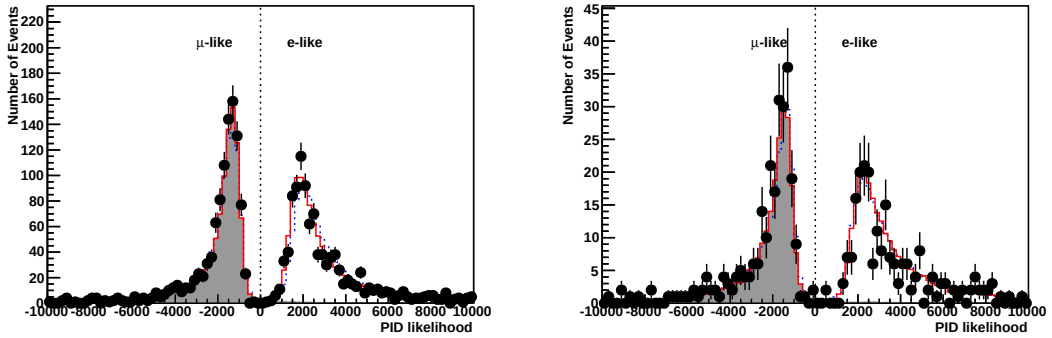

FIGURE C.9: PID likelihood distribution for multi-GeV single-ring events.

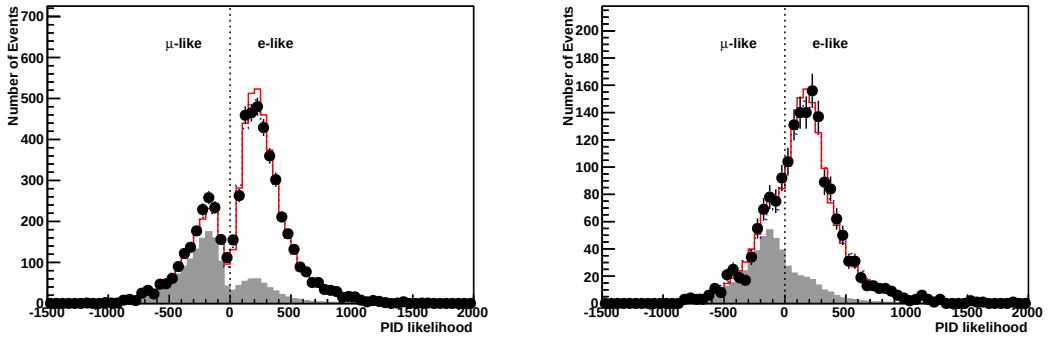

FIGURE C.10: PID likelihood distribution for sub-GeV multi-ring events.

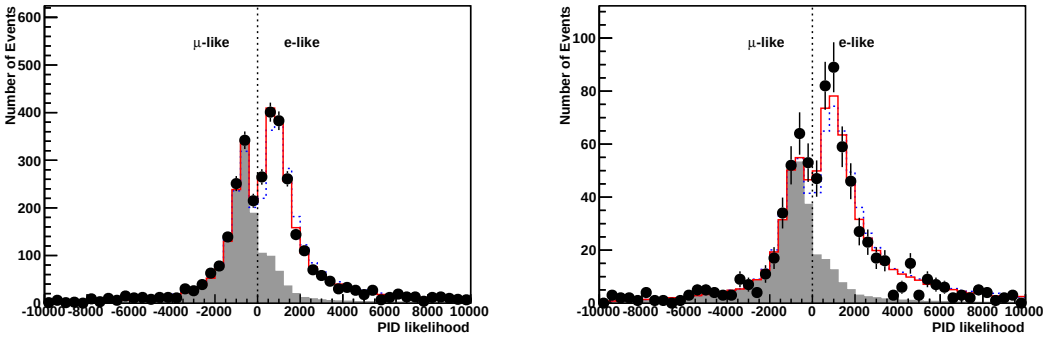

FIGURE C.11: PID likelihood distribution for sub-GeV single-ring events.

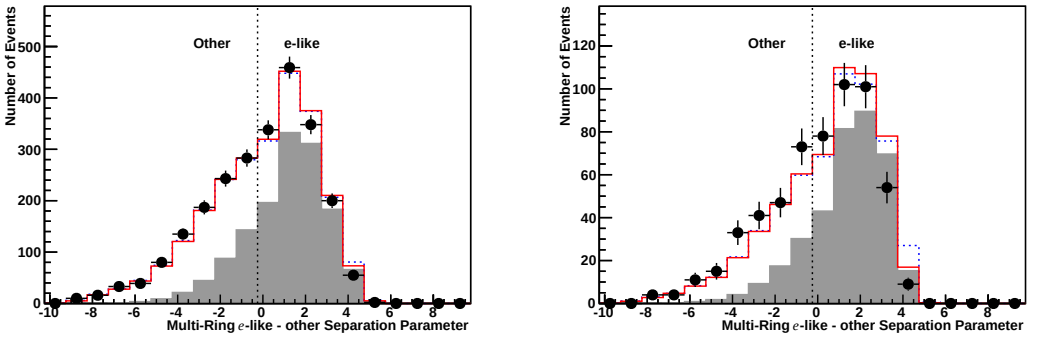

FIGURE C.12: Likelihood distribution used to separate SK-IV Multi-ring events with e-like most energetic ring into the e-like and unclassified samples. The shaded histogram show ν_e and $\bar{\nu}_e$ charged current interactions.

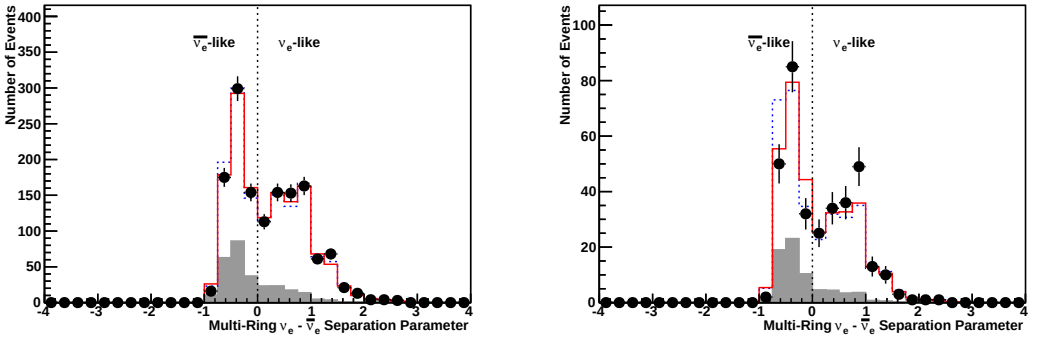

FIGURE C.13: Likelihood distribution used to separate SK-IV Multi-ring e-like events into the neutrino-like and antineutrino-like samples. The shaded histogram show $\bar{\nu}_e$ charged current interactions.

Appendix D

Statistical Study for Oscillation Analysis Result Validation

The previous Super-K atmospheric neutrino oscillation analysis paper published in 2018, which shows a best fit value at the second octant [6], utilized 328 kton-year exposure of the detector including all four SK periods, while the data recorded until Apr. 2016 of SK-IV are used. The analysis shown in this thesis, which uses two more years data: data recorded until the end of Apr. 2018 are used, shows a different octant preference. This appendix will validate the new result and discuss the reason of such change.

Figures D.1 and Table D.1 shows the normal hierarchy fit result with data until Apr. 2016 and data until Apr. 2018, assuming $\sin^2\theta_{13} = 0.0210$. Same systematic error are used in those two fits. The fit result for mass split $|\Delta m^2_{32}|$ and CP phase δ_{CP} are found to be in consistent for those two data set. However, the absolute χ^2 value of best fit result, increased from 551.6 to 575.2 when two more years data added. The preference on $\sin^2\theta_{23}$ octant also changed from second to first.

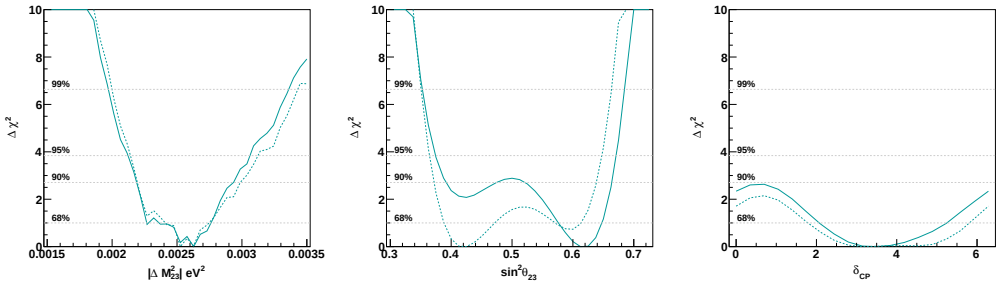

FIGURE D.1: Constraints on neutrino oscillation contours from SK-IV atmospheric neutrino data with expanded FV ($D_{\text{wall}} > 50$ cm) assuming $\sin^2\theta_{13} = 0.0210 \pm 0.0011$. Only normal hierarchy fit result is shown here. The solid line represents the result with data until Apr. 2016, while the dashed line show the result with data until Apr. 2018. Both of them are offset with their respective minimal χ^2 value.

Fit within expanded FV	Apr. 2018		Apr. 2016	
Hierarchy	NH	IH	NH	IH
χ^2	576.5	579.0	552.2	557.1
$\sin^2\theta_{23}$ (1^{st} oct.)	$0.425^{+0.046}_{-0.037}$	$0.425^{+0.055}_{-0.036}$	Excluded in 1σ	$0.413^{+0.047}_{-0.030}$
$\sin^2\theta_{23}$ (2^{nd} oct.)	$0.600^{+0.013}_{-0.030}$	$0.588^{+0.022}_{-0.037}$	$0.613^{+0.035}_{-0.036}$	$0.613^{+0.027}_{-0.049}$
$\lvert\Delta m^2_{32}\rvert$ [$\times 10^{-3}$ eV^2]	$2.53^{+0.22}_{-0.12}$	$2.53^{+0.14}_{-0.31}$	$2.63^{+0.13}_{-0.36}$	$2.63^{+0.11}_{-0.43}$
δ_{CP}	$3.14^{+2.67}_{-1.35}$	$4.89^{+1.51}_{-3.46}$	$3.49^{+1.76}_{-1.42}$	$3.49^{+2.79}_{-3.49}$

TABLE D.1: Summary of parameter estimates for analysis with data until Apr. 2016 and data until Apr. 2018.

To validate the fit result, MC ensembles were generated assuming statistical fluctuations of the pseudo data sets according to the current detector exposure, and Gaussian fluctuations of the systematic errors.

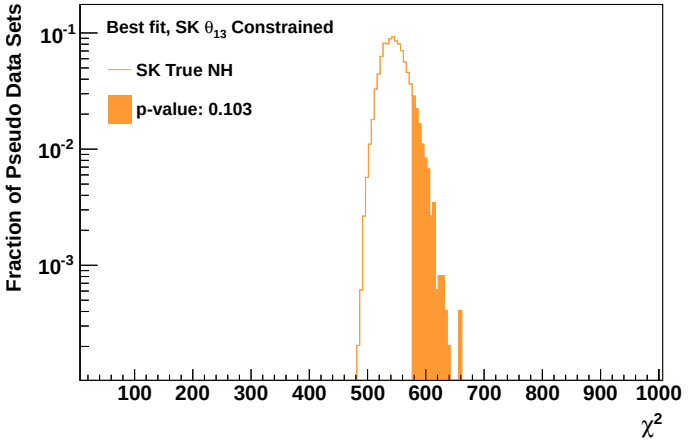

FIGURE D.2: Distributions of the best fit χ^2 values fits to pseudo data sets. The pseudo data have been generated with the best fit value in NH expanded FV θ_{13} constrained fit shown in Table 7.13. Shaded portions of the histograms denote the fraction of pseudo data sets with more extreme values than that observed in the data, $\chi^2_{NH} = 576.5$.

Figure D.2 shows the distribution of the best fit χ^2 values fits to pseudo data sets. During the pseudo data generation, only the events corresponding to the livetime from Apr. 2016 to Apr. 2018 were generated with fluctuations and then merged with the observed data, which was taken until Apr. 2016. p-value for 576.5, the best fit χ^2 of expanded FV, is 0.103. Figure D.3 shows the absolute χ^2 distribution for each event category. The error bar of pseudo data (blue box) represents one σ uncertainty from statistical fluctuations and systematic error. The observed data in this analysis is shown by red triangle. The top two categories which have largest deviation from pseudo data center value are multi-GeV single-ring ν_e-like sample and multi-GeV multi-ring $\bar{\nu}_e$-like

sample. The zenith angle distribution for both two samples are shown in Figure D.4 and Figure D.5. No abnormal is observed.

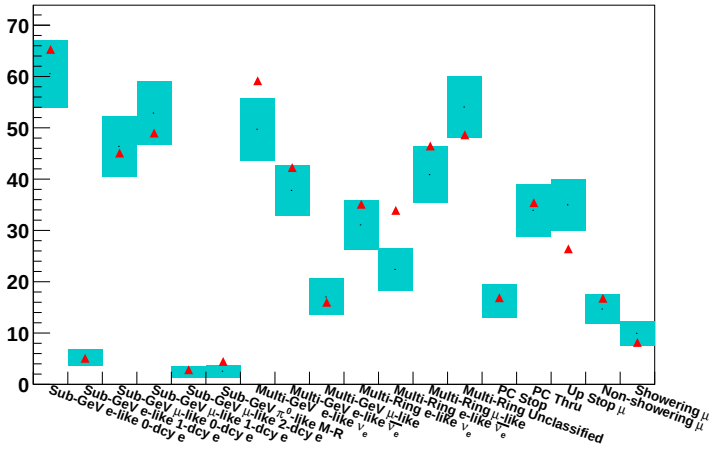

FIGURE D.3: Distributions of the best fit χ^2 of observed data (red triangle) and pseudo data sets (blue box). The error bar of pseudo data sets result represents the 1 σ uncertainty from statistical fluctuations and systematic errors. The pseudo data have been generated with the best fit value in NH expanded FV θ_{13} constrained fit shown in Table 7.13.

Similar study is done to validate the octant preference change after updating data. Figure D.6 shows the distribution of the difference in the best fit χ^2 values between fits with $\sin^2\theta_{23}$ fixed to 0.4 and 0.6 to pseudo data set. In the cyan (orange) histogram the pseudo data have been generated assuming $\sin^2\theta_{23} = 0.4$ (0.6) hierarchy at normal hierarchy. Pseudo data corresponding to two years livetime were generated and then merged with the observed data taken until Apr. 2016. The p-value to observed the first octant with $\Delta\chi^2 = -0.73$ is 0.024 (0.161) when true $\sin^2\theta_{23} = 0.6$ (0.4). Figure D.7 shows the $\Delta\chi^2$ distribution for each event category. The top two categories which have largest deviation from pseudo data center value are sub-GeV single-ring μ-like 1 decay e sample and multi-GeV single-ring ν_e-like sample. The zenith angle distribution for both two samples are shown in Figure D.8 and Figure D.9. This change mainly comes from less upward-going for sub-GeV muon events and multi-GeV e-like events, and no abnormal distribution is observed.

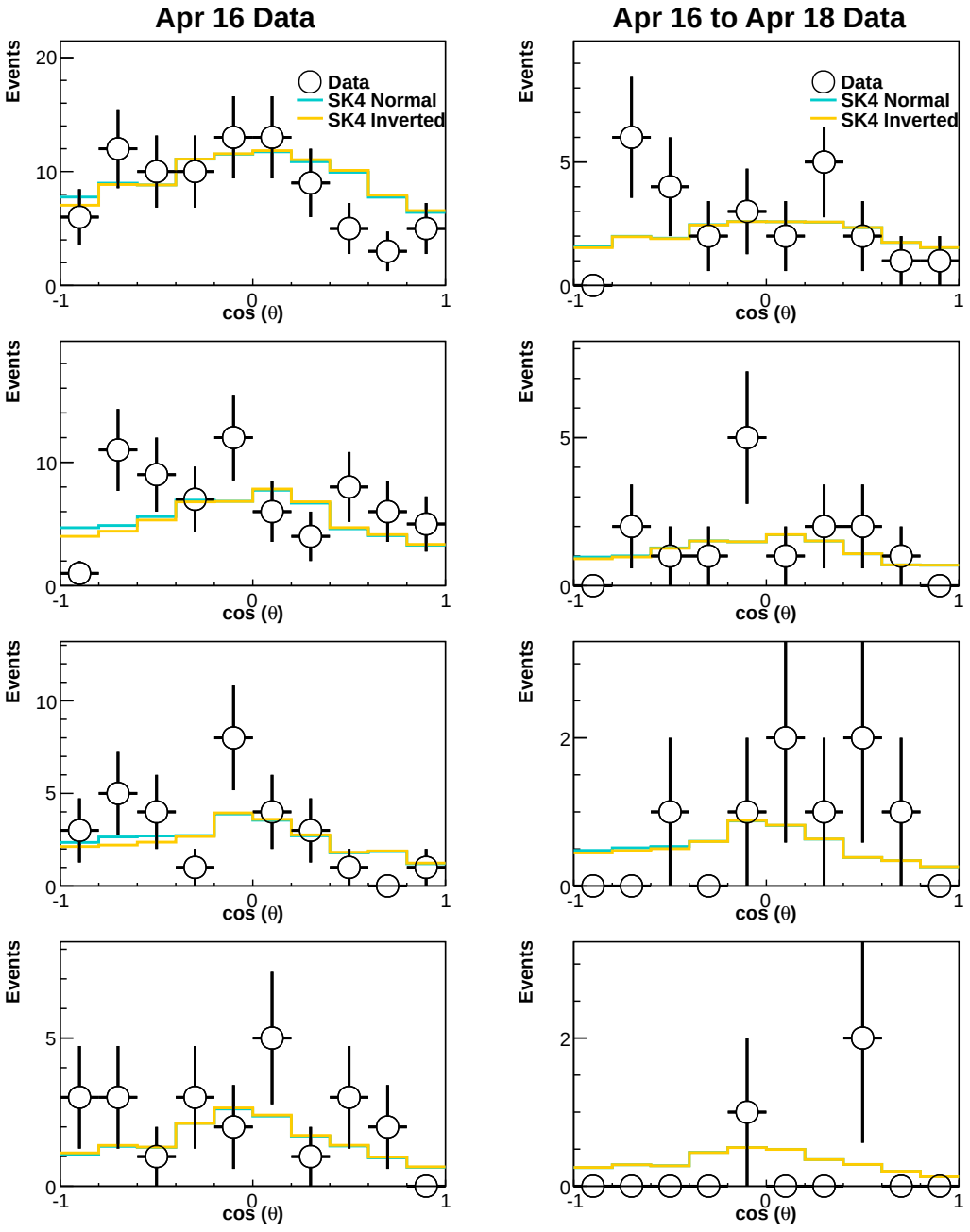

FIGURE D.4: Zenith angle distributions for of data (open circle) and best fit MC for both NH (blue line) and IH (orange line). Multi-GeV single ring ν_e-like events are shown here. Left figures are for data taken before Apr. 2016, while right figures are for data taken between Apr. 2016 to Apr. 2018. The momentum range are 1330 MeV $\sim$ 2500 MeV, 2500 MeV $\sim$ 5000 MeV, 5000 MeV $\sim$ 10000 MeV, $>$ 10000 MeV from most top figures, respectively.

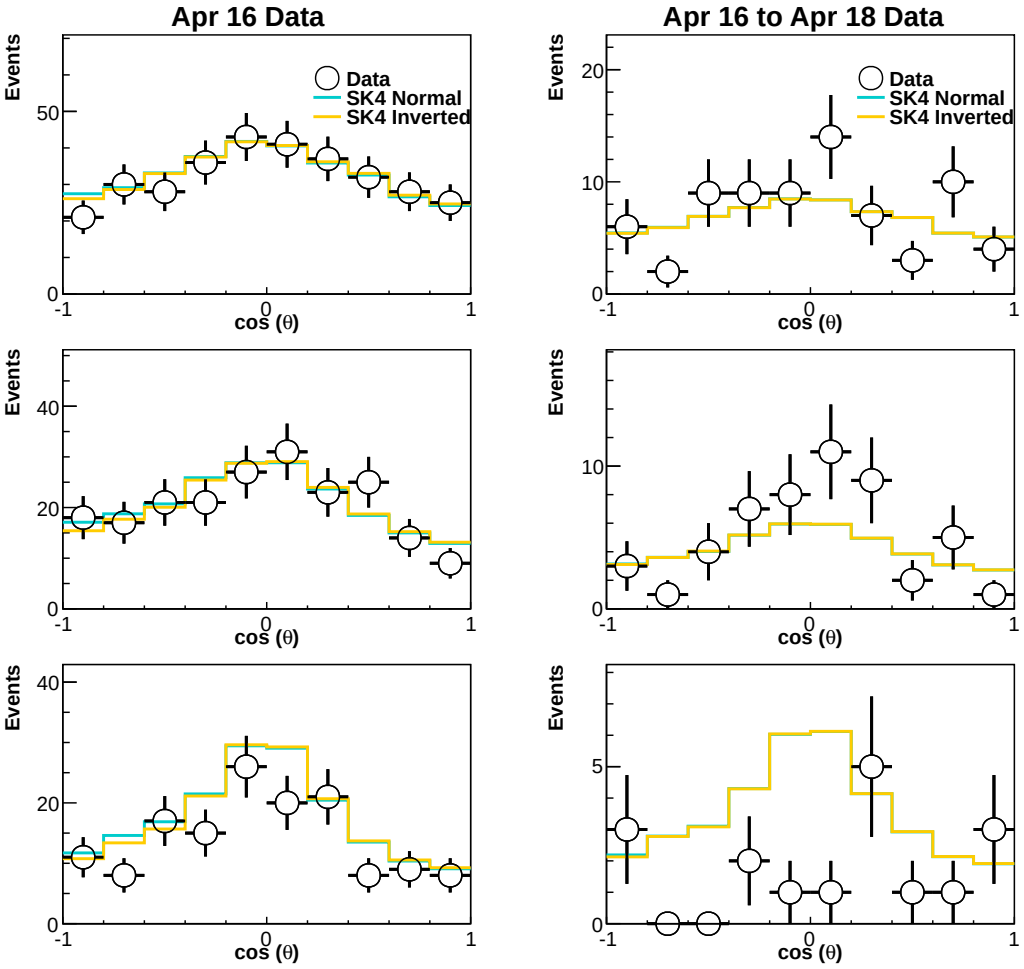

FIGURE D.5: Zenith angle distributions for of data (open circle) and best fit MC for both NH (blue line) and IH (orange line). Multi-GeV multi ring $\bar{\nu}_e$-like events are shown here. Left figures are for data taken before Apr. 2016, while right figures are for data taken between Apr. 2016 to Apr. 2018. The momentum range are 1330 MeV $\sim$ 2500 MeV, 2500 MeV $\sim$ 5000 MeV, $>$ 5000 MeV from most top figures, respectively.

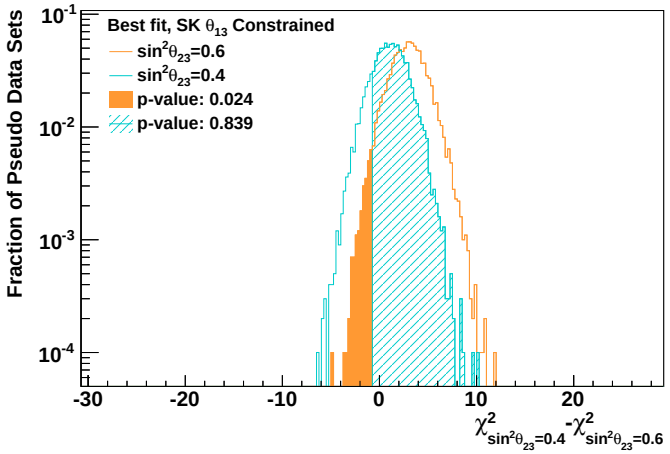

FIGURE D.6: Distributions of the difference in best fit χ^2 values between fits with $\sin^2\theta_{23}$ fixed to 0.4 and 0.6 to pseudo data sets. In the cyan (orange) histogram the pseudo data have been generated assuming $\sin^2\theta_{23} = 0.4$ (0.6) hierarchy at normal hierarchy. Shaded portions of the histograms denote the fraction of pseudo data sets with more extreme values than that observed in the data, $\Delta\chi^2_{data} = -0.73$.

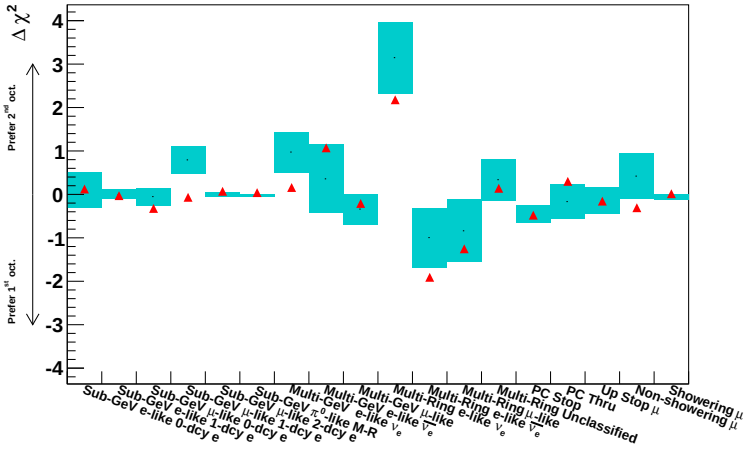

FIGURE D.7: Distributions of the best fit χ^2 of observed data (red triangle) and pseudo data sets (blue box) generated with true $\sin^2\theta_{23} = 0.6$. The error bar of pseudo data sets result represents the one σ uncertainty from statistical fluctuations and systematic errors. The pseudo data have been generated with the best fit value in NH expanded FV θ_{13} constrained fit shown in Table 7.13.

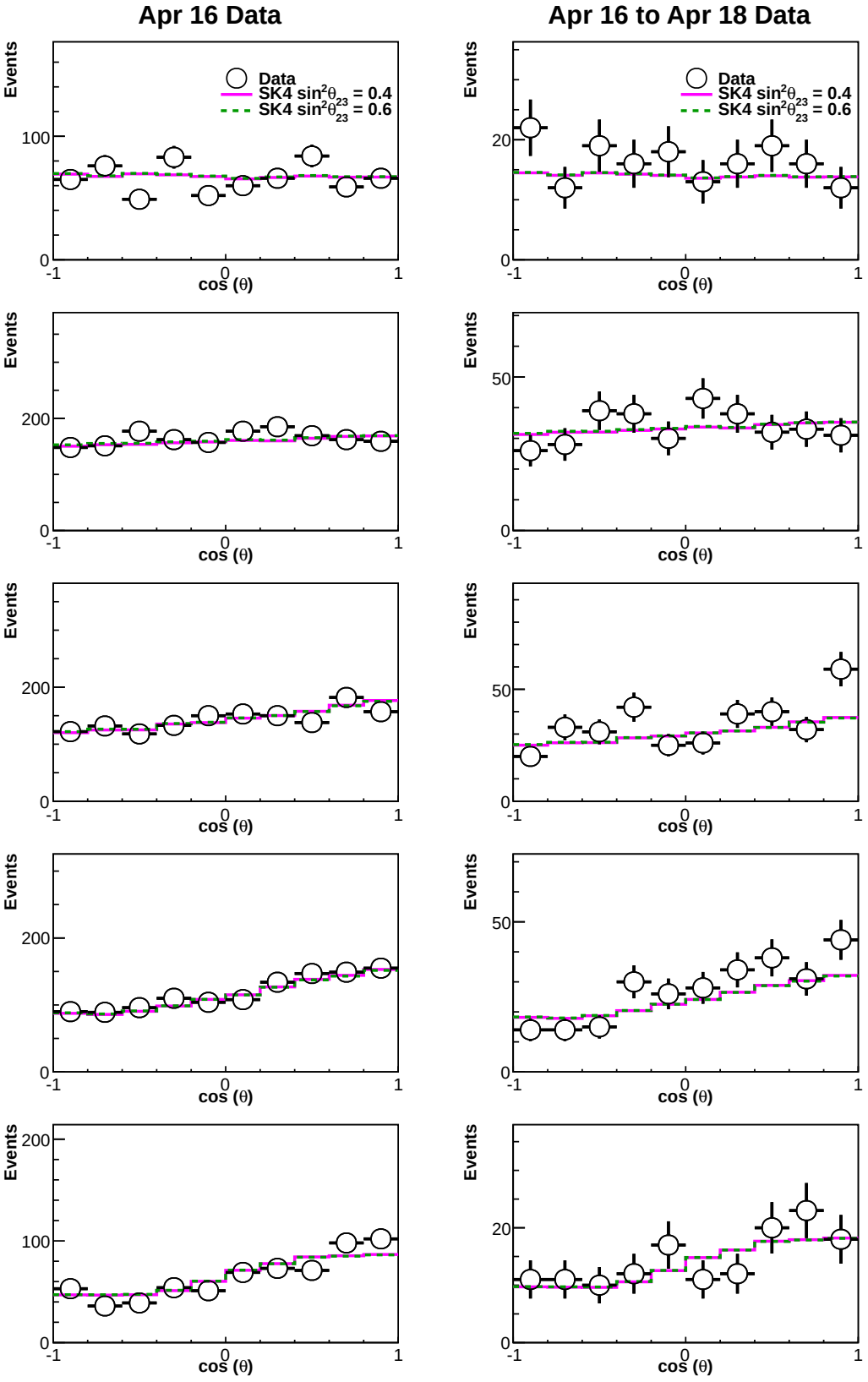

FIGURE D.8: Zenith angle distributions for of data (open circle) and best fit MC for $\sin^2\theta_{23} = 0.4$ (magenta line) and 0.6 (green dashed line). Sub-GeV single ring μ-like 1-decay electron events are shown here. Left figures are for data taken before Apr. 2016, while right figures are for data taken between Apr. 2016 to Apr. 2018. The momentum range are 100 MeV $\sim$ 200 MeV, 200 MeV $\sim$ 300 MeV, 300 MeV $\sim$ 600 MeV, 600 MeV $\sim$ 1000 MeV, 1000 MeV $\sim$ 1330 MeV from most top figures, respectively.

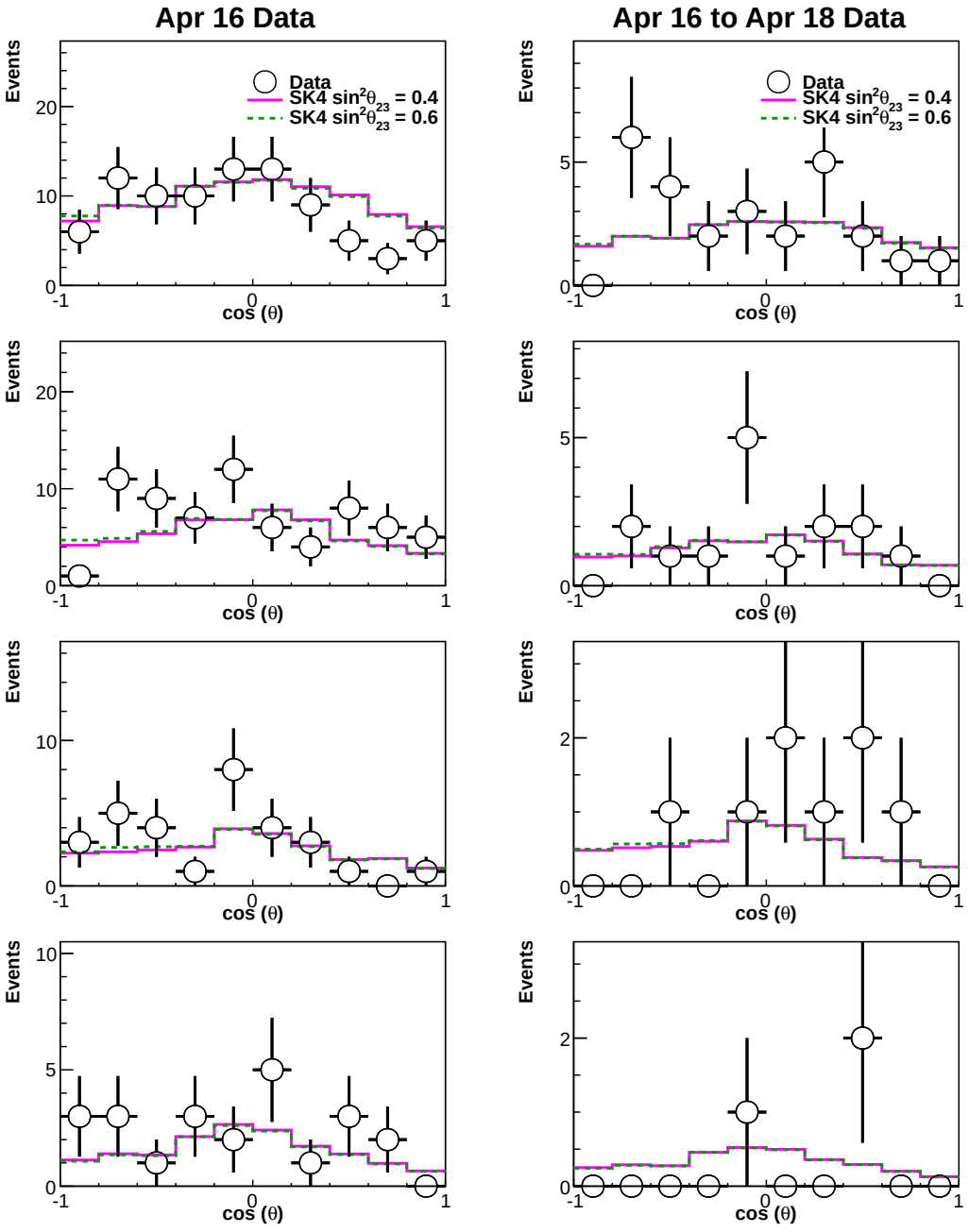

FIGURE D.9: Zenith angle distributions for of data (open circle) and best fit MC for both $\sin^2\theta_{23} = 0.4$ (magenta line) and 0.6 (green dashed line). Multi-GeV single ring ν_e-like events are shown here. Left figures are for data taken before Apr. 2016, while right figures are for data taken between Apr. 2016 to Apr. 2018. The momentum range are 1000 MeV $\sim$ 2500 MeV, 2500 MeV $\sim$ 5000 MeV, 5000 MeV $\sim$ 10000 MeV, >10000 MeV from most top figures, respectively.

Appendix E

Improvement of decay electron detection for fiTQun

Decay electrons (or positrons) from muons or charged pions are important in the atmospheric neutrino analysis at Super-K, therefore, a higher tagging efficiency is desirable. The decay electron tagging efficiency is evaluated by taking the ratio of the number of detected Michel electrons and the number of the stopping cosmic ray muon events.

The event selection criteria for the stopping cosmic ray muon are as following:

1. Total charge in ID $>$ 1000 p.e.
2. Goodness of stopping muon fit algorithm $>$ -0.9, which means the algorithm fit the stopping muon track successfully.
3. Estimated muon stopping point is within fiducial volume, which is defined as the region located more than 2 m from the ID wall here.

Figure E.1 shows the distribution of the decay time of the tagged Michel electron, which is defined as the time difference with the parent muon. The tagging efficiency, which is defined as the ratio between the number of tagged electron and the expectation, is near 100% when the decay time is long (i.e. $>$ 1200 ns) for both of APFit and fiTQun. However, the tagging efficiency decreases significantly for the Michel electrons with short decay time, especially for multi-GeV muon, as shown in Figure E.2. The decay e detection efficiency of the old version fiTQun (v4r2) is also lower than that of APFit.

As introduced in Section 6.2.2, the decrease for multi-GeV muon in the short decay time region is mainly to the assumption: all vertex positions are assumed to lie close to the

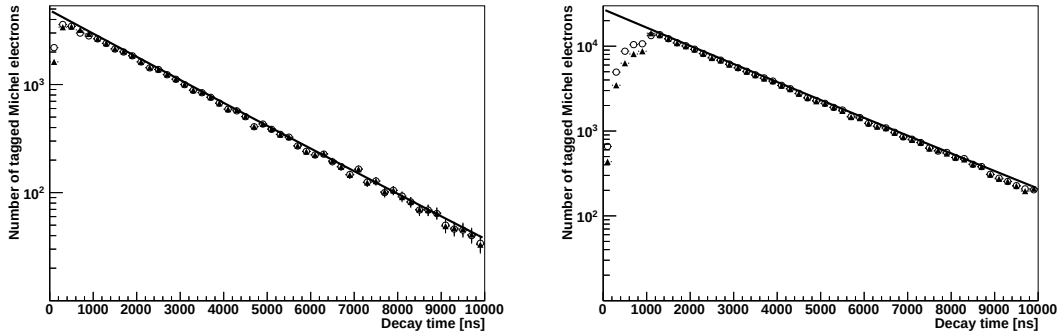

FIGURE E.1: Distribution of the decay time of tagged Michel electron (or position) from cosmic ray muon. The left figure shows the sub-GeV cosmic ray muon while the right figure is for multi-GeV muon. Open circles are the electrons tagged by APFit, and full triangles are for fiTQun. The solid line is the expectation based on the number of cosmic ray muons.

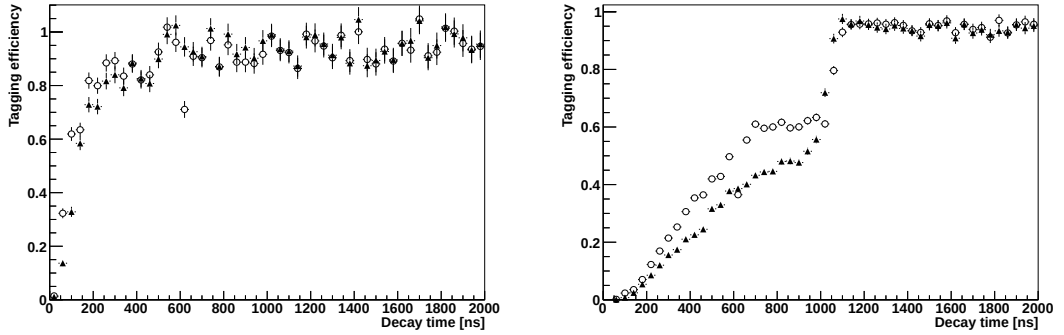

FIGURE E.2: Tagging efficiency for the Michel electron from cosmic ray muon. The left figure shows the sub-GeV cosmic ray muon while the right figure is for multi-GeV muon. Open circles are the electrons tagged by APFit, and full triangles are for fiTQun. The error bars indicate the statistical error.

pre-fit vertex when the peak-finding algorithm runs. This assumption is broken when the primary particle travels a significant distance from the interaction vertex, as for high momenta muons, which leads that the peak formed by the Michel electron smeared.

To resolve this issue, the vertex pre-fitting and peak-finding algorithm are rerun after masking the hits caused by the primary particle to improve decay electron reconstruction efficiency. The vertex position used in the goodness function $\boldsymbol{x}$ is then close to the vertex of the secondary particle, and the peak on goodness function becomes larger, as shown in Figure E.3.

Besides, the original time window, which is defined from -180 ns $\sim$ 800 ns around the main peak, will also be extended if many hits are around the edge during this process, to deal with the particle activity occurred near the time window boundary. The cut to extend the time window is 9hits / 70ns, which is consistent with the threshold defined in Equation 6.6.

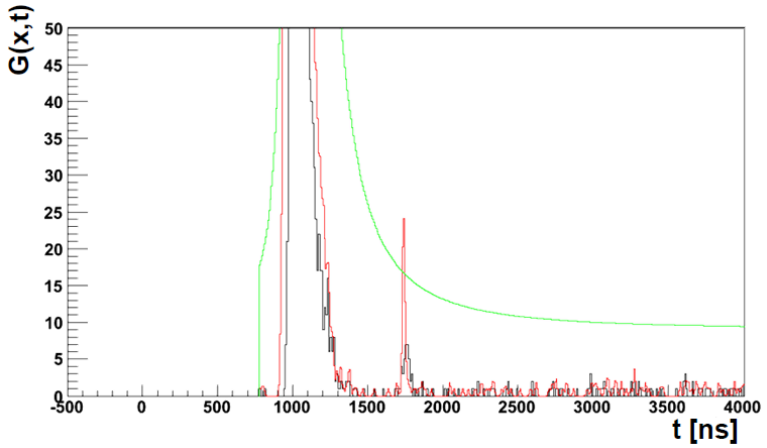

FIGURE E.3: Goodness as a function of hit time for an event with a mutli-GeV muon and a Michel electron. The black line shows the goodness as a function of hit time with the vertex fixed to the pre-fix vertex (muon vertex). The red line is for the goodness with the vertex at the decay electron position. Green curves denot threshold for identifying candidate peaks.

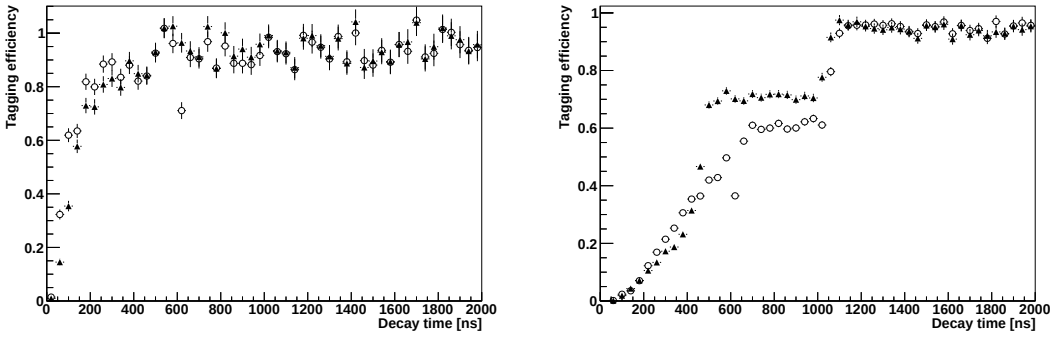

FIGURE E.4: Tagging efficiency for the Michel electron from cosmic ray muon after improvement. The left figure shows the sub-GeV cosmic ray muon while the right figure is for multi-GeV muon. Open circles are the electrons tagged by APFit, and full triangles are for fiTQun.

The tagging efficiency of fiTQun for the Michel electron from cosmic ray muon is improved significantly for multi-GeV muon after revision, as shown shown in Figure E.4. The efficiency are summarized in Table E.1.

The flat from 500 ns to 1000 ns on the fiTQun tagging efficiency is due to effect of time window. It is required that each PMT hits at most once in one time window. More hits at the same PMT within the same time window will be ignored. As shown in Figure E.5, the tagging efficiency decreases as the increase of parent muon's momentum. More PMTs will be hit by the light from the muon with a higher momentum, which makes the hits from the decay electron ignored. The tagging efficiency is limited by this effect and keeps stable until the end of the time window.

In this appendix, all the study described until now uses a fiducial volume defined as

Reconstruction		fiTQun After improvement	fiTQun Before improvement	APFit
Sub-GeV Muon	Data	89.31% ±0.16%	89.55% ±0.53%	88.93% ±0.35%
	MC	88.43% ±0.39%	88.64% ±0.31%	88.53% ±0.39%
Multi-GeV Muon	Data	74.48% ±0.10%	69.01% ±0.33%	72.31% ±0.20%
	MC	73.55% ±0.22%	67.86%±0.20%	71.38% ±0.23%

TABLE E.1: Decay e tagging efficiency for cosmic ray muon.

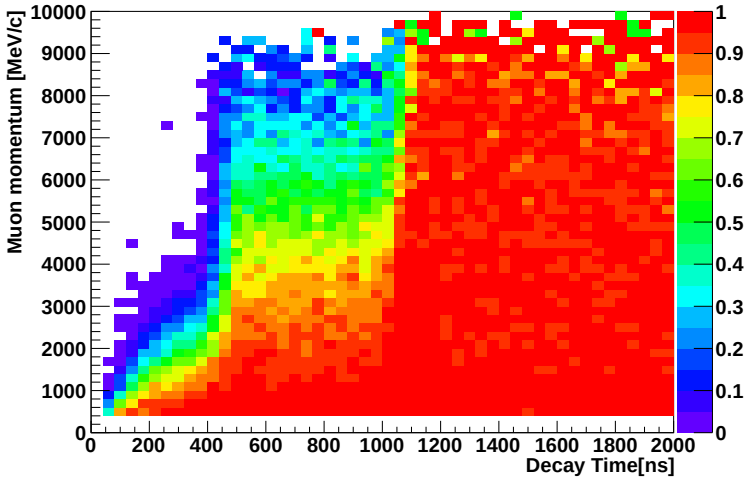

FIGURE E.5: Tagging efficiency for the Michel electron from cosmic ray muon. The horizontal axis shows the decay time, while the vertical axis represents the momentum of parent muon. The efficiency is denoted by the color.

the region located more than 2 m from the ID wall. As introduced Section 7.3, the fiducial volume used in atmospheric neutrino analysis has been extended to the region located more than 50 cm. Comparing with the efficiency within the conventional FV (c.f. Table E.1), Table E.2 shows that the tagging efficiency decreased for multi-GeV muon when the predicted stopping point of muon near the wall. Besides the effect of the time window introduced before, the resolution of predicted stopping point will also affect the tagging efficiency evaluation. The stopping point is predicted based on track length, which is estimated by the momentum of muon and the energy loss in water (∼2.3 MeV/ cm), and the entrance position. The resolution of the predicted stopping point for a high energy muon is not as good as the one for low energy muon, which makes that the muon stopped out of the ID might be reconstructed within the region of 50 cm $< D_{\mathrm{wall}} <$ 200 cm. The Michel electron out of the ID is another reason of such decrease.

50 cm $< D_{\text{wall}} <$ 200 cm		fiTQun	APFit
Sub-GeV Muon	Data	89.47% ±0.08%	88.79% ±0.08%
	MC	88.72% ±0.15%	88.69% ±0.15%
Multi-GeV Muon	Data	61.98% ±0.12%	60.59% ±0.12%
	MC	59.91% ±0.23%	58.76%±0.24%

TABLE E.2: Decay e tagging efficiency for cosmic ray muon in new region 50 cm$< D_{\text{wall}} <$ 200 cm.

Bibliography

[1] Y. Fukuda et al. Evidence for oscillation of atmospheric neutrinos. *Phys. Rev. Lett.*, 81:1562–1567, 1998. doi: 10.1103/PhysRevLett.81.1562.

[2] S. Fukuda et al. Determination of solar neutrino oscillation parameters using 1496 days of Super-Kamiokande I data. *Phys. Lett.*, B539:179–187, 2002. doi: 10.1016/S0370-2693(02)02090-7.

[3] B. Aharmim et al. Electron energy spectra, fluxes, and day-night asymmetries of B-8 solar neutrinos from measurements with NaCl dissolved in the heavy-water detector at the Sudbury Neutrino Observatory. *Phys. Rev.*, C72:055502, 2005. doi: 10.1103/PhysRevC.72.055502.

[4] Stephen J. Parke. Determining the neutrino mass hierarchy. In *Third NO-VE International Workshop on Neutrino Oscillations in Venice : Fifty years after the neutrino esperimental discovery : Venezia, February 7-10, 2006, Istituto Veneto di Scienze, Lettere ed Arti, Campo Santo Stefano*, pages 115–125, 2006. URL `http://lss.fnal.gov/cgi-bin/find_paper.pl?conf-06-248`.

[5] A. Gando et al. Search for Majorana Neutrinos near the Inverted Mass Hierarchy Region with KamLAND-Zen. *Phys. Rev. Lett.*, 117(8):082503, 2016. doi: 10.1103/PhysRevLett.117.109903,10.1103/PhysRevLett.117.082503. [Addendum: Phys. Rev. Lett.117,no.10,109903(2016)].

[6] K. Abe et al. Atmospheric neutrino oscillation analysis with external constraints in Super-Kamiokande I-IV. *Phys.Rev.*, D97:072001, 2018.

[7] Y. Fukuda et al. The Super-Kamiokande detector. *Nucl. Instrum. Meth.*, A501: 418–462, 2003. doi: 10.1016/S0168-9002(03)00425-X.

[8] Chizue Ishihara. *Full three flavor oscillation analysis of atmospheric neutrino data observed in Super-Kamiokande.* PhD thesis, Tokyo U., 2010. URL `http://www-rccn.icrr.u-tokyo.ac.jp/kajita/thesis/isihara_dthesis.pdf`.

[9] H. Nishino, K. Awai, Y. Hayato, S. Nakayama, K. Okumura, M. Shiozawa, A. Takeda, K. Ishikawa, A. Minegishi, and Y. Arai. High-speed charge-to-time converter ASIC for the Super-Kamiokande detector. *Nucl. Instrum. Meth.*, A610: 710–717, 2009. doi: 10.1016/j.nima.2009.09.026.

[10] M. Honda, T. Kajita, K. Kasahara, and S. Midorikawa. Improvement of low energy atmospheric neutrino flux calculation using the JAM nuclear interaction model. *Phys.Rev.*, D83:123001, 2011. doi: 10.1103/PhysRevD.83.123001.

[11] Veronique Bernard, Latifa Elouadrhiri, and Ulf-G. Meissner. Axial structure of the nucleon: Topical Review. *J. Phys.*, G28:R1–R35, 2002. doi: 10.1088/0954-3899/28/1/201.

[12] S. J. Barish et al. Study of Neutrino Interactions in Hydrogen and Deuterium. 1. Description of the Experiment and Study of the Reaction Neutrino d –¿ mu- p p(s). *Phys. Rev.*, D16:3103, 1977. doi: 10.1103/PhysRevD.16.3103.

[13] S. Bonetti, G. Carnesecchi, D. Cavalli, P. Negri, A. Pullia, et al. Study of Quasielastic Reactions of Neutrino and anti-neutrino in Gargamelle. *Nuovo Cim.*, A38: 260–270, 1977. doi: 10.1007/BF02730023.

[14] M. Pohl et al. EXPERIMENTAL STUDY OF THE REACTION neutrino N —> MU- P. *Lett. Nuovo Cim.*, 26:332–336, 1979. doi: 10.1007/BF02746631. [,75(1979)].

[15] A.I. Mukhin, V.F. Perelygin, K.E. Shestermanov, A.A. Volkov, A.S. Vovenko, et al. ENERGY DEPENDENCE OF TOTAL CROSS-SECTIONS FOR NEUTRINO AND ANTI-NEUTRINO INTERACTIONS AT ENERGIES BELOW 35-GeV. *Sov.J.Nucl.Phys.*, 30:528, 1979.

[16] S.V. Belikov, A.P. Bugorsky, V.Sh. Epshtein, N.V. Kalganov, L.A. Klimenko, et al. QUASIELASTIC NEUTRINO AND ANTI-NEUTRINOS SCATTERING: TOTAL CROSS-SECTIONS, AXIAL VECTOR FORM-FACTOR. *Z.Phys.*, A320: 625, 1985. doi: 10.1007/BF01411863.

[17] J. Brunner et al. QUASIELASTIC NUCLEON AND HYPERON PRODUCTION BY NEUTRINOS AND ANTI-NEUTRINOS WITH ENERGIES BELOW 30-GeV. *Z.Phys.*, C45:551, 1990. doi: 10.1007/BF01556267.

[18] Yoshinari Hayato. A neutrino interaction simulation program library NEUT. *Acta Phys.Polon.*, B40:2477–2489, 2009.

[19] Patrick de Perio. NEUT pion FSI. *AIP Conf. Proc.*, 1405:223–228, 2011. doi: 10.1063/1.3661590.

[20] E. S. Pinzon Guerra et al. Measurement of σ_{ABS} and σ_{CX} of π^+ on carbon by the Dual Use Experiment at TRIUMF (DUET). *Phys. Rev.*, C95(4):045203, 2017. doi: 10.1103/PhysRevC.95.045203.

[21] K. Abe, Y. Hayato, T. Iida, K. Iyogi, J. Kameda, et al. Calibration of the Super-Kamiokande Detector. *Nucl.Instrum.Meth.*, A737:253–272, 2014. doi: 10.1016/j.nima.2013.11.081.

[22] K. Abe et al. Combined Analysis of Neutrino and Antineutrino Oscillations at T2K. *Phys. Rev. Lett.*, 118(15):151801, 2017. doi: 10.1103/PhysRevLett.118.151801.

[23] P. Adamson et al. Measurement of the neutrino mixing angle θ_{23} in NOvA. *Phys. Rev. Lett.*, 118(15):151802, 2017. doi: 10.1103/PhysRevLett.118.151802.

[24] M. G. Aartsen et al. Neutrino oscillation studies with IceCube-DeepCore. *Nucl. Phys.*, B908:161–177, 2016. doi: 10.1016/j.nuclphysb.2016.03.028.

[25] P. Adamson et al. Combined analysis of ν_μ disappearance and $\nu_\mu \to \nu_e$ appearance in MINOS using accelerator and atmospheric neutrinos. *Phys. Rev. Lett.*, 112:191801, 2014. doi: 10.1103/PhysRevLett.112.191801.

[26] K. Abe et al. The T2K Experiment. *Nucl.Instrum.Meth.*, A659:106–135, 2011. doi: 10.1016/j.nima.2011.06.067.

[27] C. Patrignani et al. Review of Particle Physics. *Chin. Phys.*, C40(10):100001, 2016. doi: 10.1088/1674-1137/40/10/100001. and 2017 update.

[28] Lee Ka Pik. *Study of the neutrino mass hierarchy with the atmospheric neutrino data observed in Super-Kamiokande.* PhD thesis, Tokyo U., 2012. URL `http://www-sk.icrr.u-tokyo.ac.jp/sk/pub/index.html#dthesis`.

[29] C. L. Cowan, F. Reines, F. B. Harrison, H. W. Kruse, and A. D. McGuire. Detection of the free neutrino: A Confirmation. *Science*, 124:103–104, 1956. doi: 10.1126/science.124.3212.103.

[30] G. Danby, J. M. Gaillard, Konstantin A. Goulianos, L. M. Lederman, Nari B. Mistry, M. Schwartz, and J. Steinberger. Observation of High-Energy Neutrino Reactions and the Existence of Two Kinds of Neutrinos. *Phys. Rev. Lett.*, 9:36–44, 1962. doi: 10.1103/PhysRevLett.9.36.

[31] K. Kodama et al. Observation of tau neutrino interactions. *Phys. Lett.*, B504:218–224, 2001. doi: 10.1016/S0370-2693(01)00307-0.

[32] S. Schael et al. Precision electroweak measurements on the Z resonance. *Phys. Rept.*, 427:257–454, 2006. doi: 10.1016/j.physrep.2005.12.006.

[33] A. A. Aguilar-Arevalo et al. Significant Excess of ElectronLike Events in the MiniBooNE Short-Baseline Neutrino Experiment. *Phys. Rev. Lett.*, 121(22):221801, 2018. doi: 10.1103/PhysRevLett.121.221801.

[34] K. Abe et al. Search for CP Violation in Neutrino and Antineutrino Oscillations by the T2K Experiment with 2.2×10^{21} Protons on Target. *Phys. Rev. Lett.*, 121 (17):171802, 2018. doi: 10.1103/PhysRevLett.121.171802.

[35] Raymond Davis, Jr., Don S. Harmer, and Kenneth C. Hoffman. Search for neutrinos from the sun. *Phys. Rev. Lett.*, 20:1205–1209, 1968. doi: 10.1103/PhysRevLett.20.1205.

[36] E. Aliu et al. Evidence for muon neutrino oscillation in an accelerator-based experiment. *Phys. Rev. Lett.*, 94:081802, 2005. doi: 10.1103/PhysRevLett.94.081802.

[37] F. P. An et al. Observation of electron-antineutrino disappearance at Daya Bay. *Phys. Rev. Lett.*, 108:171803, 2012. doi: 10.1103/PhysRevLett.108.171803.

[38] J.K. Ahn et al. Observation of Reactor Electron Antineutrino Disappearance in the RENO Experiment. *Phys.Rev.Lett.*, 108:191802, 2012. doi: 10.1103/PhysRevLett.108.191802.

[39] Z. Maki, M. Nakagawa, and S. Sakata. Remarks on the unified model of elementary particles. *Prog. Theor. Phys.*, 28:870, 1962. doi: 10.1143/PTP.28.870.

[40] B. Pontecorvo. Neutrino experiments and the question of leptonic-charge conservation. *Sov. Phys. JETP*, 26:984–988, 1968.

[41] P. Adamson et al. Constraints on Oscillation Parameters from ν_e Appearance and ν_μ Disappearance in NOvA. *Phys. Rev. Lett.*, 118(23):231801, 2017. doi: 10.1103/PhysRevLett.118.231801.

[42] R. Acciarri et al. Long-Baseline Neutrino Facility (LBNF) and Deep Underground Neutrino Experiment (DUNE). 2016.

[43] Fengpeng An et al. Neutrino Physics with JUNO. *J. Phys.*, G43(3):030401, 2016. doi: 10.1088/0954-3899/43/3/030401.

[44] K. Abe et al. Hyper-Kamiokande Design Report. 2018.

[45] K. S. Hirata et al. Observation of a small atmospheric muon-neutrino / electron-neutrino ratio in Kamiokande. *Phys. Lett.*, B280:146–152, 1992. doi: 10.1016/0370-2693(92)90788-6.

[46] R. Becker-Szendy et al. The Electron-neutrino and muon-neutrino content of the atmospheric flux. *Phys. Rev.*, D46:3720–3724, 1992. doi: 10.1103/PhysRevD.46.3720.

[47] M. Ambrosio et al. Measurement of the atmospheric neutrino induced upgoing muon flux using MACRO. *Phys. Lett.*, B434:451–457, 1998. doi: 10.1016/S0370-2693(98)00885-5.

[48] Y. Fukuda et al. Measurement of the flux and zenith angle distribution of upward through going muons by Super-Kamiokande. *Phys. Rev. Lett.*, 82:2644–2648, 1999. doi: 10.1103/PhysRevLett.82.2644.

[49] Y. Ashie et al. Evidence for an oscillatory signature in atmospheric neutrino oscillation. *Phys. Rev. Lett.*, 93:101801, 2004. doi: 10.1103/PhysRevLett.93.101801.

[50] M. H. Ahn et al. Measurement of Neutrino Oscillation by the K2K Experiment. *Phys. Rev.*, D74:072003, 2006. doi: 10.1103/PhysRevD.74.072003.

[51] P. Adamson et al. Measurement of Neutrino Oscillations with the MINOS Detectors in the NuMI Beam. *Phys. Rev. Lett.*, 101:131802, 2008. doi: 10.1103/PhysRevLett.101.131802.

[52] A. I. Abazov et al. Search for neutrinos from sun using the reaction Ga-71 (electron-neutrino e-) Ge-71. *Phys. Rev. Lett.*, 67:3332–3335, 1991. doi: 10.1103/PhysRevLett.67.3332.

[53] P. Anselmann et al. Solar neutrinos observed by GALLEX at Gran Sasso. *Phys. Lett.*, B285:376–389, 1992. doi: 10.1016/0370-2693(92)91521-A.

[54] K. S. Hirata et al. Observation of B-8 Solar Neutrinos in the Kamiokande-II Detector. *Phys. Rev. Lett.*, 63:16, 1989. doi: 10.1103/PhysRevLett.63.16.

[55] Q. R. Ahmad et al. Direct evidence for neutrino flavor transformation from neutral current interactions in the Sudbury Neutrino Observatory. *Phys. Rev. Lett.*, 89:011301, 2002. doi: 10.1103/PhysRevLett.89.011301.

[56] J. Boger et al. The Sudbury neutrino observatory. *Nucl. Instrum. Meth.*, A449:172–207, 2000. doi: 10.1016/S0168-9002(99)01469-2.

[57] L. Wolfenstein. Neutrino oscillations in matter. *Phys. Rev.*, D17:2369–2374, 1978. doi: 10.1103/PhysRevD.17.2369.

[58] S. P. Mikheev and A. Yu. Smirnov. Resonance enhancement of oscillations in matter and solar neutrino spectroscopy. *Sov. J. Nucl. Phys.*, 42:913–917, 1985.

[59] S. Abe et al. Precision Measurement of Neutrino Oscillation Parameters with KamLAND. *Phys. Rev. Lett.*, 100:221803, 2008. doi: 10.1103/PhysRevLett.100.221803.

[60] M. Apollonio et al. Search for neutrino oscillations on a long baseline at the CHOOZ nuclear power station. *Eur. Phys. J.*, C27:331–374, 2003. doi: 10.1140/epjc/s2002-01127-9.

[61] Y. Abe et al. Indication for the disappearance of reactor electron antineutrinos in the Double Chooz experiment. *Phys.Rev.Lett.*, 108:131801, 2012. doi: 10.1103/PhysRevLett.108.131801.

[62] K. Abe et al. Observation of Electron Neutrino Appearance in a Muon Neutrino Beam. 2013.

[63] M. Fukugita and T. Yanagida. Baryogenesis Without Grand Unification. *Phys. Lett.*, B174:45–47, 1986. doi: 10.1016/0370-2693(86)91126-3.

[64] K. Abe et al. Neutrino oscillation physics potential of the T2K experiment. *PTEP*, 2015(4):043C01, 2015. doi: 10.1093/ptep/ptv031.

[65] C. Giunti, C.W. Kim, and M. Monteno. Atmospheric neutrino oscillations with three neutrinos and a mass hierarchy. *Nucl.Phys*, B521:3–36, 1998. doi: 10.1016/S0550-3213(98)00105-9.

[66] M. V. Chizhov and S. T. Petcov. New conditions for a total neutrino conversion in a medium. *Phys. Rev. Lett.*, 83:1096–1099, 1999. doi: 10.1103/PhysRevLett.83.1096.

[67] O. L. G. Peres and A. Yu. Smirnov. Testing the solar neutrino conversion with atmospheric neutrinos. *Phys. Lett.*, B456:204–213, 1999. doi: 10.1016/S0370-2693(99)00487-6.

[68] O. L. G. Peres and A. Yu. Smirnov. Atmospheric neutrinos: LMA oscillations, U(e3) induced interference and CP violation. *Nucl. Phys.*, B680:479–509, 2004. doi: 10.1016/j.nuclphysb.2003.12.017.

[69] Hiroyuki Sekiya. The Super-Kamiokande Gadolinium Project. *PoS*, ICHEP2016:982, 2016. doi: 10.22323/1.282.0982.

[70] I. M. Frank and I. E. Tamm. Coherent visible radiation of fast electrons passing through matter. *Compt. Rend. Acad. Sci. URSS*, 14(3):109–114, 1937. doi: 10.1007/978-3-642-74626-0_2,10.3367/UFNr.0093.196710o.0388. [Usp. Fiz. Nauk93,no.2,388(1967)].

[71] H. Kume, S. Sawaki, M. Ito, K. Arisaka, T. Kajita, A. Nishimura, and A. Suzuki. 20-INCH DIAMETER PHOTOMULTIPLIER. *Nucl. Instrum. Meth.*, 205:443–449, 1983. doi: 10.1016/0167-5087(83)90007-8.

[72] A. Suzuki, M. Mori, K. Kaneyuki, T. Tanimori, J. Takeuchi, H. Kyushima, and Y. Ohashi. Improvement of 20-inch diameter photomultiplier tubes. *Nucl. Instrum. Meth.*, A329:299–313, 1993. doi: 10.1016/0168-9002(93)90949-I.

[73] R. Becker-Szendy et al. IMB-3: A Large water Cherenkov detector for nucleon decay and neutrino interactions. *Nucl. Instrum. Meth.*, A324:363–382, 1993. doi: 10.1016/0168-9002(93)90998-W.

[74] Y. Takeuchi et al. Measurement of radon concentrations at Super-Kamiokande. *Phys. Lett.*, B452:418–424, 1999. doi: 10.1016/S0370-2693(99)00311-1.

[75] Hirokazu Ikeda, Masaki Mori, Tohru Tanimori, Ken-ichi Kihara, Yoichiro Suzuki, and Yasuhiko Haren. Front end hybrid circuit for Super-Kamiokande. *Nucl. Instrum. Meth.*, A320:310–316, 1992. doi: 10.1016/0168-9002(92)90791-2.

[76] Morihiro Honda, T. Kajita, K. Kasahara, S. Midorikawa, and T. Sanuki. Calculation of atmospheric neutrino flux using the interaction model calibrated with atmospheric muon data. *Phys.Rev.*, D75:043006, 2007. doi: 10.1103/PhysRevD.75.043006.

[77] G. Battistoni, A. Ferrari, T. Montaruli, and P. R. Sala. The FLUKA atmospheric neutrino flux calculation. *Astropart. Phys.*, 19:269–290, 2003. doi: 10.1016/S0927-6505(02)00246-3. [Erratum: Astropart. Phys.19,291(2003)].

[78] G. D. Barr, T. K. Gaisser, P. Lipari, Simon Robbins, and T. Stanev. A Three - dimensional calculation of atmospheric neutrinos. *Phys. Rev.*, D70:023006, 2004. doi: 10.1103/PhysRevD.70.023006.

[79] T. Sanuki et al. Precise measurement of cosmic ray proton and helium spectra with the BESS spectrometer. *Astrophys. J.*, 545:1135, 2000. doi: 10.1086/317873.

[80] Sadakazu Haino et al. Measurements of primary and atmospheric cosmic - ray spectra with the BESS-TeV spectrometer. *Phys. Lett.*, B594:35–46, 2004. doi: 10.1016/j.physletb.2004.05.019.

[81] J. Alcaraz et al. Cosmic protons. *Phys. Lett.*, B490:27–35, 2000. doi: 10.1016/S0370-2693(00)00970-9.

[82] NASA. U.S. Standard Atmosphere, 1976. `http://nssdc.gsfc.nasa.gov/space/model/atmos/us_standard.html`.

[83] Stefan Maus, Susan McLean, Hermann Luhr, Martin Rother, Wolfgang Mai, and Sungchan Choi. Ngdc/gfz candidate models for the 10th generation international geomagnetic reference field. *Earth, Planets and Space*, 57(12):1151–1156, 2005. doi: 10.1186/BF03351898.

[84] Koji Niita, Tatsuhiko Sato, Hiroshi Nakashima, Hiroshi Iwase, Hiroyuki Nose, and Lembit Sihver. PHITS: A particle and heavy ion transport code system. *Radiat. Meas.*, 41:1080–1090, 2006. doi: 10.1016/j.radmeas.2006.07.013.

[85] Stefan Roesler, Ralph Engel, and Johannes Ranft. The Monte Carlo event generator DPMJET-III. In *Advanced Monte Carlo for radiation physics, particle transport simulation and applications. Proceedings, Conference, MC2000, Lisbon, Portugal, October 23-26, 2000*, pages 1033–1038, 2000. doi: 10.1007/978-3-642-18211-2_166. URL `http://www-public.slac.stanford.edu/sciDoc/docMeta.aspx?slacPubNumber=SLAC-PUB-8740`.

[86] M. Motoki et al. Precise measurements of atmospheric muon fluxes with the BESS spectrometer. *Astropart. Phys.*, 19:113–126, 2003. doi: 10.1016/S0927-6505(02)00195-0.

[87] P. Achard et al. Measurement of the atmospheric muon spectrum from 20-GeV to 3000-GeV. *Phys. Lett.*, B598:15–32, 2004. doi: 10.1016/j.physletb.2004.08.003.

[88] Y. Hayato. NEUT. *Nucl. Phys. Proc. Suppl.*, 112:171–176, 2002. doi: 10.1016/S0920-5632(02)01759-0. [,171(2002)].

[89] S. Jadach, Z. Was, R. Decker, and Johann H. Kuhn. The tau decay library TAUOLA: Version 2.4. *Comput. Phys. Commun.*, 76:361–380, 1993. doi: 10.1016/0010-4655(93)90061-G.

[90] C. H. Llewellyn Smith. Neutrino Reactions at Accelerator Energies. *Phys. Rept.*, 3:261–379, 1972. doi: 10.1016/0370-1573(72)90010-5.

[91] J. Nieves, I. Ruiz Simo, and M. J. Vicente Vacas. The nucleon axial mass and the MiniBooNE Quasielastic Neutrino-Nucleus Scattering problem. *Phys. Lett.*, B707:72–75, 2012. doi: 10.1016/j.physletb.2011.11.061.

[92] R. Gran, J. Nieves, F. Sanchez, and M. J. Vicente Vacas. Neutrino-nucleus quasi-elastic and 2p2h interactions up to 10 GeV. *Phys. Rev.*, D88:113007, 2013. doi: 10.1103/PhysRevD.88.113007.

[93] J. Nieves, I. Ruiz Simo, and M. J. Vicente Vacas. Inclusive Charged–Current Neutrino–Nucleus Reactions. *Phys. Rev.*, C83:045501, 2011. doi: doi:10.1103/PhysRevC.83.045501.

[94] Dieter Rein and Lalit M. Sehgal. Neutrino Excitation of Baryon Resonances and Single Pion Production. *Annals Phys.*, 133:79–153, 1981. doi: 10.1016/0003-4916(81)90242-6.

[95] Krzysztof M. Graczyk and Jan T. Sobczyk. Form Factors in the Quark Resonance Model. *Phys. Rev.*, D77:053001, 2008. doi: 10.1103/PhysRevD.79.079903,10.1103/PhysRevD.77.053001. [Erratum: Phys. Rev.D79,079903(2009)].

[96] Callum Wilkinson, Philip Rodrigues, Susan Cartwright, Lee Thompson, and Kevin McFarland. Reanalysis of bubble chamber measurements of muon-neutrino induced single pion production. *Phys. Rev.*, D90(11):112017, 2014. doi: 10.1103/PhysRevD.90.112017.

[97] D. Rein. Angular Distribution in Neutrino Induced Single Pion Production Processes. *Z. Phys.*, C35:43–64, 1987. doi: 10.1007/BF01561054.

[98] S. K. Singh, M. J. Vicente-Vacas, and E. Oset. Nuclear effects in neutrinoproduction of Delta at intermediate energies. *Phys. Lett.*, B416:23–28, 1998. doi: 10.1016/S0370-2693(97)01325-7. [Erratum: Phys. Lett.B423,428(1998)].

[99] Ch. Berger and L. M. Sehgal. PCAC and coherent pion production by low energy neutrinos. *Phys. Rev.*, D79:053003, 2009. doi: 10.1103/PhysRevD.79.053003.

[100] M. Gluck, E. Reya, and A. Vogt. Dynamical parton distributions revisited. *Eur. Phys. J.*, C5:461, 1998. doi: 10.1007/s100529800978.

[101] Arie Bodek and Un-ki Yang. A Unified model for inelastic e - N and nu - N cross-sections at all Q**2. *AIP Conf. Proc.*, 792:257–260, 2005. doi: 10.1063/1.2122031. [,257(2005)].

[102] M. Derrick et al. Properties of the Hadronic System Resulting from anti-Muon-neutrino p Interactions. *Phys. Rev.*, D17:1, 1978. doi: 10.1103/PhysRevD.17.1.

[103] S. Barlag et al. Charged Hadron Multiplicities in High-energy Anti-muon Neutrino n and Anti-muon Neutrino p Interactions. *Z. Phys.*, C11:283, 1982. doi: 10.1007/BF01578279. [Erratum: Z. Phys.C14,281(1982)].

[104] Roger D. Woods and David S. Saxon. Diffuse Surface Optical Model for Nucleon-Nuclei Scattering. *Phys. Rev.*, 95:577–578, 1954. doi: 10.1103/PhysRev.95.577.

[105] B. R. Martin and M. K. Pidcock. Anti-K n Interactions in the Resonance Region. 1. Analysis of Data. *Nucl. Phys.*, B126:266–284, 1977. doi: 10.1016/0550-3213(77)90382-0.

[106] B. R. Martin and M. K. Pidcock. Anti-K n Interactions in the Resonance Region. 2. Amplitudes. *Nucl. Phys.*, B126:285–297, 1977. doi: 10.1016/0550-3213(77)90383-2.

[107] J. S. Hyslop, R. A. Arndt, L. D. Roper, and R. L. Workman. Partial wave analysis of K+ nucleon scattering. *Phys. Rev.*, D46:961–969, 1992. doi: 10.1103/PhysRevD.46.961.

[108] David A. Sparrow. Effects of the Nuclear Medium on the Observation of Baryon Number Violation. *AIP Conf. Proc.*, 123:1019–1025, 1984. doi: 10.1063/1.34840.

[109] Rene Brun, F. Bruyant, Federico Carminati, Simone Giani, M. Maire, A. McPherson, G. Patrick, and L. Urban. GEANT Detector Description and Simulation Tool. 1994.

[110] C. Zeitnitz and T. A. Gabriel. The GEANT - CALOR interface and benchmark calculations of ZEUS test calorimeters. *Nucl. Instrum. Meth.*, A349:106–111, 1994. doi: 10.1016/0168-9002(94)90613-0.

[111] Y. Ashie. et al. A Measurement of Atmospheric Neutrino Oscillation Parameters by Super-Kamiokande I. *Phys.Rev.*, D71:112005, 2005. doi: 10.1103/PhysRevD.71.112005.

[112] M. Shiozawa et al. Reconstruction algorithms in the Super-Kamiokande large water Cherenkov detector. *Nucl.Instrum.Meth.*, A433:240–246, 1999.

[113] R. B. Patterson, E. M. Laird, Y. Liu, P. D. Meyers, I. Stancu, and H. A. Tanaka. The extended-track reconstruction for MiniBooNE. *Nucl.Instrum.Meth*, A608:206–224, 2009. doi: 10.1016/j.nima.2009.06.064.

[114] F. James. MINUIT Function Minimization and Error Analysis: Reference Manual Version 94.1. 1994.

[115] Y. Fukuda et al. Measurements of the solar neutrino flux from Super-Kamiokande's first 300 days. *Phys. Rev. Lett.*, 81:1158–1162, 1998. doi: 10.1103/PhysRevLett.81.1158,10.1103/PhysRevLett.81.4279. [Erratum: Phys. Rev. Lett.81,4279(1998)].

[116] Y. Fukuda et al. Measurement of the solar neutrino energy spectrum using neutrino electron scattering. *Phys. Rev. Lett.*, 82:2430–2434, 1999. doi: 10.1103/PhysRevLett.82.2430.

[117] S. Fukuda et al. Solar B-8 and hep neutrino measurements from 1258 days of Super-Kamiokande data. *Phys. Rev. Lett.*, 86:5651–5655, 2001. doi: 10.1103/PhysRevLett.86.5651.

[118] R. Wendell et al. Atmospheric neutrino oscillation analysis with sub-leading effects in Super-Kamiokande I, II, and III. *Phys.Rev.*, D81:092004, 2010. doi: 10.1103/PhysRevD.81.092004.

[119] G. L. Fogli, E. Lisi, A. Marrone, D. Montanino, and A. Palazzo. Getting the most from the statistical analysis of solar neutrino oscillations. *Phys.Rev.*, D66:053010, 2002. doi: 10.1103/PhysRevD.66.053010.

[120] Gaku Mitsuka. *Study of Non-Standard Neutrino Interactions with Atmospheric Neutr ino Data in Super-Kamiokande*. PhD thesis, Tokyo U., 2009. URL `http://www-sk.icrr.u-tokyo.ac.jp/sk/pub/dthesis_feb9-mitsuka.pdf`.

[121] W. K. Hastings. Monte Carlo sampling methods using Markov chains and their applications. *Biometrika*, 57:97–109, 1970. doi: 10.1093/biomet/57.1.97.

[122] Yumiko Takenaga. *Atmospheric neutrino oscillation analysis with solar terms in Super-Kamiokande*. PhD thesis, Tokyo U., 2008. URL `http://www-sk.icrr.u-tokyo.ac.jp/sk/pub/index.html#dthesis`.

[123] J. Nieves, Jose Enrique Amaro, and M. Valverde. Inclusive quasi-elastic neutrino reactions. *Phys. Rev.*, C70:055503, 2004. doi: 10.1103/PhysRevC.70.055503,10.1103/PhysRevC.72.019902. [Erratum: Phys. Rev.C72,019902(2005)].

[124] A. Capella, A. Kaidalov, C. Merino, and J. Tran Thanh Van. Structure functions and low x physics. *Phys. Lett.*, B337:358, 1994.

[125] M. Gluck, E. Reya, and A. Vogt. Dynamical parton distributions revisited. *Eur.Phys.J.*, C5:461–470, 1998. doi: 10.1007/s100520050289.

[126] E. Hernandez, J. Nieves, and M. Valverde. Weak pion production off the nucleon. *Phys. Rev.*, D76:033005, 2007.

[127] E. Pinzon. *Measurement of Pion-Carbon Cross Sections at DUET and Measurement of Neutrino Oscillation Parameters at the T2K Experiment*. PhD thesis, York U., 2017.

[128] Alexander L. Read. Presentation of search results: The CL(s) technique. *J. Phys.*, G28:2693–2704, 2002. doi: 10.1088/0954-3899/28/10/313. [11(2002)].

[129] K. Abe et al. Updated T2K measurements of muon neutrino and antineutrino disappearance using 1.5e21 protons on target. 2017.

[130] K. Abe et al. Physics potentials with the second Hyper-Kamiokande detector in Korea. *PTEP*, 2018(6):063C01, 2018. doi: 10.1093/ptep/pty044.